



Lee, Kyung Ha (2019) *Suspension upgrades for future gravitational wave detectors*. PhD thesis.

<https://theses.gla.ac.uk/40954/>

Copyright and moral rights for this work are retained by the author

A copy can be downloaded for personal non-commercial research or study, without prior permission or charge

This work cannot be reproduced or quoted extensively from without first obtaining permission in writing from the author

The content must not be changed in any way or sold commercially in any format or medium without the formal permission of the author

When referring to this work, full bibliographic details including the author, title, awarding institution and date of the thesis must be given

Enlighten: Theses

<https://theses.gla.ac.uk/>
research-enlighten@glasgow.ac.uk

University of Glasgow

Suspension Upgrades for Future Gravitational Wave Detectors

by

Kyung Ha Lee, B.Sc. (Honors)

Department of Physics and Astronomy,
University of Glasgow

Presented as a thesis for the degree of Ph.D.
in the University of Glasgow, University Avenue,
Glasgow G12 8QQ.

Glasgow, United Kingdom

Sep, 2018

Contents

Table of Contents	iii
List of Figures	ix
List of Tables	xxi
Acknowledgements	xxv
Preface	xxvii
Summary	xxxii
1 Gravitational Waves	1
1.1 Introduction to Gravitational Waves	1
1.2 Sources of Gravitational Waves	3
1.2.1 Transient Sources	4
1.2.2 Continuous Sources	6
1.2.3 Stochastic Sources	7
1.3 Ground-based Gravitational Wave Detectors	8
1.3.1 Resonant Bar Detectors	8
1.3.2 Laser Interferometers	9
1.4 Noise Sources	14
1.4.1 Seismic Noise	15

1.4.2	Newtonian Noise	18
1.4.3	Quantum Noise Sources	20
1.4.4	Suspension Thermal Noise	22
1.4.5	Coating Brownian Noise	22
1.5	Status of Current Detectors and Future Upgrades	24
1.5.1	Advanced LIGO	24
1.5.2	Advanced Virgo	25
1.5.3	KAGRA	26
1.5.4	Discovery of Gravitational Waves	27
1.5.5	Future Detectors	34
1.6	Conclusions	37
2	Thermal Noise	39
2.1	Introduction	39
2.2	Sources of Dissipation	41
2.2.1	External Sources of Dissipation	41
2.2.2	Internal Sources of Dissipation	41
2.3	Thermal Noise in terms of Mechanical Loss	44
2.3.1	Thermal Noise in a Single Resonant System	44
2.3.2	Thermal Noise in Multi-Resonant Systems	46
2.4	Mechanical Loss in Fibres	47
2.4.1	Thermoelastic Loss	47
2.4.2	Surface Loss	52
2.4.3	Bulk Loss and Weld Loss	53
2.4.4	Dissipation Dilution	54
2.5	Resonant Modes of the Suspension Elements	57
2.5.1	Pendulum Modes	57
2.5.2	Violin Modes	57
2.5.3	Vertical Bounce Modes	59

2.5.4	Other Modes: Pitch, Yaw, Roll	60
2.5.5	Critical Resonant Modes in the Advanced LIGO	61
2.6	Quadruple Monolithic Suspension in Advanced LIGO	62
2.7	Conclusion	64
3	Advanced LIGO Room-Temperature Upgrade: High Stress Fibres	67
3.1	Introduction	67
3.2	Dominant Noise Sources in the Low Frequency Range	68
3.2.1	Seismic Noise	69
3.2.2	Suspension Thermal Noise	72
3.2.3	Coating Brownian Noise	74
3.3	Investigated Conditions: Stress on Fibres	75
3.4	Results	75
3.5	Conclusion	78
4	Enhanced Fibre Fabrication Technology	79
4.1	Introduction	79
4.2	Current Fibre Fabrication Technique	80
4.3	Enhanced Fibre Fabrication Technique	83
4.3.1	Camera Monitoring System and PID Feedback Control	83
4.3.2	Water Flow	91
4.3.3	Wait Time Before the Pull	94
4.3.4	Stabilised Polishing	96
4.3.5	Pull PID Gain Adjustment	98
4.3.6	Auto-peak	103
4.3.7	Possible future studies for the stabilisation system	110
4.4	Profiling the fibres	111
4.5	Results	116
4.6	Conclusions	127

5	Strength Tests	129
5.1	Introduction	129
5.2	Experimental Design	130
5.3	Detailed Analysis Methods	133
5.4	Results and Analysis	140
5.4.1	Breaking Stress Comparison	140
5.4.2	Breaking Point Analysis	143
5.5	Conclusion	149
6	Stress Corrosion Experiment	153
6.1	Introduction	153
6.2	Motivations for the Experimental Conditions	154
6.2.1	In-air and Vacuum	154
6.2.2	Range of Stress Tested	155
6.3	High Stress Fibre Fabrication	157
6.4	Experimental Design	162
6.5	Results	167
6.5.1	In-air Condition	167
6.5.2	Vacuum Condition	170
6.5.3	Comparison to Proctor data	172
6.6	Conclusions	176
7	Advanced LIGO Room-Temperature Upgrades	179
7.1	Introduction	179
7.2	Investigated Conditions	180
7.2.1	Mass	180
7.2.2	Length	183
7.2.3	Stress	185

7.2.4	Suspension Thermal Noise Calculation: Thermoelastic Nulling and Dilution Factor	186
7.3	Results	188
7.3.1	Stress Condition Comparison	188
7.3.2	Mass Condition Comparison	190
7.3.3	Length Condition Comparison	191
7.3.4	Investigation of the Optimum Condition	193
7.4	Conclusion	204
8	Conclusion	205
A	Derivation of Seismic Noise Optimisation Equations	209
A.1	Generalised System	210
A.2	Vertical Seismic Isolation	211
A.3	Longitudinal Stiffness Derivation	213
A.4	Optimal Masses	215
B	Calculation of Coating Brownian Noise Estimate	219
C	Matlab Codes Used for Noise Source Simulations	223
D	Python Code Used for the Stress Corrosion Experiment	225
E	Peak pixel intensity and fibre diameter	227

List of Figures

1.1	Impact of each polarisation on a ring of test particles when the gravitational waves pass through. The travelling direction of the gravitational waves is perpendicular to the plane of the page.	2
1.2	The gravitational wave spectrum with sources and detectors. (Credit: NASA Goddard Space Flight Center)	3
1.3	Global network of ground based interferometric detectors.	9
1.4	Schematic diagram of a simple Michelson Interferometer.	10
1.5	Schematic diagram of a Michelson Interferometer with Fabry-Perot arm cavities implemented.	11
1.6	Schematic diagram of a Michelson Interferometer with a Power Recycling Mirror and a Signal Recycling Mirror implemented.	12
1.7	Quantum strain noise for different Michelson interferometer configurations; (1) Red: simple Michelson interferometer, (2) Orange: Michelson interferometer with a Fabry-Perot cavity (FP), (3) Green: Michelson interferometer with FP and Power Recycling (PR), (4) Blue: Michelson interferometer with FP, PR, and Signal Recycling (SR).	13
1.8	Various noise sources in Advanced LIGO.	15
1.9	The LIGO Livingston Observatory seismic background in different representative conditions.	16
1.10	Modeled transfer function of aLIGO quadruple pendulum system.	17

1.11 Schematic drawing of the gravitational interaction between the Earth's surface and the test mass when the seismic surface wave passes.	18
1.12 Newtonian noise estimate for each LIGO site and different sources.	19
1.13 (a) CAD image of the suspension system of the Advanced LIGO detectors (b) SEM image of the mirror coating: multilayer stack of SiO ₂ (light) and TiO ₂ doped Ta ₂ O ₅ (dark)	23
1.14 Two LIGO detectors in the United States.	24
1.15 A drawing of the Advanced LIGO quadruple monolithic fused silica suspension design. The coordinate system is indicated in the diagram.	25
1.16 Sensitivity curve comparison between the initial Virgo and the Advanced Virgo.	26
1.17 Schematic diagram of KAGRA detector.	27
1.18 Estimated gravitational wave strain from GW150914.	28
1.19 Gravitational wave data from GW150914 for both Advanced LIGO detectors. The Hanford data have been time shifted in time and inverted to consider the relative orientation of detectors.	29
1.20 Gravitational wave signals from binary black hole systems.	30
1.21 Gravitational wave signals from binary neutron star system (GW170817) compared to previously detected signals from binary black hole systems.	31
1.22 Sky localisation for GW170817. The light blue contours show the localisation result from Hanford-Livingston analysis and the dark blue contours show that of Hanford-Livingston-Virgo analysis.	32
1.23 Sky localisation result for gravitational wave detections. For GW170814 and GW170817, which were detected by three detectors, the addition of Advanced Virgo data further constrained the sky position.	33
1.24 Design sensitivity for the A+ upgrade compared to the aLIGO strain noise in the Observing run 2 (O2) and the design sensitivity of the aLIGO.	35
1.25 Gravitational wave detectors' sensitivity curve and sources.	36

1.26	Differential acceleration spectrum of LISA Pathfinder (LPF) and the requirements for the LPF and LISA.	37
2.1	Suspension thermal noise comparison between different mechanical loss values (ϕ).	45
2.2	Finite element model of the monolithic suspension stage. The bonds to connect the ears to the test masses are also another source of thermal noise.	48
2.3	Schematic diagram showing the fundamental mechanism of thermoelastic loss.	49
2.4	Illustration of pendulum mode, violin mode, and vertical bounce mode.	58
2.5	Vertical motions are coupled into horizontal motion due to the curvature of the earth.	59
2.6	Other modes of the pendulum: Yaw, Pitch, Roll.	60
2.7	Different modes of suspension thermal noise.	61
2.8	A diagram of the Advanced LIGO quadruple monolithic fused silica suspension design.	63
2.9	Dumbbell-shaped fibre for the aLIGO suspension system. FEA ANSYS model image is provided by Dr. Alan Cumming.	64
3.1	Schematic diagram of the quadruple pendulum system. x_g and z_g represent longitudinal and vertical seismic motion respectively; x_1 to x_4 and z_1 to z_4 represent the motion of stages 1 to 4; m_1 to m_4 the mass of these stages; L_1 to L_4 the lengths of wire suspending these stages; k_1 to k_4 the stiffness of these stages, and σ the stress on the fused silica fibres.	69
3.2	The BSC-ISI requirement for the Advanced LIGO detectors.	71
3.3	Impact of varying the stress while keeping all other conditions the same. The current aLIGO condition was compared to the higher stress conditions (1 GPa, 2 GPa).	76

3.4	Impact of the fibre stress on the suspension thermal noise. The current aLIGO condition was compared to the higher stress conditions (1 GPa to 5 GPa).	77
4.1	Schematic drawing of the fused silica fibre pulling machine at the University of Glasgow. A rotating 45° mirror and two conical mirrors allow uniform heating 360° around the stock. When pulling starts, the upper stage travels upwards to pull a fibre, while the lower stage slowly travels downwards to feed new fused silica material into laser beam.	80
4.2	Uniform heating system applied to the pulling machine. Two conical mirrors and a rotating 45° mirror enable uniform heating of 360° around the fused silica stock.	81
4.3	Variation of the upper motor speed during a pull process corresponding to different regions of a fibre.	82
4.4	Laser power variation observed for 900 seconds. Although the power fluctuation is within the specification, which is $\pm 10\%$ for cold start and $\pm 6\%$ for 2 minutes after with the average power of 131.5 W, this instability becomes more critical when it is translated to the heating temperature of fused silica stock by the pulling machine.	84
4.5	(a) Fused silica fibre pulling machine with a camera feedback system to monitor the heating point. (b) Uniformly heated fused silica stock, as viewed by a camera (shown without ND filters). (c) Image of heating point taken by the camera feedback system. The green vertical line indicates the region where pixel data were taken.	86
4.6	Simplified diagram to show the stabilisation process.	87
4.7	Demonstration of combined impulse tests to confirm the obtained PID parameter set. A series of impulses were applied to the system in rapid succession for both unstabilised stabilised conditions.	88

4.8	Peak pixel intensity observed for 900 seconds without the stabilisation system, while the pulling machine was kept stationary.	89
4.9	Peak pixel intensity observed for 900 seconds with the stabilisation system, while the pulling machine was kept stationary (Typical).	90
4.10	Peak pixel intensity observed for 900 seconds with the stabilisation system, while the pulling machine was kept stationary (Best).	90
4.11	Peak pixel intensity data and laser feed values for (a) low water flow rate, (b) medium water flow rate, (c) high water flow rate.	92
4.12	Typical fluctuations due to mode hopping, overlaid on peak pixel intensity data for three pulls. To clearly show the comparison between the mode hop line and other pull peak pixel intensity lines, an offset of 1000 was added to the pull data (Pull 1, 2, 3).	94
4.13	Polishing and pulling area of the fused silica stock.	96
4.14	Comparison between unstabilised and stabilised polishing process. The stabilised polish process had 5 minutes of wait time before polishing. . .	97
4.15	Strength test results of unstabilised and stabilised pulls.	98
4.16	Correlation between pixel intensity stability and the upper motor velocity variation. The blue dotted line indicates the velocity of the upper motor. As the motor velocity changes, an instability was introduced. Four repetitive and identical trials were performed to confirm this pattern of two unstable regions at the beginning and at the end of the pull process.	99
4.17	Loss of light due to a smaller fibre diameter.	99
4.18	Observation of the peak pixel intensity depending on three different PID parameter adjustment timings: 2.8 mm/s, 2.1 mm/s, 0.01 mm/s	102

4.19	Correlation between pixel intensity stability and upper motor velocity variation. The red line indicates the velocity of the upper motor. Fluctuations at the beginning and at the end settled down faster but they were not completely eliminated. Four repetitive and identical trials were performed to investigate reproducibility. Each pull had the identical setpoint of 6000, but for better comparison of the fluctuation shape and timing, a consistent offset was introduced to Trial 2, 3, and 4.	103
4.20	Peak pixel intensity data and laser feed data during the pull with 3 minutes of wait time and pull PID adjustment.	104
4.21	Captured images of the fibre pulling from a video file	105
4.22	Peak pixel intensity index variation during a pull.	106
4.23	Investigation on the fluctuation tendency in different regions.	108
4.24	The index position after turning off the auto-peak function, relative to the peak pixel position.	109
4.25	Stabilised run with PID gain adjustment, 5 minutes of wait time, and the auto-peak function off.	110
4.26	Fibre profiling machine developed within the IGR	112
4.27	Correlation between the heating temperature fluctuation and the fibre geometry. As the peak pixel intensity showed a continuous sinusoidal fluctuation during the pull process, the corresponding fibre's diameter profile also showed an identical pattern.	113
4.28	A deliberate high step signal was introduced during the pull. The corresponding fibre was profiled and overlaid onto the heating intensity graph.	113
4.29	A deliberate low step signal was introduced during the pull. The corresponding fibre was profiled and overlaid onto the heating intensity graph.	114

4.30	A deliberate continuous step signal was introduced during the pull. The corresponding fibre was profiled and overlaid onto the heating intensity graph.	114
4.31	A deliberate sine signal was introduced during the pull. The corresponding fibre was profiled and overlaid onto the heating intensity graph.	115
4.32	Summary graphs of the peak pixel intensity analysis for the stabilised and the unstabilised pulls	120
4.33	One example of a pull with a random fluctuation while pulling the thin section. Despite the fluctuation, the average, standard deviation, minimum and maximum values of the peak pixel intensity were all improved compared to unstabilised pulls.	123
4.34	Comparison between unstabilised and stabilised pulls.	124
4.35	Comparison between the peak pixel intensity and the fibre diameter profile for a typical unstabilised pull and a typical stabilised pull. These figures show only the thin middle section which can demonstrate the correlation more clearly. The whole fibre comparison is shown in Appendix E. . . .	126
5.1	(a) CAD image of the strength testing machine used to investigate the maximum tensile stress of fused silica fibres (b) A high speed camera monitoring system setup in front of the strength testing machine	130
5.2	Fused silica fibre bonded to two cardboard pieces and clamped for the strength test.	131
5.3	Fused silica fibre bonded to two cardboard pieces and clamped for the strength test.	132
5.4	Screenshot of a fibre break taken from a video file (rotated 90 degrees). A ruler was attached next to the strength tester to measure the position of the breaking point. Due to a technical difficulty to show the thin fibre clearly from a screenshot, dotted lines were added to indicate the fibre. .	133

5.5	An example of the instant at which a fibre broke. The video file was investigated frame by frame to find the exact breaking frame.	135
5.6	An example of the instant at which a fibre broke. When the breaking frame was not as clear, the expected breaking point was deduced from the shattering direction of the fibre pieces.	136
5.7	The position of the top clamp and the bottom clamp before and after the strength test: (a) Initial position of the top clamp (b) Final position of the top clamp (c) Initial position of the bottom clamp (d) Final position of the bottom clamp.	138
5.8	The neck starting point for the initial length measurement of the fibre on the video file.	139
5.9	Schematic diagram of stretched fibre and how the breaking point position was adjusted with respect to the initial and final length of the fibre. . .	140
5.10	Strength test results comparison between different conditions: (1) current aLIGO condition, without stabilisation, 900 s polish, 25 fibres (2) stabilised, 900 s polish, 27 fibres (3) stabilised, 2200 s polish, 26 fibres (4) stabilised, 3000 s polish, 30 fibres. Stabilised fibres showed 30% decrease in standard deviation compared to unstabilised fibres. Longer polish conditions were chosen according to Dr. Alastair Heptonstall's data.	141
5.11	Strength test results comparison in histogram to show the breaking stress distribution.	142
5.12	Breaking point analysis for a high step fluctuation fibre, as in Figure 4.28. The fibre's peak pixel intensity data and diameter profile data are overlaid on a screenshot of the breaking moment taken by the high speed camera. Due to a technical difficulty to show the thin fibre clearly from a screenshot, dotted lines were added to indicate the fibre. Red lines indicate the breaking point of the fibre.	143
5.13	Breaking point analysis for a low step fluctuation fibre, as in Figure 4.29.	144

5.14	Breaking point analysis for a continuous fluctuation fibre, as in Figure 4.30.	144
5.15	Fibre peak pixel intensity data and diameter profile data overlaid on a screenshot of the breaking moment taken by the high speed camera. Due to the technical difficulty to show thin fibre clearly from a screenshot, dotted lines were added to indicate the fibre. Red lines indicate the breaking point of the fibre.	146
5.16	Example of a misaligned fibre: both the stock region and the fibre region have a misalignment. The stock region misalignment is due to the misaligned fibre clamps of the pulling machine. This misalignment happens during the polishing process. The misalignment in the fibre region is due to the laser beam misalignment.	148
6.1	Hang time of fused silica fibres in air and in vacuum depending on the applied tensile stress.	155
6.2	Stress corrosion experiment for different tensile stress performed in LIGO Hanford by Karl Toland.	156
6.3	A typical stabilised pull using the new 400 W laser.	158
6.4	One of the stocks bonded to fuse ends using epoxy adhesive and placed on the L-shaped cartridge.	159
6.5	One example of a misaligned fibre.	160
6.6	Two long L-section posts were attached to both the top and the bottom clamps after fabrication to minimise the risk of fibres getting touched during handling process.	161
6.7	Experimental set up to measure breaking time of fused silica fibres depending on different tensile stress.	163
6.8	Raspberry Pi 3 circuit for the stress corrosion experiment. Microswitches are operating normally closed, so that it would open when a fibre breaks.	164
6.9	Schematic diagram of experimental setup in the vacuum tank to measure breaking time of fused silica fibres.	165

6.10	Schematic diagram of the arrangement of 16 stress corrosion test setups in a vacuum tank. Red arrows indicate the order of installation.	166
6.11	Results of stress corrosion experiments performed in LIGO Hanford and Glasgow.	168
6.12	Thin section comparison between the profile data from Hanford and Glasgow.	169
6.13	Profile data comparison of the stock region.	170
6.14	Comparison of in-air stress corrosion experiments performed in LIGO Hanford and Glasgow.	171
6.15	Comparison between different trend lines calculated using different methods.	174
6.16	Summary of all stress corrosion experiments (Glasgow, Hanford, and Proctor) conducted in air and under vacuum.	175
7.1	Optimum mass configuration for: $m_4 = 80$ kg, $P = 248$ kg	183
7.2	Optimum mass configuration for: $m_4 = 160$ kg, $P = 390$ kg	183
7.3	Comparison between the aLIGO QUAD and a potential upgrade of the QUAD showing the limitation of the BSC vacuum chamber in which the suspension is located.	184
7.4	Dilution factor for different test masses calculated by Dr. Alan Cumming. (m_4 was varied from 40 kg to 200 kg in steps of 20 kg, with $L_4 = 1.1$ m) .	187
7.5	FEA ANSYS model of the fused silica fibre used to calculate the dilution factors for different test masses. Provided by Dr. Alan Cumming.	188
7.6	Impact of the stress condition change while keeping all other conditions the same. The current aLIGO condition was compared to the higher stress condition (770 MPa vs 1.2 GPa).	189
7.7	Impact of the test mass condition change while keeping all other conditions the same (40 kg vs 80 kg vs 160 kg).	190
7.8	Impact of a change in the length of the final stage (0.6 m vs 1.1 m).	192

7.9	Comparison between the current aLIGO condition, set aAH ($m_4 = 40$ kg, $L_4 = 0.6$ m, $L_T = 2.14$ m, $\sigma = 1.2$ GPa), aBH ($m_4 = 40$ kg, $L_4 = 1.1$ m, $L_T = 2.14$ m, $\sigma = 1.2$ GPa).	193
7.10	Comparison between the current aLIGO condition, set 1AH ($m_4 = 80$ kg, $L_4 = 0.6$ m, $L_T = 2.14$ m, $\sigma = 1.2$ GPa), 1BH ($m_4 = 80$ kg, $L_4 = 1.1$ m, $L_T = 2.14$ m, $\sigma = 1.2$ GPa).	194
7.11	Comparison between the current aLIGO condition, set 2AH ($m_4 = 160$ kg, $L_4 = 0.6$ m, $L_T = 2.14$ m, $\sigma = 1.2$ GPa), 2BH ($m_4 = 160$ kg, $L_4 = 1.1$ m, $L_T = 2.14$ m, $\sigma = 1.2$ GPa).	195
7.12	Total noise comparison between the current aLIGO condition, set aLIGO214 ($m_4 = 40$ kg, $L_4 = 0.6$ m, $L_T = 2.14$ m, $\sigma = 770$ MPa), set aAH ($m_4 = 40$ kg, $L_4 = 0.6$ m, $L_T = 2.14$ m, $\sigma = 1.2$ GPa), set aBL ($m_4 = 40$ kg, $L_4 = 1.1$ m, $L_T = 2.14$ m, $\sigma = 770$ MPa), and set aBH ($m_4 = 40$ kg, $L_4 = 1.1$ m, $L_T = 2.14$ m, $\sigma = 1.2$ GPa).	200
7.13	Total noise comparison between the current aLIGO condition, set 1AL ($m_4 = 80$ kg, $L_4 = 0.6$ m, $L_T = 2.14$ m, $\sigma = 770$ MPa), set 1AH ($m_4 = 80$ kg, $L_4 = 0.6$ m, $L_T = 2.14$ m, $\sigma = 1.2$ GPa), set 1BL ($m_4 = 80$ kg, $L_4 = 1.1$ m, $L_T = 2.14$ m, $\sigma = 770$ MPa), and set 1BH ($m_4 = 80$ kg, $L_4 = 1.1$ m, $L_T = 2.14$ m, $\sigma = 1.2$ GPa).	201
7.14	Total noise comparison between the current aLIGO condition, set 2AL ($m_4 = 160$ kg, $L_4 = 0.6$ m, $L_T = 2.14$ m, $\sigma = 770$ MPa), set 2AH ($m_4 = 160$ kg, $L_4 = 0.6$ m, $L_T = 2.14$ m, $\sigma = 1.2$ GPa), set 2BL ($m_4 = 160$ kg, $L_4 = 1.1$ m, $L_T = 2.14$ m, $\sigma = 770$ MPa), and set 2BH ($m_4 = 160$ kg, $L_4 = 1.1$ m, $L_T = 2.14$ m, $\sigma = 1.2$ GPa).	202

7.15	Total noise comparison between the current aLIGO condition, set aAH ($m_4 = 40$ kg, $L_4 = 0.6$ m, $L_T = 1.6$ m, $\sigma = 1.2$ GPa), set aBH ($m_4 = 40$ kg, $L_4 = 1.1$ m, $L_T = 2.14$ m, $\sigma = 1.2$ GPa), set 1BH ($m_4 = 80$ kg, $L_4 = 1.1$ m, $L_T = 2.14$ m, $\sigma = 1.2$ GPa), and set 2BH ($m_4 = 160$ kg, $L_4 = 1.1$ m, $L_T = 2.14$ m, $\sigma = 1.2$ GPa).	203
A.1	Single-axis mass spring system used to simplify and generalise the dynamics of the quadruple pendulum.	210
A.2	Forces on a suspended stage of mass m hanging from a wire of length L at an angle θ	214
E.1	Peak pixel intensity variation during a pull and corresponding fibre diameter profile.	228

List of Tables

2.1	Material properties of fused silica	52
3.1	The vertical bounce mode frequencies and the first violin mode frequencies of different sets compared to that of the aLIGO condition.	77
4.1	One example of PID gain parameters for the polishing and the pulling process.	100
4.2	Summary of the correlation analysis. The average standard deviation was 5.48, which indicates that there is a correlation between laser fluctuations and the resulting diameter of the fibres.	116
4.3	Highlights of the pull observations for various runs	117
4.4	Summary of the peak pixel intensity data for unstabilised pulls with identical conditions (polished, 18 seconds of wait time, and 49% of duty cycle).	121
4.5	Summary of the peak pixel intensity data for stabilised pulls with identical conditions (polished, PID gain adjustment, auto-peak function off, setpoint of 6000, and 5 minutes of wait time).	122
5.1	The number of mismatched fibres compared to the total number of fibres, as a function of the breaking stress range.	147
6.1	Fibre diameter calculations for different stress conditions.	158

6.2	Details of the experimental setup in the vacuum tank to measure the breaking time of fused silica fibres as a function of tensile stress.	172
7.1	List of different “test mass - total payload” sets. m_1, m_2, m_3 values were only used to calculate the total payload. After getting total payload, new m_1, m_2, m_3 values were assigned for each condition according to seismic optimisation.	181
7.2	Final mass conditions for two different test masses: 80 kg and 160 kg. The aLIGO condition is presented as a reference.	184
7.3	Final length conditions for two different L_4 (0.6 m and 1.1 m) where $L_T = 2.14$ m. The aLIGO parameters are presented as a reference.	185
7.4	Naming strategy for all possible scenarios with different mass, length, and stress conditions.	186
7.5	Thermoelastic nulling radius of fibres for different test mass conditions.	187
7.6	Summary of seismic, suspension thermal, coating Brownian noise for: test mass = 40 kg. Darker blue means lower strain, and darker orange means higher strain. For each comparison item, all sets (including 40 kg, 80 kg, 160 kg) were compared to assign the colour. The best value was assigned to be the darkest blue, and the worst value was assigned to be the darkest orange. Other values in the middle were assigned in respect of the best and the worst values.	197
7.7	Summary of seismic, suspension thermal, coating Brownian noise for: test mass = 80 kg. Darker blue means lower strain, and darker orange means higher strain. For each comparison item, all sets (including 40 kg, 80 kg, 160 kg) were compared to assign the colour. The best value was assigned to be the darkest blue, and the worst value was assigned to be the darkest orange. Other values in the middle were assigned in respect of the best and the worst values.	198

7.8 Summary of seismic, suspension thermal, coating Brownian noise for: test mass = 160 kg. Darker blue means lower strain, and darker orange means higher strain. For each comparison item, all sets (including 40 kg, 80 kg, 160 kg) were compared to assign the colour. The best value was assigned to be the darkest blue, and the worst value was assigned to be the darkest orange. Other values in the middle were assigned in respect of the best and the worst values. 199

Acknowledgments

I would like to thank everyone who helped and supported me through out my postgraduate life.

First of all, I would like to sincerely thank my supervisors, Professor Giles Hammond and Professor Sheila Rowan for giving me an opportunity to join the group and work with them. Their constant support, patience, and advice provided great help and inspiration to complete my PhD. I would like to thank Professor Jim Hough for his advice and caring for my work and research. I would also like to thank SUPA for providing the scholarship to carry out my research.

I would like to send my earnest gratitude to Dr. Alan Cumming for his help and support throughout my experimental work, from the beginning to the end. I would also like to thank Mr. Russell Jones, who provided so much help and valuable comments for designing and building experimental apparatus. I would like to thank Mr. Colin Craig and Mr. Steven Craig for their help in making parts for the experiments. I would also like to thank Dr. Jamie Scott for countless IT support throughout my 4 years in Glasgow. I would like to thank Mr. Karl Toland for his help and advice in various experiments. I would like to thank Dr. Brett Shapiro and Ms. Daniela Pascucci for their help in simulations. I would like to thank Dr. Angus Bell and Dr. Kirill Tokmakov for their support and valuable discussions regarding my work. I would like to thank Mr. Kyeong Taek Kim and Ms. Sung Hee Park for their help in image processing. I would like to thank Professor Giles Hammond and Dr. Alan Cumming again for their help and caring

for the thesis revision.

On a personal note, I would like to sincerely thank my parents for their support and unconditional love, which made everything possible for me. I would like to thank my uncle and aunts for their moral support throughout my darkest time. Lastly, I would like to thank my dear friends in Korea, United States, Japan, and Europe for their sincere caring and friendship.

Preface

This thesis is an account of work carried out by the author with support from staff in the Institute for Gravitational Research (IGR) at the University of Glasgow between October 2014 and March 2018, involving the investigation on suspension upgrades for gravitational wave detectors.

Chapter 1 contains a brief introduction of gravitational waves: their nature, potential sources, detectors and detections.

Chapter 2 contains further description of thermal noise within gravitational wave detectors.

Chapter 3 contains Matlab simulation results for upgrade scenarios of the Advanced LIGO detectors: different stress conditions. Dr. Brett Shapiro provided seismic noise estimation equations and the Matlab codes for all seismic noise related calculations. The BSC-ISI performance spectrum to estimate the seismic noise was taken from the seismic SVN server. Ms. Daniela Pascucci provided the Matlab codes for all coating thermal noise related calculations. Dr. Alan Cumming provided dilution factors for different conditions calculated by FEA.

Chapter 4 contains experimental work to develop new stabilisation technology for fused silica fibre fabrication. The aim of the experiment was to improve the statistical strength and reproducibility of fused silica fibres for further upgrades of the Advanced LIGO detectors. The fused silica fibre pulling machine used for the fabrication and the profile

machine to check the diameter of the fibres were built by the suspension group in the IGR. Dr. Alan Cumming suggested the concept of using camera for stabilisation, provided assistance throughout learning how to use both machines and installing new stabilisation system. The work was supervised by Prof. Giles Hammond.

Chapter 5 contains the strength test results for the fused silica fibres. The aim of the experiment was to test the breaking stress of fibres fabricated under different conditions to confirm the impact of the stabilisation system. Dr. Alan Cumming and Mr. Russell Jones provided assistance in learning how to use the machine. The work was supervised by Prof. Giles Hammond.

Chapter 6 contains the stress corrosion test results for the fibres. The aim of the experiment was to test the breaking time of the fibres under stress depending on two environmental conditions: in-air and vacuum. This experiment was designed with advice from Dr. Alan Cumming, Mr. Russell Jones, and Prof. Giles Hammond. Dr. Alan Cumming and Mr. Russell Jones provided assistance in installing the parts. The work was supervised by Prof. Giles Hammond.

Chapter 7 contains Matlab simulation result for upgrade scenarios of the Advanced LIGO detectors: different stress, length, mass conditions. The Matlab codes, dilution factors, and BSC-ISI performance spectrum used were identical to those used in Chapter 3.

Chapter 8 provides the conclusions of work presented in this thesis.

Appendix A contains the derivation of the seismic noise optimisation equations, which were provided by Dr. Brett Shapiro in LIGO document T1300786.

Appendix B provides the coating Brownian noise equations derived by Somiya and Yamamoto.

Appendix C provides the Matlab codes used for the noise simulations performed in Chapters 3 and 7.

Appendix D provides the Python code used for the stress corrosion experiment presented in Chapter 6.

Appendix E provides a figure that compares the peak pixel intensity variation during a pull process and corresponding fibre diameter.

Summary

According to the Theory of General Relativity [1], gravitational waves are ripples in spacetime caused by the asymmetrical acceleration of mass. There has been consistent effort to detect gravitational wave signals, from resonant bar detectors to interferometric detectors, and worldwide collaborations between detectors such as LIGO (US based), Virgo (French-Italian), GEO600 (UK-German), and KAGRA (Japanese). 100 years since Einstein first predicted the existence of gravitational waves, the Advanced LIGO detectors succeeded in first direct detection in 2015. Starting with the first signal from a binary black hole system, GW150914, multiple binary black hole systems and a binary neutron star system have been discovered.

The most important contribution that made the detections possible was the hardware upgrade to the initial LIGO detector, to Advanced LIGO or aLIGO, including increased laser power, a quadruple pendulum system, and monolithic fused silica final stage suspensions [2]. To further improve the sensitivity of the detectors, various upgrade scenarios are being considered. The main goal of the experimental and modelling work in this thesis is to investigate the suspension upgrades of the Advanced LIGO detectors, especially the fused silica fibres used for the monolithic final stages of the quadruple pendulum suspensions.

Chapter 1 provides an introduction regarding gravitational waves, their sources, detectors, and different noise sources that limit the detector's sensitivity. Among various sources,

thermal noise is introduced in depth in Chapter 2, this being the most relevant noise source for the experimental work presented in this thesis. Chapter 3 through 7 provide simulations and experimental work that have been done to support further upgrades of the Advanced LIGO detectors (e.g A+ upgrade).

Chapter 3 presents Matlab simulation results that target the minimal change that can bring improvements in the detector's sensitivity: implementing high stress fused silica fibres for the monolithic final stage to widen the detection band. This upgrade does not require any major infrastructure change, but can improve the sensitivity curve by lowering the vertical bounce mode frequency and pushing up the first violin mode frequency. Various stress conditions were investigated to show how much gain we can get for the different options. It is shown that the higher stress fibres bring improvements without any disadvantages.

As the strength of the fibre is the only limiting factor to implement higher stress fibres, experimental research was performed to improve the statistical strength of the fused silica fibres. Chapter 4 presents the stabilisation technique developed for the fused silica fibre fabrication process. Currently, a bespoke pulling machine with a CO₂ laser is used to fabricate fused silica fibres used for the detectors. From multiple fibre pulls, it is shown that instabilities of the laser intensity happen during the fabrication process, causing dips and bumps on the surface of the fibres, which can potentially weaken the fibres. To minimise these fluctuations, various enhanced fibre fabrication techniques, including a camera monitoring system and PID feedback control, were investigated. Applying all developed techniques for stabilisation, laser intensity fluctuations during fibre fabrication were minimised, producing fused silica fibres without significant dips in their profile.

In Chapter 5, strength test results are presented to compare the statistical strength of conventional fibres and those fabricated with the enhanced techniques explained in Chapter 4. From the breaking stress analysis, it is shown that the stabilised fibres

have a decreased spread of the breaking stress, and a higher percentage of strong fibres, an increased maximum breaking stress, and a higher average breaking stress. As it was possible to achieve the average breaking stress of 4.2 GPa utilising enhanced fibre fabrication technologies, the potential A+ upgrade stress of 1.2 GPa should have a reasonable safety factor. In addition, through the breaking point analysis, it is also shown that we can predict potential weak fibres by inspecting the laser stability during the fabrication process.

After confirming the positive impact of the stabilisation system, a stress corrosion experiment was performed to investigate the durability of these enhanced fibres by monitoring the time it takes for the fibre to break. Chapter 6 presents the results of stress corrosion tests in-air and in vacuum, for various stress conditions. Tests in vacuum are important since the detector's operation condition is vacuum, and in-air tests are also meaningful because the fibres are fabricated and stored in-air until the installation. 16 fibres were setup in a vacuum chamber on 4th of February 2018, and 15 fibres are still hanging. The result of this experiment provides another confirmation of sufficient safety factor for the potential A+ upgrade.

With this confirmation, the upgraded stress condition was set as 1.2 GPa and further upgrade scenarios including mass and length were investigated. The Matlab simulation result is presented in Chapter 7. It is shown that heavier test masses of large diameter, longer final stage suspension, and higher stress in the fibre can improve noise sources in the low frequency range (seismic noise, suspension thermal noise, and coating Brownian noise). Although a longer final stage increases the seismic noise by shortening upper stages due to the limited total length of the suspension, it can be compensated by increasing the stress in the fibre and the total length of the suspension to the maximum length that the current aLIGO vacuum chamber can allow.

The work has been presented in following conferences and meetings:

- The 11th Edorado Amaldi Conference in Gravitational Waves

- 2015 Gravitational Wave Advanced Detector Workshop (GWADW)
- 2016 LSC-Virgo September Meeting
- The 5th ELiTES General Meeting
- 2017 LSC-Virgo August Meeting

Chapter 1

Gravitational Waves

1.1 Introduction to Gravitational Waves

In 1916, Albert Einstein predicted the existence of gravitational waves in the Theory of General Relativity [1]. According to the theory, gravity is described as a curvature of spacetime caused by mass and energy, and gravitational waves are ripples in spacetime caused by asymmetrically accelerated masses. The lowest order of gravitational wave radiation is quadrupole. Since the mass does not change with time, the conservation of mass does not allow monopole radiation and the conservation of momentum does not allow dipole radiation [3]. Quadrupole accelerations of mass stretch and squeeze spacetime with these waves propagating away from the source at the speed of light, with the deformation orthogonal to the direction of travel of the wave.

The stretching and squeezing of spacetime caused by the gravitational waves is called strain, h . Gravitational waves have two independent polarisations: h_+ and h_\times . Figure 1.1 shows the impact of each polarisation on a ring of test particles when the gravitational waves pass through. The travelling direction of the gravitational waves is normal to the plane of the page. The initial diameter of the ring is L , and the change in the diameter

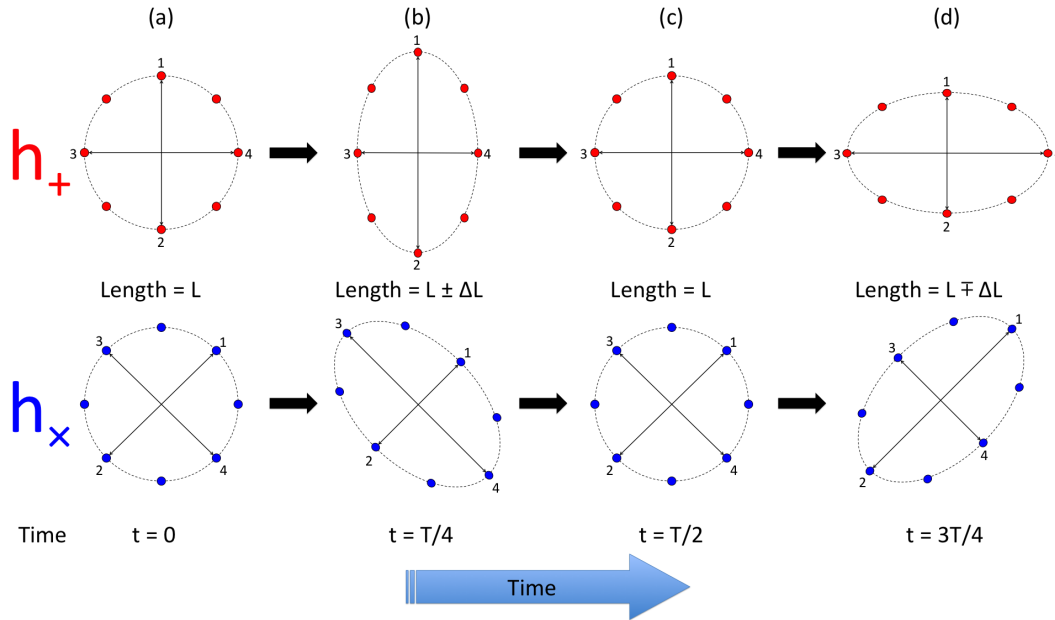


Figure 1.1: Impact of each polarisation on a ring of test particles when the gravitational waves pass through. The travelling direction of the gravitational waves is perpendicular to the plane of the page.

is ΔL . Let's consider the h_+ polarisation as an example. The initial diameter of the test particle ring was L (stage (a)). In the next stage (b), the ring was compressed in the horizontal direction (particles 3 and 4, which are along the x-axis, move towards each other) and extended in the vertical direction (particles 1 and 2, which are along the y-axis, move apart). Therefore, the length becomes $L \pm \Delta L$. The strain h , the amplitude of the gravitational waves, is defined as [3]:

$$h = \frac{2\Delta L}{L} \quad (1.1)$$

1.2 Sources of Gravitational Waves

Gravitational waves are emitted by masses which accelerate and move non-axisymmetrically. Theoretically, most objects, including ourselves, are constantly producing gravitational waves, but it is impossible to even create any detectable gravitational waves in a laboratory with the limitation in detector's sensitivity, since gravity is the weakest force among four forces of nature. According to Saulson's thought experiment [3], the strain amplitude expected from two 1-tonne masses distanced by 2 m and spun at 1 kHz about their centre of mass is about $h \simeq 10^{-38}$. Therefore, the main sources that detectors are targeting are astronomical sources, since astronomical scale masses and motions can create relatively bigger signals for the detection (h in the order of $\sim 10^{-21}$). Even among astronomical sources, the targeted sources are much bigger than the solar system scale: for the Earth-Sun system, the frequency of the signal would be approximately $6 \times 10^{-8} Hz$ with the power output of only 200 W.

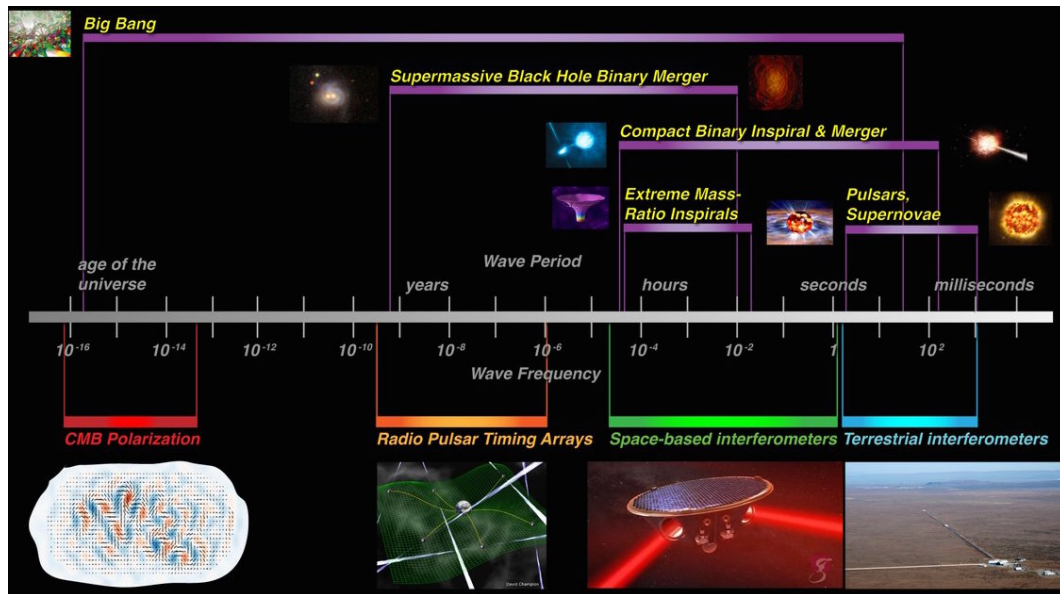


Figure 1.2: The gravitational wave spectrum with sources and detectors. (Credit: NASA Goddard Space Flight Center [4])

Figure 1.2 shows the gravitational wave spectrum with sources and detectors [4]. Broadly, they can be divided into transient sources, continuous sources, and stochastic sources.

1.2.1 Transient Sources

Transient sources, also called burst sources, emit very strong gravitational wave signal for very short time, usually caused by violent astronomical events. Supernovae, and coalescence of compact binary systems are examples of sources in this category.

1.2.1.1 Supernovae

Supernovae are one form of a massive star's death. At the end of their life, smaller stars become white dwarfs which are quietly cooling star remnants, after their fuel runs out [5]; but bigger stars (bigger than 10 solar masses [6]) end their life with a huge explosion called a supernova [7]. After a supernova explosion, if the core of the star has a mass greater than the Chandrasekhar limit (1.4 solar mass), this remaining core becomes a neutron star [8]. If the core has a mass above 3 solar masses, it will become a black hole.

When the collapse is spherically symmetrical, it will not produce any gravitational waves. However, when an asymmetric supernova happens, perhaps due to fast rotation [9], a burst of gravitational waves will be emitted. According to Sathyaprakash [10] and Ott [11], the estimated strain for a supernova at a distance of 10 kpc, emitting energy of $10^{-7}M_{\odot}$ at a frequency of 1 kHz, and lasting for 1 ms would be:

$$h \simeq 6 \times 10^{-21} \left(\frac{E}{10^{-7}M_{\odot}} \right)^{\frac{1}{2}} \left(\frac{1ms}{T} \right)^{\frac{1}{2}} \left(\frac{1kHz}{f} \right) \left(\frac{10kpc}{r} \right) \quad (1.2)$$

where E is the total energy radiated at a frequency f , M_{\odot} is the mass of the sun, r is the distance from the source, T is the time for the collapse. The gravitational wave signal

with this level of strain can be detected with relatively high confidence, but the event rate of supernovae within 10 kpc is too small to make an early detection [12].

1.2.1.2 Coalescing Compact Binary System

Binary star systems comprise two stars orbiting around their common center of mass. While the stars orbit, they can be classified as a continuous source since the lost energy from inspiral is emitted as gravitational waves, but this level of signal has not been detected, as its expected strain is below the sensitivity of current detectors, such as the Advanced Laser Interferometer Gravitational wave Observatory (Advanced LIGO or aLIGO) [13]. However, when the stars lose enough energy to come close together and ultimately collide, we get a burst collision signal which can generate a high enough strain, of $h \simeq 10^{-19}$ [3], which can be detected. Indeed, the direct observations of gravitational waves so far are all signals from compact binary systems [14, 15, 16, 17, 18, 19]. There are three types of binary systems which produce gravitational waves in the Advanced LIGO detection band (above 10 Hz): neutron star - neutron star (NS/NS), neutron star - black hole (NS/BH), black hole - black hole (BH/BH). More details on significant detections will be introduced in Section 1.5.4.

The estimated strain amplitude from a coalescing neutron star binary system is given as [20]:

$$h \simeq 1 \times 10^{-23} \left(\frac{100 \text{Mpc}}{r} \right) \left(\frac{M_B}{1.2 M_\odot} \right)^{\frac{5}{3}} \left(\frac{f}{200 \text{Hz}} \right)^{\frac{2}{3}} \quad (1.3)$$

where $M_B = (M_1 M_2)^{\frac{3}{5}} / (M_1 + M_2)^{\frac{1}{5}}$, M_1 and M_2 are the masses of each star, r is the distance from the source, and f is the frequency of the emitted gravitational wave.

1.2.2 Continuous Sources

Continuous sources do not emit as strong signals as transient sources, but they constantly emit gravitational waves, which may be helpful for long term study in astrophysics and cosmology. As mentioned in Section 1.2.1.2, binary systems emit gravitational waves during inspiral, but the signal is very low when the separation is reasonably large [21]. Instead, there are some other stably rotating systems in the universe that have better potential to be detected on Earth. Pulsars and Wagoner stars are two examples.

1.2.2.1 Pulsars

Pulsars are rotating highly magnetised neutron stars discovered by Bell and Hewish in 1967 [22]. When the core of a massive star collapses to create a neutron star, the rotation speed increases to conserve the angular momentum. During this process, irregularities in the surface and precession due to accretion may cause non-axisymmetric motion [23], which can produce gravitational waves.

In 1975, Russell Hulse and Joseph Taylor showed the first indirect evidence of gravitational waves from their work on the system PSR B1913+16 [24, 25]. For over 20 years, they measured the radio wave emission which showed that the binary system's rate of change of the orbital period matched the energy loss due to gravitational waves predicted from the theory of general relativity [1, 26]. Providing the first indirect evidence of gravitational waves, Hulse and Taylor won the Nobel Prize in 1993.

The estimated strain of the gravitational waves emitted from a pulsar rotating with frequency f is [27, 28]:

$$h = \frac{4\pi^2 G}{c^4} \frac{I_{zz} f^2}{d} \epsilon \quad (1.4)$$

where G is the gravitational constant, c is the speed of light, I_{zz} is the principal moment

of inertia of the object, f is the gravitational wave frequency which is 2ν , d is the distance from the Earth, and $\epsilon = (I_{xx} - I_{yy})/I_{zz}$ is the ellipticity, which shows the degree of asymmetry in the star. Because of the quadrupole nature of the gravitational waves, this asymmetry is necessary to have any gravitational wave radiation.

1.2.2.2 Low Mass X-Ray Binaries

Other than NS-NS binaries such as Hulse-Taylor pulsar, there are different forms of neutron star binaries such as low mass X-ray binaries [21]. When a neutron star has a white dwarf or main sequence star companion and if the neutron star has a large enough gravitational field to gain mass from its companion, the binary occurs as an interacting binary which emits X-rays from the mass accretion [21]. When the angular momentum increases to a certain point, the Chandrasekhar-Friedman-Schutz instability point can be reached, beyond which the rotation becomes non-axisymmetric to emit gravitational waves. Stars at this instability point are called Wagoner stars, and the estimated strain for such system is [29]:

$$h \simeq 3 \times 10^{-27} \left(\frac{1kHz}{mf} \right)^{\frac{1}{2}} \left(\frac{L_\gamma}{10^{-8} \text{ergs cm}^{-2} \text{sec}^{-1}} \right)^{\frac{1}{2}} \quad (1.5)$$

where m is the mode number, f is the frequency which is expected to be around 500 Hz, and L_γ is the x-ray flux.

1.2.3 Stochastic Sources

Lastly, stochastic background of gravitational wave signals comes from a superposition of many different sources such as gravitational waves produced during the inflationary period after the big bang [3], a collapse of a population of black holes [3], and cosmic string production [30, 31]. For the stochastic sources, the high-enough amplitude is not the only requirement. Even when the signal is big enough to be detected, it requires

two or more detectors to catch the signal for the data analysis since the stochastic background signal has a noise-like nature. By cross-correlating the results from multiple detectors, the stochastic background can be identified [32].

1.3 Ground-based Gravitational Wave Detectors

As shown in Figure 1.2, there are various directions of research to detect gravitational waves in different frequency ranges. Since the research to be presented in this thesis is relevant to ground based interferometric detectors, this area will be covered in more detail. Others will be briefly introduced later in this chapter.

1.3.1 Resonant Bar Detectors

In the 1960s, Joseph Weber attempted to directly detect the gravitational waves using resonant bar detectors [33]. This detector consisted of aluminum cylinders (“bars”) which acted as antennae. These bars were in the order of a few tonnes and were separated by 1000 km to ensure independent signal detection without coincidental error from external noise [33, 34]. When a gravitational wave passed, it would set one of the cylinders vibrating at its resonant frequency and piezoelectric crystals attached around the cylinder’s waist would convert that ringing into an electrical signal. Despite claims of detection in the late 1960s [34, 35, 36], the experimental result could not be repeated so Weber’s claim could not be confirmed [37, 38]. However, this claim started the new exciting research field of gravitational waves: some groups carried on the Webers idea for further improvement, and others came up with another approach of using laser interferometers.

To improve the seismic noise and acoustic noise in the bar detectors, vibration isolation stages were implemented. In addition, the detectors operate under cryogenic condition to reduce the thermal noise. AURIGA [39, 40], EXPLORER [41, 42], NAUTILUS [43],

ALLEGRO [44, 45] are four detectors that could achieve the best sensitivity of $h \simeq 10^{-20}$ over a bandwidth of $\simeq 900$ Hz but the main limiting factor is that these detectors have very narrow bandwidth (only around the resonant frequency) [46, 47].

1.3.2 Laser Interferometers

Most current ground based detectors are interferometers including LIGO [48], GEO 600 (German-British Gravitational-Wave Observatory) [49], Virgo (Italian-French Gravitational-Wave Observatory) [50] and KAGRA (Kamioka Gravitational Wave Detector) [51] are interferometric detectors. Currently, LIGO and Virgo are at their second generation, known as the Advanced LIGO and the Advanced Virgo. In addition to these detectors, LIGO India is approved and funded to be constructed [52, 53]. By having a network of detectors around the world, independent verification of detections and sky localisation of gravitational wave sources was possible using triangulation [54] (Figure 1.3). Further details on each detector will be described in Section 1.5.

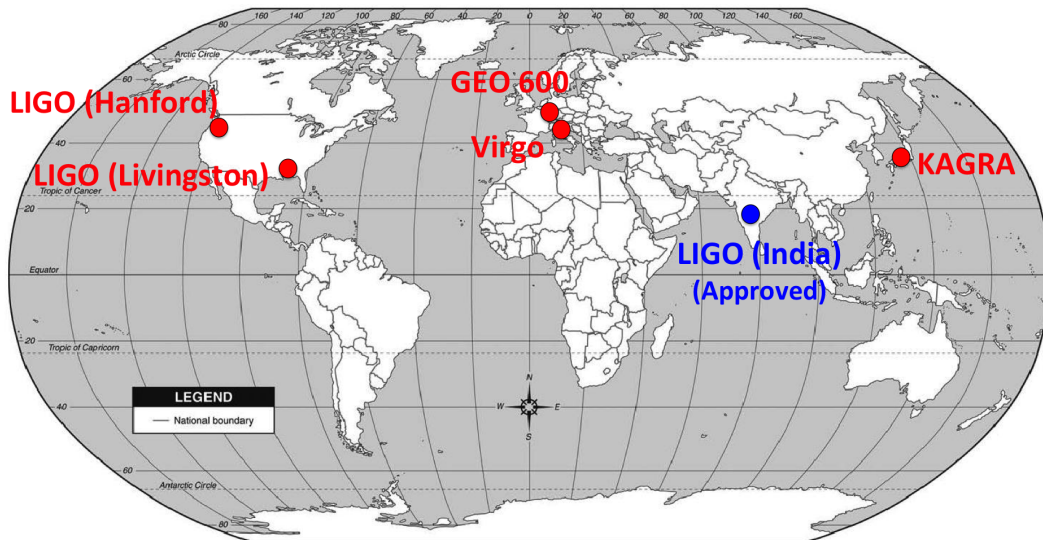


Figure 1.3: Global network of ground based interferometric detectors (blank map credit: Outline world map [55]).

1.3.2.1 Michelson Interferometer with a Fabry-Perot Cavity

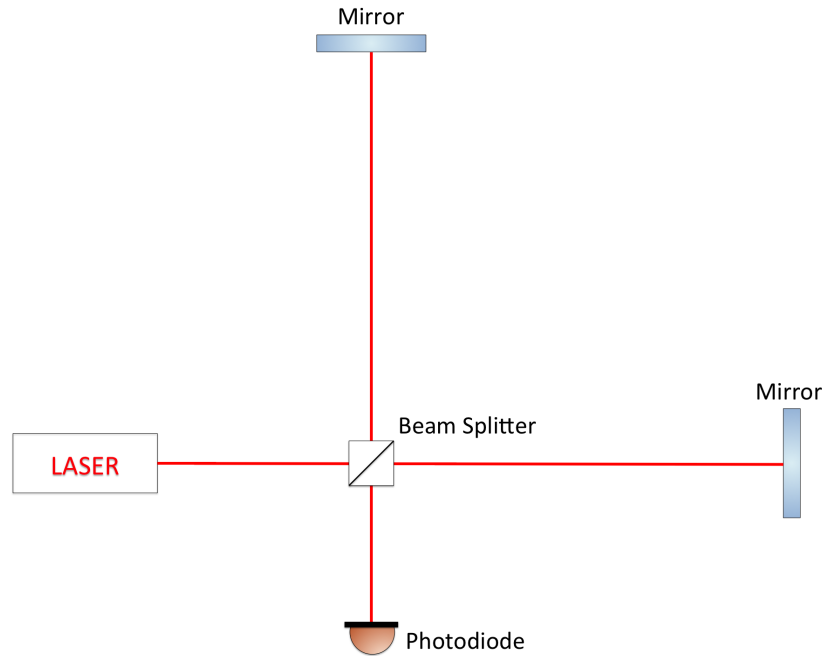


Figure 1.4: Schematic diagram of a simple Michelson Interferometer.

In 1962, Gertsenshtein and Pustovoit first suggested to build an interferometric detector for gravitational waves [3, 56], and Forward first attempted to investigate this idea by experiment [57]. The Michelson interferometer [58] is the basis of most current ground based interferometers. Figure 1.4 shows a schematic diagram to show the topology of the Michelson interferometer. It consists of two orthogonal arms with mirrors at the end of each arm, a beam splitter to split light from a laser source, and a photodiode to observe the interference pattern.

The detectors are designed to run at (or close to) a dark fringe, which means the mirrors are held at positions where the interference pattern of the output beam is destructive. This is known as “locking” the interferometer [48, 59]. The advantage gained from this system is that more light power can be kept inside the interferometer by minimising the light power coming out to the photo-detector, which can improve one of the noise

sources called photon shot noise [60], which will be explained in Section 1.4.3. When gravitational waves pass by, the stretch and squeeze in the spacetime can cause partially constructive interference pattern, instead of destructive, to provide the output signal. Since the detector is “locked” to run at dark fringe, when the output signal is generated due to change in arm length, a force proportional to the output signal is applied to the mirrors to compensate that change [61].

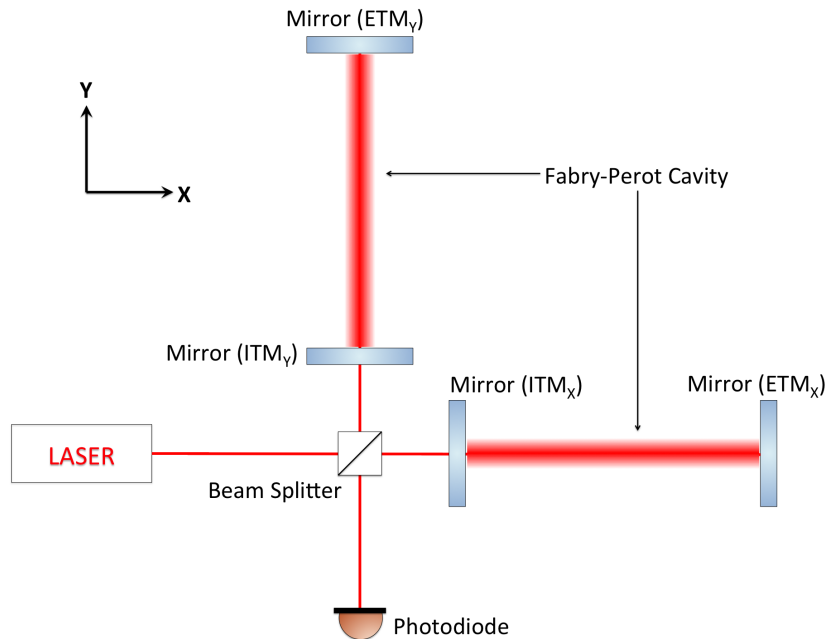


Figure 1.5: Schematic diagram of a Michelson Interferometer with Fabry-Perot arm cavities implemented.

As mentioned in Section 1.1, the strength of the gravitational wave signal is proportional to the length of the arm, it is desirable to have longer arms for better detector’s sensitivity. However, the arm length is limited by various factors, such as the curvature of the Earth surface and the cost of infrastructure. One of the solutions to overcome these restrictions is to implement Fabry-Perot cavities [10]. A Fabry-Perot cavity uses additional mirrors in the arms to increase the beam’s total travelling distance by reflecting photons back and forth multiple times along the arm before they escape the cavity. For instance,

in case of the aLIGO detectors, the implementation of Fabry-Perot cavities make the arms effectively 1120 km long by reflecting parts of each laser beam about 280 times before they escape the cavity [62, 63]. Each arm has one fully reflecting mirror (end test mass, ETM) and one partially reflecting mirror (input test mass, ITM) to form each arm cavity, as shown in Figure 1.5.

1.3.2.2 Power Recycling and Signal Recycling

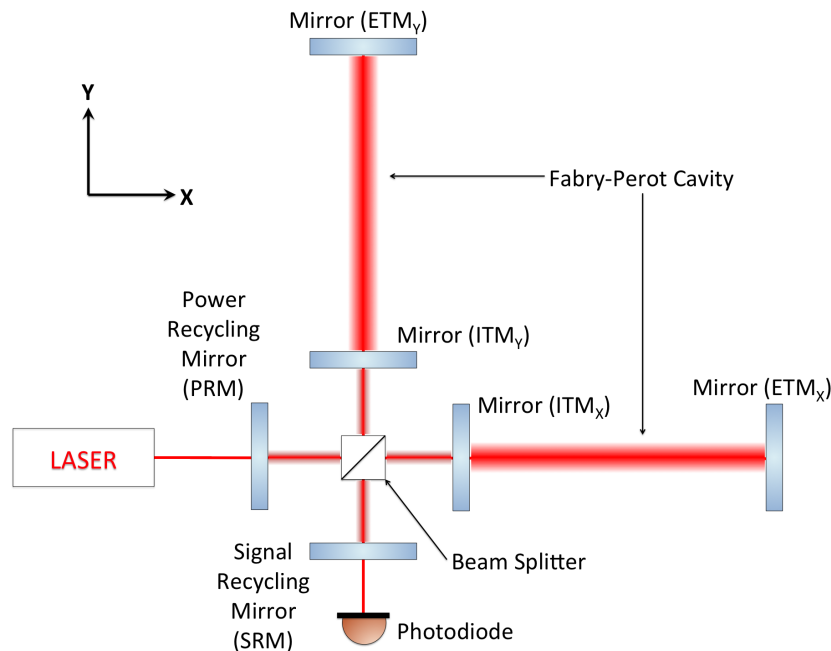


Figure 1.6: Schematic diagram of a Michelson Interferometer with a Power Recycling Mirror and a Signal Recycling Mirror implemented.

Power recycling and signal recycling are two other important concepts in increasing the stored light power in the detectors [64, 65, 66]. For power recycling, a partially transmissive mirror (known as the Power Recycling Mirror, PRM) is placed between the laser and the beam splitter to create a cavity between them (Figure 1.6). When the light reflected from ETMs is transmitted through the beam splitter back towards the

laser instead of being lost, it is reflected back into the interferometer, to be “recycled”. The advantage of implementing PRM is that the laser power within the interferometer can be increased, without physically increasing the actual input laser power; for the Advanced LIGO, the power recycling gain is about 45 [67]. The Fabry-Perot cavities combined with PRM can boost up the 200 W laser power up to 750 kW.

Signal recycling is a very similar concept. Another partially transmissive mirror (Signal Recycling Mirror, SRM) is placed between the photodiode and the beam splitter to create a cavity which can amplify the signal light (Figure 1.6). By adjusting the position of the SRM, the peak frequency sensitivity can be adjusted [68], which means that the detector’s peak sensitivity can be tuned specifically for different astronomical sources.

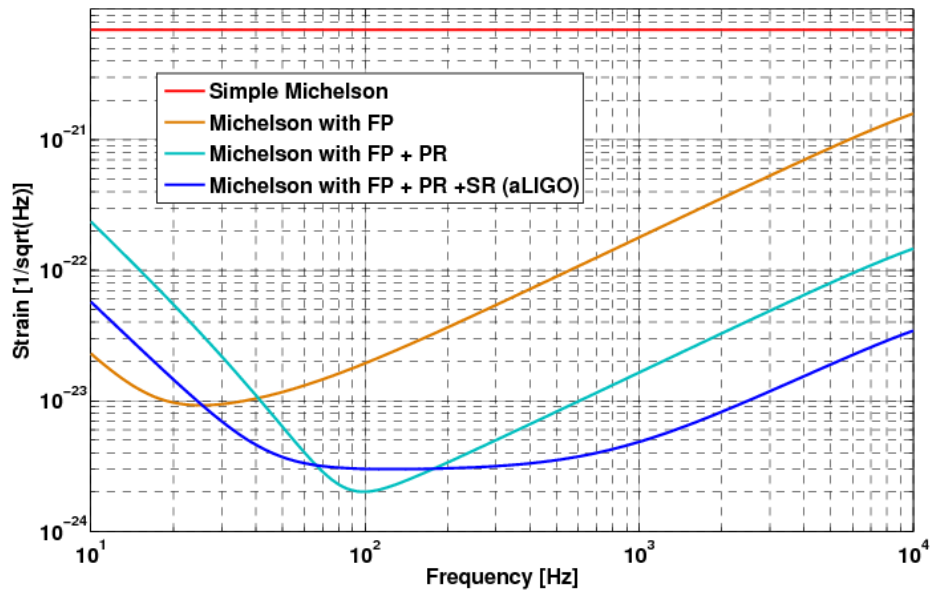


Figure 1.7: Quantum noise strain for different a Michelson interferometer configurations; (1) Red: simple Michelson interferometer, (2) Orange: Michelson interferometer with a Fabry-Perot cavity (FP), (3) Green: Michelson interferometer with a FP and Power Recycling (PR), (4) Blue: Michelson interferometer with a FP, PR, and Signal Recycling (SR) [69].

Figure 1.7 shows the quantum strain noise for different Michelson interferometer configurations [69]: the red line is a simple Michelson interferometer, the orange line is a Michelson interferometer with a Fabry-Perot (FP) cavity, the green line is a Michelson interferometer with a FP cavity and Power Recycling (PR), and the blue line is a Michelson interferometer with a FP cavity, PR, and Signal Recycling (SR). The graph shows a progressive improvement in the quantum noise and bandwidth as FP cavity, PR, and SR are implemented. When the FP cavity is implemented, the cavity acts as a low pass filter for the gravitational wave signal with a arm cavity pole, which causes the noise to go up above 30 Hz. Furthermore, the laser power is greatly increased by using FP cavities that the radiation pressure noise dominates the quantum noise in the low frequency range. When PR is added, the laser power is further increased to improve the shot noise in the high frequency range but the radiation pressure noise becomes worse in the low frequency range. Lastly, when SR is added, both low frequency range and the high frequency quantum noise were improved to widen the sensitive detection band of the detector.

1.4 Noise Sources

The main challenge in obtaining suitable gravitational wave detector performance is reducing various environmental and technical noise sources that vibrate the mirrors, including seismic noise, Newtonian noise, quantum noise, and thermal noise. Figure 1.8 shows various noise sources in Advanced LIGO. In this section, a brief explanation of each noise source, except thermal noise, will be provided. Since the thermal noise is directly related to the main experiment of this thesis, the thermal noise will be discussed more in depth in the next chapter.

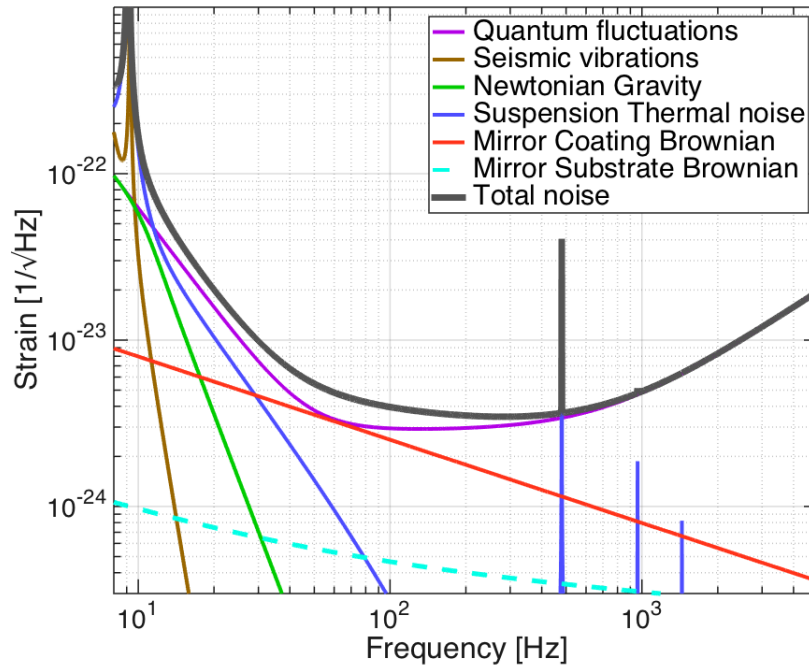


Figure 1.8: Various noise sources in Advanced LIGO [70].

1.4.1 Seismic Noise

For ground-based detectors, it is inevitable to get noise from natural sources that vibrate the surface of the earth (e.g big storms and violent motions of ocean) and man made sources (e.g traffic and air conditioning) [71] which couple into the mirrors of the detector. Therefore, the seismic noise is highly dependant on the location of the detector and the time of the measurement. Seismic motion is a significant noise source at low frequencies [72]. Figure 1.9 shows the LIGO Livingston Observatory seismic background in different representative conditions [73]. The noisy day (green) line shows the impact of strong, nearby seismic disturbances caused by human activity (a few miles away, timber logging). The earthquake (blue dotted) line shows the impact of large far-away earthquakes (5.9 magnitude earthquake near Peru). The quiet (black) line shows an example of the quietest seismic environment. The microseism (red dotted) line shows the impact of

storms in the oceans (storms in the Gulf of Mexico).

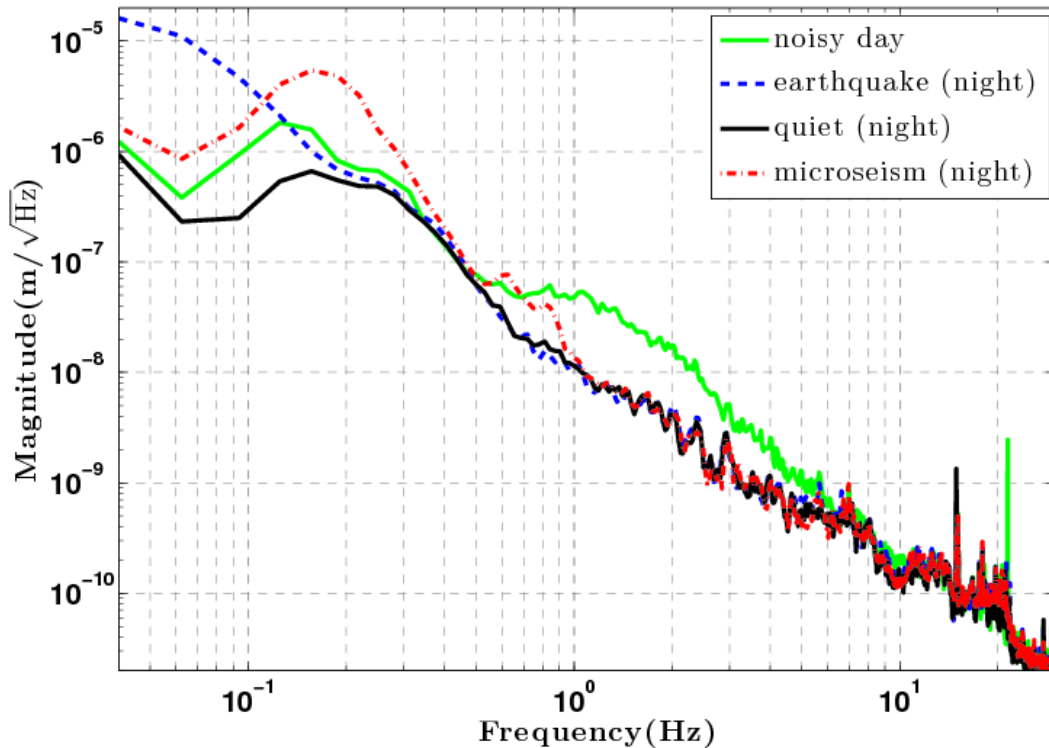


Figure 1.9: The LIGO Livingston Observatory seismic background in different representative conditions [73].

To reduce the impact of seismic noise, the test masses are suspended as pendulum systems for maximum isolation from the outside environment. The transfer function of the test mass motion (x_m) in respect to the ground motion (x_g) for a pendulum system is [69]:

$$\frac{x_m}{x_g} = \frac{\omega_0^2}{\sqrt{(\omega_0^2 - \omega^2)^2 + \omega^2\gamma^2}} \quad (1.6)$$

where $\omega_0 = \sqrt{\frac{k}{m}}$ is resonant angular frequency, k is the spring constant, m is the mass, and $\gamma = \frac{b}{m}$ is a the damping factor with b being the damping constant. Therefore, at low

frequency ($\omega \ll \omega_0$), $\frac{x_m}{x_g} \approx 1$, which means that most of the ground motion transfers to the test mass motion. However, at high frequency ($\omega \gg \omega_0$), $\frac{x_m}{x_g} \approx \frac{\omega_0^2}{\omega^2}$, meaning the test mass motion is significantly reduced compared to the ground motion. This pendulum system is therefore effective to reduce horizontal seismic noise. However, due to the curvature of the Earth, the horizontal and the vertical seismic noise are coupled. To reduce the vertical seismic component, cantilever springs are implemented [72], which work on the same principle.

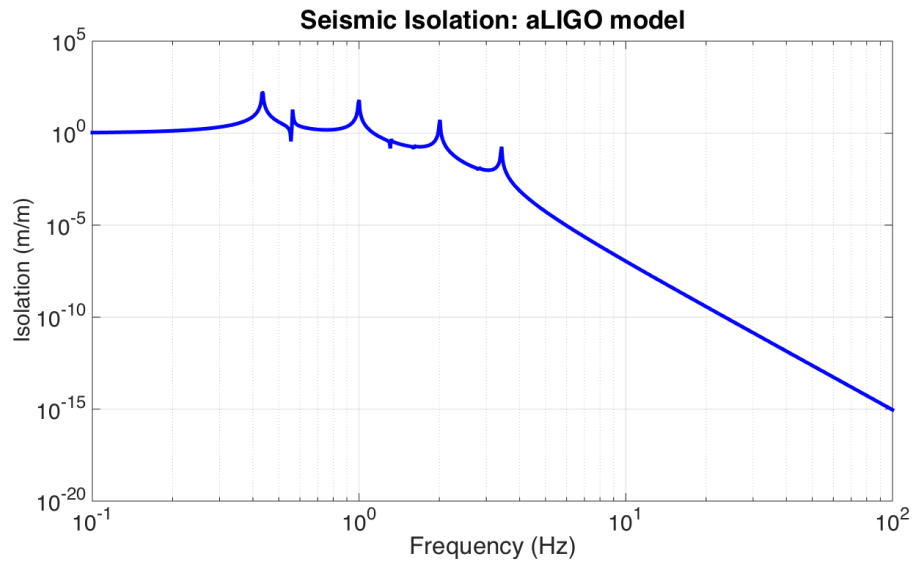


Figure 1.10: Modeled transfer function of aLIGO quadruple pendulum system [74].

To further reduce the seismic noise, another solution is to implement multiple layer pendulums, instead of a single pendulum suspension. This can attenuate the ground motion above the resonant frequency (f_0) of the pendulum by approximately $\sim f_0^2/f^2$. The attenuation of the ground motion can be further increased by having more pendulum stages.

Therefore, a quadruple pendulum system is used for the Advanced LIGO project for even better reduction of the seismic noise (Figure 1.10). For frequencies above the resonant frequency of the pendulum system, using quadruple pendulum system to suspend the

mirrors will reduce the magnitude of the seismic motion by a factor of $1/f^8$. In the case of the Advanced LIGO, the seismic isolation level at 10 Hz is in the order of 10^{-7} [74].

1.4.2 Newtonian Noise

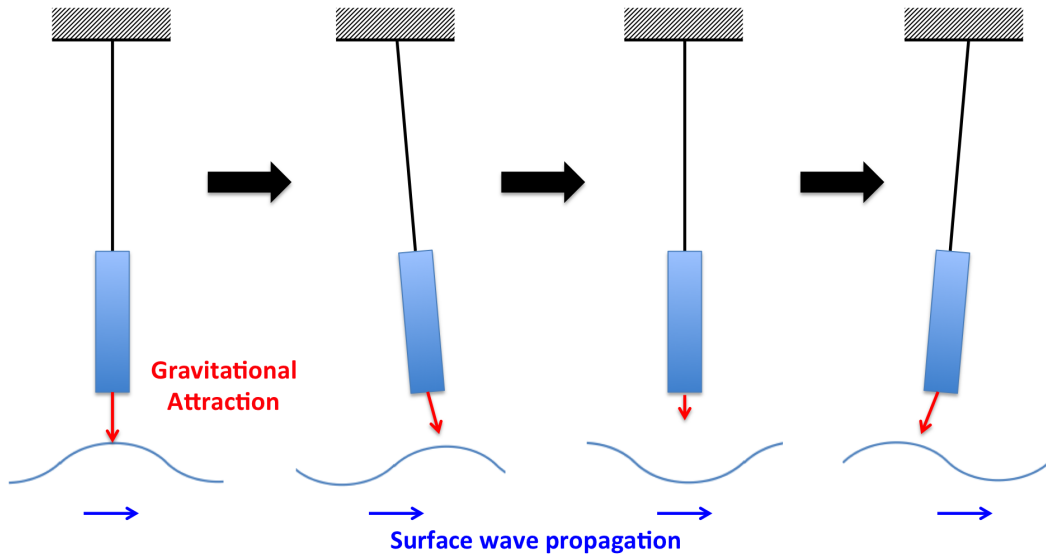


Figure 1.11: Schematic drawing of the gravitational interaction between the Earth's surface and the test mass when the seismic surface wave passes.

Newtonian noise, also known as gravity gradient noise, is caused by local fluctuations in the gravitational field [75]. Possible sources of this fluctuation include seismic surface waves, and local motions of terrestrial masses. This noise has stronger impact in low frequency range below 10 Hz [76] and cannot be shielded. Figure 1.11 shows a schematic drawing of the gravitational interaction between the Earth's surface and the test mass when the seismic surface wave passes.

There are several theoretical solutions to lower the Newtonian noise: choosing a seismically quiet place for the detector, intelligent architecture of buildings, subtracting the estimated Newtonian noise contribution from the detector output, or combining all solutions

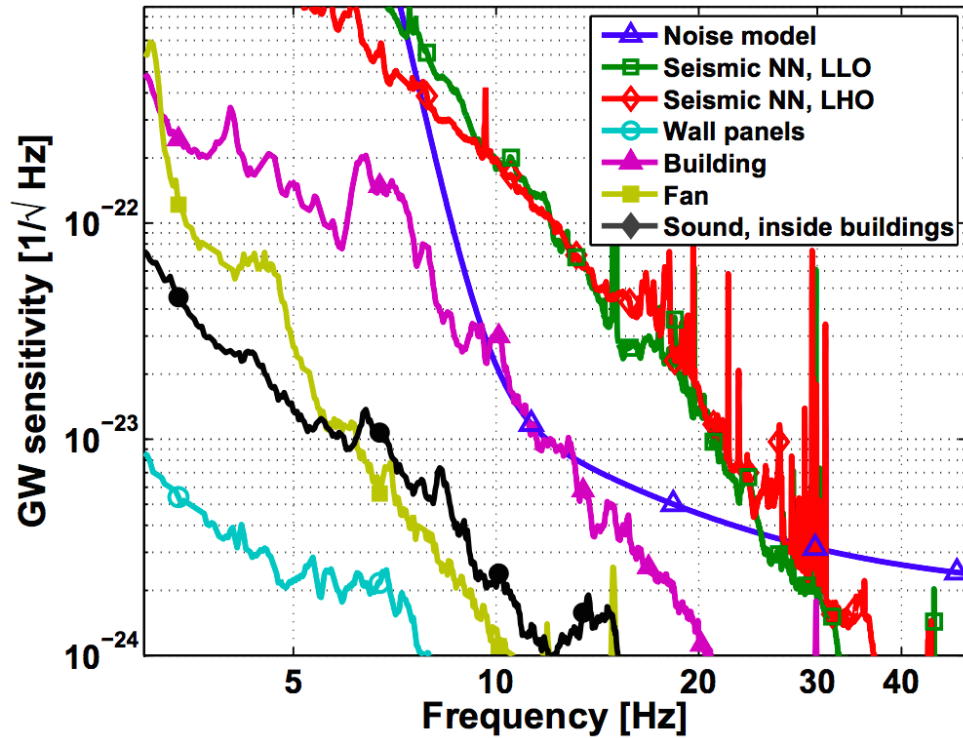


Figure 1.12: Newtonian noise estimate for each LIGO site and different sources [77].

together [78]. Possible option in terms of building detectors at seismically quiet places is to build underground detectors (such as KAGRA [79] and ET [80]) as the depth can exponentially decrease the impact of surface waves [81], or space-based detectors (such as LISA [82, 83]) since they will not get influences from terrestrial masses. However, that is not an option for the Advanced LIGO. Instead, the most feasible solution for the Advanced LIGO is to subtract the estimated Newtonian noise contribution. Currently, we do not have the technology to precisely measure gravity gradients. Instead, the seismic field around the detector is monitored and the data are applied to a gravity gradient generation model, so that the modelled Newtonian noise contribution can be subtracted from the detector output [78, 77]. To accomplish this, accelerometers are used to measure the vibrations on different sources in the LIGO sites, such as water pipes, fans, building, and walls. Figure 1.12 shows the Newtonian noise estimate for

each LIGO site and different sources. Further R&D is in progress to develop active noise cancellation due to the Newtonian noise [77].

1.4.3 Quantum Noise Sources

1.4.3.1 Photon Shot Noise

Photon shot noise is caused by quantum fluctuations in the number of photons reaching the photodiode detector [84]. There is always an uncertainty which is proportional to the square root of the number of photons reaching the photodiode [84]. This noise is one of the dominant sources in the higher frequency range, around few hundred Hz and above. Since the amplitude spectral density of photon shot noise in a simple Michelson interferometer can be described as [3]:

$$h_{shot}(f) = \frac{1}{L} \sqrt{\frac{\hbar c \lambda}{2\pi P}} \quad (1.7)$$

where L is the arm length of the detector, \hbar is the reduced Planck's constant, c is the speed of light, λ is the laser wavelength, P is the laser power, the shot noise can be minimised when the power of the laser is increased.

1.4.3.2 Radiation Pressure Noise

Radiation pressure noise occurs when the photon hits the suspended test masses and transfers momentum to the masses, which results in applying a force to the masses. Since the number of photons that reach the test masses fluctuates, the force applied to the mirror also fluctuates, causing variations in its position. The radiation pressure noise in a simple Michelson interferometer can be expressed as [3]:

$$h_{rad}(f) = \frac{1}{m f^2 L} \sqrt{\frac{\hbar P}{2\pi^3 c \lambda}} \quad (1.8)$$

where m is the mirror mass, f is the gravitational wave frequency, L is the arm length of the detector, \hbar is the reduced Planck's constant, P is the laser power, c is the speed of light, and λ is the laser wavelength. Therefore, opposite to the photon shot noise, the radiation pressure noise can be lowered when the laser power is decreased.

1.4.3.3 Standard Quantum Limit (SQL)

Since the photon shot noise can be minimised when the laser power is increased, and the radiation pressure noise can be minimised when the laser power is decreased, they cannot be minimized at the same time. The minimum of both noise sources can be reached when $h_{shot}(f) = h_{rad}(f)$. This limit due to quantum noises are called “standard quantum limit (SQL)” which is consistent with Heisenberg's uncertainty principle [84, 85].

As the photon shot noise and the radiation pressure noise are not correlated to each other in Michelson interferometers [86], they can be combined as:

$$h(f) = \sqrt{h_{shot}^2(f) + h_{rad}^2(f)} \quad (1.9)$$

The optimal input power can be found by applying $h_{shot}(f) = h_{rad}(f)$ in Equation 1.9:

$$P_{opt} = \pi c m \lambda f^2. \quad (1.10)$$

Applying Equation 1.10, 1.7, 1.8 to Equation 1.9,

$$h_{SQL}(f) = \frac{1}{\pi f L} \frac{\hbar}{m}. \quad (1.11)$$

One of potential approaches to beat this SQL is “squeezing” [87]. By squeezing light, which has amplitude and phase quadratures, the quantum noise in one quadrature can be reduced in the expense of the other. In other words, the uncertainty in two

quadratures can be redistributed according to the Heisenberg Uncertainty Principle, with one quadrature having reduced variance while the other quadrature having increased variance, in order to reduce the total quantum noise in the detector. This technique was first used in GEO600 detector [88], and now it will be applied to the A+ upgrade of LIGO detectors [89].

1.4.4 Suspension Thermal Noise

Thermal noise is generated by random thermal motion of the atoms in the material. From equipartition of energy theorem, we know that $\frac{1}{2}k_B T$ is the average thermal energy for each quadratic term in the energy equation of the system, and is stored in thermal motions (vibration, rotation, etc) of atoms. As Advanced LIGO operates at room temperature, the thermal noise is one of the limits to sensitivity especially in the low frequency range below 100 Hz. The suspension thermal noise comes from dissipation in different parts of the suspension system, such as mirrors and fibres. More details of this noise source will be discussed in the next chapter.

1.4.5 Coating Brownian Noise

Each test mass of the detector has special optical coatings to obtain the desired reflectivity and low absorption level. For Advanced LIGO, the requirement for the reflectivity is $> 99.9\%$ and the absorption level is < 0.5 ppm [90]. To meet these requirements, the Advanced LIGO uses the multi-layer dielectric coatings, alternating layers of ion beam-sputtered amorphous silica (SiO_2 , high index material) and tantalum pentoxide (Ta_2O_5 , low index material) with each having an optical thickness of a quarter of the laser wavelength used in the detector (1064 nm) [91]. Figure 1.13 shows a CAD image of the suspension system and a SEM image of the mirror coating.

Since the mirror can be modelled as half-infinite structure when the mirror radius is

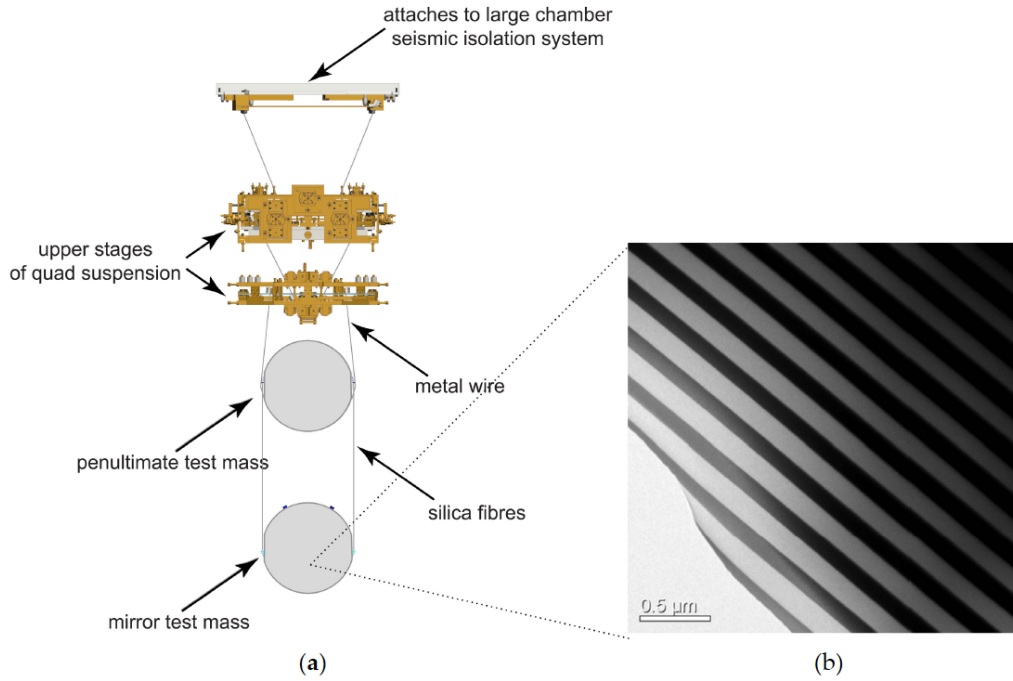


Figure 1.13: (a) CAD image of the suspension system of the Advanced LIGO detectors (b) SEM image of the mirror coating: multilayer stack of SiO_2 (light) and TiO_2 doped Ta_2O_5 (dark) [92]

considerably larger than the beam radius of the incident laser beam [93, 94], the power spectral density of the coating Brownian noise can be expressed as [92]:

$$S_C(f) = \frac{4k_B T (1 + \sigma)(1 - 2\sigma)}{\pi^2 f Y} \frac{d}{r_{beam}} \phi_C \quad (1.12)$$

where σ is Poisson's ratio, d is the thickness of the coating, r_{beam} is the incident beam radius, and ϕ_C is the mechanical loss of the coating. This equation provides several possibilities to reduce the coating Brownian noise: minimising the coating thickness, increasing the beam diameter, and reducing the mechanical loss of the coating.

1.5 Status of Current Detectors and Future Upgrades

1.5.1 Advanced LIGO



(a) *LIGO Hanford, Washington [95].*



(b) *LIGO Livingston, Louisiana [95].*

Figure 1.14: *Two LIGO detectors in the United States.*

The LIGO detectors first began the operation as the “Initial LIGO” from 2002. After its 5th science run, the initial LIGO was upgraded to the “Enhanced LIGO”. In 2010, after its 6th science run, the LIGO detectors went through a major upgrade for five years, the “Advanced LIGO” (aLIGO) [2], which aimed to improve the sensitivity by a factor of 10 compared to that of the initial LIGO and push the bandwidth down to 10 Hz [48]. The arms are 4 km long each, and test masses are 40 kg [48, 72, 96]. Two detectors are located in the United States: one in Hanford, Washington and the other in Livingston, Louisiana (Figure 1.14).

The important features of this upgrade include signal recycling mirrors, increased laser power, quadruple pendulum system, and monolithic fused silica final stage suspensions [2]. Among new implementations, the quadruple monolithic suspensions are directly related to the work presented in this thesis. Figure 1.15 shows a design of quadruple monolithic fused silica suspension used for the aLIGO upgrade: thin fused silica fibres to hang fused silica masses. The key features of this suspension will be discussed in

Chapter 2, after discussing thermal noise in more depth.

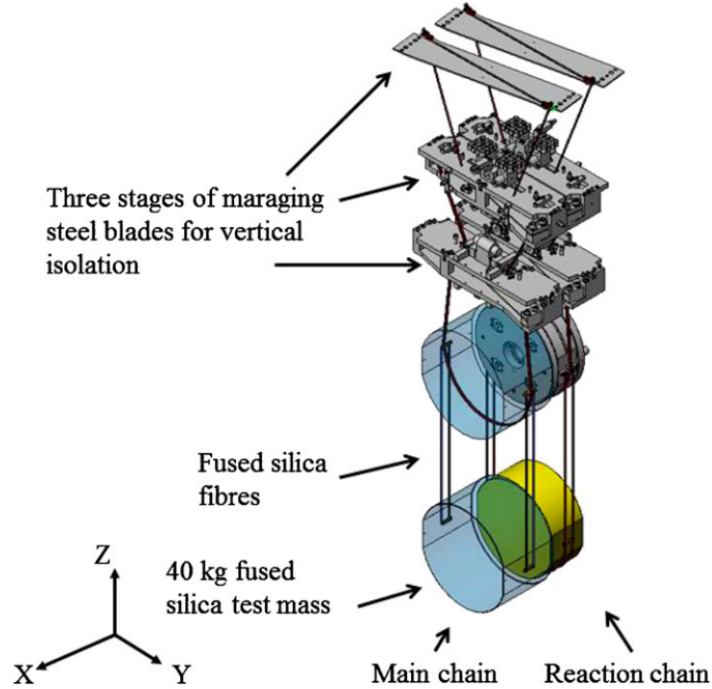


Figure 1.15: A drawing of the Advanced LIGO quadruple monolithic fused silica suspension design [72]. The coordinate system is indicated in the diagram.

1.5.2 Advanced Virgo

Since 2007, LIGO scientific collaboration (LSC) and Virgo scientific collaboration agreed to cooperate and share the data and jointly publish the results. The Virgo detector, located in Italy, has two 3 km long perpendicular arms with Fabry-Perot cavities. The initial Virgo detector collected data from 2007 to 2011, until it was decommissioned for the major upgrades. The main features of the upgrade include higher laser power and heavier test masses. After the upgrades which aimed to be 10 times more sensitive compared to the initial Virgo (Figure 1.16), the Advanced Virgo detector joined the aLIGO detectors in 2017 to observe gravitational wave signals. The first detection from

the Advanced Virgo was GW170814, which was a binary black hole merger.

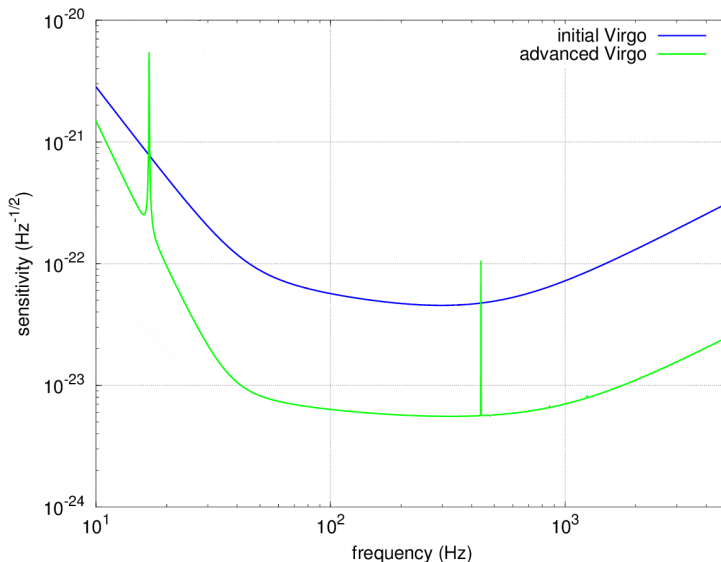


Figure 1.16: Sensitivity curve comparison between the initial Virgo and the Advanced Virgo [97].

1.5.3 KAGRA

Kamioka Gravitational Wave Detector (KAGRA), which used to be called Large Scale Cryogenic Gravitational-wave Telescope (LCGT), is located in Japan. Unlike LIGO detectors, KAGRA is located underground and will operate at cryogenic temperatures (Figure 1.17). The KAGRA project consists of two phases: the initial KAGRA (iKAGRA) and the baseline KAGRA (bKAGRA). The main purpose of the iKAGRA phase was to test all the basic system from the underground interferometer controls to the data analysis pipelines in room temperature, and this was successfully done in 2017. The bKAGRA phase, which aims for a full cryogenic operation, is in progress at the moment. Although there were delays from unexpected sources such as excess water in the tunnels, KAGRA is expected to start the observation runs in early 2020s [79].

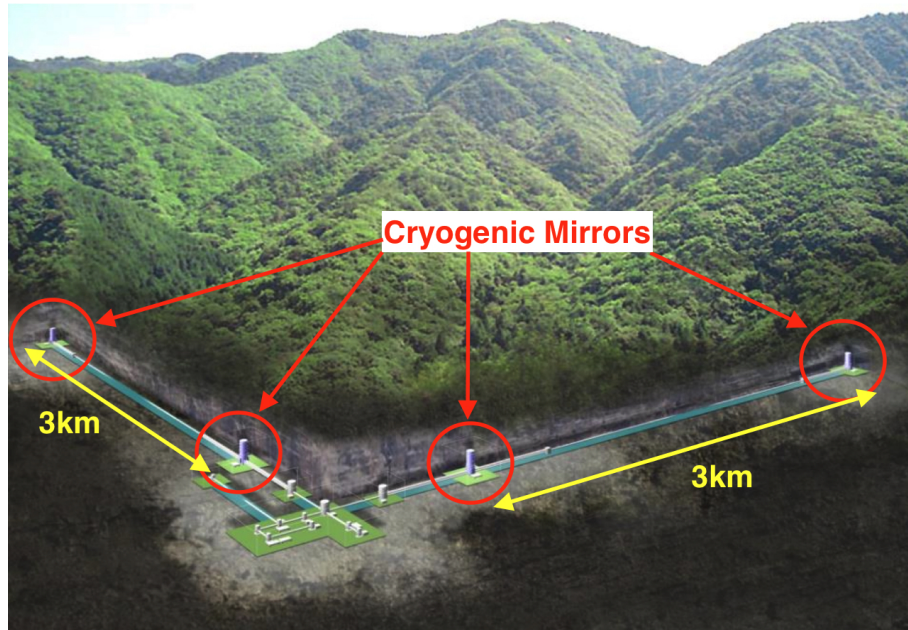


Figure 1.17: Schematic diagram of KAGRA detector [98].

1.5.4 Discovery of Gravitational Waves

1.5.4.1 Binary Black Hole Mergers

In 2015, 100 years since Einstein first predicted the existence of gravitational waves [1], the Advanced LIGO detectors succeeded in the first direct detection of gravitational waves: GW150914 [14]. The GW150914 signal came from a binary black hole collision; one black hole with a mass of 29 solar masses and the other with a mass of 36 solar masses merged to create a single black hole with mass of 62 solar masses, and releasing 3 solar masses worth energy as gravitational waves. Figure 1.18 shows the stages of binary black hole collision and the estimated gravitational wave strain from GW150914 [14].

The signal was detected by two Advanced LIGO detectors (Hanford, Livingston) based in the United States, which showed a very similar waveform not only to the theoretically

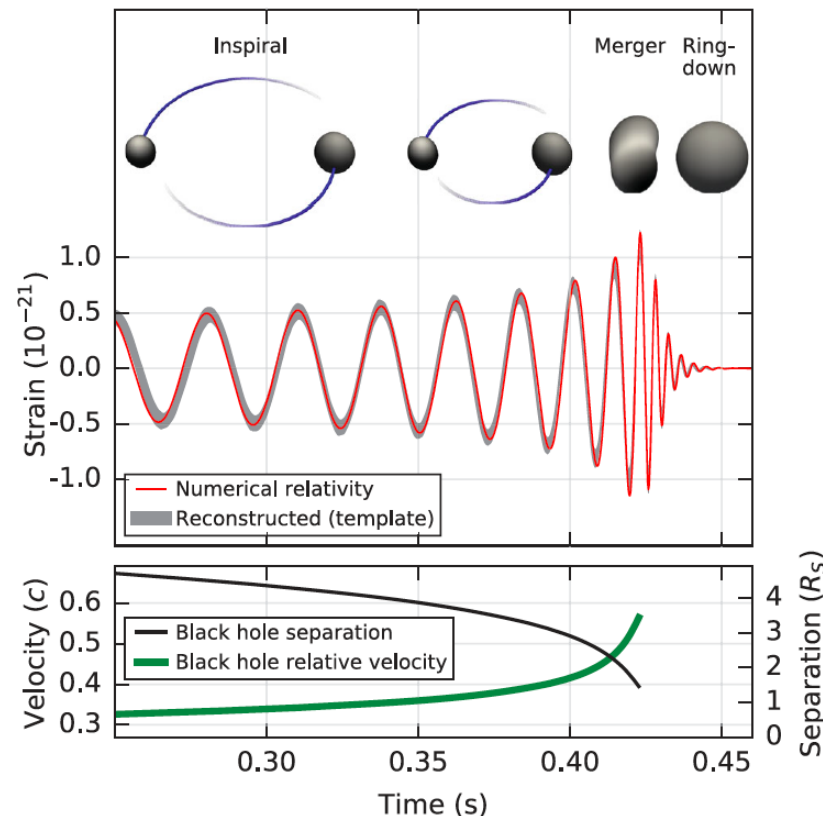


Figure 1.18: Estimated gravitational wave strain from GW150914 [14].

modelled signal for a binary black hole merger [14], but also to each other with 7 ms of time difference. Figure 1.19 shows the observed GW150914 signals from both detectors.

As this was the first detection of gravitational waves, there were significant scientific outcomes from this result. First of all, it was the first time that “heavy” binary black hole system with more than 25 solar mass was observed, which proved that such heavy black holes can exist and can be formed in nature [14]. In addition, this detection confirmed that such binary black holes can merge within the age of the universe at a detectable rate [99]. Through multiple tests [100, 101, 102, 103], it was also confirmed that the GW150914 is consistent with the predictions of binary black hole systems in general relativity [14]. Finally, this result determines the rate that binary black holes

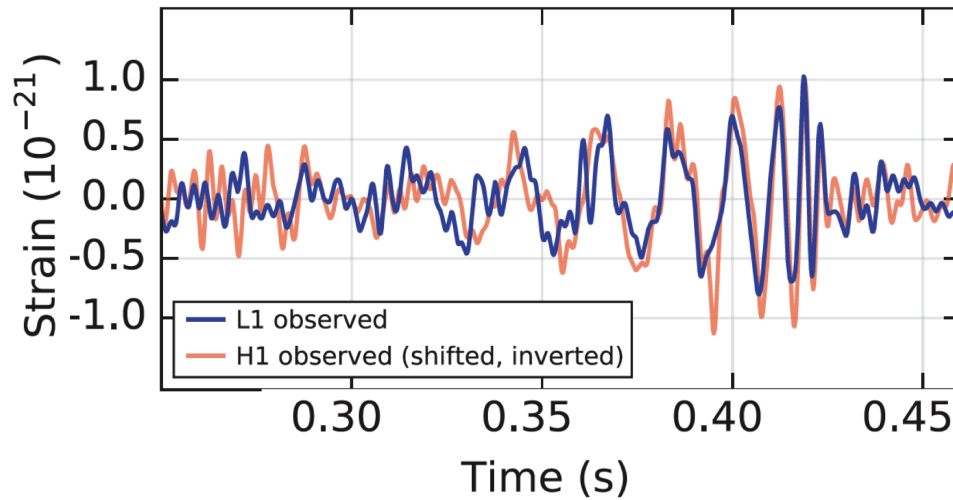


Figure 1.19: Gravitational wave data from GW150914 for both Advanced LIGO detectors. The Hanford data has been time shifted in time and inverted to consider the relative orientation of detectors [14].

merge is in range from $2\text{-}400 \text{ Gpc}^{-3}\text{yr}^{-1}$ [104, 105].

Starting from this first detection, four more black hole mergers were found: GW151226 [15], GW170104 [16], GW170608 [17], GW170814 [18]. Figure 1.20 shows the gravitational wave signals from different binary black hole merger events. Among these detections, the most significant one is GW170814, which happened when three detectors, two Advanced LIGO detectors and the Advanced Virgo detector, were in their observation runs. The LIGO Livingston detector first detected the signal, and after 8 ms, the signal reached the LIGO Hanford detector, and finally reached the Advanced Virgo detector after 14 ms. The addition of the Virgo data provided another independent baseline which could lower the positional uncertainty by an order of magnitude for GW170814 [106]. For instance, the area of the 90% credible region was reduced from 1160 deg^2 to 60 deg^2 by the contribution from the Virgo data. Furthermore, the gravitational-wave polarisations could be determined more accurately. Since two LIGO detectors have very similar orientations, it was difficult to get enough information for the polarisations but

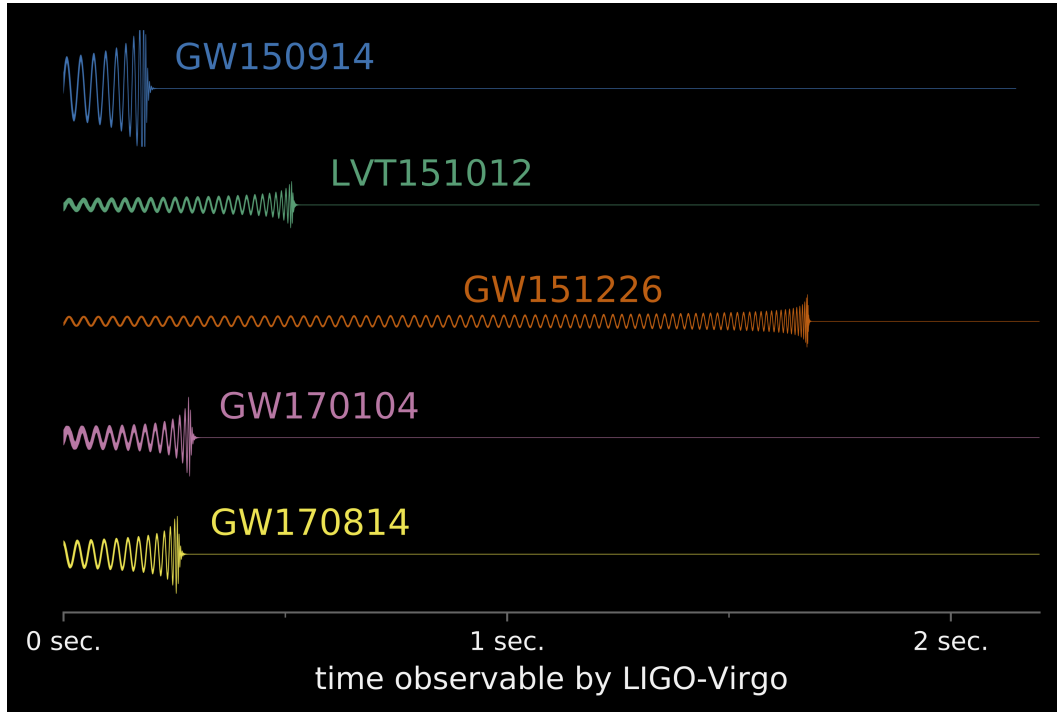


Figure 1.20: Gravitational wave signals from binary black hole systems [62].

now, with the Advanced Virgo data, the polarisations could be found geometrically by projecting the signal onto three detectors [19].

1.5.4.2 Binary Neutron Star Mergers

A few days after the detection of GW170814, another significant signal was detected: GW170817 with merger time 12:41:04 UTC [19], which came from a binary neutron star inspiral. Initially, this event was identified only from the LIGO Hanford detector, since there was a glitch (short instrumental noise) in the LIGO Livingston data and the signal was invisible in the Advanced Virgo data [19]. However, through visual inspection and reanalysis to mitigate the glitch, a significant signal was confirmed in the LIGO detectors. For the Virgo data, the signal was too low to contribute to other parameters, but it did provide better sky localisation [19]. The signal was first detected at the Advanced Virgo

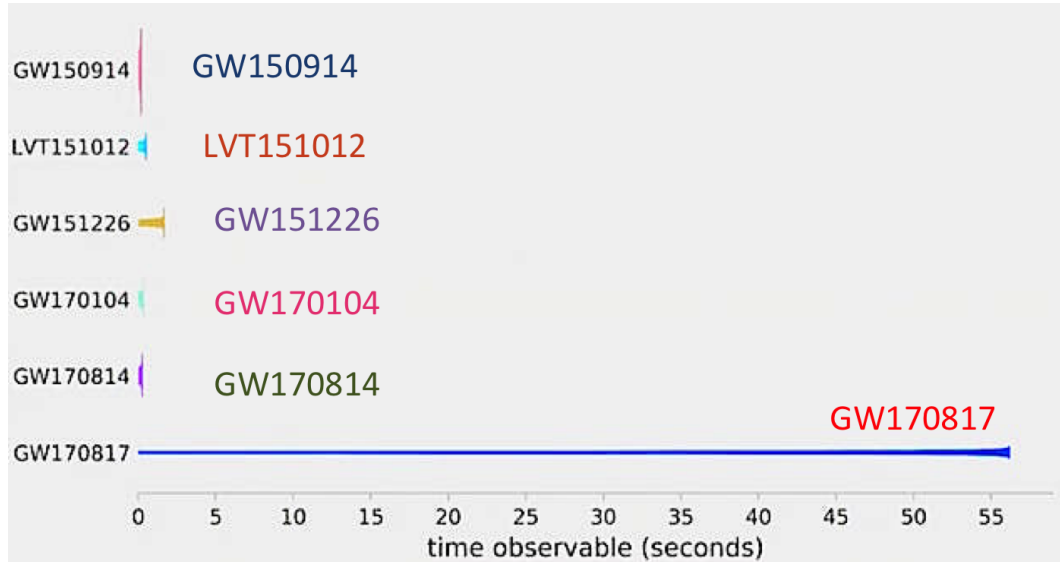


Figure 1.21: Gravitational wave signals from binary neutron star system (GW170817) compared to previously detected signals from binary black hole systems [62].

detector, arrived at the LIGO Livingston detector after 22 ms, and finally reached the LIGO Hanford detector after another 3 ms [107]. Component masses are in the range 1.17 - 1.6 solar masses, and the total mass of the system is estimated to be $2.74^{+0.04}_{-0.01}$ solar masses. Figure 1.22 shows the sky localisation for this event. The light blue contours show the localisation result from Hanford-Livingston analysis and the dark blue contours show that of Hanford-Livingston-Virgo analysis. The additional detection from the Advanced Virgo detector contributed to narrowing down the contours. As Figure 1.23 shows, the two events that were detected by three detectors, GW170814 and GW170817, show better sky localisation results compared to previous events that were detected by two detectors.

This signal was not only detected by three gravitational wave detectors, but also confirmed by other multi-messenger collaborators around the world [108]. 1.7 s after the collision, the gamma ray burst (GRB170817A) was detected by Fermi-GBM (12:41:06 UTC) [109, 110], and later confirmed by INTEGRAL detection [108]. As the first gravitational wave

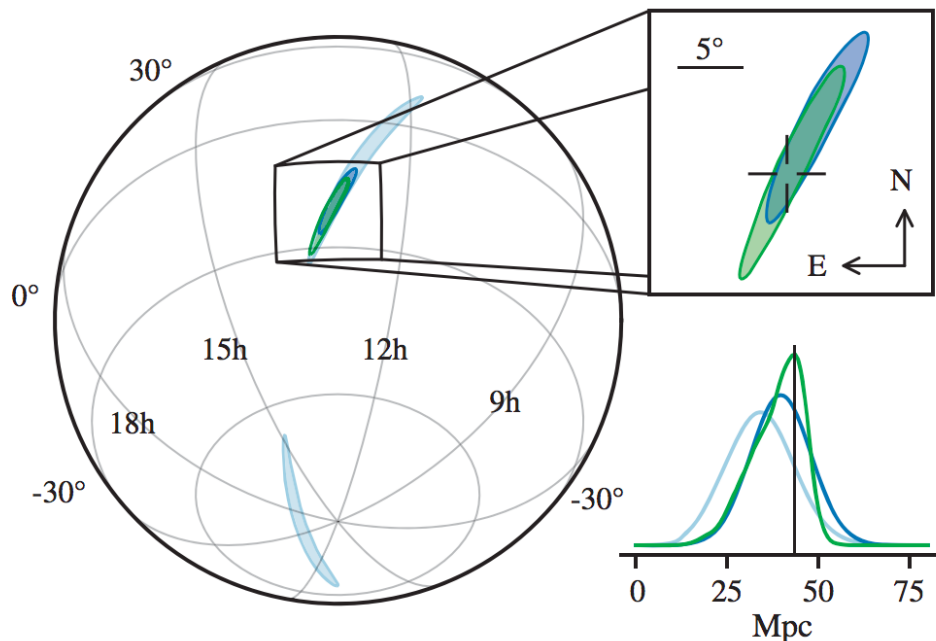


Figure 1.22: Sky localisation for GW170817. The light blue contours show the localisation result from Hanford-Livingston analysis and the dark blue contours show that of Hanford-Livingston-Virgo analysis [19].

detection event that opened the window of multi-messenger observations, GW170817 has various scientific significance. This multi-messenger observation not only confirmed that the gravitational wave signal indeed came from a neutron star merger, but also provided the first direct evidence that a neutron star merger creates a short gamma ray burst. In addition, using the luminosity distance of the source measured from the gravitational wave signals and the redshift measurement from the electromagnetic emission, the Hubble constant, which represents the expansion rate of the universe, was determined to be $70_{-8.0}^{+12.0} \text{ km s}^{-1} \text{ Mpc}^{-1}$ [111], which is consistent with the recent measurements [112]. Using the time delay of 1.7 s between the gravitational wave detection and the gamma ray burst detection, fundamental physics of gravity could be investigated: the difference between the speed of gravity and the speed of light was constrained between -3×10^{-15} to $+7 \times 10^{-16}$ times of the speed of light [113], new test of equivalence principle through

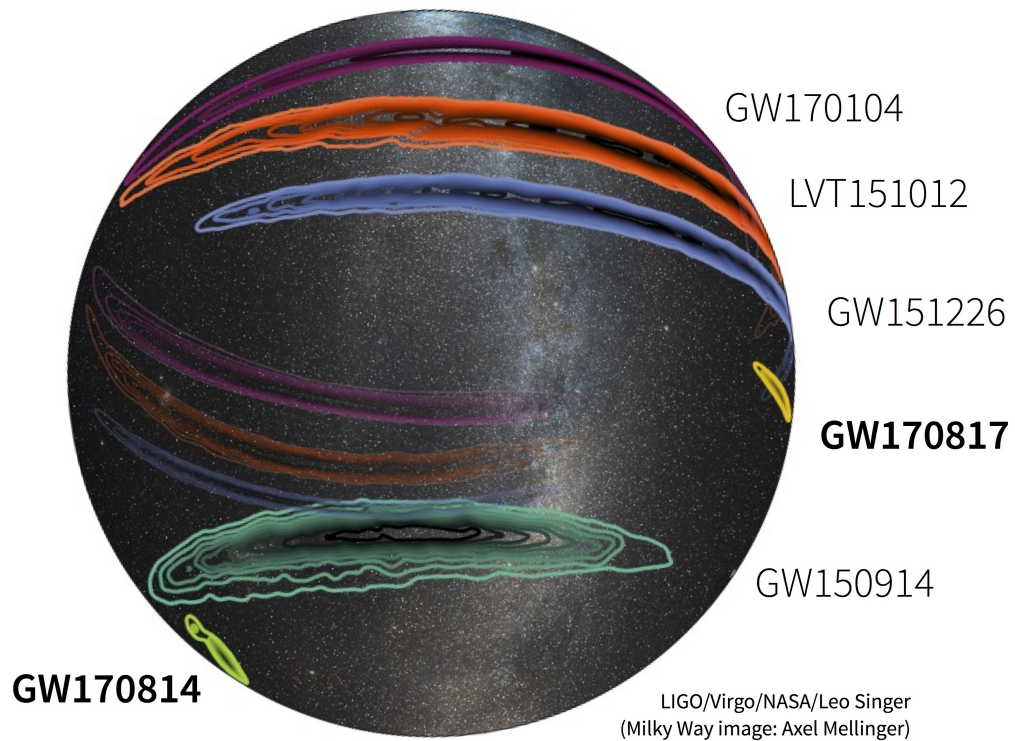


Figure 1.23: Sky localisation result for gravitational wave detections [62]. For GW170814 and GW170817, which were detected by three detectors, the addition of Advanced Virgo data further constrained the sky position.

Shapiro delay was presented [113], and new bounds were placed on the Lorentz invariance violation [113]. The optical emission data taken for few days after the GW170817 event showed a tendency that was broadly consistent with that expected from a kilonova, and AT 2017gfo was concluded to be a kilonova associated with GW170817 [114]. The data also indicates that at least 0.05 solar masses of heavy elements were produced from AT 2017gfo [115]. These collaborative detections around the world showed the significance and bright future of multi-messenger observations.

1.5.5 Future Detectors

The second generation detectors, including the Advanced LIGO and Advanced Virgo, have achieved a great success detecting gravitational wave signals from binary black holes and binary neutron stars. However, further upgrades are required to detect less powerful sources, such as pulsars, and to have more precise astronomical analysis for the detected sources. Obviously, upgrade plans with significant changes such as building underground detectors will bring bigger advantages, but they require more time and further R&D. Meanwhile, “near-term upgrades” on the current detectors can also contribute to increasing sensitivity without major changes in the infrastructure. For instance, in terms of reducing thermal noise, implementing new fused silica fibres and new mirror coatings can be examples of near-term upgrades, while putting the whole suspension system in a cryogenic chamber is an example of a “long-term upgrade”. Both upgrade plans have pros and cons, thus R&D for both upgrades are in progress.

The A+ upgrade plan is the current “near-term upgrade” of the Advanced LIGO detectors which aims to be completed in 2023 [116]. Figure 1.24 shows the design sensitivity for the A+ Upgrade compared to the aLIGO strain noise in the Observing run 2 (O2) and the design sensitivity of the aLIGO. Depending on the type of source, this upgrade will bring factor of 4 to 7 improvement in the detector’s sensitivity [116]. Important noise sources to be targetted include quantum noise, coating thermal noise, and suspension thermal noise. The squeezing technique will be implemented to improve both photon shot noise in the high frequency range and radiation pressure noise in the low frequency range. New coating materials are under development, aiming to have mechanical dissipation as low as 25% of the current coatings. Most importantly in terms of the work presented in this thesis, the A+ upgrade will potentially implement thinner fused silica fibres to increase the tensile stress on the fibres, which will improve the suspension thermal noise. The great advantage of implementing thinner fibres is that it will only bring improvements in the noise without any side effects. However, the limiting factor is the strength of the

fibres, and this will be discussed further in this thesis.

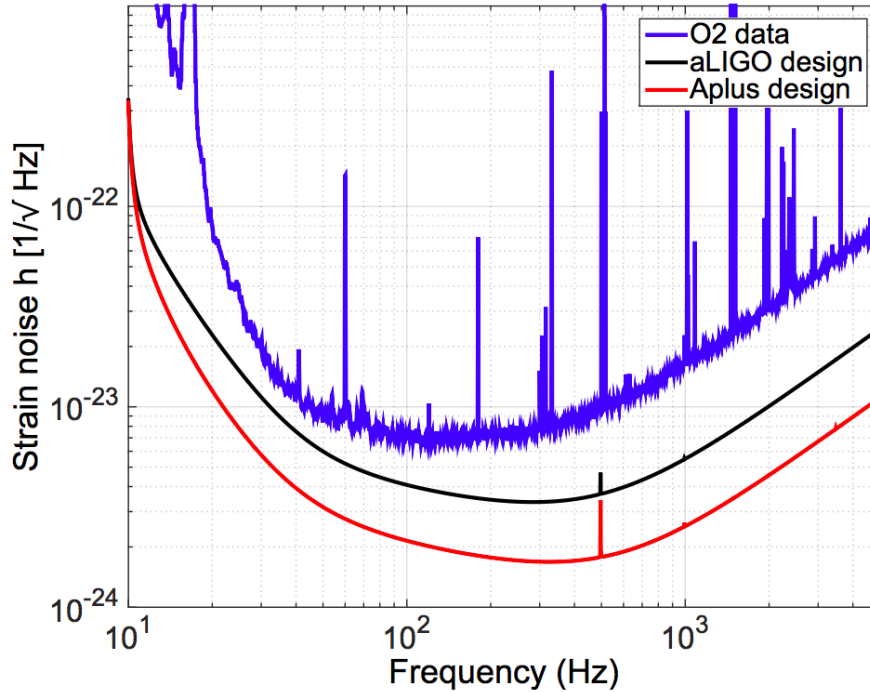


Figure 1.24: Design sensitivity for the A+ upgrade compared to the aLIGO strain noise in the Observing run 2 (O2) and the design sensitivity of the aLIGO [116].

The third generation detectors, which can be classified as “long-term upgrades”, are most likely to move on to cryogenic operation, instead of running at room temperature [117, 118], to reduce the thermal noise. However, to operate the detector cryogenically, more investigation is required to find suitable materials for the suspension system and the mirror coatings that can work better at low temperature [118]. Constructing the detector underground can also improve the sensitivity by reducing Newtonian noise. KAGRA (underground, cryogenic) [79], the Einstein telescope (ET High Frequency: underground, room temperature, ET Low Frequency: underground, cryogenic) [118], LIGO Voyager (ground, cryogenic) [119], and Cosmic Explorer (ground or underground, cryogenic) [120] are examples of next generation detectors. KAGRA consists of two 3 km-arms perpendicular to each other and plans to start operating in 2020 [79]. LIGO-Voyager is

the third generation upgrade plan for the current LIGO detector sites [119]. The ET consists of three interferometers with 10 km arms [118] and Cosmic Explorer will have 40 km arms [120], but both of them are in their design and development stage that it is difficult to predict the operation schedule.

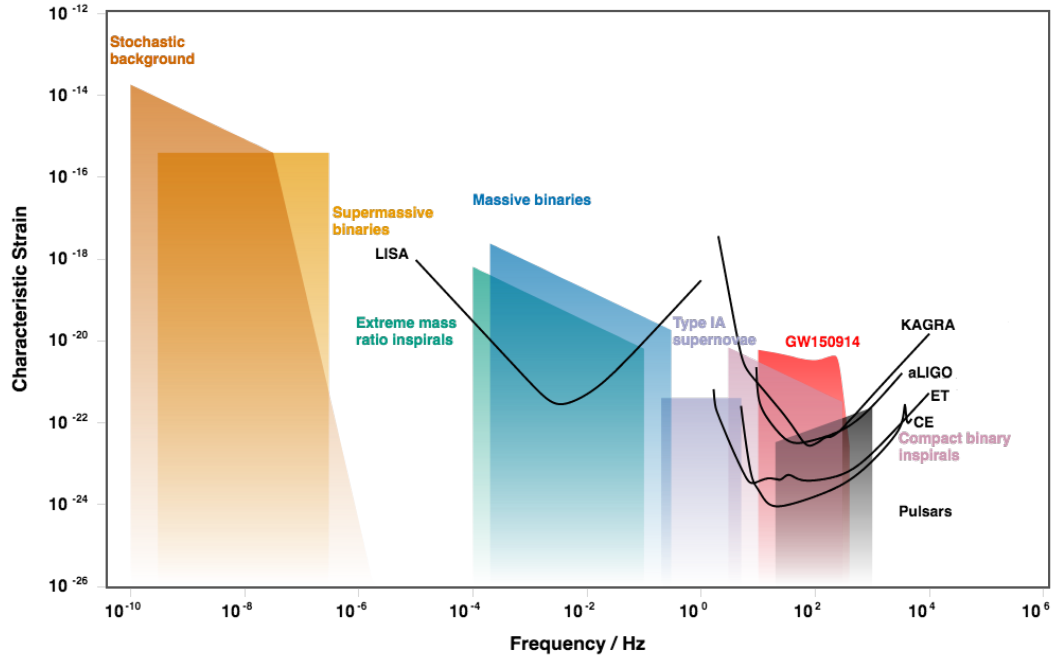


Figure 1.25: Gravitational wave detectors' sensitivity curve and sources [121].

To investigate the low frequency range below 1 Hz, space-based detectors are necessary. Figure 1.25 shows the different target frequency range for ground-based detectors and space-based detectors. Each type of detector covers a different range of frequency allowing more sources to be investigated. Space-based detectors have advantages in not being susceptible to terrestrial seismic noise and the detector's arm length is not limited by the Earth's curvature. Thus, the sensitivity in the low frequency range, where the seismic, Newtonian, suspension thermal noise are dominant in ground-based detectors, can be greatly improved. The Laser Interferometric Space Antenna (LISA) is an example of the space-based detector [122]. In 2015, LISA Pathfinder was launched to test the components

and technology required for the space-based detectors [123, 124]. Demonstrating the sensitivity that was better by factor of two than the requirement suitable for LISA, the LISA Pathfinder mission successfully ended in 2016 [123]. Figure 1.26 shows the final data collected from the LISA Pathfinder and the LISA requirement to confirm the success of the mission [125]. The estimated launch for the LISA is 2034 [126].

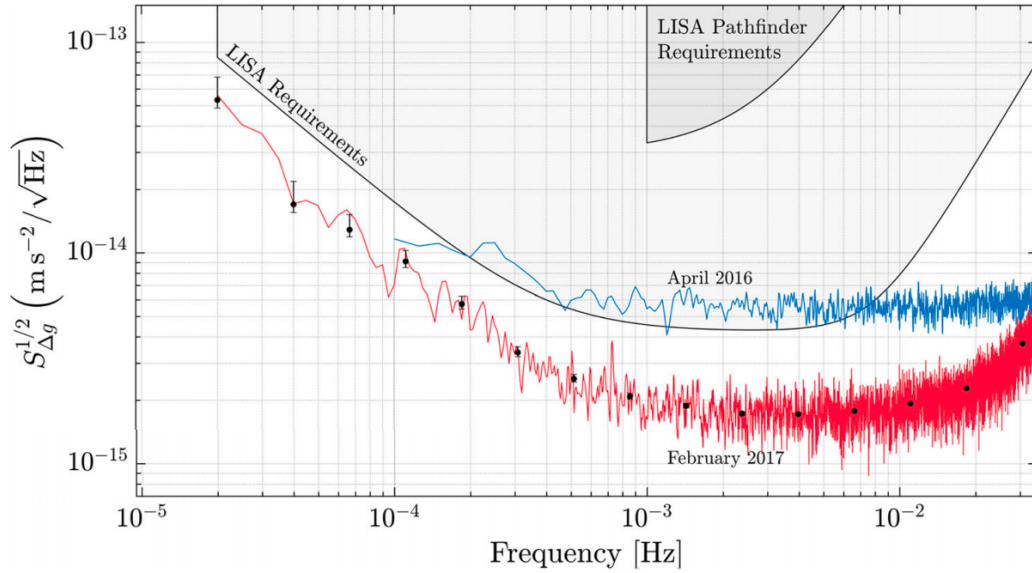


Figure 1.26: Differential acceleration spectrum of LISA Pathfinder (LPF) and the requirements for the LPF and LISA. [125].

1.6 Conclusions

Starting from the first direct detection of the gravitational waves in 2015, the Advanced LIGO detectors have successfully detected multiple signals from different sources, opening up a new window of astrophysics research. Various detectors around the world are collaborating for better sky localisation and multi-messenger observations and collaborations. To further improve the sensitivity of detectors, upgrade plans, such as A+ upgrade, are now under investigation. The work presented in this thesis is closely

related to the A+ upgrade, especially reducing thermal noise of the detector. Thus, thermal noise will be discussed in depth in the following chapter, along with detailed features of suspension systems in the Advanced LIGO detectors.

Chapter 2

Thermal Noise

2.1 Introduction

Thermal noise is generated by Brownian motion and temperature fluctuations due to thermal energy in a material. From the equipartition of energy theorem, we know that $\frac{1}{2}k_B T$ is the average thermal energy for each quadratic term in the energy equation of the system, and is stored in thermal motions (vibration, rotation, etc) of atoms.

As the Advanced LIGO detectors operate at room temperature, thermal noise is one of the important noise sources. Thermal noise from the mirror coatings, pendulum systems, and other infrastructures all combine to induce thermal motion of the mirrors across the important highest sensitivity band and the low frequency band of the detectors. Since this noise source is dominant at these frequencies, it is very critical to reduce its magnitude.

One obvious solution is to cryogenically cool suspension systems to directly reduce the thermal noise. However, this change will require enormous increase in the cost of infrastructure and intensive investigation on finding new materials suitable for cryogenic operation. Therefore, at least for the near-term upgrades of the aLIGO detectors, it is

not an option to lower the temperature. However, thermal noise can still be reduced without cryogenics.

Brownian motion is the stochastic motion of thermally excited atoms [127]. In 1827, Robert Brown discovered this random motion from pollen particles freely floating on the surface of water [128]. Later, Einstein showed that the pollen particles moved because of the fluctuation in the number of collisions with water molecules, which lose kinetic energy through collisions [129], thus connecting fluctuation and dissipation of the system. Later, Callen *et al.* developed this further to explain the general relation between the fluctuation and the dissipation of a system, which is known as the Fluctuation-Dissipation Theorem [130, 131].

According to the Fluctuation-Dissipation Theorem, the power spectral density of the thermal driving force of a system ($S_f(\omega)$) can be described as:

$$S_f(\omega) = 4k_B T \Re[Z(\omega)] \quad [N^2/Hz] \quad (2.1)$$

where k_B is the Boltzmann constant, T is the temperature and $Z(\omega) = \frac{F}{v} = \frac{F}{i\omega x}$ is the mechanical impedance of the system (the dissipation), F is the applied force, and v is the resulting velocity response of the system. In an alternative useful form, the power spectral density in terms of displacement can be given as [3]:

$$S_x(\omega) = \frac{4k_B T}{\omega^2} \Re[Y(\omega)] \quad [m^2/Hz] \quad (2.2)$$

where $Z = \frac{1}{Y}$. This equation is the most general form of the equation that will be used to calculate the thermal noise in the gravitational wave detectors. As mentioned in Section 1.4.4, the thermal noise is one of the dominant noise sources in the low frequency range below 100 Hz.

2.2 Sources of Dissipation

2.2.1 External Sources of Dissipation

In gravitational wave detectors, the possible external sources of dissipation are:

- Dissipation caused by residual gas molecules colliding in the suspension system.
- Motion of the suspension elements causing recoil of the supporting structure.
- Damping due to magnetic hysteresis and eddy currents.
- Dissipation caused by friction at the suspending points, such as clamping points of the masses.

However, these external dissipative sources can be reduced sufficiently, via optimised design [132] and implementation, such that the internal sources of dissipation become the dominant factor.

2.2.2 Internal Sources of Dissipation

The internal dissipation is caused by the anelastic behaviour of the suspension system. For an ideal oscillator, which is perfectly elastic and “without dissipation”, Hooke’s law can be used to describe the system:

$$F_{spring} = -kx \quad (2.3)$$

where F_{spring} is the applied force, k is the spring constant, and x is the displacement. However, this equation does not consider the time lag happening in real world oscillators. To take this into account, Equation 2.3 can be modified as:

$$F_{spring}(\omega) = -k(1 + i\phi(\omega))x \quad (2.4)$$

where $\phi(\omega)$ is the “mechanical loss” of the material, which is the phase angle between the force and the strain response. The mechanical loss is related to the damping due to the internal friction of the anelastic material, representing a measure of the dissipated energy per oscillation cycle. For a perfectly elastic material, the mechanical loss will be 0, but all real materials will have some degree of anelasticity.

Using Equation 2.4, we can describe the equation of motion of a damped harmonic oscillator with internal friction:

$$m\ddot{x} = F_{thermal} - k(1 + i\phi(\omega))x \quad (2.5)$$

where m is the mass, k is the spring constant, \ddot{x} is the acceleration, x is the displacement, and $F_{thermal}$ is the thermal driving force. In terms of velocity (\dot{x}) and angular frequency (ω),

$$\ddot{x} = i\omega\dot{x} \quad (2.6)$$

$$x = \frac{\dot{x}}{i\omega} \quad (2.7)$$

Using Equation 2.6 and 2.7, the thermal driving force of the oscillator can be described as:

$$i\omega m\dot{x} = -\frac{k}{i\omega}(1 + i\phi(\omega))\dot{x} + F_{thermal} \quad (2.8)$$

$$\dot{x} \left[i\omega m + \frac{k}{i\omega}(1 + i\phi(\omega)) \right] = F_{thermal} \quad (2.9)$$

Using $\Re[Z(\omega)] = \frac{F}{v}$ and Equation 2.8,

$$Z = \frac{F}{\dot{x}} \quad (2.10)$$

$$= i\omega m + \frac{k}{i\omega}(1 + i\phi(\omega)) \quad (2.11)$$

$$= \frac{-\omega^2 m + k + ik\phi(\omega)}{i\omega} \quad (2.12)$$

Since $Z = \frac{1}{Y}$,

$$Y(\omega) = \frac{1}{Z(\omega)} = \frac{i\omega}{-\omega^2 m + k + ik\phi(\omega)} \quad (2.13)$$

$$= \frac{i\omega}{-\omega^2 m + k + ik\phi(\omega)} \times \begin{bmatrix} i \\ i \end{bmatrix} \quad (2.14)$$

$$= \frac{\omega}{i\omega^2 m - ik + k\phi(\omega)} \quad (2.15)$$

Multiplying by the complex conjugate of the denominator,

$$Y(\omega) = \frac{\omega}{i\omega^2 m - ik + k\phi(\omega)} \quad (2.16)$$

$$= \frac{\omega}{k\phi(\omega) - i(k - \omega^2 m)} \times \begin{bmatrix} k\phi(\omega) + i(k - \omega^2 m) \\ k\phi(\omega) + i(k - \omega^2 m) \end{bmatrix} \quad (2.17)$$

$$= \frac{k\omega\phi(\omega) + ik\omega - i\omega^3 m}{k^2\phi^2(\omega) + (k - \omega^2 m)^2} \quad (2.18)$$

Applying Equation 2.2 to Equation 2.18, we get:

$$S_x(\omega) = \frac{4k_B T}{\omega^2} \frac{k\omega\phi(\omega)}{k^2\phi^2(\omega) + (k - \omega^2 m)^2} \quad (2.19)$$

Since $k = \omega_0^2 m$,

$$S_x(\omega) = \overline{x^2}_{thermal}(\omega) = \frac{4k_B T}{\omega^2} \frac{\omega_0^2 m \omega \phi(\omega)}{(\omega_0^2 m)^2 \phi^2(\omega) + (\omega_0^2 m - \omega^2 m)^2} \quad (2.20)$$

$$= \frac{4k_B T}{\omega m} \frac{\omega_0^2 \phi(\omega)}{[\omega_0^4 \phi^2(\omega) + (\omega_0^2 - \omega^2)^2]} \quad [m^2/Hz] \quad (2.21)$$

2.3 Thermal Noise in terms of Mechanical Loss

2.3.1 Thermal Noise in a Single Resonant System

Equation 2.21 shows two important points: the thermal noise displacement is correlated with the mechanical loss, and the thermal noise is dependent on the frequency considered. Therefore, depending on the frequency range of interest, Equation 2.21 can be simplified.

When the frequency is well below the resonant frequency, $\omega \ll \omega_0$,

$$S_x(\omega) = \overline{x^2}_{thermal}(\omega) = \frac{4k_B T}{\omega m} \frac{\omega_0^2 \phi(\omega)}{[\omega_0^4 \phi^2(\omega) + (\omega_0^2 - \omega^2)^2]} \quad (2.22)$$

$$\approx \frac{4k_B T}{\omega} \frac{\omega_0^2 \phi(\omega)}{m[\omega_0^4 \phi^2(\omega) + \omega_0^4]} \quad (2.23)$$

$$= \frac{4k_B T}{\omega} \frac{\phi(\omega)}{m\omega_0^2[\phi^2(\omega) + 1]} \quad (2.24)$$

When a material with a very low mechanical loss, $\phi(\omega) \ll 1$, is considered, Equation 2.24 can be further reduced to:

$$S_x(\omega) = \overline{x^2}_{thermal}(\omega) \approx \frac{4k_B T \phi(\omega)}{\omega m \omega_0^2} \quad (2.25)$$

Equation 2.25 shows that the low loss material can reduce the thermal noise for the frequency band well below the resonant frequency. Figure 2.1 shows a suspension thermal

noise ($\sqrt{S_x(\omega)} = \sqrt{x^2}$) comparison between different mechanical loss values (ϕ). The black line represents $\phi = 10^{-1}$, the red line represents $\phi = 10^{-2}$, and the blue line represents $\phi = 10^{-5}$. As the mechanical loss decreases, the resonant peak becomes higher and the off-peak noise becomes lower.

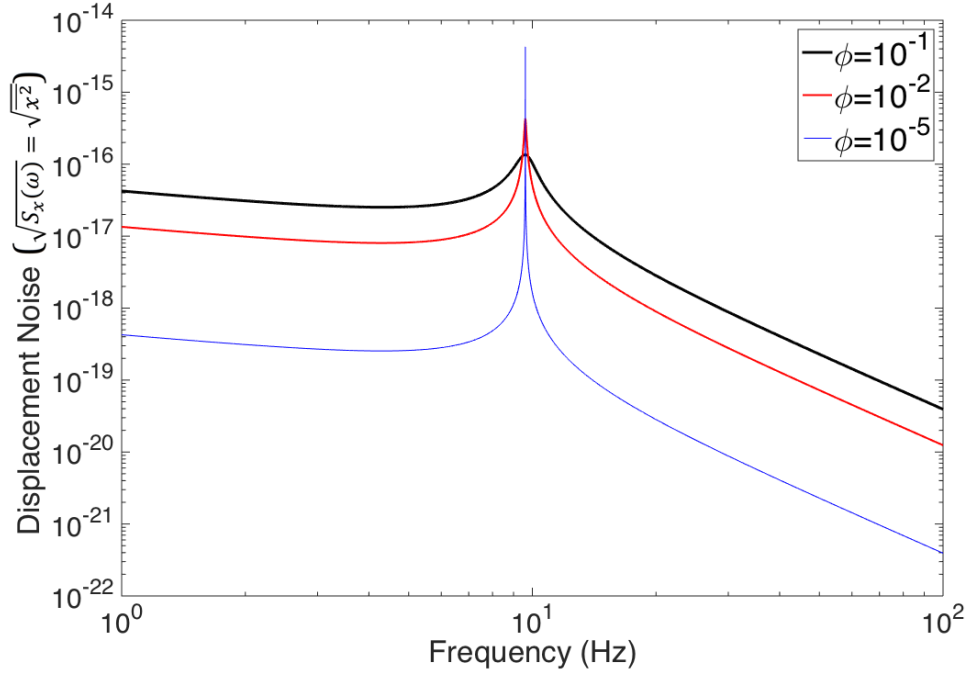


Figure 2.1: Suspension thermal noise comparison between different mechanical loss values (ϕ).

Similarly, when the frequency is well above the resonant frequency, $\omega \gg \omega_0$,

$$S_x(\omega) = \overline{x^2}_{thermal}(\omega) = \frac{4k_B T}{\omega m} \frac{\omega_0^2 \phi(\omega)}{[\omega_0^4 \phi^2(\omega) + (\omega_0^2 - \omega^2)^2]} \quad (2.26)$$

$$\approx \frac{4k_B T}{\omega} \frac{\omega_0^2 \phi(\omega)}{m[\omega_0^4 \phi^2(\omega) + \omega^4]} \quad (2.27)$$

$$= \frac{4k_B T \phi(\omega) \omega_0^2}{m \omega^5} \quad (2.28)$$

When a material with a very low mechanical loss, $\phi(\omega) \ll 1$, is considered, Equation 2.28 shows that the low loss material can reduce the thermal noise for the frequency band well above the resonant frequency.

Lastly, at the resonant frequency, $\omega = \omega_0$,

$$S_x(\omega_0) = \overline{x^2}_{thermal}(\omega) = \frac{4k_B T}{\omega m} \frac{\omega_0^2 \phi(\omega)}{[\omega_0^4 \phi^2(\omega) + (\omega_0^2 - \omega^2)^2]} \quad (2.29)$$

$$\approx \frac{4k_B T}{\omega} \frac{\omega_0^2 \phi(\omega)}{m[\omega_0^4 \phi^2(\omega)]} \quad (2.30)$$

$$= \frac{4k_B T}{m\omega_0^3 \phi(\omega_0)} \quad (2.31)$$

When a material with a very low mechanical loss, $\phi(\omega) \ll 1$, is considered, Equation 2.31 shows that the thermal noise significantly increases at the resonant frequency.

It can be deduced from these equations that finding a material with lower the mechanical loss (ϕ) is the key to minimise the off-resonance thermal noise in the test masses and the suspension system. Therefore, the mechanical design should be carefully considered to ensure the resonances minimally encroach into detection band. Although the thermal noise at the resonant frequency will increase when the mechanical loss is low, it reduces the noise in all other range away from the peak (Figure 2.1), which is beneficial to the detector's sensitivity. As fused silica is known to have low mechanical loss at room temperature [133, 134, 135, 136], the Advanced LIGO detectors implemented the quasi-monolithic fused silica suspension system where the final stage of the suspension is all made of fused silica.

2.3.2 Thermal Noise in Multi-Resonant Systems

In any real mechanical system, including the mirror suspensions in the detectors, there are multiple resonant modes that can be excited. Equation 2.32 shows a generalised form of thermal noise in a system with n resonant modes [137]:

$$S_x(\omega) = \overline{x^2}_{thermal}(\omega) \approx \sum_n \frac{4k_B T}{\alpha_n m \omega_n^2} \frac{\phi_n(\omega)}{\omega} \quad (2.32)$$

where $\phi_n(\omega)$ is the mechanical loss of n th mode, and $\alpha_n m$ is the effective mass of each mode.

However, this general form assumes that the mechanical loss distribution is homogeneous, and that there is no correlation of resonant motion between modes. Considering these issues, Levin applied Fluctuation-Dissipation theorem to revise the equation [138]:

$$S_x(\omega) = \overline{x^2}_{thermal}(\omega) = \frac{2k_B T}{\pi^2 \omega^2} \frac{W_{diss}}{F_0^2} \quad (2.33)$$

where F_0 is the amplitude of the oscillating force applied to the surface, W_{diss} is the time-averaged power dissipated in the test mass when F_0 is applied. The dissipated power W_{diss} is given by:

$$W_{diss} = \omega \int_{vol} (\epsilon(x, y, z) \phi(x, y, z, f)) dV \quad (2.34)$$

where $\epsilon(x, y, z)$ is the energy density of the elastic deformation and $\phi(x, y, z, f)$ is the mechanical loss, which can be analytically calculated using FEA. One of the examples of the application of Levin's equation is the calculation of the thermal noise due to the bonds between the test masses and fused silica ears (Figure 2.2).

2.4 Mechanical Loss in Fibres

2.4.1 Thermoelastic Loss

Thermoelastic loss is another source of dissipation which is frequency dependent [140, 141]. Figure 2.3 shows the fundamental principle of thermoelastic loss. When the material

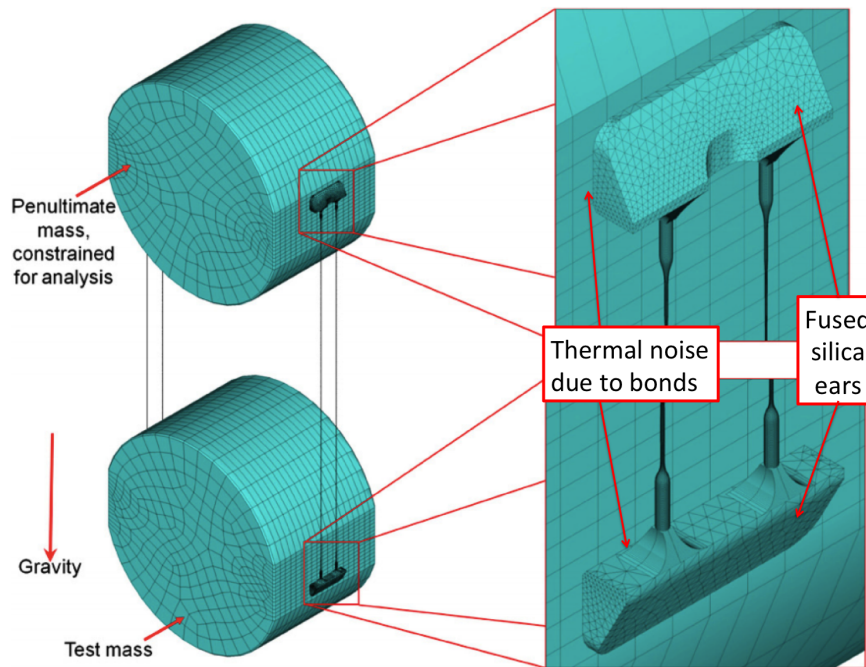


Figure 2.2: Finite element model of the monolithic suspension stage. The bonds to connect the ears to the test masses are also another source of thermal noise [139].

(e.g suspension fibre) gets bent, the temperature of the compressed side will slightly increase while that of the stretched side will cool down. To regain equilibrium, this thermal gradient causes thermal energy from the compressed side to flow to the stretched side. As the material bends back and forth, the energy also flows back and forth. This mechanism works in reverse, too; if a section of the material is heated, the thermal gradient causes the material to bend. (the second is more commonly seen in the detectors; local temperature variations along the fibre cause bending of the fibre.) The loss due to this heat transfer is thermoelastic loss.

The amount of temperature-dependent compression and expansion can be determined from the thermal expansion coefficient of the material:

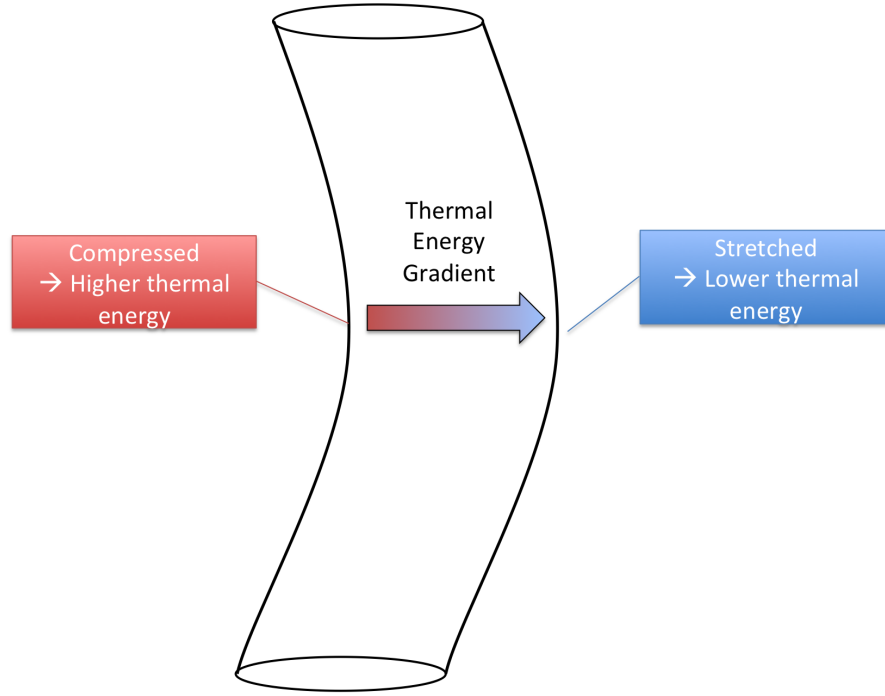


Figure 2.3: Schematic diagram showing the fundamental mechanism of thermoelastic loss.

$$\alpha = \frac{1}{L} \frac{dL}{dT} \Rightarrow dL = \alpha L dT \quad (2.35)$$

where L is the length of the fibre, dL is the change in length, and dT is the change in temperature. Using Equation 2.35, the thermoelastic loss can be described as [141, 140]:

$$\phi_{\text{Thermoelastic}} = \frac{YT\alpha^2}{\rho C} \left[\frac{\omega\tau}{1 + (\omega\tau)^2} \right] \quad (2.36)$$

where Y is the Young's modulus, T is the temperature, ρ is the density of the material, C is the specific heat capacity, ω is the angular frequency, and τ is the characteristic time for the heat to flow across the sample, which can be written as,

$$\tau = \frac{\rho C d^2}{13.55 \kappa} \quad (2.37)$$

for a circular cross-section, where d is the diameter of the fibre, and κ is the thermal conductivity.

However, Equation 2.36 doesn't take into account the fact that the Young's modulus is dependent on temperature. This temperature dependence of Young's modulus can be described as a parameter, β , which is called elastic thermal coefficient [142]:

$$\beta = \frac{1}{Y} \frac{dY}{dT}. \quad (2.38)$$

By definition, the Young's modulus is

$$Y = \frac{\sigma}{\epsilon} \quad (2.39)$$

where σ is the static stress, $\sigma = Tension/Area$, and ϵ is the strain, $\epsilon = dL/L$.

Therefore, Equation 2.39 can be written as,

$$\sigma = Y \left[\frac{dL}{L} \right] \Rightarrow dL = \frac{\sigma L}{Y} \quad (2.40)$$

dL in Equation 2.40 is the change in length due to the change in the Young's modulus, which is caused by the temperature change. To clearly distinguish this dL from the change in length due to the thermal expansion coefficient α (Equation 2.35), the dL from the change in Young's modulus will be stated as dL_Y and the dL from the thermal expansion coefficient will be stated as dL_α . The static stretch due to σ will be stated as dL_σ .

Equation 2.40 can be written as,

$$dL_Y = \frac{\sigma L}{Y} \quad (2.41)$$

Taking derivative,

$$\frac{dL_Y}{dT} = \frac{-\sigma L}{Y^2} \frac{dY}{dT} \Rightarrow dL_Y = \frac{-\sigma L}{Y^2} \frac{dY}{dT} dT \quad (2.42)$$

$$= \frac{-\sigma L}{Y} \frac{1}{Y} \frac{dY}{dT} dT \quad (2.43)$$

Applying Equation 2.38,

$$dL_Y = \frac{-\sigma L}{Y} \beta dT \quad (2.44)$$

Therefore, from dL_α and dL_Y ,

$$dL_{Total} = \alpha L dT + \frac{-\sigma L}{Y} \beta dT + \frac{\sigma L}{Y} = (\alpha - \frac{\sigma}{Y} \beta) L dT + \frac{\sigma L}{Y} \quad (2.45)$$

Since the term $\frac{\sigma L}{Y}$ is from the static stretch, the effective thermal coefficient of expansion is

$$\alpha_{eff} = \alpha - \frac{\sigma}{Y} \beta \quad (2.46)$$

Applying Equation 2.46 to Equation 2.36 [142],

$$\phi_{Thermoelastic} = \frac{YT}{\rho C} \frac{\omega \tau}{1 + (\omega \tau)^2} (\alpha - \beta \frac{\sigma}{Y})^2 \quad (2.47)$$

One of the most important properties of fused silica that is very different from most other materials is that this β is positive, which means that the Young's modulus of fused

silica tends to increase as the temperature rises. In terms of material, this means that the material becomes stiffer as the temperature increases. Therefore, the last term of the thermoelastic loss, $(\alpha - \beta \frac{\sigma}{Y})^2$, can be, theoretically, totally cancelled out by controlling the stress applied to the fibre. Table 2.1 shows the conditions that the Advanced LIGO is designed to run.

$\alpha(K^{-1})$	$\beta(K^{-1})$	$Y(N/m^2)$	$\kappa(W/mK)$	$C(J/kgK)$	$\rho(kg/m^3)$	$\sigma(MPa)$
3.9×10^{-7}	1.52×10^{-4}	7.2×10^{10}	1.38	770	2200	770

Table 2.1: Material properties of fused silica [143]

From the definition of the static stress,

$$\sigma = \frac{F}{A}, \quad (2.48)$$

the theoretical value of area the fibre, A , can be calculated: $5.3 \times 10^{-7} m^2$, which leads to a required radius of $411 \mu m$ to cancel thermoelastic noise. The Advanced LIGO fibres are designed to have a “thermoelastic nulling diameter region” at both ends to minimise the impact of thermoelastic loss. More details will be discussed in Section 2.6.

2.4.2 Surface Loss

Surface loss can result from a variety of sources, for example damage on the surface of the fibre [144]. From previous studies, it is known that the effect of surface loss on the total loss of fibre has a diameter dependence [145, 144]. Since the fibre has a very high surface to volume ratio, the impact from surface loss is significantly greater than that of bulk loss (Section 2.4.3). If the thermoelastic loss can be cancelled out as the above calculation suggests, the surface loss will have the dominant impact on total loss. The total surface loss ϕ_S can be written as [146, 147]:

$$\phi_{Surface} = \mu h \phi_S \frac{S}{V} \quad (2.49)$$

where μ is the geometrical factor, which is 2 for fibres [147], h is the depth where the surface loss occurs, ϕ_S is the dissipation in the thin surface layer of the fibre, and S/V is the ratio of surface area to volume.

Therefore,

$$\phi_{Surface} = \mu h \phi_S \frac{2\pi r L}{\pi r^2 L} = \mu h \phi_S \frac{2}{r} = \mu h \phi_S \frac{4}{d} \quad (2.50)$$

$$= \frac{8h\phi_S}{d} \quad (2.51)$$

where r and d are the radius and the diameter of the fibre, respectively.

From Section 2.4.1, it is shown that the ideal radius of the fibre that can cancel out the thermoelastic noise can be calculated. For a given surface loss, this then sets the thermal noise contribution from horizontal displacements of the mirror surface. The only way to improve this further is to either reduce the surface loss or reduce temperature.

2.4.3 Bulk Loss and Weld Loss

Bulk loss is the term given to internal friction occurring in the bulk of the material. One of the sources is the dissipation due to inherent material microstructure [148]. A molecular bond inside the material flips back and forth between two stable bond angles [149], causing the bond angle to change, which results in energy being lost. Phonon damping [150], structural defects [141], and electronic effects [141] can also cause dissipation in bulk of the material. However, as mentioned in Section 2.4.2, bulk loss is negligible compared to the loss of surface of the fibre.

Weld loss comes from the welding region of the fibres. For the final stage of the suspension, the test mass is supported by four fused silica fibres which are welded to the fused silica ears (Figure 2.2). The loss from this welding region is derived from measurements [143]:

$$\phi_{weld} = 5.8 \times 10^{-7} \frac{E_i}{E_{total}} \quad (2.52)$$

where $\frac{E_i}{E_{total}}$ elastic energy ratio ¹ calculated by FEA [143].

2.4.4 Dissipation Dilution

As described in Section 1.4.1, the Advanced LIGO detectors use quadruple pendulum suspensions to reduce the seismic noise. In addition to this advantage, the pendulum system can also benefit further by reducing the thermal noise by storing most of the energy in the gravitational field, which is non-dissipative [151]. Let's consider a simple pendulum where a mass m is attached to a wire of length L . Vertical motion is relatively simple: simple harmonic motion determined by the spring constant of the wire. However, when the mass is horizontally excited, swinging as a pendulum, the restoring force comes from both the wire and the gravitational field. The spring constant from the gravitational field is given by:

$$k_g = \frac{mg}{L} \quad (2.53)$$

The energy stored in the bending section of the wire can be described as:

$$E_{fibre} = \frac{1}{2} k_{fibre} x^2 \quad (2.54)$$

¹The FEA model of a bending fibre is divided into number of elements. While bending, the strain energy is stored in each element (i) of the fibre and that ratio is calculated in the program.

where x is the horizontal displacement. If we define γ as the fraction of energy dissipated per cycle:

$$E_{cycle} = \gamma \frac{1}{2} k_{fibre} x^2. \quad (2.55)$$

The quality factor Q is [3]:

$$Q = 2\pi \frac{E_{fibre}}{E_{cycle}} = \frac{1}{\phi_{fibre}}. \quad (2.56)$$

Thus,

$$\phi_{fibre} = \frac{\gamma}{2\pi}. \quad (2.57)$$

The total potential energy stored in the pendulum can be found by adding the energy stored in the fibre and the gravitational field:

$$E_{pendulum} = E_{fibre} + E_g = \frac{1}{2} k_{fibre} x^2 + \frac{1}{2} k_g x^2 \quad (2.58)$$

$$= \frac{1}{2} (k_{fibre} + k_g) x^2 \quad (2.59)$$

Therefore,

$$\phi_{pendulum} = \frac{E_{cycle}}{2\pi E_{pendulum}} \quad (2.60)$$

$$= \frac{\gamma \frac{1}{2} k_{fibre} x^2}{2\pi \frac{1}{2} (k_{fibre} + k_g) x^2} \quad (2.61)$$

$$= \frac{\gamma}{2\pi} \frac{k_{fibre}}{k_{fibre} + k_g}. \quad (2.62)$$

By dividing Equation 2.62 by ϕ_{fibre} ,

$$\frac{\phi_{pendulum}}{\phi_{fibre}} = \frac{k_{fibre}}{k_{fibre} + k_g}. \quad (2.63)$$

Since the fibres used for the suspensions are very thin, we can apply $k_g \gg k_{fibre}$:

$$\phi_{pendulum} \approx \phi_{fibre} \frac{k_{fibre}}{k_g} \quad (2.64)$$

Therefore, the loss of the pendulum is reduced by $\frac{k_{fibre}}{k_g}$, which is defined as $\frac{1}{D}$ where D is the dilution factor.

When the mass is suspended by more than one fibre, the spring constant of the fibres, k_{fibres} , can be expressed as [151]:

$$k_{fibres} = \frac{n\sqrt{TYI}}{2L^2} \quad (2.65)$$

where n is the number of fibres, T is the tension of the fibre, Y is the Young's modulus, I is the moment of inertia of the fibre, and L is the length of the fibre. The area moment of inertia of a fibre is given by [152]:

$$I = \frac{\pi r^4}{4} \quad (2.66)$$

where r is the radius of the fibre. Applying Equation 2.65 and 2.53 to Equation 2.64,

$$\phi_{pendulum} \approx \phi_{fibre} \frac{\frac{n\sqrt{TYI}}{2L^2}}{\frac{mg}{L}} \quad (2.67)$$

$$= \phi_{fibre} \frac{n\sqrt{TYI}}{2mgL} \quad (2.68)$$

Since the dilution factor is $\frac{1}{D} = \frac{k_{fibre}}{k_g}$,

$$D = \frac{2mgL}{n\sqrt{TYI}} \quad (2.69)$$

For the Advanced LIGO, the typical dilution factor is approximately 91 [153].

2.5 Resonant Modes of the Suspension Elements

2.5.1 Pendulum Modes

When energy is put into pendulum mode, the center of mass gets lifted up a little at the ends, as the mass swings back and forward (Figure 2.4). This displacement of the mass can change the laser path length to cause the noise. However, by implementing long and thin fibres, the resonant frequency of this mode can be pushed down very low that it does not overlap with the targeted detection band of the current ground-based detectors. The impact of the pendulum mode is also decreased by the dilution factor. The pendulum modes for the Advanced LIGO lie in a frequency range of 0.4 - 5 Hz [154].

2.5.2 Violin Modes

Thin fibres holding the mirrors also experience transverse vibrational modes, which are known as violin modes (Figure 2.4). The violin modes form a harmonic series. Like pendulum modes, the violin modes also decrease by the dilution factor. Since there are two bending points per fibre, instead of one in the pendulum mode [155],

$$\phi_{violin} = 2\phi_{pendulum} \quad (2.70)$$

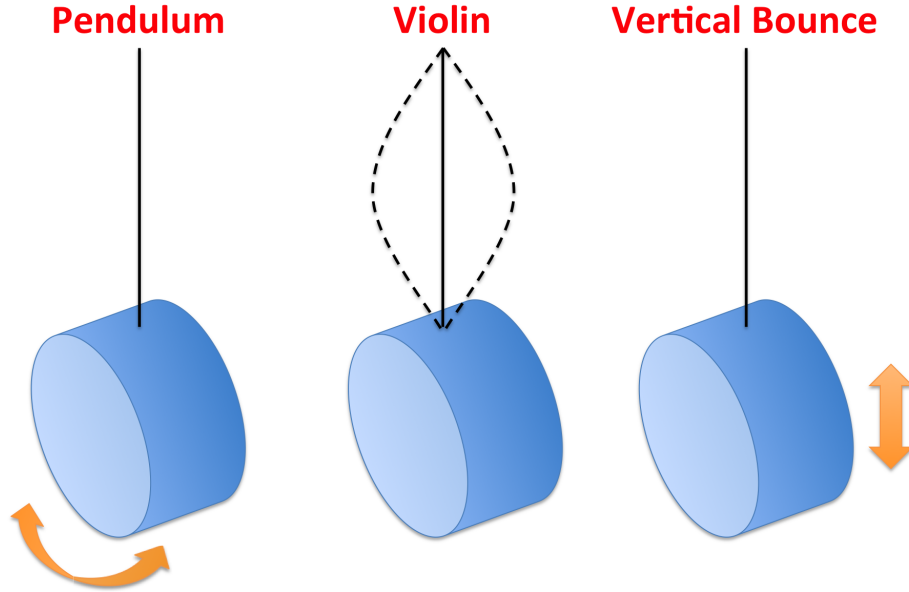


Figure 2.4: Illustration of pendulum mode, violin mode, and vertical bounce mode.

Assuming the mass displacement caused by the violin mode is extremely small (since the mass is large), the resonant frequency of the n th harmonic can be described as [156]:

$$f_n = \frac{n}{2L} \sqrt{\frac{T}{\mu}} \left[1 + \frac{2}{L} \sqrt{\frac{YI}{T}} + \frac{YI}{2T} \left(\frac{n\pi}{L} \right)^2 \right] \quad (2.71)$$

where L is the length of the fibre, T is the tension in the fibre, μ is the mass per unit length of the fibre.

Unlike pendulum modes, the resonant frequencies of violin modes fall within the targeted detection band. The first violin mode frequency of the Advanced LIGO is approximately 516 Hz, which meets the requirement of >400 Hz, but pushing it higher up would improve the detector's sensitivity curve. By using a low loss material such as fused silica, most of

the thermal noise can be concentrated around the resonant peak, leaving the rest of the frequency band relatively quiet. However, this also makes the noise level higher at the resonant frequency that it is more critical to have the peak in the detection band. To resolve this issue, one of the solutions is to apply higher tension on the fibres to push the resonant peak away from the detection band. The experimental work of this thesis, presented in Chapter 4, 5, 6, are closely related to this concept.

2.5.3 Vertical Bounce Modes

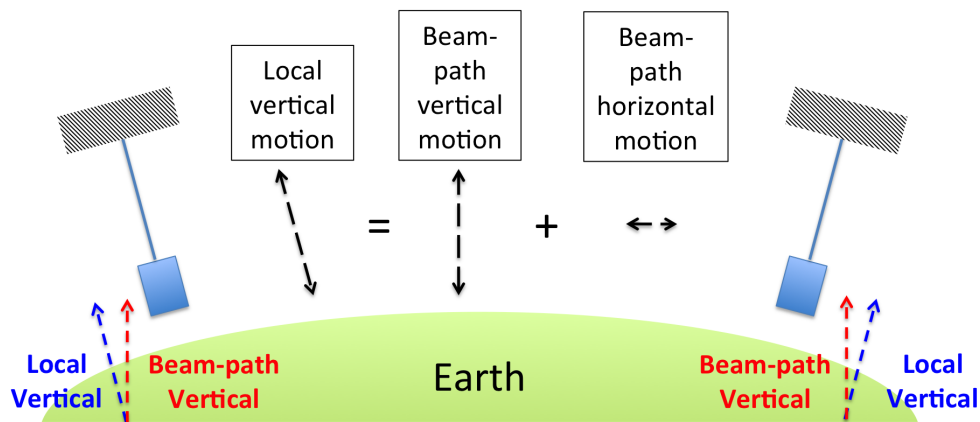


Figure 2.5: Vertical motions are coupled into horizontal motion due to the curvature of the earth.

The coupling of the vertical bounce mode (Figure 2.4) into horizontal noise is one of the limiting factors of the detector's sensitivity in the low frequency range around 10 Hz. This coupling is caused by the curvature of the Earth's surface. Figure 2.5 shows how the curvature of the Earth impacts the vertical to horizontal coupling. Since the local vertical direction and beam-path vertical direction are different, whenever there is local vertical motion, it couples into beam-path horizontal motion. The vertical bounce frequency can be described as,

$$f_{\text{Vertical}} = \frac{1}{2\pi} \sqrt{\frac{YA_{\text{Total}}}{mL}} \quad (2.72)$$

where Y is the Young's modulus, A_{Total} is the cross sectional area for the fibre, m is the test mass, and L is the length of the fibre [157]. The vertical bounce mode of the Advanced LIGO is approximately 9.7 Hz. The noise from the vertical bounce modes can be reduced by adjusting the suspension length and the stress applied to the fibres. Thus, applying higher stress on the fibres not only pushes the violin mode resonant frequency away from the detection band, but also lowers the vertical bounce mode peak to widen the sensitive region of the detection band.

2.5.4 Other Modes: Pitch, Yaw, Roll

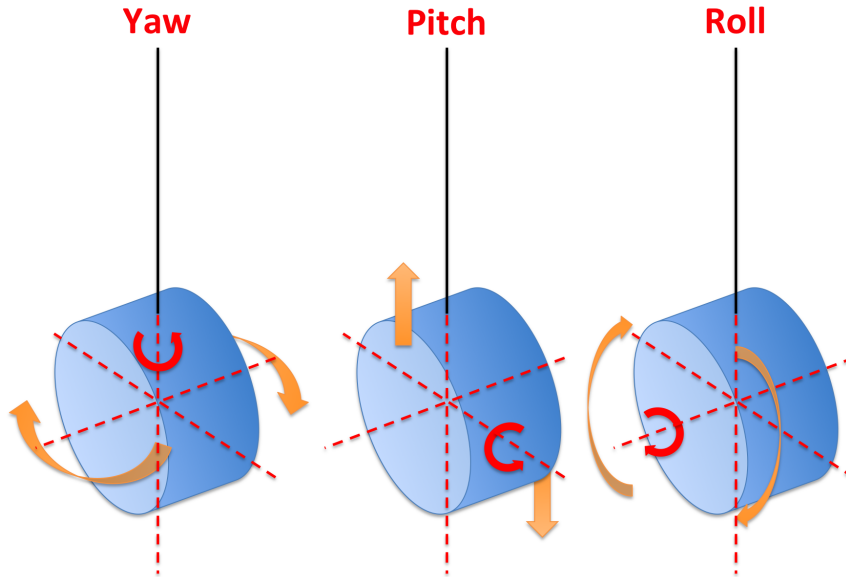


Figure 2.6: Other modes of the pendulum: Yaw, Pitch, Roll.

Other than the pendulum, violin, and vertical bounce mode, there are pitch, yaw and roll modes also exist in the pendulum system. Figure 2.6 shows the yaw, pitch, and roll mode of a pendulum. Among these modes, yaw and pitch modes can be minimised by

keeping the beam aligned to the centre of the test mass [158]. In addition, the damping system attached to the test mass structure also reduces the impact from these modes [159]. Since they do not coincide in the middle of the detection band, these modes are not on the priority to be reduced.

2.5.5 Critical Resonant Modes in the Advanced LIGO

Three important modes that have critical in the Advanced LIGO detection band (10 Hz to 10 kHz with the most sensitive range around 100 Hz [160]) are the pendulum mode, vertical bounce mode, and the violin modes. The Advanced LIGO design sensitivity requirement of the vertical bounce mode frequency is < 10 Hz and that of the violin mode frequency is > 400 Hz.

Figure 2.7 shows these modes with the total suspension thermal noise of the Advanced LIGO detector. (Analytical expressions used for the calculation are presented in Chapter 3.)

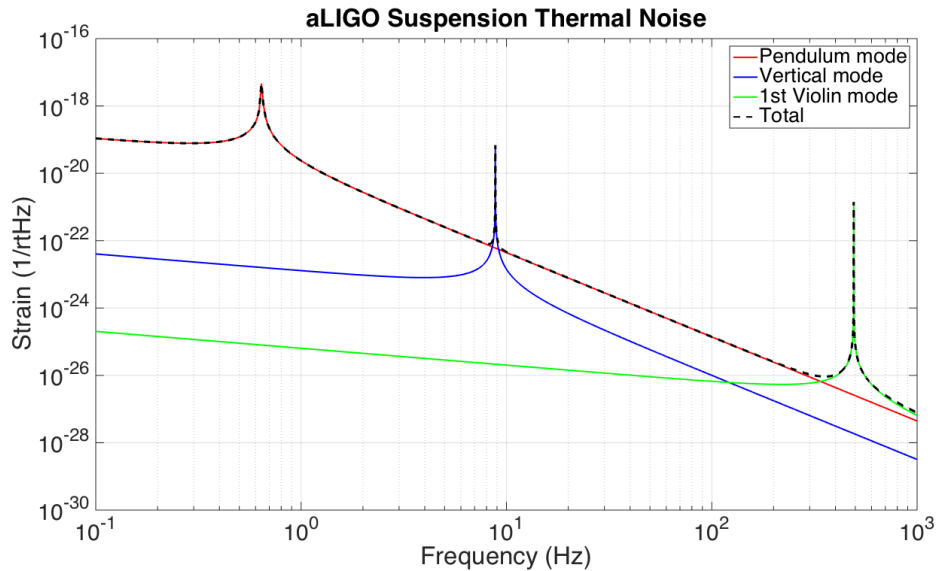


Figure 2.7: Different modes of suspension thermal noise.

For the pendulum mode (red line, peak at 0.6 Hz), the resonance peak can be lowered to be away from the detection band, but it is the dominant source of the suspension thermal noise in the off-peak region. The other two modes, the vertical bounce mode (blue line, peak at 9 Hz) and the violin modes (green line, peak at 492 Hz), are relatively small off resonance but their peaks fall into the detection band range that it is important to push them away from the band.

2.6 Quadruple Monolithic Suspension in Advanced LIGO

Among various upgrade features for the Advanced LIGO detector, one of the main changes is the quadruple monolithic suspension system for the test masses. As explained in Section 1.4.1, a quadruple pendulum system was implemented to reduce the seismic noise. When considering the thermal noise in the suspension, it is important that the suspension has a monolithic fused silica final stage. In addition, details such as fibre design also contributed to further reduce the thermal noise. Figure 2.8 shows the essential details of the last two stages of the suspension system.

First of all, as the name implies, all components of the final stage of the suspension are made of fused silica only: test masses, fibres to hang the test masses, and welding to connect the fibres to the masses [72]. As explained earlier in Section 2.3, fused silica is a low loss material at room temperature, so that the thermal noise can be concentrated around the resonant peak and reduced at frequencies away from resonance.

Another advantage that we can gain from monolithic fused silica final stage comes from the fibres. As explained in Section 2.4.1, since the Young's modulus of the fused silica increases with the temperature, the thermoelastic noise can be cancelled out by controlling the diameter of the bending area of the fibres. When the test mass moves to bend the fibres, only the sections near the end of the fibre get bent. Therefore, the fibre is carefully fabricated to have this “thermoelastic nulling section” to minimise the

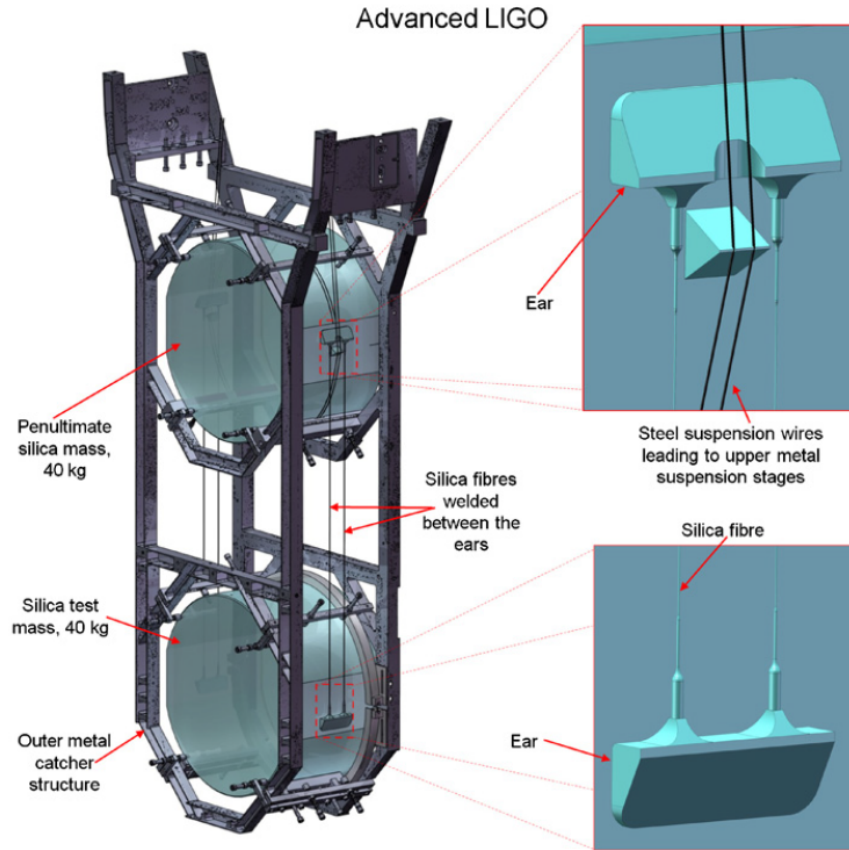


Figure 2.8: A diagram of the Advanced LIGO quadruple monolithic fused silica suspension design [139].

impact from the thermoelastic loss. This specific nulling diameter is calculated from Equation 2.47. For the Advanced LIGO detectors with 40 kg test masses supported by 4 fibres, the thermoelastic nulling diameter is 800 μm . Figure 2.9 [139] shows the fused silica fibre geometry with the thermoelastic nulling section.

In addition, fused silica fibres can handle the tensile stress of 770 MPa with safety factor of up to 6 [162]. Although the fibre with tensile stress of 770 MPa meets the Advanced LIGO requirement for the vertical bounce mode frequency (12 Hz or below [163]), it is better to push it down further in frequency to widen the sensitive detection band. As the vertical bounce mode frequency can be lowered with thinner fibres (Equation 2.72), the

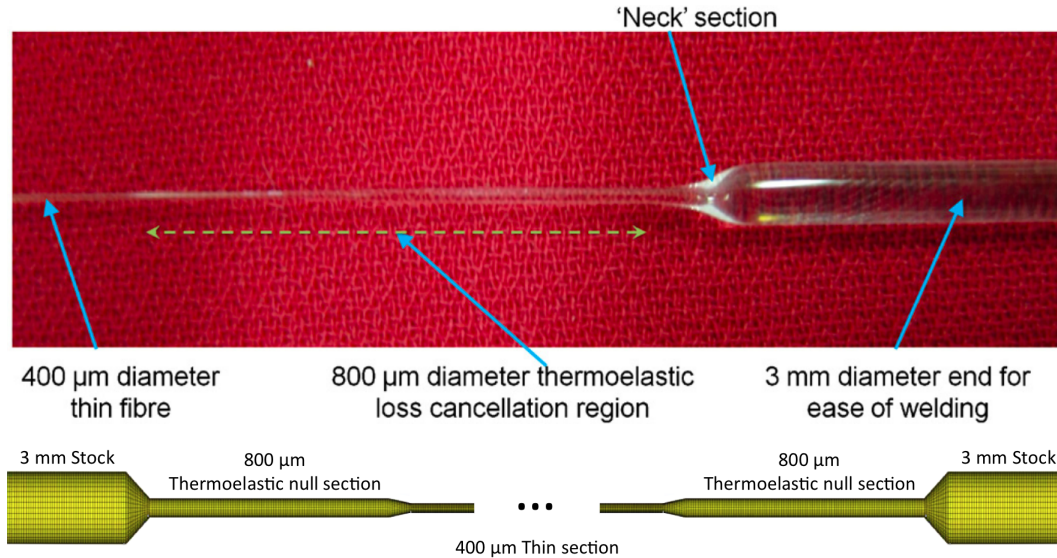


Figure 2.9: Dumbbell-shaped fibre for the aLIGO suspension system [139]. FEA ANSYS model image is provided by Dr. Alan Cumming [161].

fact that fused silica fibres can endure high tensile stress gives a possibility to improve the low frequency sensitivity by pushing down the vertical bounce mode frequency, which sits around 10 Hz for the current aLIGO detectors. Thus, the middle section of the fibre is fabricated to be thinner, with the diameter of 400 μm (Figure 2.9).

Lastly, thinner fibre (higher stress) can also push the violin mode up, as mentioned in Section 2.5.2. Both together, lower vertical bounce mode frequency and higher first violin mode frequency, can broaden the detection band for the Advanced LIGO detectors. The investigation of fabricating fibres with even thinner middle section is the focus of this thesis.

2.7 Conclusion

Among different noise sources, the thermal noise is a dominant noise source at low frequencies. In this chapter, the relation between the mechanical loss of a system and the

thermally induced displacement was explained through Fluctuation-Dissipation Theorem, providing possible options to lower the thermal noise of the system. In the Advanced LIGO suspension upgrade, the improvement of dilution factor and the benefit from low mechanical loss material could bring significant advantage in the detector's sensitivity. However, to bring further improvements to observe more astronomical sources, additional upgrades are required for the next generation detectors. In the next chapter, among various upgrade options, increasing the static stress in the monolithic stage suspension fibres will be investigated to see its impact on the suspension thermal noise.

Chapter 3

Advanced LIGO

Room-Temperature Upgrade:

High Stress Fibres

3.1 Introduction

To further improve the aLIGO detectors' sensitivity, various upgrade options can be considered for the near and far term future. Among different objectives, one of the important factors is to reduce the different detector noise sources in the low frequency range, 10 Hz and below. Better sensitivity at low frequency will, firstly, enable us to observe more astronomical sources such as intermediate mass black holes (IMBHs) which have masses in range of ~ 100 to 10000 solar mass [164, 165]. Secondly, by expanding the detection band to lower frequencies, the observation time can be increased to give higher accuracy in source parameter measurements [166]. In addition, earlier warning of an event, and more accurate sky localisation would be possible, giving a better chance to perform multi-messenger observations [167].

In this chapter, the analytical models were generated for different suspension configurations to investigate the low frequency noise sources such as seismic noise, suspension thermal noise, and coating Brownian noise. Among various options for upgrade scenarios, such as heavier payload, higher stress in fibres, and longer suspension, this chapter will concentrate on the higher working stress in fibres, which is directly relevant to the A+ Upgrade. Practically, implementing higher stress fibres is relatively simple, as all that is needed to be done is to replace the current fibres with thinner fibres. However, it can bring an efficient improvement in widening the sensitive detection band. As mentioned in Chapter 2, applying higher stress on the fibres can push down the vertical bounce mode frequency while pushing the first violin mode frequency higher up. The current working stress of the Advanced LIGO detector is 770 MPa. In the simulations, higher stress conditions, from 1 GPa to 5 GPa, were investigated.

3.2 Dominant Noise Sources in the Low Frequency Range

Firstly, three dominant noise sources in the low frequency range will be discussed in detail. As a basic explanation for each noise source was already presented in Chapter 1, the main focus of this section is on the analytical expressions used for the Matlab simulation with various suspension geometric conditions such as the length and mass.

Figure 3.1 shows a schematic diagram of the quadruple pendulum system: x_g and z_g represent longitudinal and vertical seismic motion respectively; m_1 to m_4 the mass of these stages; L_1 to L_4 the lengths of wire suspending these stages; k_1 to k_4 the spring constants of these stages, and σ the stress on the final stage fused silica fibres. As such, it is clear that there are many conditions that can be changed: m_1 to m_4 , P , L_1 to L_4 , L_T .

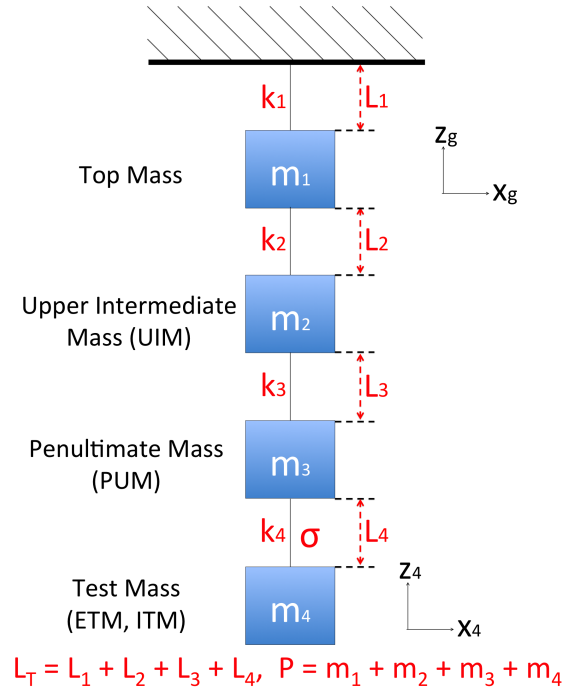


Figure 3.1: Schematic diagram of the quadruple pendulum system x_g and z_g represent longitudinal and vertical seismic motion respectively; x_1 to x_4 and z_1 to z_4 represent the motion of stages 1 to 4; m_1 to m_4 the mass of these stages; L_1 to L_4 the lengths of suspension wire/fibre; k_1 to k_4 the spring constants, and σ the stress on the fused silica fibres [74].

3.2.1 Seismic Noise

Seismic noise, caused by different terrestrial ground motions such as human activities and natural sources, is one of the dominant noise sources in the low frequency range [71]. The transfer function of the pendulum for the horizontal motion for frequencies above the pendulum's resonant frequency is $1/f^{2n}$, where n is the number of pendulums, which allows $1/f^8$ reduction of seismic noise in the quadruple pendulum system used for the Advanced LIGO detectors (Figure 1.10).

In T1300786-v7 (LIGO Technical Note) [74], Dr. Brett Shapiro has established some analytical equations to optimise the longitudinal and vertical seismic isolation properties of suspension system. Simplifying the quadruple pendulum system to a single axis system (Figure 3.1), equations of motion were found. Since the approximation used to find transfer functions was that frequencies are above the resonance frequency, these isolation equations are valid above the resonance. Derivation of the following equations are provided in Appendix A.

Longitudinal seismic isolation equation:

$$\frac{x_4}{x_g} \approx \frac{g^4}{(2\pi f)^8} \frac{1}{L_1 L_2 L_3 L_4} \frac{(m_1 + m_2 + m_3 + m_4)(m_2 + m_3 + m_4)(m_3 + m_4)m_4}{m_1 m_2 m_3 m_4} \quad (3.1)$$

$$C_1 = \frac{g^4 P}{(2\pi f)^8} \min \left[\frac{1}{L_1 L_2 L_3 L_4} \frac{(m_2 + m_3 + m_4)(m_3 + m_4)}{m_1 m_2 m_3} \right] \quad (3.2)$$

Vertical seismic isolation equations:

$$\frac{z_4}{z_g} \approx \frac{1}{(2\pi f)^8} \frac{1}{m_1 m_2 m_3 m_4} k_1 k_2 k_3 k_4 \quad (3.3)$$

$$C_2 = \frac{k_4}{m_4 (2\pi f)^8} \min \left[\frac{1}{m_1 m_2 m_3} k_1 k_2 k_3 \right] \quad (3.4)$$

where m is the mass, L is wire length, g is gravity, f is frequency, k is stiffness, σ_4 is the stress in fibres between PUM and test mass, E_4 is Young's modulus. C represents a cost term to be minimised. Basically, Equations 3.1 and 3.2 are identical, and so are Equations 3.3 and 3.4. The only difference is that Equation 3.2 and Equation 3.4 have separated constants and variables so that we can easily see what needs to be changed for better longitudinal and vertical seismic isolation, respectively.

Equation 3.1 provides the high frequency approximation (asymptote) of the longitudinal seismic transmission between the seismic isolation structure (Beam Splitter Chamber - Internal Seismic Isolation, BSC-ISI) displacement (that is, the displacement at the top of the pendulum suspension) and the test mass displacement. In the process of derivation, the frequency was assumed to be greater than resonance frequencies, for efficient calculation [74]. (See Appendix A for more details on the derivation and the approximation.) Therefore, this equation is valid for all frequencies above the resonance, as the approximation error goes to 0 when f approaches infinity [74]. Equation 3.3 uses the same approximation.

Similarly, Equation 3.3 provides the high frequency approximation (asymptote) of the vertical seismic transmission between the seismic isolation structure displacement and test mass displacement. Using the approximation ($\omega > resonance$), both equations are valid for all frequencies greater than the resonances [74].

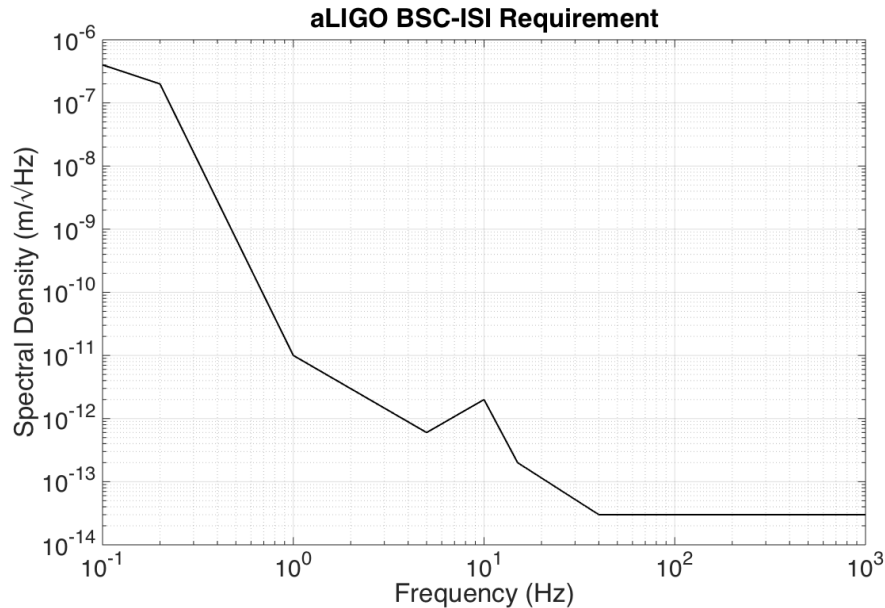


Figure 3.2: The BSC-ISI requirement for the Advanced LIGO detectors [168].

Using the same approximations and assumptions Shapiro used for those equations and

the seismic isolation structure performance requirement curve (BSC-ISI requirement) provided in the LIGO seismic Subversion (SVN) server [168], isolation properties were calculated [74]. Figure 3.2 shows the aLIGO BSC-ISI requirement curve. The Matlab code was provided by Dr. Brett Shapiro (Link is provided in Appendix C). From Equation 3.4, the vertical isolation is dependant on k_1, k_2, k_3, k_4 . In Shapiro's calculation, C_2 and its corresponding vertical isolation requirement was ignored, assuming that it is possible to design springs with appropriate k values regardless of the mass and wire values [74].

3.2.2 Suspension Thermal Noise

Another dominant noise source in the low frequency range is the suspension thermal noise. As explained in Chapter 2, only the suspension thermal noise from the final stage of the suspension will be considered, since the noise created from upper stages will be filtered by the pendulum system [151]. Therefore, the variables that have direct influence on this noise are the final stage variables L_4, m_4 , and σ .

The longitudinal, vertical, and violin mode thermal noise were calculated separately and added in quadrature to give the total suspension thermal noise. The equations were derived from the fluctuation-dissipation theorem applied to coupled harmonic oscillators (Equation 2.21, Equation 2.32):

$$S_x(\omega) = \overline{x^2}_{thermal}(\omega) = \frac{4k_B T}{\omega m} \frac{\omega_0^2 \phi(\omega)}{[\omega_0^4 \phi^2(\omega) + (\omega_0^2 - \omega^2)^2]} \quad (3.5)$$

$$(3.6)$$

$$S_x(\omega_0) = \overline{x^2}_{thermal}(\omega) \approx \sum_n \frac{4k_B T}{\alpha_n m \omega_n^2} \frac{\phi_n(\omega)}{\omega} \quad (3.7)$$

The total mechanical loss is:

$$\phi_{Total} = \phi_{thermoelastic} + \phi_{surface} + \phi_{bulk} + \phi_{weld} \quad (3.8)$$

where the thermoelastic loss is defined as Equation 2.47, the surface loss is defined as Equation 2.51, the bulk loss [169] and the weld loss are derived from measurements and given by $\phi_{bulk} = 4.1 \times 10^{-12} \omega^{0.77}$ and $\phi_{weld} = 5.8 \times 10^{-7} \times E_{weld}$ where E_{weld} is the weld energy estimated using FEA [146]. (Section 2.4 described more details on mechanical losses.)

Considering the various sources of loss ², the thermal displacement was calculated.

Longitudinal thermal displacement:

$$x_{longitudinal} = \sqrt{\frac{4k_B T}{\omega m} \frac{\omega_l^2 \phi_l(\omega)}{[\omega_l^4 \phi_l^2(\omega) + (\omega_l^2 - \omega^2)^2]}} \quad (3.9)$$

where ω_l is the longitudinal resonant frequency, and ϕ_l is the longitudinal mechanical loss divided by the dilution factor (D).

Vertical thermal displacement:

$$x_{vertical} = C \sqrt{\frac{4k_B T}{\omega m} \frac{\omega_z^2 \phi_z(\omega)}{[\omega_z^4 \phi_z^2(\omega) + (\omega_z^2 - \omega^2)^2]}} \quad (3.10)$$

where C is the cross-coupling factor of 10^{-3} [170], ω_z is the vertical resonant frequency, and ϕ_z is the vertical mechanical loss.

Violin mode thermal displacement:

$$x_{violin} = \sqrt{\frac{8k_B T \omega_v^2 \phi_v(\omega) \rho L}{\pi^2 m^2 \omega [\omega_v^4 \phi_v^2(\omega) + (\omega_v^2 - \omega^2)^2]}} \quad (3.11)$$

where ω_v is the violin mode resonant frequency, ϕ_v is the violin mode mechanical loss divided by the dilution factor (D), and ρ is the density of the fibre.

²Thermoelastic loss is considered to be cancelled.

Total suspension thermal noise:

$$x_{total} = \sqrt{x_{longitudinal}^2 + x_{vertical}^2 + x_{violin}^2} \quad (3.12)$$

The link to the Matlab code used for this calculation is provided in Appendix C.

3.2.3 Coating Brownian Noise

The last dominant noise source in the low frequency range is the coating Brownian noise. As shown in Chapter 2 (Equation 1.12), coating Brownian noise does not have a “direct” correlation to the mass of the test masses (m_4). However, Somiya *et al.* [171] showed that the coating Brownian noise decreases when the mirror thickness increases. Therefore, when the aspect ratio (radius/thickness) of the mirror is kept constant and the mass of the mirror increases, the radius and the thickness also increase to reduce the coating Brownian noise.

The analytical expression for the coating Brownian noise is also derived from fluctuation-dissipation theorem [171]:

$$S_x(\omega) = \frac{4k_B T}{\omega} \times \Re[1/Z(\omega)] \quad (3.13)$$

where $Z(\omega)$ is the impedance:

$$Z(\omega) = \frac{F(\omega)}{\dot{x}(\omega)} = \frac{F(\omega)}{i\omega x(\omega)} \quad (3.14)$$

where F is the imposed force ($F = F_0 \cos(\omega t)$) and x is the resulting motion ($x = x_0 \cos(\omega t - \phi)$). ϕ is the loss angle, which is the phase difference between F and x .

Using $W = F_0 x_0 \omega \phi / 2$ and Equation 3.14,

$$S_x(\omega) = \frac{8k_B T W}{\omega^2 F_0^2} = \frac{8k_B T}{\omega F_0^2} U \phi \quad (3.15)$$

where U is the maximum elastic energy that the imaginary force can generate.

Detailed equations on calculating U are provided in Appendix B. The Matlab code to calculate this noise was written by Daniela Pascucci (PhD student in IGR) and the link for the code is provided in Appendix C.

3.3 Investigated Conditions: Stress on Fibres

As mentioned in Chapter 2, higher working stress on fibres can bring overall advantage to the noise curve of the detector by lowering the vertical bounce mode frequency (Equation 2.72) and pushing up the violin mode frequency (Equation 2.71). In this chapter, higher stress conditions of 1, 2, 3, 4, and 5 GPa were investigated and compared to the current aLIGO condition of 770 MPa.

Other than working stress on fibres, all other conditions such as mass and length were kept the same as the current aLIGO condition: 40 kg test mass (m_4), final stage length (L_4) of 0.6 m, total length (L_T) of 1.1 m.

3.4 Results

Using Matlab, each stress condition was thoroughly investigated for the seismic noise, suspension thermal noise, and coating Brownian noise. For all comparison figures, the current aLIGO condition was included as a reference.

Figure 3.3 shows a comparison between three conditions: aLIGO condition (770 MPa), 1 GPa and 2 GPa. As shown in the graph, both seismic noise and coating Brownian noise do not show any difference when the stress condition changes, because they are

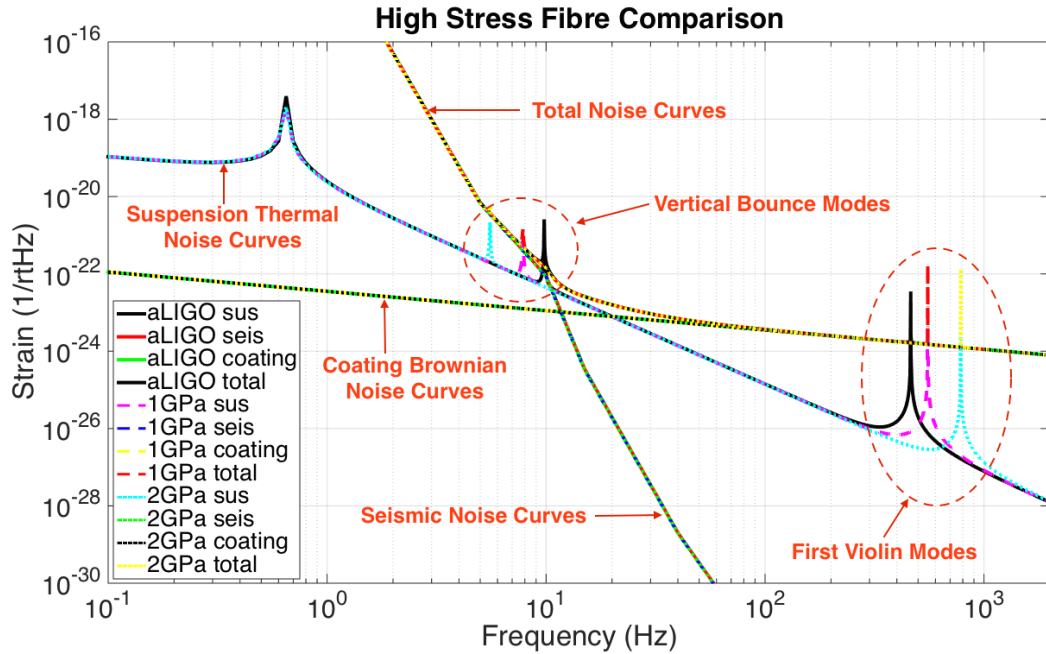


Figure 3.3: Impact of varying the stress while keeping all other conditions the same. The current aLIGO condition was compared to the higher stress conditions (1 GPa, 2 GPa).

independent of the stress condition of fused silica fibres. All three curves for each condition perfectly overlapped for those noise sources. For suspension thermal noise, it is confirmed that the vertical bounce mode frequency and the first violin mode frequency move down and up respectively (red dotted circles).

Thus, in Figure 3.4, only suspension thermal noise was plotted to investigate the impact of higher working stress on the suspension thermal noise. As shown in Figure 3.4, the stress condition change does not influence the pendulum mode, thus there is no advantage in overall longitudinal suspension thermal noise level (Equation 2.21). However, both vertical bounce mode and first violin mode move away from the detection band. (The height of peaks are not the same due to the plotting resolution.)

Table 3.1 shows the vertical bounce mode frequencies and the first violin mode frequencies

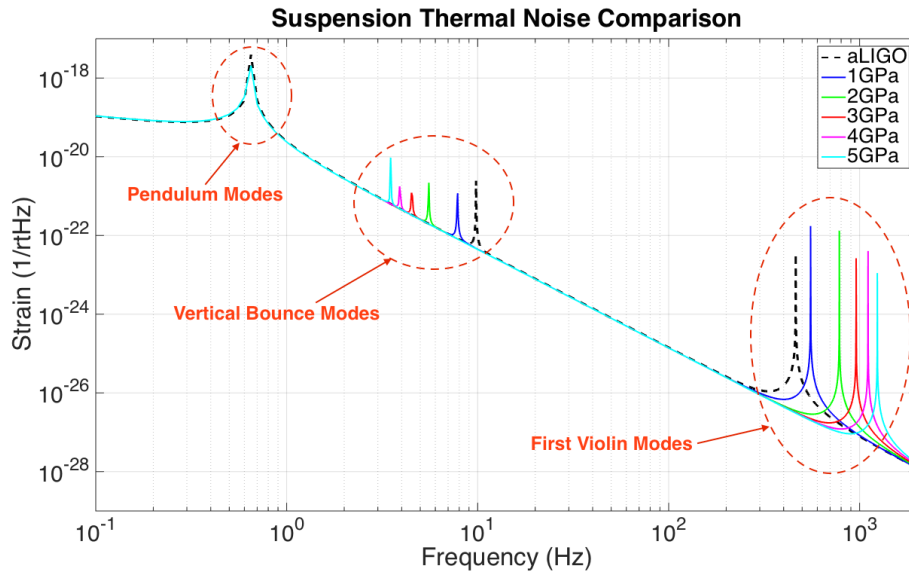


Figure 3.4: Impact of the fibre stress on the suspension thermal noise. The current aLIGO condition was compared to the higher stress conditions (1 GPa to 5 GPa).

Set Number	Vertical Bounce Mode Frequency (Hz)	First Violin Mode Frequency (Hz)
aLIGO	9.3	480.2
1 GPa	7.8	553.6
2 GPa	5.5	783
3 GPa	4.5	958.9
4 GPa	3.9	1107
5 GPa	3.5	1238

Table 3.1: The vertical bounce mode frequencies and the first violin mode frequencies of different sets compared to that of the aLIGO condition.

of different sets compared to that of the aLIGO condition. Even for 1 GPa, the vertical bounce mode frequency shows a 15% decrease. The first violin mode frequency went up to 553 Hz, which is well above the aLIGO requirement. 3 GPa fibres have the first violin mode frequency approaching 1000 Hz, and for 4 GPa and 5 GPa fibres, they go above

1100 and 1200 Hz. For 5 GPa, the vertical bounce mode frequency decreased by 62%. However, extremely high stress conditions such as 4 GPa and 5 GPa are not feasible at the current stage, due to the limitation of the fibre's strength.

Clearly, it is therefore desirable to make the stress condition as high as possible to remove the impact of resonant frequencies from the sensitive detection band. To achieve higher stress in the fibres, it is essential to fabricate such fused silica fibres that are thin and sturdy enough to hold the mass. In the next chapter, the experimental work to develop fibre fabrication technologies to improve the statistical strength of the fibres will be presented.

3.5 Conclusion

From Matlab simulation results, it is shown that higher stress in the fibre can push both vertical bounce mode frequency and violin mode frequency away from the detection band, without any disadvantages on other low frequency noise sources such as seismic noise and coating Brownian noise. Implementing high stress fibres is a low-effort, high-gain upgrade option, as all that is required is to replace the current fibres with thinner fibres. This is one of the potential features of the A+ upgrade. The biggest challenge for implementing high stress fibres is the strength of fused silica fibres. The following chapters will present experimental work on understanding and improving the statistical strength of silica fibres.

Chapter 4

Enhanced Fibre Fabrication Technology

4.1 Introduction

From the Matlab modelling work in Chapter 3, it was shown that implementing higher stress fibres in the final stage can expand the sensitive detection band. Since the final stage of the suspension is held by fused silica fibres, which have very low loss to minimise suspension thermal noise, one of the challenges for this upgrade will be producing thinner and durable fibres that can hold the test mass safely. In this chapter, current fibre fabrication techniques will be introduced, followed by an investigation into enhanced techniques for fibre production. Finally, the impact of this enhanced technique will be explored.

4.2 Current Fibre Fabrication Technique

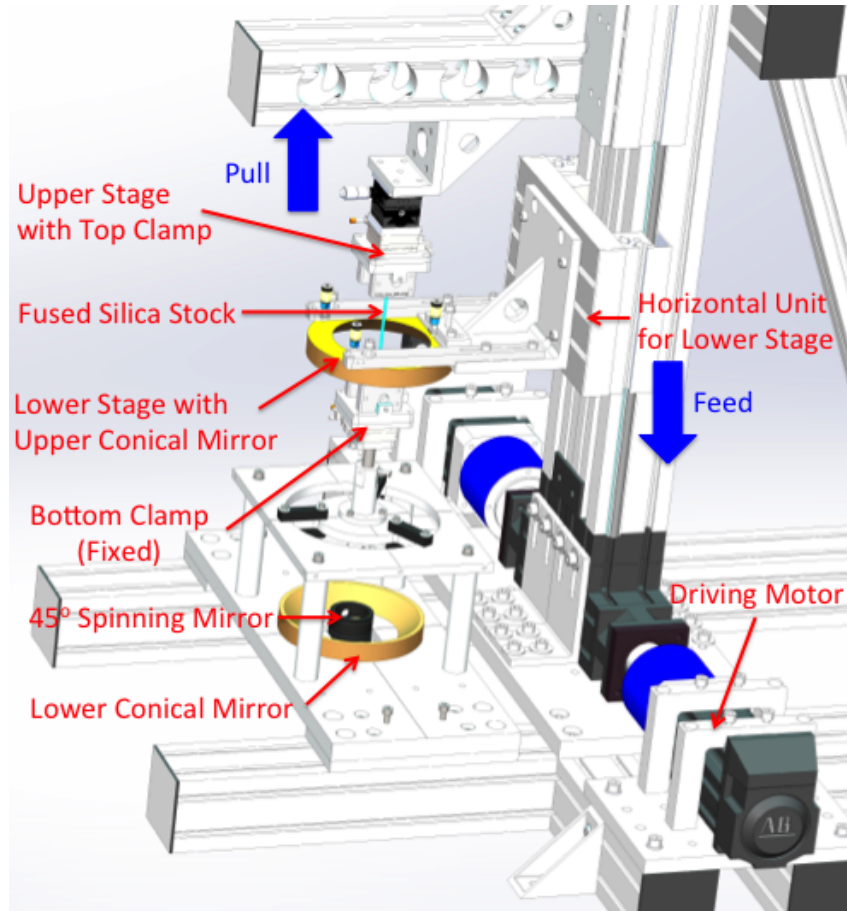


Figure 4.1: Schematic drawing of the fused silica fibre pulling machine at the University of Glasgow. A rotating 45° mirror and two conical mirrors allow uniform heating 360° around the stock. When pulling starts, the upper stage travels upwards to pull a fibre, while the lower stage slowly travels downwards to feed new fused silica material into laser beam.

Fused silica fibres currently used for suspending the final mirror stage in aLIGO were produced using a bespoke pulling machine (Figure 4.1) [172]. Since the purity of the fused silica stock can affect the strength of the fibre, the stock material chosen for the

aLIGO fibres was Suprasil 2 Grade A from Heraeus [173].

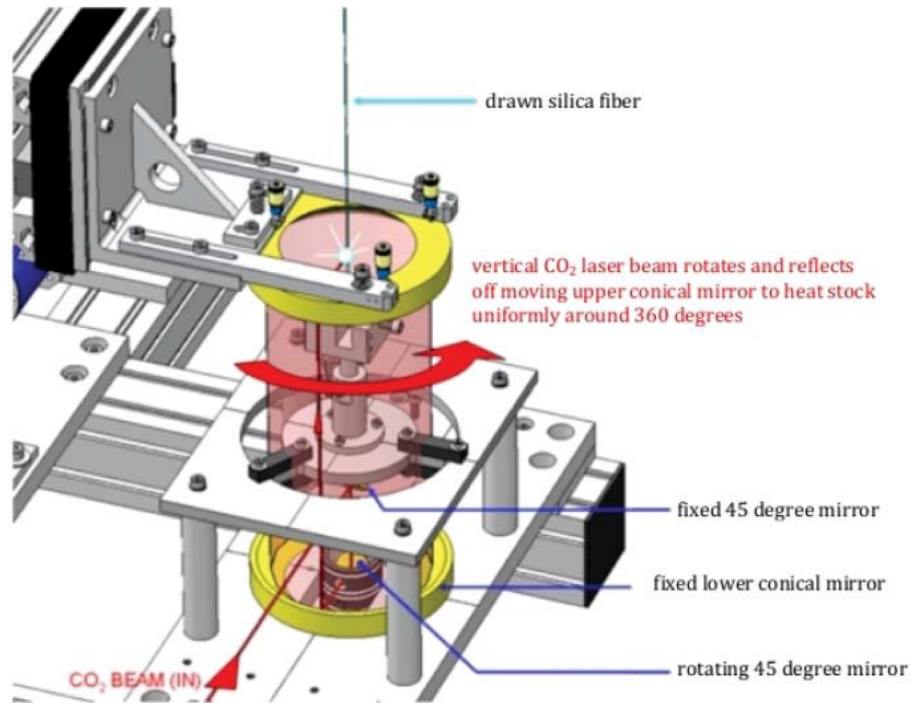


Figure 4.2: Uniform heating system applied to the pulling machine. Two conical mirrors and a rotating 45° mirror enable uniform heating of 360° around the fused silica stock [174].

A Synrad 120 W CO_2 laser (wavelength of $10.6\ \mu\text{m}$, beam diameter of $3.5\ \text{mm}$, beam divergence of $4.0\ \text{mrad}$) was used as a heating source of a length of circular cross section fused silica stock material, clamped at its ends between two clamps allowing its central region to be heated. A rotating 45° mirror and two conical mirrors allow uniform heating of 360° around the stock. (Figure 4.2) While the bottom clamp is kept stationary, the top clamp which is connected to the upper stage travels upwards to pull a fibre. To feed in more material, the lower stage with upper conical mirror travelled slowly down with a speed of $0.3\ \text{mm/s}$ typically, which results in $14\ \text{mm}$ for an aLIGO fibre. Machine pulled fibres have more consistent geometry than those produced previously using a flame-pulling system or a rig system [143], as the pulling machine can heat up a fused

silica stock more uniformly and the pulling speed can be more easily controlled via computer during the pull.

Since the strength of fused silica fibres is directly related to the surface cracks of the silica stock [175], the stock is ‘polished’ before the pull to improve the strength [144]. Polishing comprises of the lower stage moving down and up slowly (typically taking 900sec with a speed of 0.1mm/sec for the aLIGO fibres) while the stock surface is uniformly heated to its melting point to smooth and fuse together any surface cracks. After polishing, the upper stage travels upwards to pull a fibre, while the lower stage slowly travels downwards in a constant speed to feed in fused silica material. As the volume of fused silica fed in is kept constant, the geometry of the fibre is determined by the relative speeds of the upper and lower stages. The typical speed ratio for the thin section is 57:1. A LabVIEW program [161] was used to control the polishing and pulling processes, including the polished area, heating point, and motor speeds for the upper stage and the lower stage.

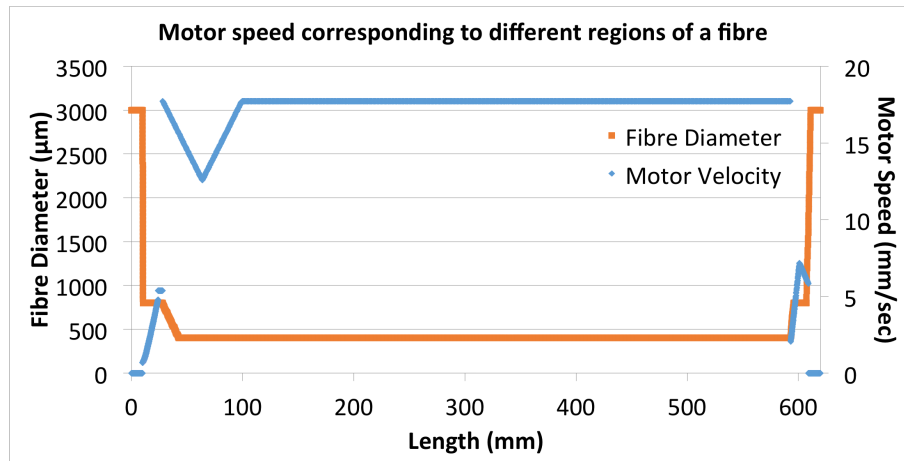


Figure 4.3: Variation of the upper motor speed during a pull process corresponding to different regions of a fibre.

Figure 4.3 shows a typical upper motor speed variation during a fibre pull process, and corresponding regions of a fibre. For a typical fibre, the total length is 600 mm, where

18 mm is the first thermoelastic null section (800 μm), 565 mm is the thin middle section, and 15 mm is the second thermoelastic null section.

In this current system, there is no monitoring of heating other than by eye, which is one of the more loosely controlled variables in the fabrication process. In this chapter, investigations to enhance the control over the heating process and the impact of introducing a heating stabilisation system on the fibre geometry will be the main focus.

4.3 Enhanced Fibre Fabrication Technique

4.3.1 Camera Monitoring System and PID Feedback Control

Previous research has always used the laser system run in an open loop configuration, where the duty cycle of the laser power has been set manually. In this regime, the laser power has been observed to vary throughout the polishing and the pulling process, particularly on startup. Figure 4.4 shows the manufacturer's measurement of the laser power variation observed for 900 seconds after startup, and measured directly on a water cooled power meter.

As clearly shown, it takes some time to settle the instability of the laser after turning it on. This is mainly due to mode hopping, which is a phenomenon that a laser exhibits sudden jumps of optical frequency, which are associated with transitions between different modes of its resonator cavity [176]. Although this power fluctuation is within the laser's specification which is $\pm 10\%$ for cold start and $\pm 6\%$ for 2 minutes after, this instability becomes more pronounced when it is translated to the heating intensity of fused silica stock by the pulling machine. These variations in laser power are likely to cause variation in the temperature of the molten fused silica stock material, which in turn may have an influence on the fibre geometry.

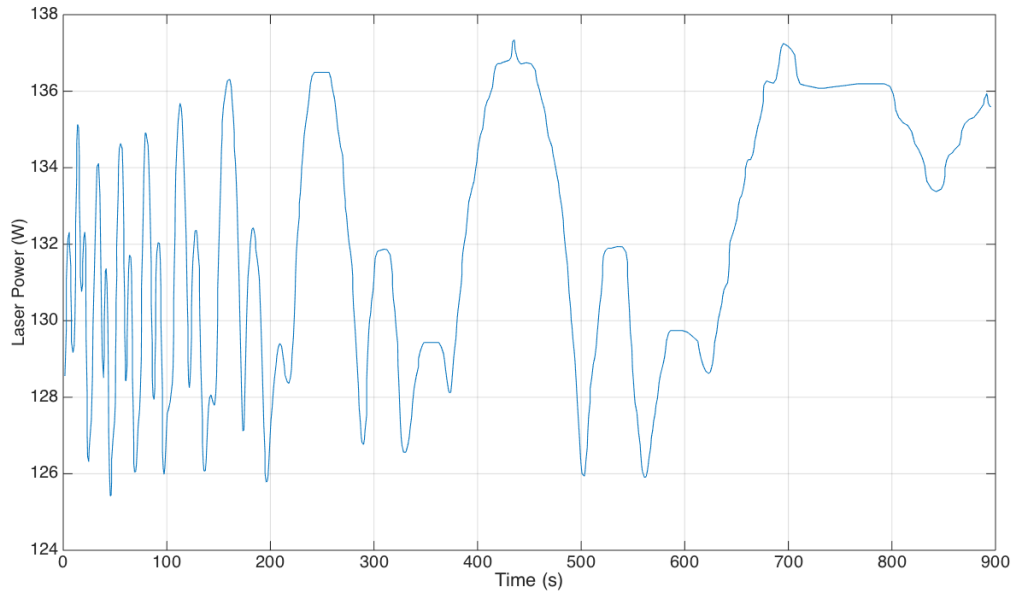


Figure 4.4: Laser power variation observed for 900 seconds. Although the power fluctuation is within the specification, which is $\pm 10\%$ for cold start and $\pm 6\%$ for 2 minutes after with the average power of 131.5 W, this instability becomes more critical when it is translated to the heating temperature of fused silica stock by the pulling machine.

The evidence of this correlation, which is the comparison between the heating intensity and the fibre diameter profile, will be presented in Section 4.4, after explaining the profiling process. To improve the stability of the heating intensity, a PID control with camera feedback system was set up and the impact of laser intensity stabilisation on the fused silica fibres was investigated and developed.

There are four main challenges in monitoring the heating intensity of the silica stock. Firstly, the monitoring device cannot directly touch the stock, as the heating point of the stock is molten from the heat deposited by the laser beam. Any thermometer attached to the stock at its heating point will have direct exposure to the laser beam, because the stock is uniformly heated all around. In addition, the strength of fused silica fibres is very sensitive to the surface cracks and contamination, and any direct contact on the surface of the stock can consequently lower the fibre strength. Secondly, since the pulling

process happens quickly, the monitoring device should not have much delay in recording the temperature information. Thirdly, the temperature monitoring device should be able to handle very high temperatures up to 2700 °C, which is the approximate vapour point of fused silica [177]. Thus, the resistance thermometers are eliminated. Lastly, the temperature monitoring device should not be at a risk of damage due to “reflected” CO_2 laser light from the heating point. This condition eliminates infrared cameras, such as FLIR cameras [178], as their CCD sensors are very vulnerable to damage from exposure to even minor CO_2 laser reflections [179]. Since most temperature monitoring devices are not qualified for all these conditions, an optical camera feedback system was used to monitor the brightness of the heated stock. As fused silica glows as it gets heated, this camera system can act as a responsive optical pyrometer with brightness as a temperature proxy.

Among various camera options, a Ximea MD028MU-SY was chosen according to criteria such as bit depth (14-bit), frame rate (>500 fps at VGA and 90 fps at 4Mpixel resolutions), resolution (1940 × 1460), LabVIEW compatibility, and price. High bit depth was desirable to have better pixel gradient to accurately monitor the heating intensity change, and high frame rate was necessary to keep track of instantaneous changes in heating intensity. This camera was set up on the horizontal unit for the lower stage to monitor the heating point of the fused silica stock. A neutral density (ND) filter was fitted in front of the camera to avoid intensity saturation. To optimise the response time, while keeping a reasonable resolution (1936 × 1456), the exposure was set to 8 ms to maximise the frame rate (100 fps) so that the response time would not be limited by the camera’s frame rate. Since the maximum pixel value was 16383 (14-bit), the setpoint chosen by eye was kept around the 5000~6000 range with an ND filter of 3.5 to prevent saturation during the pull.

Figure 4.5 shows an image of heated fused silica stock taken by the camera monitoring system. Using the original LabVIEW program [161] for the pulling machine control as a base, an additional section with a PID control system was implemented. The pixel data

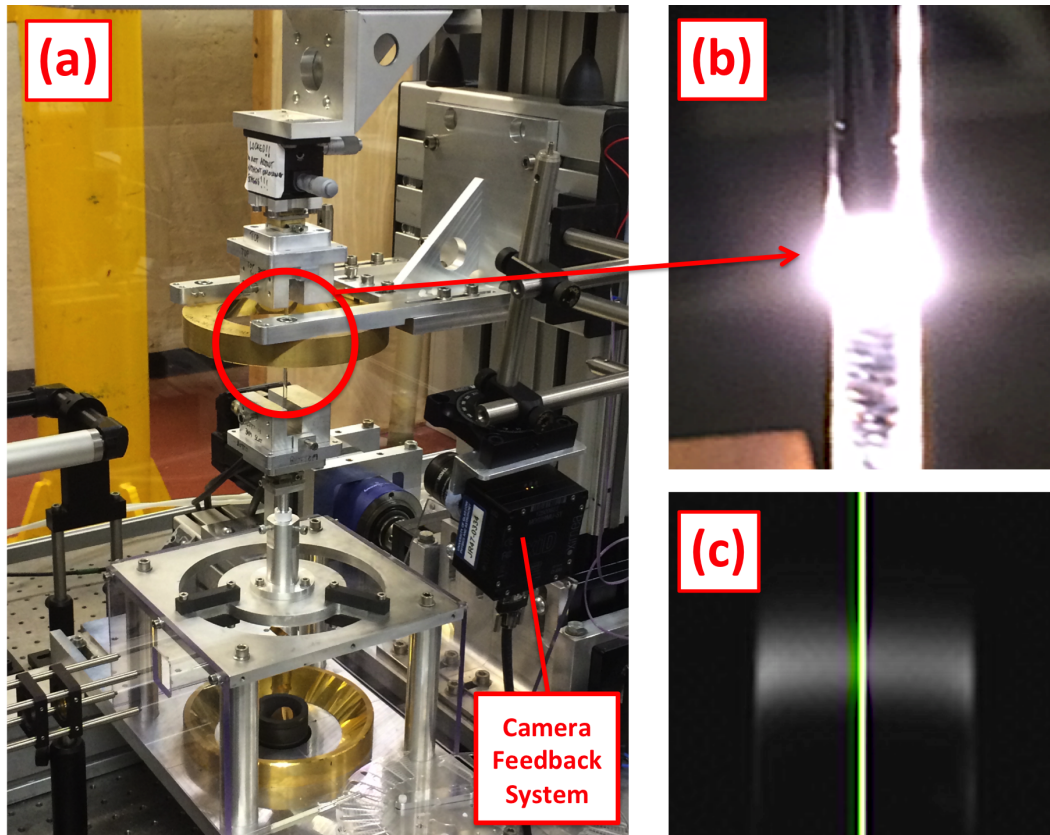


Figure 4.5: (a) Fused silica fibre pulling machine with a camera feedback system to monitor the heating point. (b) Uniformly heated fused silica stock, as viewed by a camera (shown without ND filters). (c) Image of heating point taken by the camera feedback system. The green vertical line indicates the region where pixel data were taken.

of the vertical line in the middle of the fibre was taken, and the brightest pixel value was used to monitor the temperature (auto-peak function). The heating power was stabilised by controlling its power via analogue voltage input to maintain the brightest pixel value consistent throughout the run. (Figure 4.6) To achieve this goal, a Proportional Integral Derivative (PID) feedback system was applied within LabVIEW to give appropriate analogue drive voltage to the laser:

$$u(t) = k_p e(t) + k_i \int_0^t e(\tau) d\tau + k_d \frac{de}{dt} \quad (4.1)$$

where u is the control signal, e is the control error ($e = r - y$), r is the reference value (setpoint), y is the measured intensity.

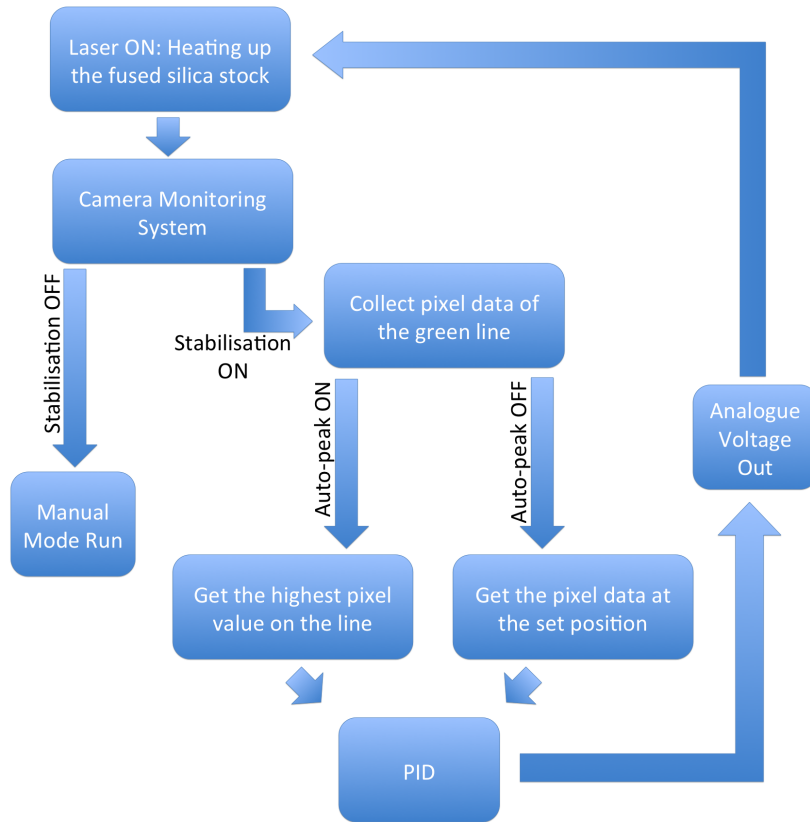


Figure 4.6: Simplified diagram to show the stabilisation process.

The proportional control takes the difference between the setpoint and the observed peak pixel intensity data to determine the error term. High proportional gain will cause oscillations of the peak pixel intensity, but an appropriate gain will increase the response speed of the system to quickly reach the setpoint. The integral control adds up the error term over time. High integral gain will cause a big overshoot and possibly instability, but an appropriate gain will enable the system to have quick and fine adjustment of the

peak pixel intensity. The derivative control takes the rate of change of the observed peak pixel intensity data. High derivative gain will make the system unstable due to noise but an appropriate gain will reduce the noise to provide stability. The controller works by summing the proportional gain k_p , the integral gain k_i , and the derivative gain k_d and sending the analogue voltage signal to adjust the laser output.

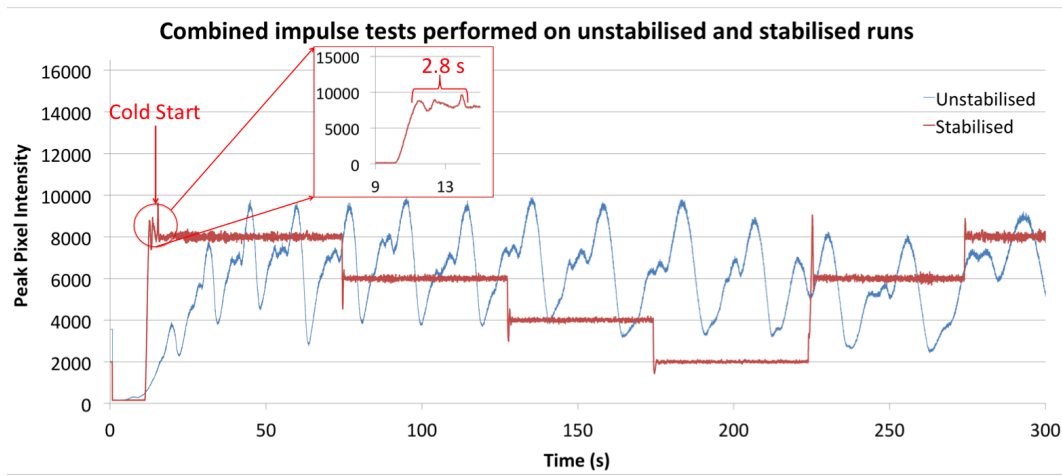


Figure 4.7: Demonstration of combined impulse tests to confirm the obtained PID parameter set. A series of impulses were applied to the system in rapid succession for both unstabilised stabilised conditions.

The optimal gain values were tuned by combinations of a step test, a pulse test, and a double test along with the Ziegler–Nichols method, so that the overshoot, settling time, and oscillation behaviour can be optimised. To perform step tests, the controller output was stepped up or down to observe the time required to see a clear response in the measured process variable. For pulse tests, the controller output was stepped up and, as soon as the measured process variable showed a clear response, the controller output was then returned to its original value. For double tests, a series of pulse tests were performed in rapid succession and in opposite directions.

Figure 4.7 shows a demonstration of combined impulse tests to confirm the obtained PID parameters. The stabilised condition was tested first, using the LabVIEW program

to control the setpoint. Using the laser feed data ³ from that run, the unstabilised condition was also tested. For each setpoint, the average laser feed was calculated and those numbers were used to manually control the duty cycle of the laser without the stabilisation system. As shown in the graph, for the unstabilised condition, it is difficult to even specify what kind of step signal was injected, due to continuous fluctuations. On the other hand, for the stabilised condition, the average settling time was 0.8 seconds, excluding the cold start point where it took 2.8 seconds to settle. The minimum settling time was 0.4 seconds. The average overshoot or undershoot percentage was 25%.

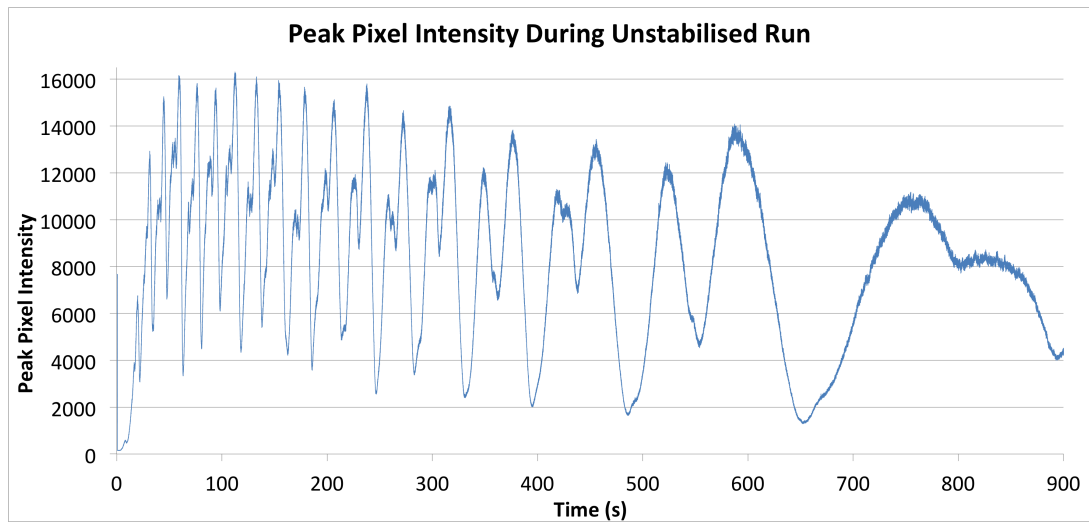


Figure 4.8: Peak pixel intensity observed for 900 seconds without the stabilisation system, while the pulling machine was kept stationary.

Figure 4.8, 4.9, 4.10 show the pixel intensity stability comparison between unstabilised and stabilised conditions while running the laser for 15 minutes with stationary motors, without a polish or a pull process. The blue line indicates a typical unstabilised run, the red line indicates a typical stabilised run ⁴, and the green line indicates the best

³The definition of the “laser feed data” in this experiment is the resulting duty cycle of the laser after the analogue signal was fed in to the system.

⁴The water flow rate was low for the typical unstabilised and stabilised runs. The impact of the water flow will be discussed in the next section.

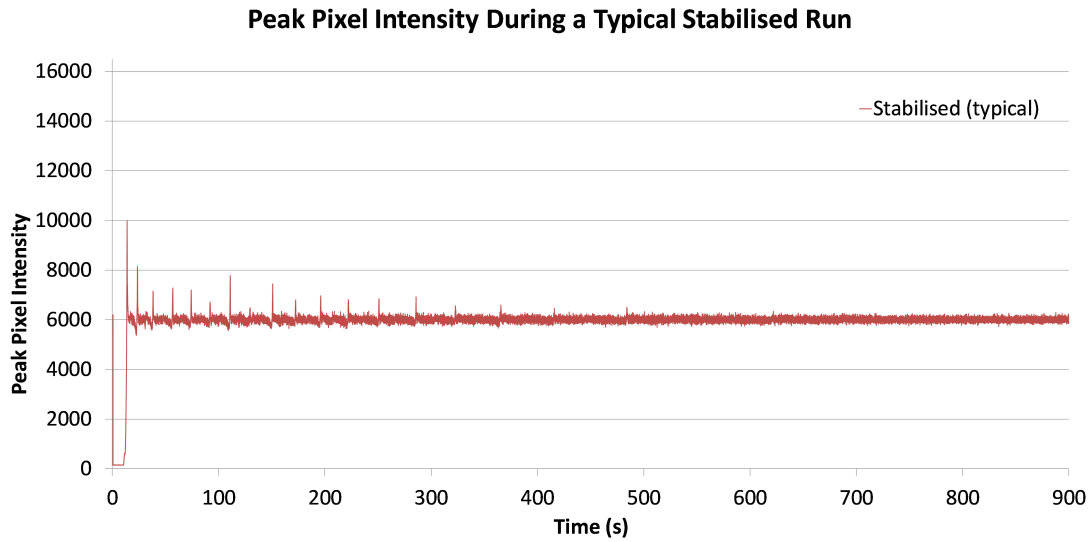


Figure 4.9: Peak pixel intensity observed for 900 seconds with the stabilisation system, while the pulling machine was kept stationary (Typical).

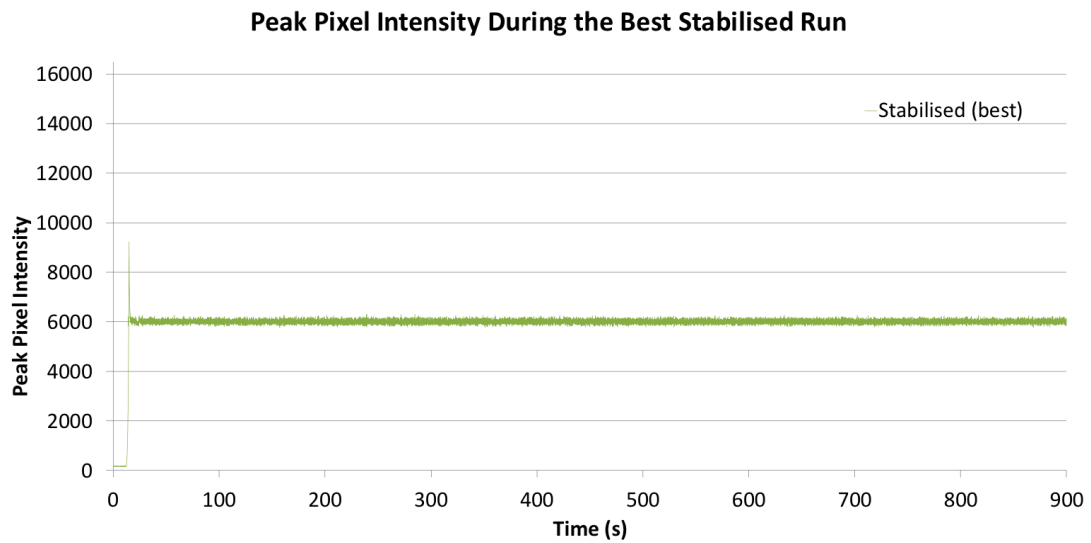


Figure 4.10: Peak pixel intensity observed for 900 seconds with the stabilisation system, while the pulling machine was kept stationary (Best).

stabilised run result. For the unstabilised run, the laser was run with a constant duty cycle of 49%, and for the stabilised run, laser power was varied by the PID controller to keep the constant heating power for the stock. The duty cycle was set to 49% since previous aLIGO fibres were pulled at that duty cycle. As clearly shown, the unstabilised run had significantly more fluctuations in brightness throughout the run, which means its output power was not kept constant, and thus, the temperature of the heated fused silica stock was also not kept constant. In addition, we can confirm the same behaviour and tendency that was observed from the laser power variation in Figure 4.4. This confirms that the brightness fluctuation directly results from the laser startup instability from cold start mode hopping.⁵ When the stabilisation system was applied, the magnitude and duration of each fluctuation significantly decreased. For the typical run, the average peak pixel intensity of fluctuations was 7042 (1042 above the setpoint of 6000) with minimum fluctuation of 6387 (387 above the setpoint) and maximum fluctuation of 7892 (1892 above the setpoint), and all of them settled down within 0.8 seconds. Other than 16 fluctuations in the beginning, the rest of the run was kept stable around 6000, with an average of 5998. For the best run, the peak pixel intensity stayed constant around 6000, with average of 5998 excluding the initial overshoot (0.03% of error), which indicates that the heating temperature of the stock was held constant.

4.3.2 Water Flow

Although runs using the camera system showed much more stable power, there were still some small peaks due to the mode hopping of the laser. The PID control system could handle laser power fluctuations that go up to a quarter of the average duty cycle,

⁵One potential reason for the amplified impact of laser fluctuations, from Figure 4.4 to Figure 4.8, is that even a small change in the laser power in respect of the full capacity of the laser can give major influence in heating up a 3 mm fused silica stock. For instance, when 6% error which is about 8 W is added to 45% duty cycle to make resulting duty cycle of 53%, the amount of vaporisation increases significantly.

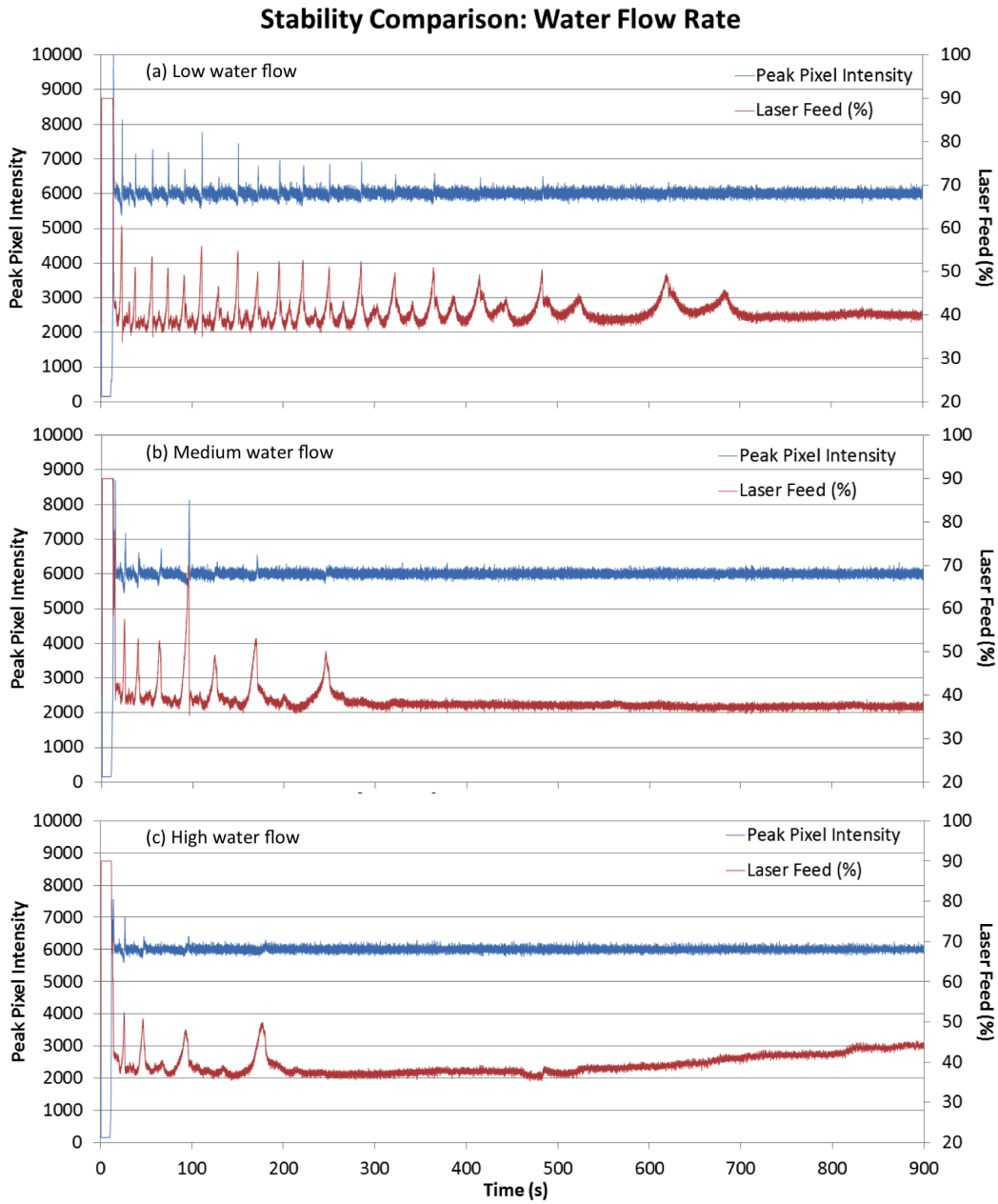


Figure 4.11: Peak pixel intensity data and laser feed values for (a) low water flow rate, (b) medium water flow rate, (c) high water flow rate.

but ones beyond that magnitude were transmitted to the peak pixel intensity data. For instance, in Figure 4.11, when the average duty cycle was 40.2%, the PID control could handle fluctuations that went up to 50% duty cycle (average duty cycle of $40.2\% + 1/4$ of 40.2%). To improve this performance, the flow of the laser coolant, water in this case, was controlled. As the flow rate increased, the water flow became more stable. Since the only method to control the water flow was by turning tap, results of low flow rate (200° turned water tap, on average 6 L/m), mid flow rate (300° turned water tap, on average 8 L/m), and high flow rate (maximum flow rate with 360° turned water tap, on average 9 L/m) were compared. Figure 4.11 shows typical graphs of peak pixel intensity data and the laser feed values for each run with (a) low coolant flow rate, (b) medium flow rate, and (c) high flow rate, observed for 900 seconds. As clearly shown from Figure 4.11, when the water flow rate increased to have a more stable and consistent flow rate, the stability of the peak pixel intensity was also improved. The low flow rate run showed about 17 fluctuations within the first 450 seconds, while the medium flow rate run showed 6 fluctuations within the first 250 seconds. The best result was the high flow rate run, which showed 3 fluctuations within first 200 seconds. Compared to the low flow rate run, it showed over 80% decrease in the number of fluctuations, and 55% decrease in the settling time. According to the laser manual, the recommended coolant flow rate is 7.6 L/m, which is rather closer to the mid flow rate. One potential reason why the high flow rate, which is higher than the recommended rate, showed better results is that the overall water flow rate from the tap is inconsistent, so that when it is set to be mid flow rate, the flow rate sometimes become lower than the average. Due to the water supply system used for this laser, the water flow sometimes varied, for instance, from 4 L/m to 7 L/m for low flow rate, depending on the usage of water from other places in the building. Since the usage of water cannot be controlled or predicted, the exact quantitative data for this variation could not be recorded every time. To further improve the stability, the installation of a coolant flow control system could be an appropriate future modification.

4.3.3 Wait Time Before the Pull

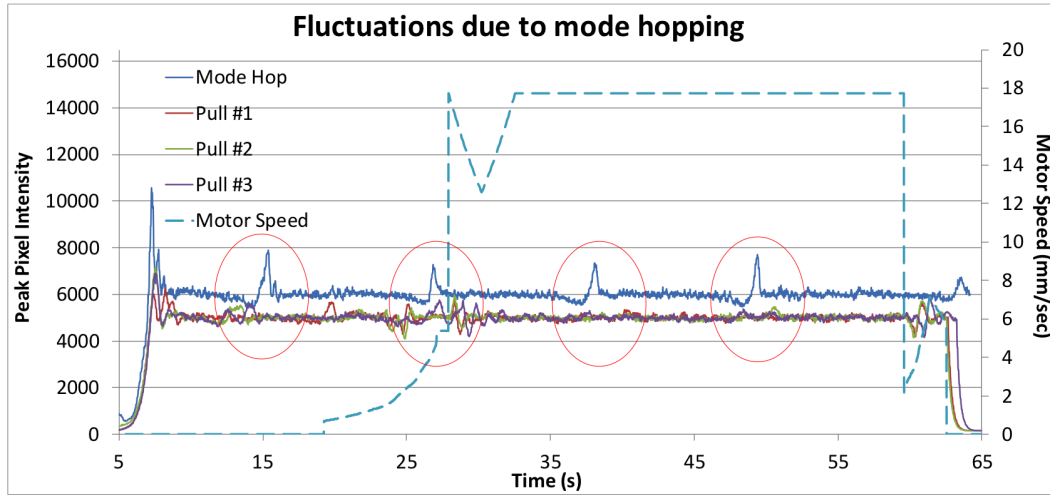


Figure 4.12: Typical fluctuations due to mode hopping, overlaid on peak pixel intensity data for three pulls. To clearly show the comparison between the mode hop line and other pull peak pixel intensity lines, an offset of 1000 was added to the pull data (Pull 1, 2, 3).

Higher water flow rate reduced the intensity of the small peaks and showed significant decrease in number of mode hopping fluctuations after 200 seconds, compared to those with lower water flow rate, but some fluctuations were still evident. In addition, when the pull was repeated multiple times under the same conditions (Pull 1, 2, 3 in Figure 4.12), the fluctuation positions were repeated at similar times in the process. Red circles show the timings when the instabilities were introduced during pulls, and as shown in the graph, they coincided with the timings when the mode hops happened (the blue line). This tendency also agreed with the fluctuations shown in the manufacturer's measurement of laser power variation (Figure 4.4), which confirmed that this instability occurred due to the laser's mode hopping. Figure 4.12 shows a typical fluctuation graph due to the laser's mode hopping overlaid on the typical peak pixel intensity data of three pulls. The blue line indicates the mode hopping fluctuations during a stationary run, while the other three lines (red, green, purple) show the fluctuations during pull processes.

The dotted line shows the motor speed. We can see that the fluctuations which happened during the pull process match up with mode hopping fluctuations that happened during stationary run, which indicates that these fluctuations happen regardless of the speed of the motor.

To avoid this unstable period, when most of mode hopping happens during the pull, a longer pre-pull wait time condition was implemented. The current aLIGO pulling condition uses 18 seconds of wait time to make sure that the stock is heated enough for pulling and to avoid the most significant fluctuations in the beginning. However, from previous stabilisation experiments, Figure 4.4 and 4.11, it had been observed that the laser mode hopping fluctuation is the most severe for the first few minutes and reduces after about 3~5 minutes. Therefore, several different wait time conditions were applied to check the optimum condition. Applying 3 minutes of wait time eliminated most mode hop associated fluctuations except for the ones in the beginning and at the end of the pull. (Figure 4.16) However, from time to time, there have been cases where mode hop fluctuations happened in between 3 to 5 minutes range. Therefore, 5 minutes of wait time was chosen to minimise the possibility of this disturbance.

4.3.4 Stabilised Polishing

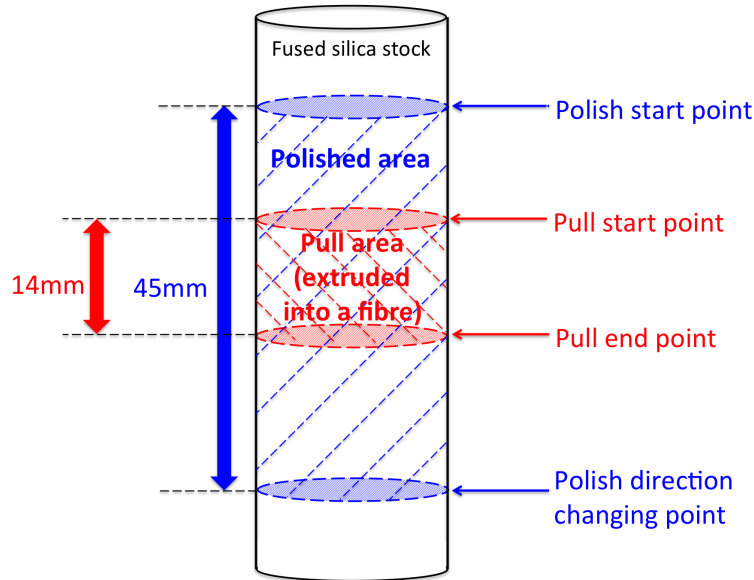
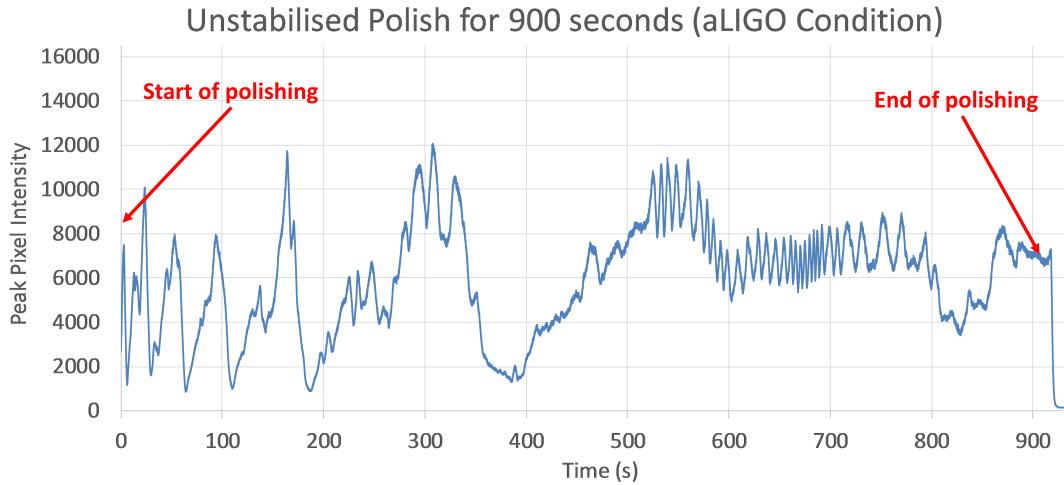


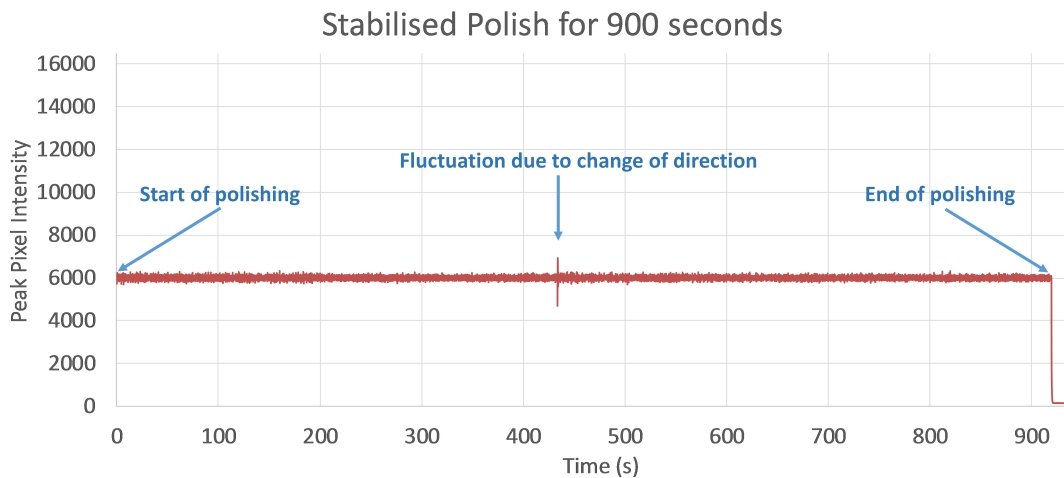
Figure 4.13: Polishing and pulling area of the fused silica stock.

As mentioned in Section 4.2, polishing is an important factor to improve the strength of fused silica fibres. To make sure that all stock material to be used for pulling process is polished, 45 mm of stock was polished, while only 14 mm of the middle section is actually used for the pulling process. Figure 4.13 shows a schematic diagram of fused silica stock area for polishing and pulling process. The figure is colour coded with blue indicating the polishing process and red indicating the pulling process.

Figure 4.14 shows a comparison between a typical unstabilised and stabilised polishing for 900 seconds. Unstabilised polishing started after 18 seconds of wait time and stabilised polishing had 5 minutes of wait time. After waiting for 5 minutes, most mode hopping fluctuations were eliminated before starting the polishing process. In the middle of polishing, when the direction of polishing changed from down to up, one instantaneous fluctuation happened, but that point of the stock is far enough from the area to be used for pulling that it cannot affect the pulling process. (Figure 4.13)



(a) Unstabilised polishing process for 900 seconds (aLIGO condition).



(b) Stabilised polishing process for 900 seconds.

Figure 4.14: Comparison between unstabilised and stabilised polishing process. The stabilised polish process had 5 minutes of wait time before polishing.

According to previous research, the polishing conditions including polishing duration could also have an impact on fibre strength [144]. As Figure 4.15 shows, the polishing duration of 2200 seconds and 3000 seconds produced stronger fibres on average, compared to 900 seconds which is the current aLIGO condition [144]. Therefore, 900 seconds, 2200 seconds, and 3000 seconds polishes were compared. The polishing duration was

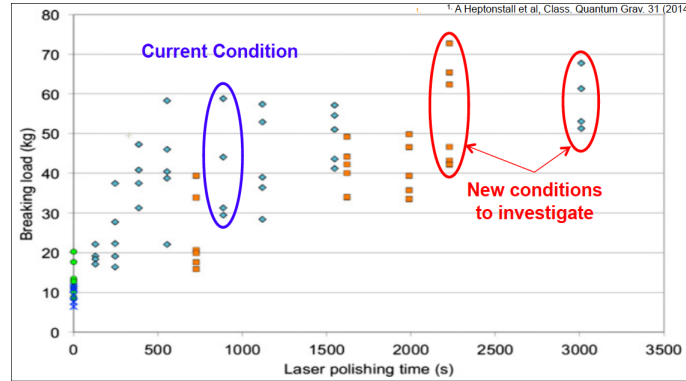


Figure 4.15: Strength test results of unstabilised and stabilised pulls [144].

controlled by changing the drive voltage of the lower stage. For each condition, 24 to 30 fibres were produced for strength tests.

4.3.5 Pull PID Gain Adjustment

In addition to the PID parameters optimised for polishing of the fibre stock, it was found that a further set of PID gain values were required for the pulling process to minimise heating intensity fluctuations. When the motor started to move faster in the early part of the pull and when the motor slowed down at the end of the pull, the pixel brightness showed fluctuations (Figure 4.16). When both upper and lower stages were stationary, the heating region did not change and the amount of the laser beam hitting each point of the stock was kept constant (“equilibrium” status between the stock and the laser heating system). However, as the upper stage moved faster, this equilibrium status was lost with varying shape and diameter of the fused silica stock, as well as a loss of light due to a smaller fibre diameter. (Figure 4.17)

This behaviour is proven by multiple pulls shown in Figure 4.16. In Figure 4.16, trials 1 to 4 show peak pixel intensity data for 4 independent pull processes under the same conditions, compared to the velocity of the upper stage. All 4 trials show a consistent

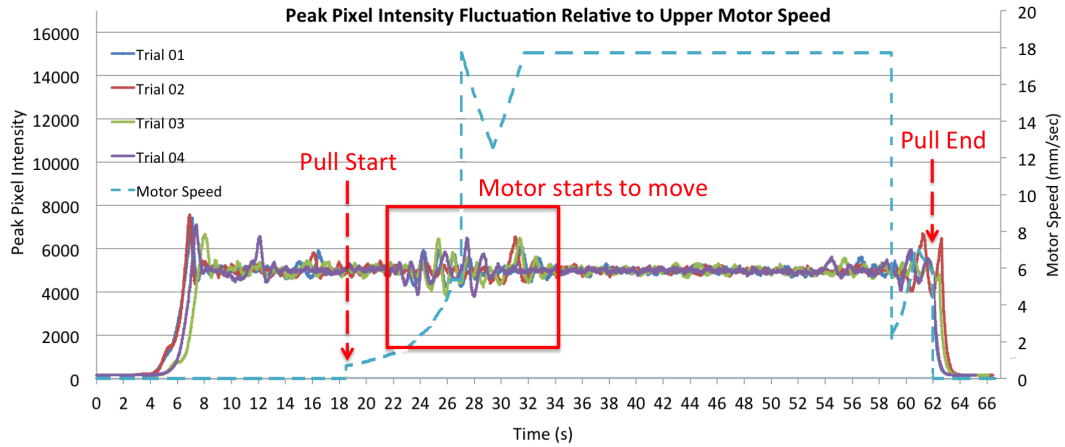


Figure 4.16: Correlation between pixel intensity stability and the upper motor velocity variation. The blue dotted line indicates the velocity of the upper motor. As the motor velocity changes, an instability was introduced. Four repetitive and identical trials were performed to confirm this pattern of two unstable regions at the beginning and at the end of the pull process.

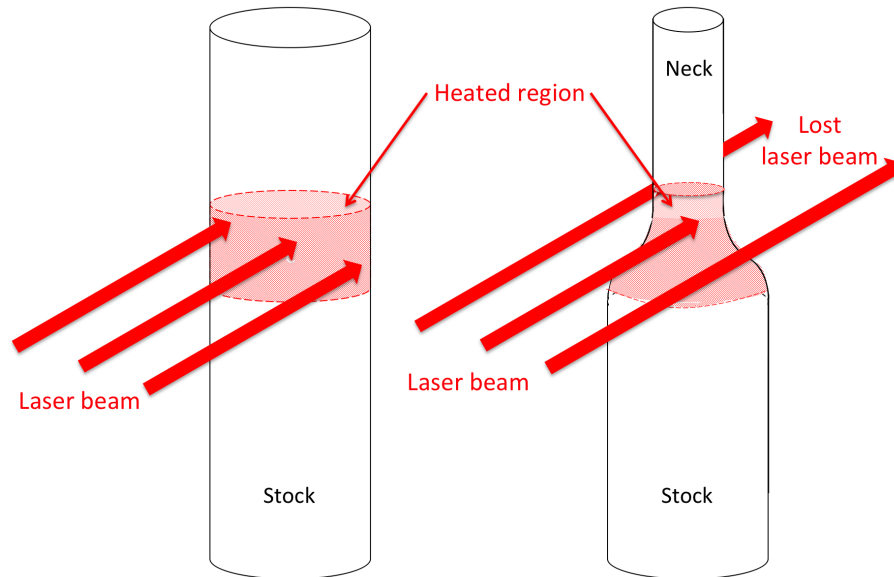


Figure 4.17: Loss of light due to a smaller fibre diameter.

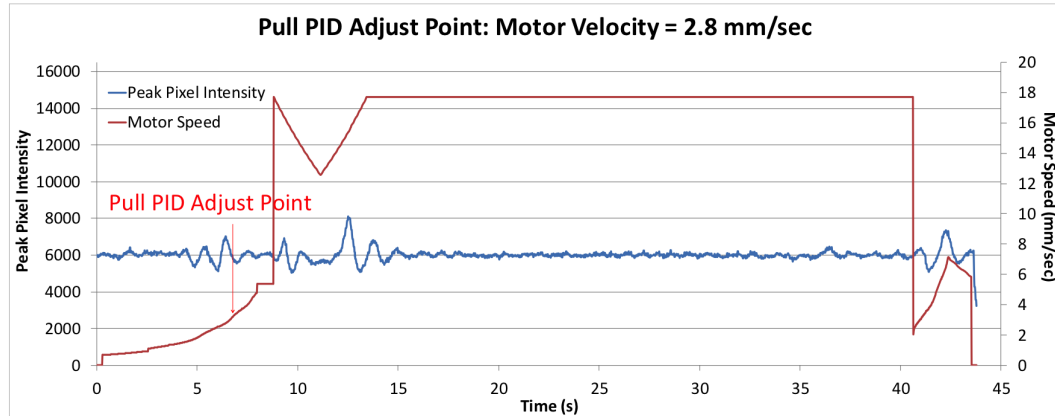
fluctuation pattern at the beginning and at the end with an average percentage error of 26%, while the centre section of the pull (after the first fluctuation settled down until the motor speed dropped down to pull the second neck, in Figure 4.16, 35 seconds to 58 seconds) shows a percentage error of 4.3%. The starting point of the fluctuation varied slightly for each run, but they all consistently fell in the range where the motor speed varied. Therefore, an automatic PID parameter adjustment was implemented in the LabVIEW program so that a new set of parameters can be applied as soon as the motor starts to move, to take the motor speed change into account. Another significant change happening during the pull is the change in the diameter of the stock. As the pull progresses, the diameter of fused silica stock decreases from 3 mm to 400 ~ 800 μm , which amplifies the impact of the laser beam on the stock material. In addition, more beam misses the stock when the heating region becomes narrower (Figure 4.17). Therefore, a new set of PID gains were adjusted when the diameter of the heating region decreased to around 800 μm to take the impact of rapid diameter changes into account.

Condition	P gain	I gain	D gain
Polishing (stationary)	8×10^{-5}	1.3×10^{-6}	0.0105
Pulling	2.5×10^{-5}	1.5×10^{-6}	0.018

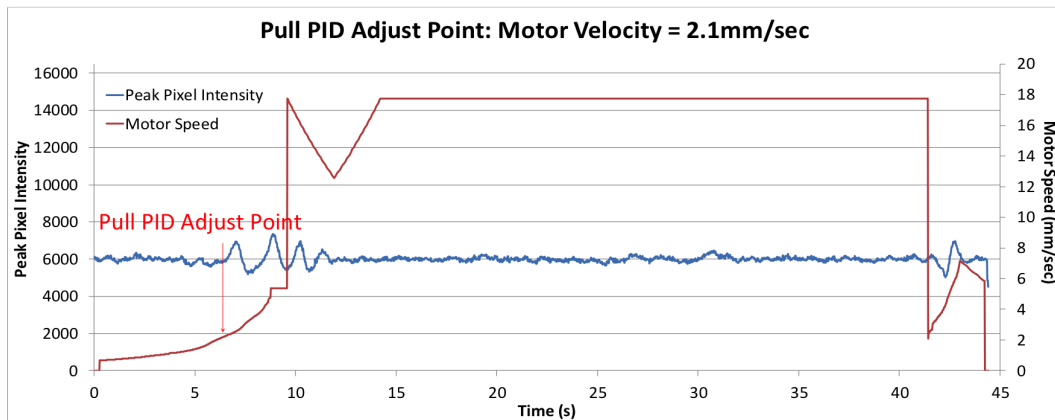
Table 4.1: One example of PID gain parameters for the polishing and the pulling process.

To adjust the pull PID gain parameters, a pulling process was deliberately stopped when the top neck was pulled, and a fine PID gain adjustment for that neck shape and fibre diameter was performed. Table 4.1 shows one example of PID gain parameters for the polishing and the pulling process. The general tendency for the pull PID adjustment was that the P gain decreased, and the I and the D gain increased. As the diameter decreased, the impact of the laser feed was translated faster, since there was less material to be heated. Thus, I gain was increased to quickly make fine adjustments, and the P gain was decreased to balance out the overshoot, and the D gain was increased to

control the noise due to the higher I gain.

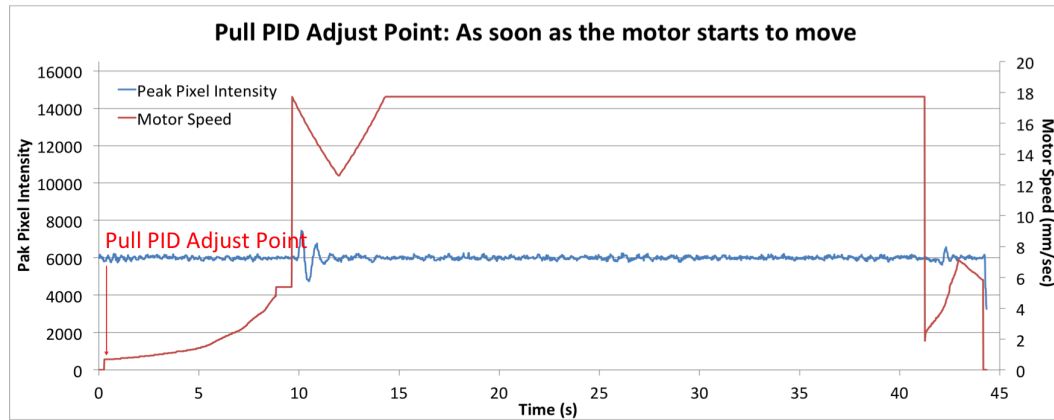


(a) PID adjusted when the motor speed became 2.8 mm/s



(b) PID adjusted when the motor speed became 2.1 mm/s

To find the optimum time for the pull PID parameter adjustment, various change points were investigated. Figure 4.18 shows the result of PID adjustment when the motor speed became (a) 2.8 mm/s, (b) 2.1 mm/s and (c) 0.01 mm/s (as soon as the motor started to move). Firstly, 2.8 mm/s was chosen because it was the peak point of the fluctuation from multiple repeated pulls. However, even after changing the PID value at the 2.8 mm/s point, fluctuations still occurred, hence not showing much improvement. 2.1 mm/s was then chosen as it corresponded to the point where most fluctuations started. Compared to (a), the duration and peak height were improved but fluctuations were not eliminated.



(c) PID adjusted when the motor speed became 0.01 mm/s, as soon as the motor started to move.

Figure 4.18: Observation of the peak pixel intensity depending on three different PID parameter adjustment timings: 2.8 mm/s, 2.1 mm/s, 0.01 mm/s

Finally, the PID parameters were adjusted at the 0.01 mm/s point, which was as soon as the motor started to move. The peak pixel intensity was kept the most stable when the PID parameters were adjusted as soon as the motor started to move. Fluctuations at the beginning and at the end settled down significantly faster, from 10 seconds to 1.5 seconds, but still, they were not able to be completely eliminated.

To confirm this trend, multiple repetitive pulls were done under the same condition where the pull PID parameters were adjusted as soon as the motor started to move. Figure 4.19 shows the peak pixel intensity data of four pulls under the identical condition overlaid to the motor's speed. The shape of two fluctuations were identical for all pulls: the peak pixel intensity went up suddenly to introduce a fluctuation when the motor started to move fast, and the peak pixel intensity went down suddenly when the motor slowed down. In addition, both fluctuations happened at the same time during all pulls: when the motor speed changed rapidly. This indicated that these were not random fluctuations, but some factor related to the motor speed that caused these instabilities.

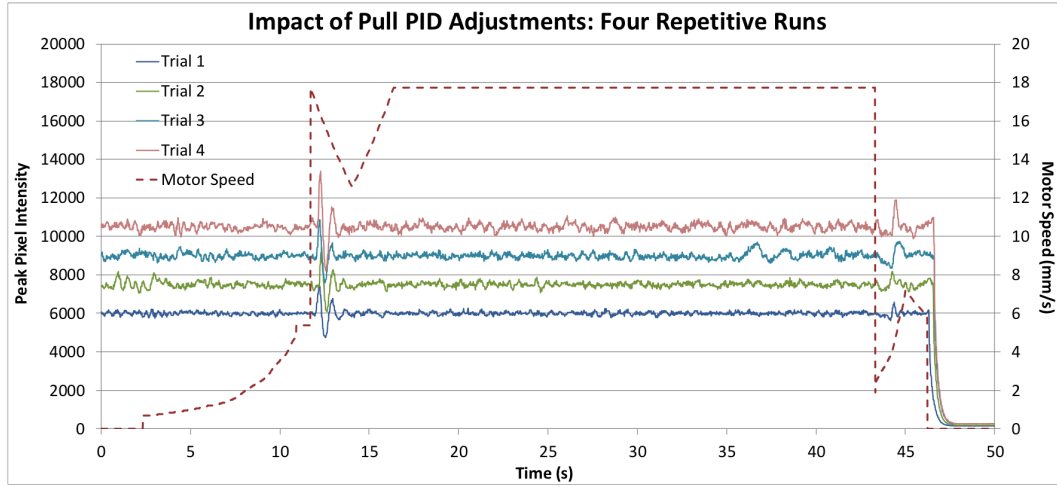
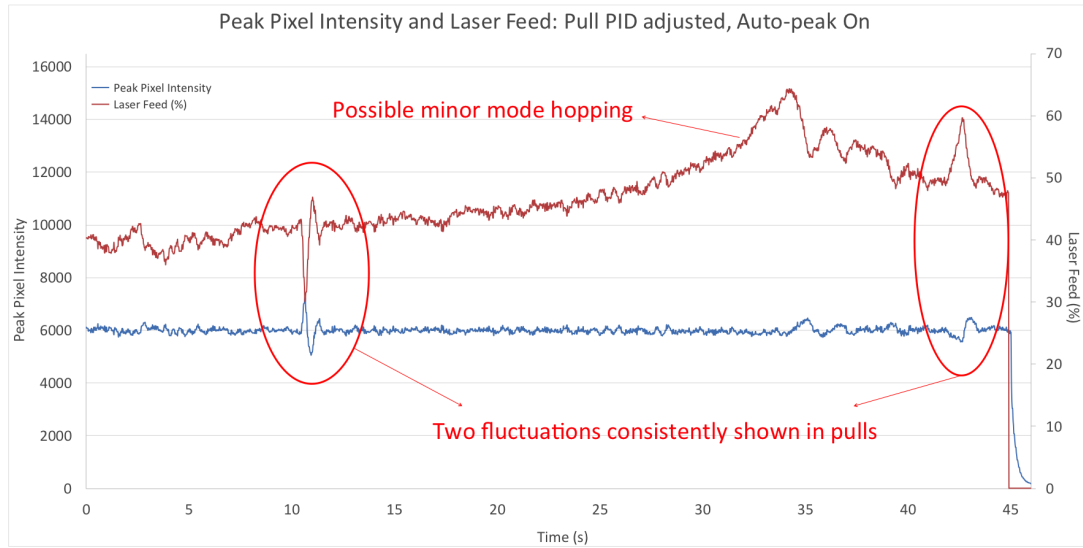


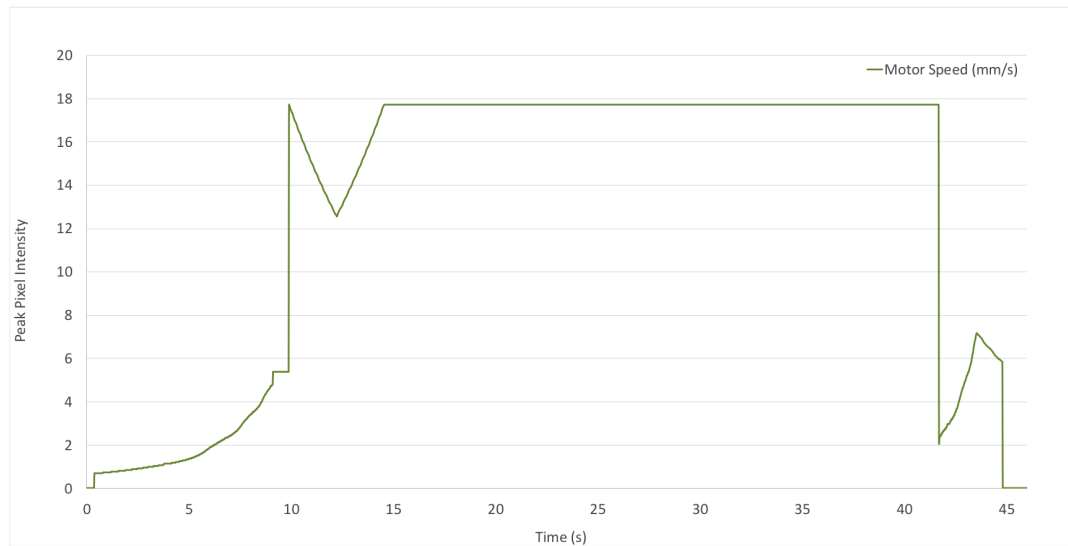
Figure 4.19: Correlation between pixel intensity stability and upper motor velocity variation. The red line indicates the velocity of the upper motor. Fluctuations at the beginning and at the end settled down faster but they were not completely eliminated. Four repetitive and identical trials were performed to investigate reproducibility. Each pull had the identical setpoint of 6000, but for better comparison of the fluctuation shape and timing, a consistent offset was introduced to Trial 2, 3, and 4.

4.3.6 Auto-peak

The two fluctuations shown in Figure 4.19 and Figure 4.20 were repeated every time a fibre was pulled under the same condition. Even when other conditions such as wait time and water flow rate were changed, not only the timing of two fluctuations but also the shape of them were identical. Figure 4.20 shows both peak pixel intensity data and the laser feed data during the pull. The blue line indicates the peak pixel intensity and the red line indicates the corresponding laser feed. At the beginning of the pull, the pixel brightness increased suddenly and caused the laser power feed to drop accordingly, and resulted in a small oscillation. At the end of the pull, the pixel brightness decreased, to increase the laser power feed, which caused another overshoot in pixel brightness.

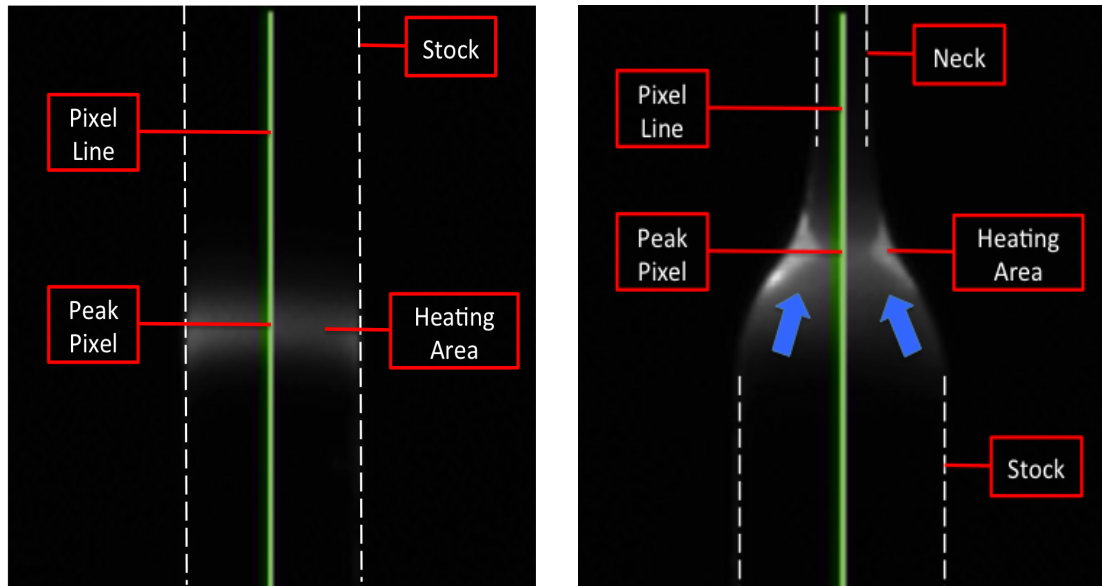


(a) Peak pixel intensity data and laser feed data during the pull with 3 minutes of wait time and pull PID adjustment.



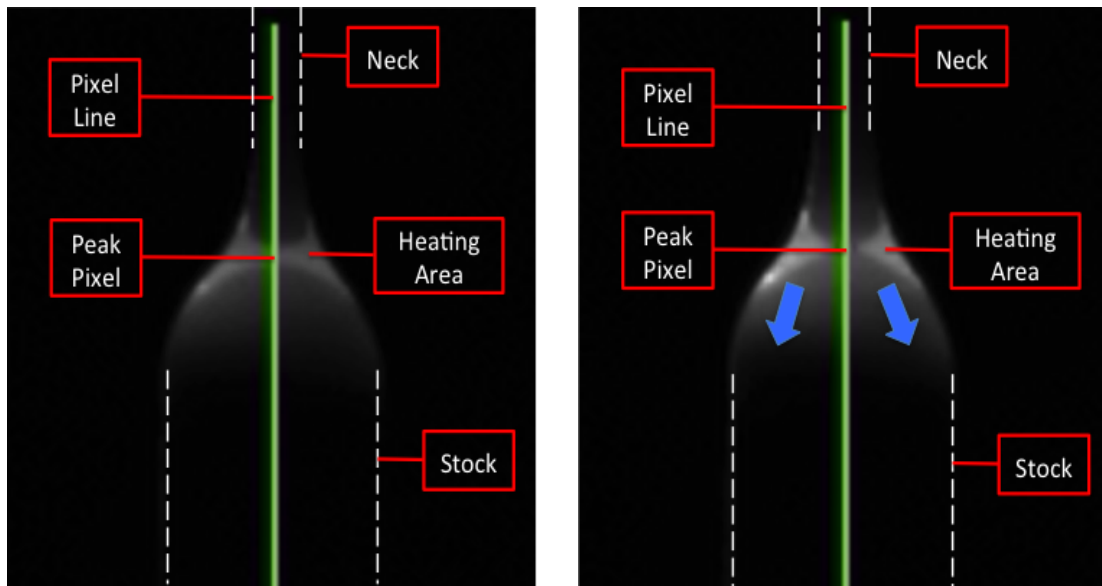
(b) Motor speed graph corresponding to Figure 4.20a.

Figure 4.20: Peak pixel intensity data and laser feed data during the pull with 3 minutes of wait time and pull PID adjustment.



(a) Before the pull started. Fused silica stock was heated uniformly.

(b) When the upper motor started to move up, two bright sections appeared on the edge.



(c) When the upper motor moved faster, the two bright sections were connected.

(d) At the end of the pull, the bright section was disconnected into two regions.

Figure 4.21: Captured images of the fibre pulling from a video file

To investigate these fluctuations, video files of the camera output were recorded during the pulling process. Figure 4.21 shows the captured images from the video files. Due to the ND filter to prevent saturation, only the bright heated area is visible from the video. Dotted lines have been added to show the shape of the stock and the neck. Figure 4.21a shows the heated stock. As the diameter and stock shape changes, a lensing effect due to refraction in the stock being heated is produced, and the area near the fibre edge became brighter (Figure 4.21b). Then, two bright areas on the left and on the right connected, to cause the first fluctuation of peak pixel intensity (Figure 4.21c). By the end of the pull, as the motor slowed down and the stock got thicker again, the bright region was disconnected into two sections (Figure 4.21d), causing the pixel intensity to decrease and resulting in a small fluctuation. Since the fluctuation caused by this “connection” does not help in keeping the heating intensity of the stock constant, the application of the auto peak track function, which automatically finds the brightest pixel along the green line, needed some modification.

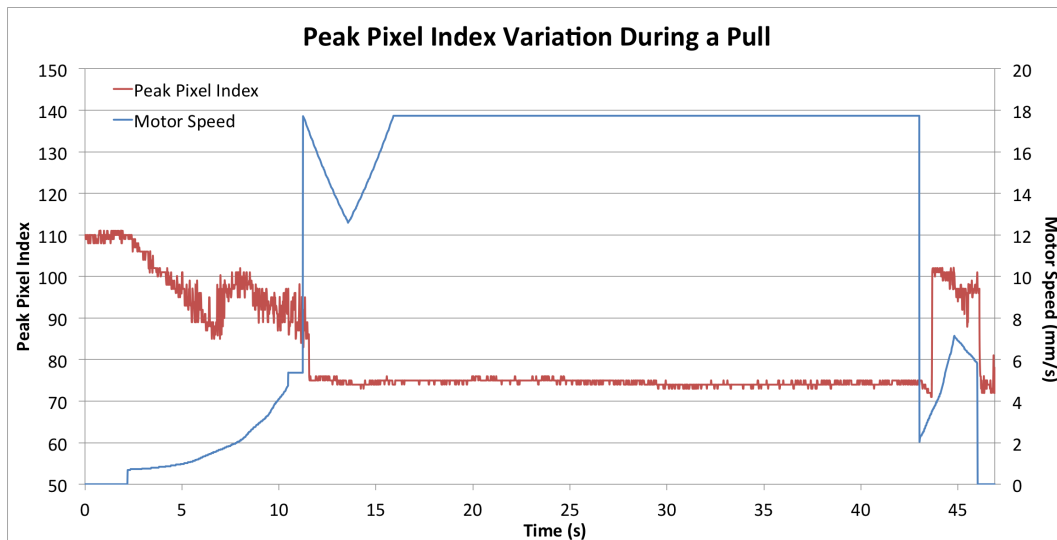


Figure 4.22: Peak pixel intensity index variation during a pull.

Firstly, the position of the peak pixel intensity was investigated. In the LabVIEW program, this position of the peak pixel intensity was referred to as an “index”. The

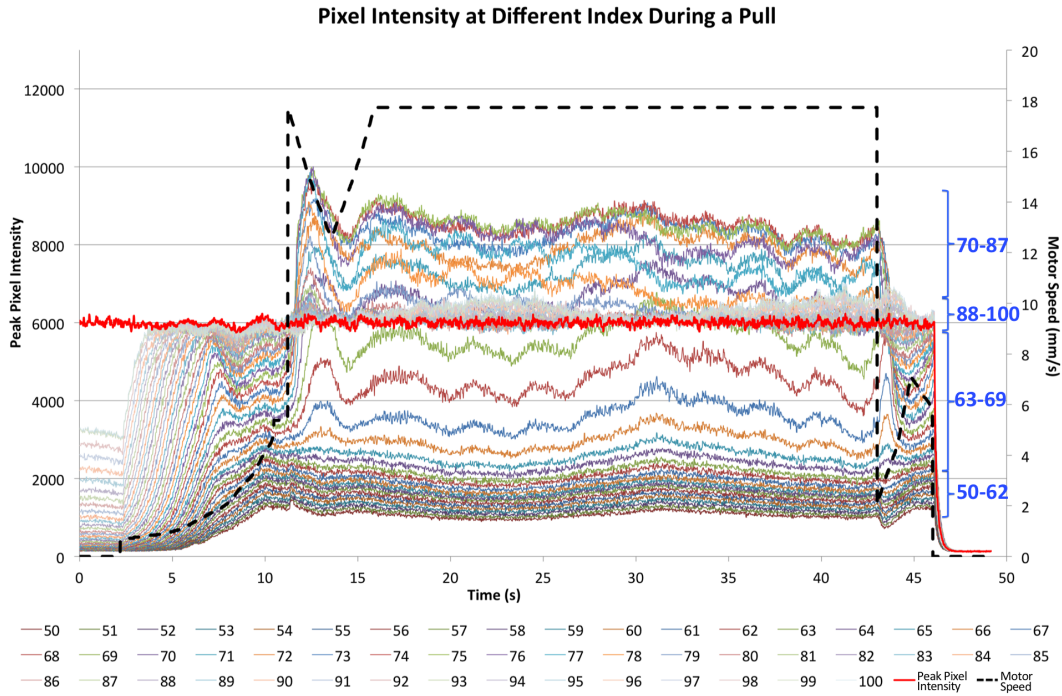
index was counted from the top of the green line to the bottom, 1 to 300 respectively. (in Figure 4.21, the image was cropped at the bottom so it does not show the full length of the green line.)

Figure 4.22 shows the variation of the index during a pull. As the pull starts and the shape of the heating area changes, the position of peak pixel intensity moves up. In other words, the index is decreased. Before the pull started (Figure 4.21a), the index stayed around 110, but as the top neck was formed (Figure 4.21b), the index was reduced to 90 - 100 range. When the thin middle section was pulled (Figure 4.21c), the index was further reduced to 72 - 76 range. Finally, when the bottom neck was formed (Figure 4.21d), the index increased to 90 to 100 range.

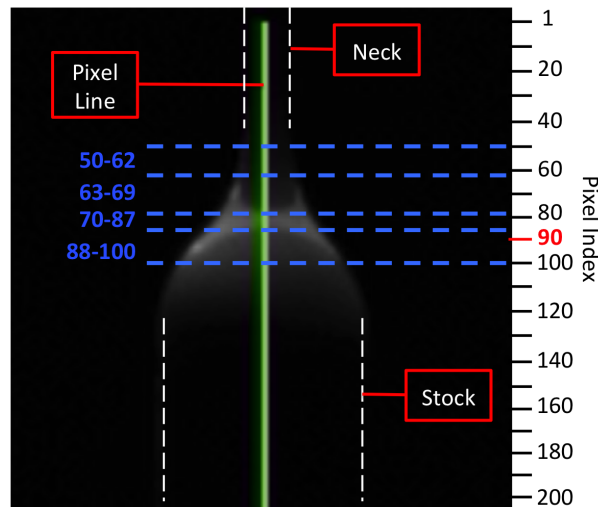
By correlating the timescale of the video file and the index data, it was determined that the jump from '90 - 100 range' to '72 - 76 range' was due to the impact of "connection". Thus, the auto-peak function was turned off right before that moment and the pixel intensity at the index of 90, which is right below the connection region, was observed instead of the peak pixel intensity from that moment. The timing to turn off the auto-peak function was determined by eye, monitoring the live video.

To confirm that the index of 90 is a suitable choice that does not get fluctuations from a lensing effect ("connections"), the pixel intensity data for wider range of indices during a pull was collected to investigate the fluctuation tendency in different region (Figure 4.23a). Since the main index range involved in the connection is 72 - 76, a wider range of indices (50 - 100) which includes the 72 - 76 range in the middle was monitored.

Figure 4.23b shows the 4 ranges marked in the graph (blue). The top two ranges, which indicate the region above and at the connection (index range of 50 - 87), showed the fluctuation of pixel intensity when the connection happened, while the region below the connection (index range of 88 - 100) showed a stable pixel intensity tendency even during the connection. This graph confirmed that the range of 88 - 100 does not get the



(a) Pixel intensity monitored for a range of indices (50 to 100) during a pull.



(b) The index position after turning off the auto-peak function, relative to the peak pixel position.

Figure 4.23: Investigation on the fluctuation tendency in different regions.

optical influence from the connection.

In that range (88 - 100), it is desirable to set the observation point as close as possible to the heating region. However, 88 is too close to the connection region that it can be risky. Therefore, the index of 90 was confirmed to be a reasonable choice of observation point. The red line shows the resulting peak pixel intensity data, which show a more stable tendency compared to other ranges with fluctuations (50 - 87). Figure 4.24 shows the index position after turning off the auto-peak function, relative to the peak pixel position.

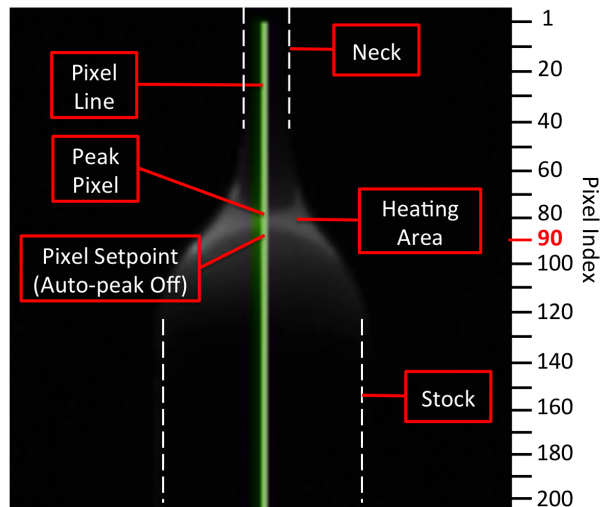


Figure 4.24: The index position after turning off the auto-peak function, relative to the peak pixel position.

Figure 4.25 shows the pull result with 5 minutes of wait time under the auto-peak off condition. The fluctuation at the beginning and at the end of the pull was improved to show almost constant pixel brightness near the setpoint of 6000, with no distinguishable oscillations in the start and the end region.

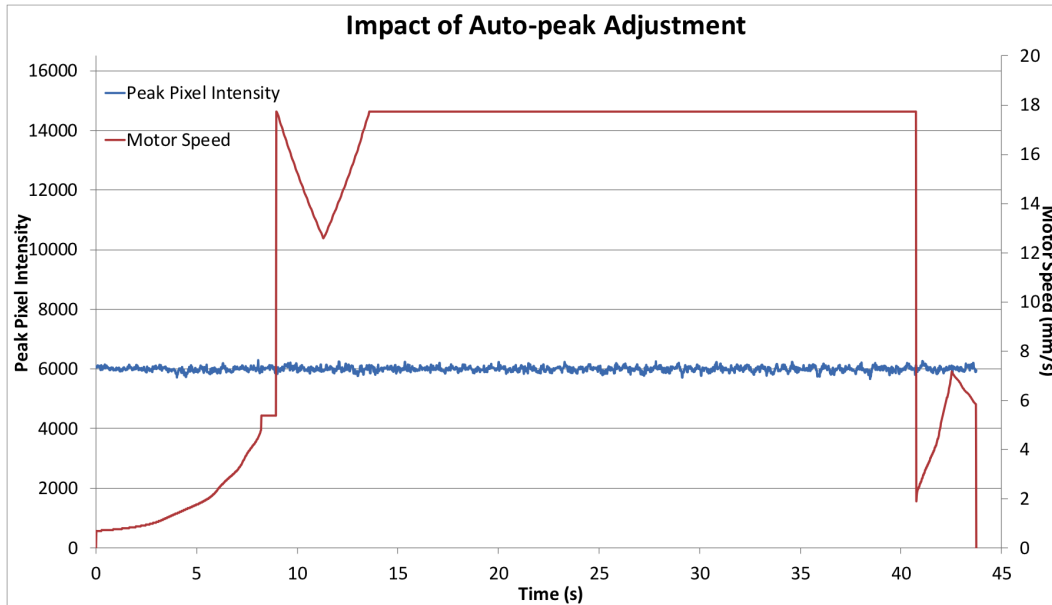


Figure 4.25: Stabilised run with PID gain adjustment, 5 minutes of wait time, and the auto-peak function off.

4.3.7 Possible future studies for the stabilisation system

Although the stabilisation system significantly improved the fluctuations during the fibre fabrication process, there are still some possible future studies to further enhance the stability of this system. One of the key areas is the alignment of the optics for the pulling machine. There are many factors that can influence the alignment.

First of all, the alignment of optics varies slightly depending on the temperature changes in the lab. During winter, when the outside temperature went down below 0°C and when the laser has been running for long time, the optics were heated up due to the laser power, and the mirror alignment was observed to change. To minimise this source of error, fans were installed to cool the optics during long laser runs and a heater was kept on during cold winter days. These solutions definitely improved the alignment consistency but there can be more effective and efficient solutions.

Furthermore, this alignment change also affects the PID parameters. Even though the alignment of the pulling machine is performed following the same procedure and checked by the same standard, it was impossible to have exactly the same alignment everytime. Minor alignment changes due to heated mirrors from long laser runs were not critical enough to require a new set of PID parameters, but for major changes, the PID parameters had to be reset. Although it does not take too long to reset the parameters, it would be useful to find a more efficient solution for this limitation. One possible option is to very precisely quantify every possible movement in the optical alignment, including the position and angle of every optic in respect to the pulling machine, and the position of both stages and fibre clamps of the pulling machine.

4.4 Profiling the fibres

The impact of fluctuations during a pulling process can be directly confirmed by profile analysis of the fibre diameter using the dimensional characterisation (“profiling”) machine previously developed within the IGR for aLIGO [180, 161]. Figure 4.26 shows a CAD image of the profiling machine.

Figure 4.27 shows the data from one of the unusual runs that had a continuous oscillation throughout the pulling process for unknown reason. The same oscillation pattern was observed for the diameter profile data set, which indicates a strong correlation between the heating intensity and the diameter of the fibre. To further investigate any correlation between the peak pixel intensity and the diameter of the fibre, different fluctuations were injected by controlling input signals during the pull. The heating intensity was varied with a high step signal, low step signal, continuous step signal, and sine signal, and the corresponding fibres were profiled. Figure 4.28 (a deliberate high step signal), 4.29 (a deliberate low step signal), 4.30 (deliberate continuous step signal), 4.31 (deliberate sine signal) show the results of the analysis for those pulls. These figures show zoomed-in section of each pull to closely investigate the impact of injected signals. The red line

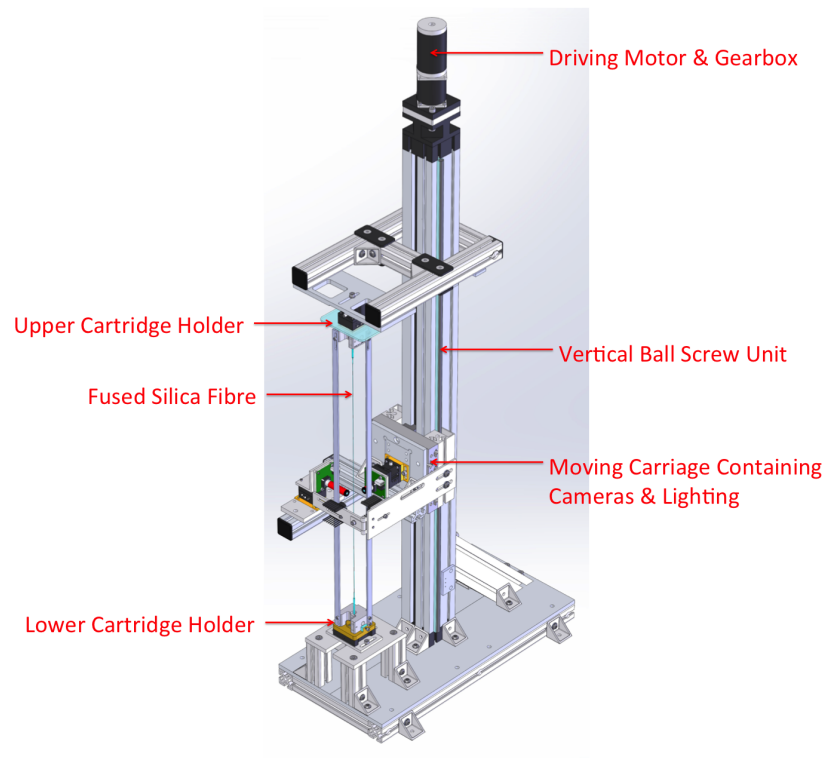


Figure 4.26: Fibre profiling machine developed within the IGR

shows the peak pixel intensity data and the purple line shows the diameter profile data.

From these deliberate fluctuation injections, it was shown that there is an inverse correlation between the heating intensity and the fibre diameter. One potential factor causing this inverse correlation is vaporisation of the stock material during power fluctuations. When the heating intensity increased, more fused silica material is vaporised on the stock surface, causing less material to pull from. To look for evidence of the vaporisation, a diameter comparison was performed for two different setpoints: 6000 and 10000. Each 3 mm stock piece was polished with a different setpoint (6000 and 10000) while all other conditions such as polishing duration were kept the same. To verify the result, 3 pieces of stock were polished under each condition. For the 6000

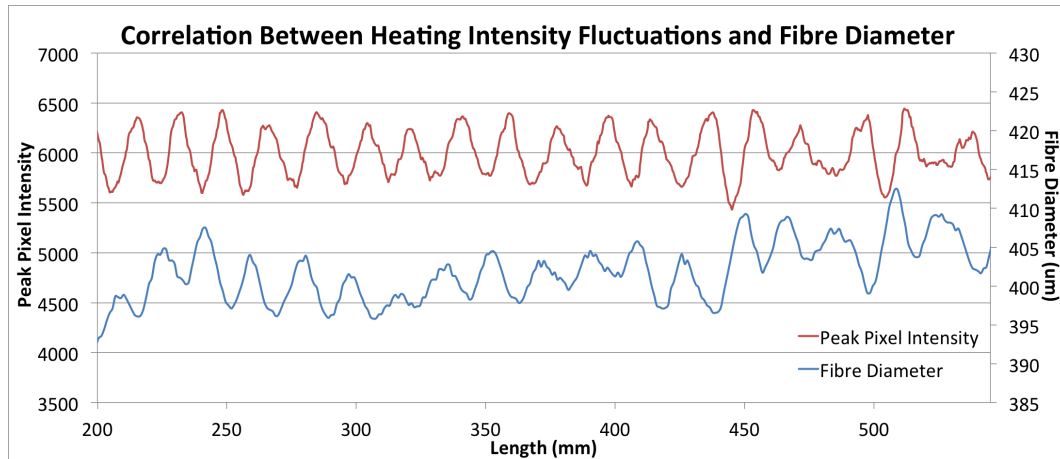


Figure 4.27: Correlation between the heating temperature fluctuation and the fibre geometry. As the peak pixel intensity showed a continuous sinusoidal fluctuation during the pull process, the corresponding fibre's diameter profile also showed an identical pattern.

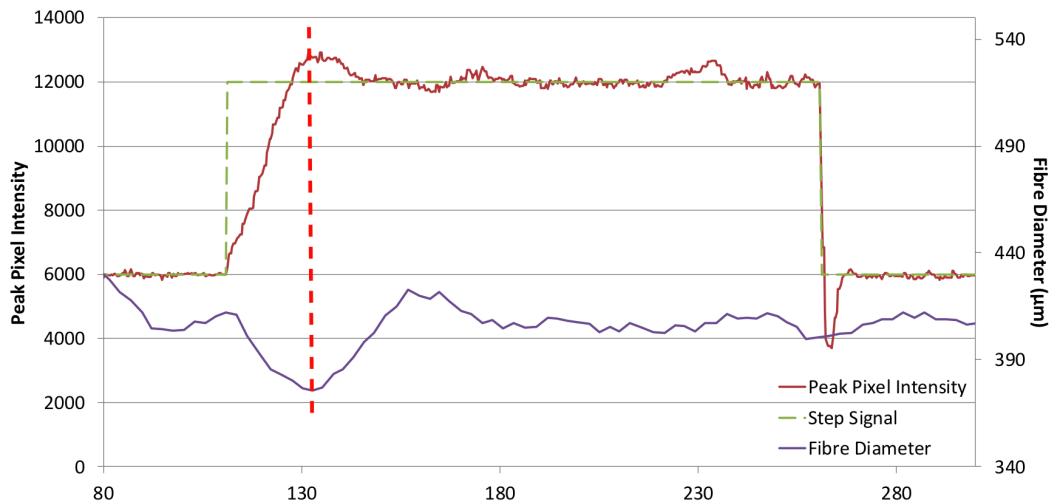


Figure 4.28: A deliberate high step signal was introduced during the pull. The corresponding fibre was profiled and overlaid onto the heating intensity graph.

setpoint polishing, the stock diameter became 2912.6 μm on average, and for the 10000 setpoint polishing, the stock diameter became 2893.3 μm on average. Compared to the 6000 setpoint condition, the 10000 setpoint polished stock showed a 19.3 μm decrease

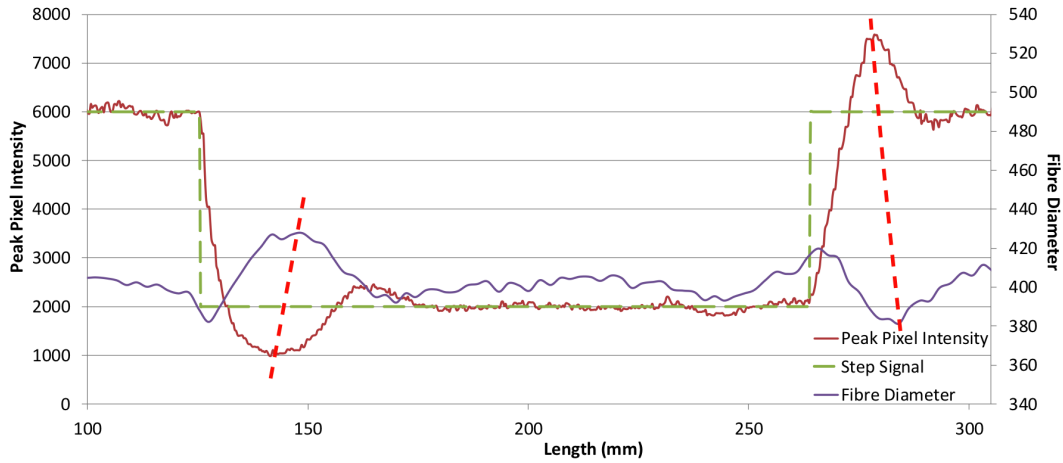


Figure 4.29: A deliberate low step signal was introduced during the pull. The corresponding fibre was profiled and overlaid onto the heating intensity graph.

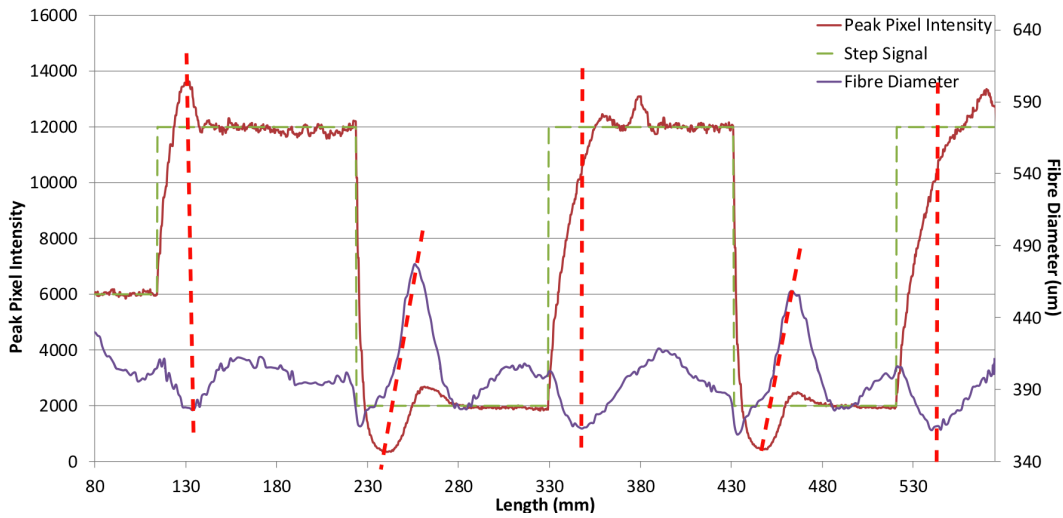


Figure 4.30: A deliberate continuous step signal was introduced during the pull. The corresponding fibre was profiled and overlaid onto the heating intensity graph.

in diameter. Applying the same ratio of vaporisation to a setpoint 12000, the expected vaporisation for Figure 4.28 (setpoint varied from 6000 to 13000) is 28.8 μm , and the observed difference between the average diameter and the dip diameter corresponding to the high signal step was 28.6 μm , which is very close to the predicted value. Using

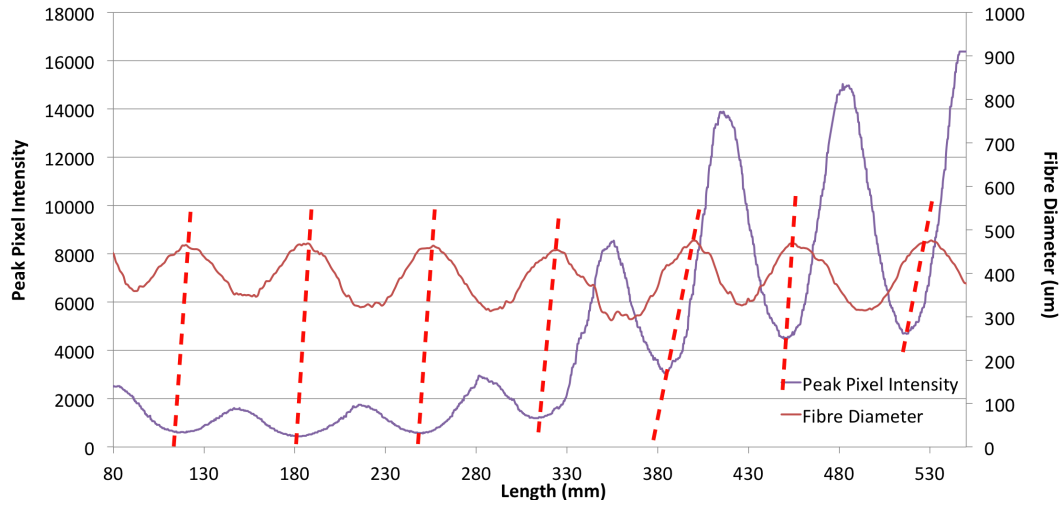


Figure 4.31: A deliberate sine signal was introduced during the pull. The corresponding fibre was profiled and overlaid onto the heating intensity graph.

the same ratio, the difference between the average diameter and the expected bump diameter for Figure 4.29 at the lower step signal (6000 to 1000) is $23.9\ \mu\text{m}$, and the observed diameter difference was $24.2\ \mu\text{m}$, which is, again, very close to the expected value.

The influence from fluctuations of the heating intensity was transferred to the fibre geometry with some lag which varied from 0.1 to 6 mm in length, which can be converted to 0.01 to 0.4 seconds in time. Red dotted lines are overlaid on the graphs to show these small lags.

These pulls prove that there is a direct correlation between instability in the heating temperature and the fibre diameter profile. These unexpected variations in the diameter can cause undesirable effects on fibres, such as tensile stress concentration in the thinner area. To quantitatively analyse the correlation between laser stability and fibre diameter, a correlation analysis was done for seven fibres which had some fluctuations during the pull.

The correlation coefficient for the peak pixel intensity and diameter profile were determined

using Matlab. Both data sets were then randomly redistributed 10,000 times and the correlation coefficient was calculated for each case. These correlation coefficients followed a gaussian distribution centred on zero. The FWHM of the distribution was determined and the sigma was then determined as the ratio of the correlation of the data to the FWHM, giving a measure of the statistical significance of the measured data. Table 4.2 shows the summary of the correlation analysis. The standard deviation of the correlation coefficients was 5.48, which gives a strong quantitative confirmation of a correlation between laser fluctuations and the resulting diameter of the fibres.

	Correlation Coefficient	FWHM of random distribution	Sigma
Fibre 1	0.2647	0.0494	5.36
Fibre 2	0.4614	0.0484	9.54
Fibre 3	0.2555	0.0479	5.34
Fibre 4	0.2151	0.0479	4.49
Fibre 5	0.1594	0.047	3.39
Fibre 6	0.1521	0.0474	3.21
Fibre 7	0.3378	0.0478	7.06
AVERAGE	0.264	0.048	5.48

Table 4.2: Summary of the correlation analysis. The average standard deviation was 5.48, which indicates that there is a correlation between laser fluctuations and the resulting diameter of the fibres.

4.5 Results

With an optimised recipe for stabilised heating, pulls using this system were compared to the current unstabilised aLIGO fibre pull technique. For unstabilised pulls, two duty cycles were used: 45.5% and 49%. Previously, when there was no camera monitoring system, the duty cycle for a pull process was chosen by the brightness checked by eye. 49% was the duty cycle chosen accordingly. However, when monitoring with the camera during manually controlled pulls, a 49% duty cycle sometimes showed brightness saturation for more than 1/3 of the pull process, which gave us limitations in analysing the correlation between the heating intensity and the fibre diameter. When this saturation

occured, another duty cycle, 45.5%, was used for further investigation on the correlation. Considering fibres can be successfully pulled under a duty cycle as low as 18%, the difference of 3.5% in the duty cycle is not significant in these analyses.

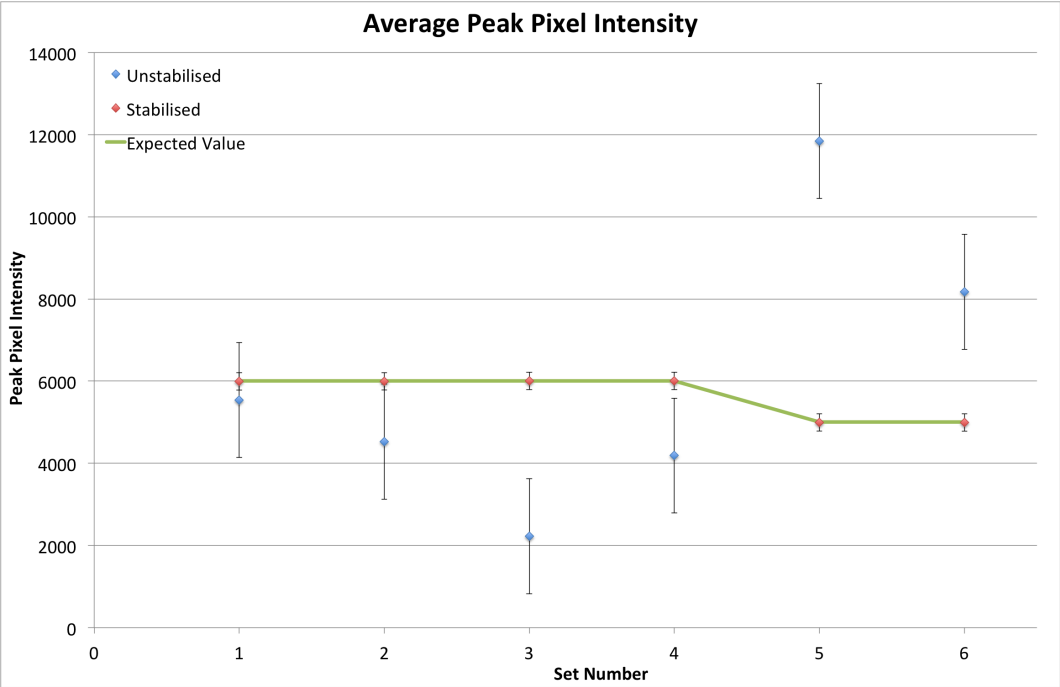
Peak Pixel Intensity Comparison Between Unstabilised and Stabilised Pulls

	Conditions	Average (% error)	Standard Deviation	Minimum	Maximum
Unstabilised	- Wait time: 18 sec - Duty cycle: 49%	5542 (7.6%)	2543	1065	16383
	- Wait time: 3 min - Duty cycle: 49%	4522 (24.6%)	2105	617	7826
	- Wait time: 4.5 min - Duty cycle: 49%	2222 (63.0%)	1554	225	5727
	- Wait time: 5 min - Duty cycle: 49%	4188 (30.2%)	3058	1370	12392
	- Wait time: 18 sec - Duty cycle: 45.5%	11845 (97.4%)	2895	1506	16383
	- Wait time: 18 sec - Duty cycle: 45.5%	8172 (36.2%)	2519	3370	14452
Stabilised (Auto PID adjust & Auto-peak OFF)	- Wait time: 18 sec - Setpoint: 6000	5991 (0.15%)	207	4184	7014
	- Wait time: 3 min - Setpoint: 6000	5996 (0.07%)	141	4872	5850
	- Wait time: 4.5 min - Setpoint: 6000	6001 (0.02%)	122	5398	6102
	- Wait time: 5 min - Setpoint: 6000	6001 (0.02%)	158	5583	6089
	- Wait time: 18 sec - Setpoint: 5000	4996 (0.08%)	163	4347	5797
	- Wait time: 18 sec - Setpoint: 5000	4994 (0.12%)	189	4113	5899

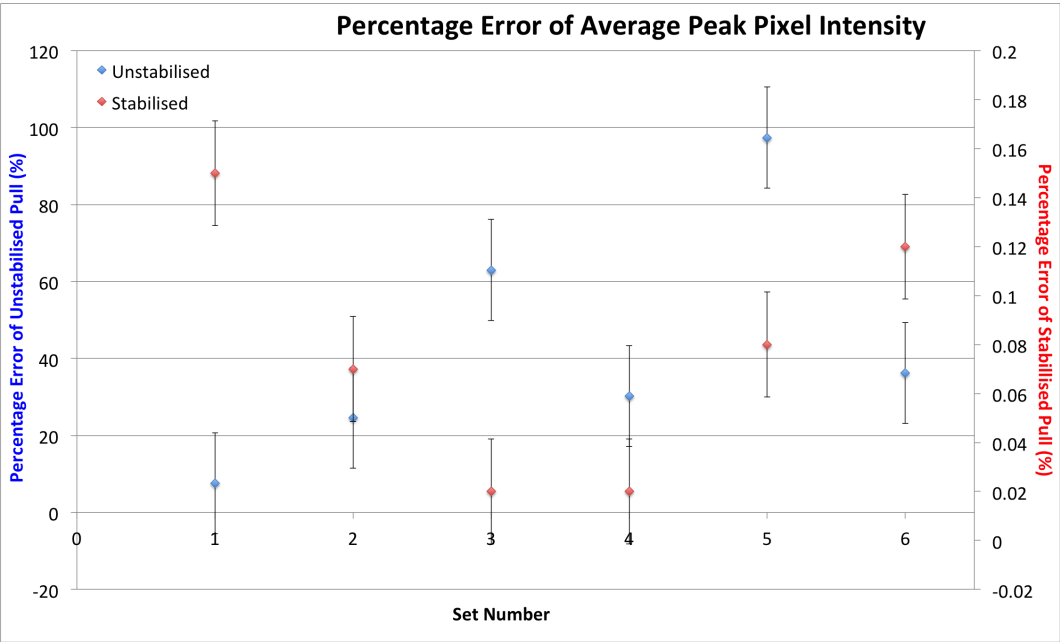
Table 4.3: Highlights of the pull observations for various runs

Table 4.3 presents some peak pixel intensity results of unstabilised and stabilised runs under different pulling conditions. For both unstabilised and stabilised runs, the wait time was varied from 18 seconds (aLIGO condition) to 3 minutes, 4.5 minutes, and 5 minutes. The heating intensity condition was also varied. As the duty cycle for unstabilised runs was varied from 49% to 45.5%, the setpoint for stabilised runs was adjusted accordingly from 6000 to 5000. Blue indicates the best value among different

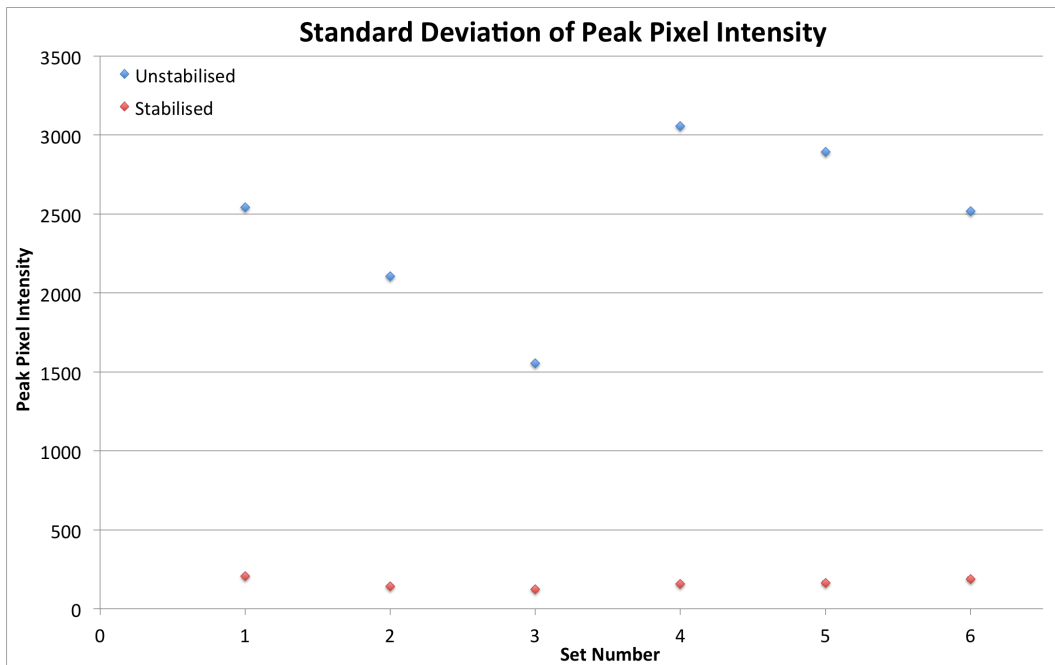
runs and red indicates the worst value. For example, the blue value in the average, minimum, and maximum value sections means that it is the closest to the expected setpoint, and the blue value in the standard deviation section means that it is the smallest value among different runs. Overall, regardless of changes in pulling conditions such as wait time and duty cycle, all stabilised runs showed much lower fluctuations and better consistency between runs. Unstabilised runs generally had inconsistent average peak pixel intensity (7.6 to 97.4% error). Even when the duty cycle was set to the same value, Set Number 5 and 6, the average peak pixel intensity had percent error of 97.4% and 36.2%. Furthermore, unstabilised runs had a large standard deviation (1554 to 3058) and a large spread between the minimum and the maximum pixel intensity values (225 to 16383), which indicates that the laser output deviated more during the pull. On the other hand, stabilised runs showed an average value very close to the setpoint; maximum 0.15% of error. Standard deviations were also 10 to 20 times smaller than that of unstabilised runs (122 to 207), and the average difference between minimum and maximum pixel intensity values was 1376, while that of unstabilised runs was 10835. In Figure 4.32, these data are plotted in four graphs. Blue dots indicate unstabilised pulls and red dots indicate stabilised pulls. For the average, minimum and maximum peak pixel intensity graphs, a green line is added to compare the values to the expected setpoint.



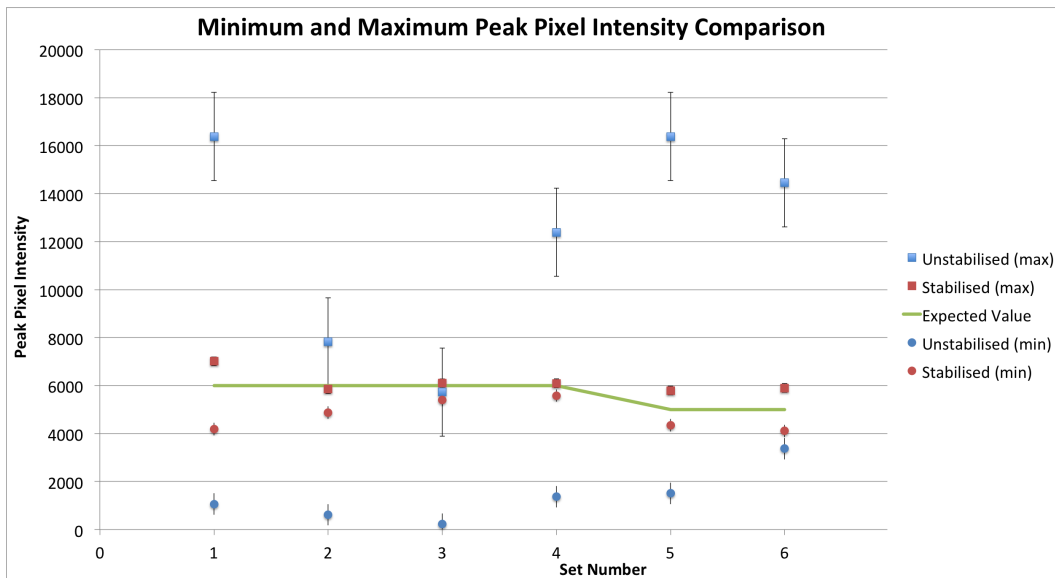
(a) Average peak pixel intensity comparison



(b) Percentage error of the average peak pixel intensity comparison



(c) Standard deviation of peak pixel intensity comparison



(d) Minimum peak pixel intensity comparison

Figure 4.32: Summary graphs of the peak pixel intensity analysis for the stabilised and the unstabilised pulls

Unstabilised - Polished - 18 sec wait time - 49% duty cycle	Average (% error)	Standard Deviation	Minimum	Maximum
Trial 01	8172 (36.2%)	2519	3370	14452
Trial 02	12546 (109.1%)	1772	6865	16383
Trial 03	5859 (2.3%)	3258	2080	12133
Trial 04	9143 (52.4%)	3117	4834	16326
Trial 05	11444 (90.7%)	2380	6136	16383
Trial 06	11407 (90.1%)	2736	5160	16383
Trial 07	14584 (143.1%)	1880	7159	16383
Trial 08	6307 (5.1%)	1362	2949	9589
Trial 09	8012 (33.5%)	1606	3468	12305
Trial 10	10872 (81.2%)	2309	6168	16383
Average	9835 (64.4%)	2294	4819(20%)	14672(144%)

Table 4.4: Summary of the peak pixel intensity data for unstabilised pulls with identical conditions (polished, 18 seconds of wait time, and 49% of duty cycle).

To have a thorough investigation on the repeatability of pixel intensity results under the same settings, unstabilised and stabilised runs were repeated 10 times, while keeping all variables the same. Table 4.4 shows the result of repeated unstabilised runs, and Table 4.5 shows the result of repeated stabilised runs. For unstabilised runs, 18 seconds of wait time and 49% of duty cycle were applied, to have the same condition that aLIGO fibres were pulled under. For stabilised runs, the optimum conditions were applied: PID adjustment at the beginning of the pull, auto-peak function off, setpoint of 6000, and 5 minutes of wait time. (Section 4.3.1)

As Table 4.4 shows, unstabilised runs have average pixel intensity values varying from a minimum of 5859 to a maximum of 14584. In addition, the standard deviation values are very high with a minimum of 1362 to a maximum of 3258 and an average of 2294. Considering the maximum pixel intensity value for the camera is 16383, these standard deviations are very large, 14% of full range in case of the average value. Overall, even though the settings were kept the same, the tendency of the laser output result varied significantly for each run.

Stabilised - Auto PID adjustment - Auto-peak OFF - Setpoint 6000 - 5 min wait time	Average (% error)	Standard Deviation	Minimum	Maximum
Trial 01	5999 (0.02%)	84	5643	6365
Trial 02	5996 (0.06%)	113	4490	6730
Trial 03	5996 (0.06%)	80	5670	6363
Trial 04	5997 (0.05%)	76	5686	6240
Trial 05	5998 (0.03%)	81	5663	6290
Trial 06	5997 (0.06%)	81	5682	6236
Trial 07	5998 (0.03%)	78	5721	6315
Trial 08	5997 (0.05%)	79	5737	6294
Trial 09	5998 (0.03%)	81	5662	6299
Trial 10	5997 (0.04%)	76	5741	6287
Average	5997 (0.04%)	83	5570(7.2%)	6342(5.7%)

Table 4.5: Summary of the peak pixel intensity data for stabilised pulls with identical conditions (polished, PID gain adjustment, auto-peak function off, setpoint of 6000, and 5 minutes of wait time).

However, the stabilised runs (Table 4.5) showed much more consistent results. The average peak pixel intensity values were within 0.02 ~ 0.06% error range, and the minimum and the maximum pixel intensity values were also kept very close to the setpoint. The standard deviation values were, on average, 25 times smaller than that of unstabilised runs (76~113).

One of the runs, Trial 02, was observed to have a random laser fluctuation while pulling the thin section (Figure 4.33). One potential cause of this fluctuation is a sudden long-term mode hop which rarely happens (less than 5% of pulls). The timing of this fluctuation matches the one caused by the “connection” effect, but the auto-peak function was turned off for this run, and the shape of the fluctuation suggests otherwise. For the connection effect, the peak pixel intensity should have a high fluctuation upward first and go down to be stabilised (Figure 4.20). However, in Figure 4.33, the fluctuation

significantly goes down first and back up later, which cannot happen in case of connection. Other similar fluctuations were occasionally observed in other pulls. Even for this run, Trial 02, the standard deviation was about 20 times smaller than that of unstabilised runs (113), and the difference between minimum and maximum peak pixel intensity values was much closer to the setpoint than unstabilised runs (average of 860). This result proves that the application of laser stabiliser contributes to the repeatability of heating conditions during fused silica fibre production.

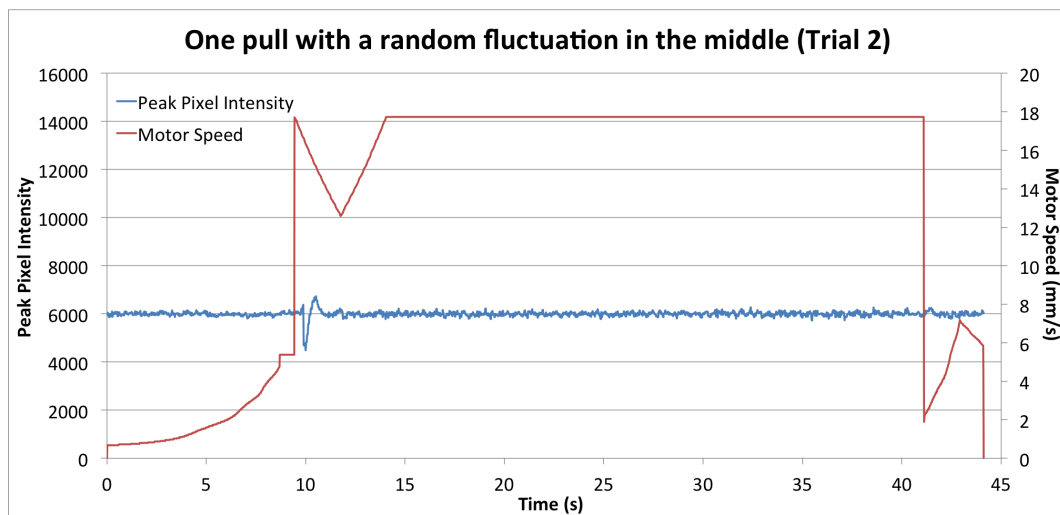
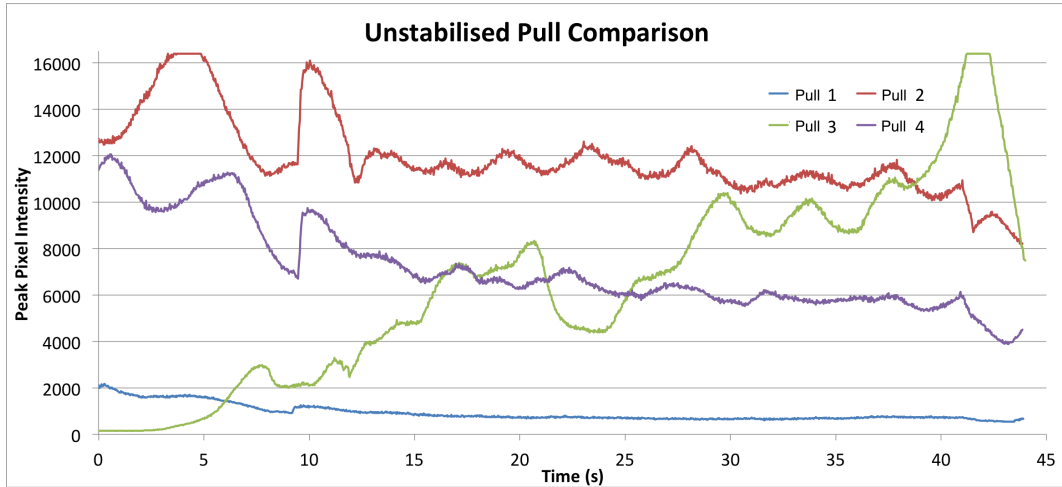


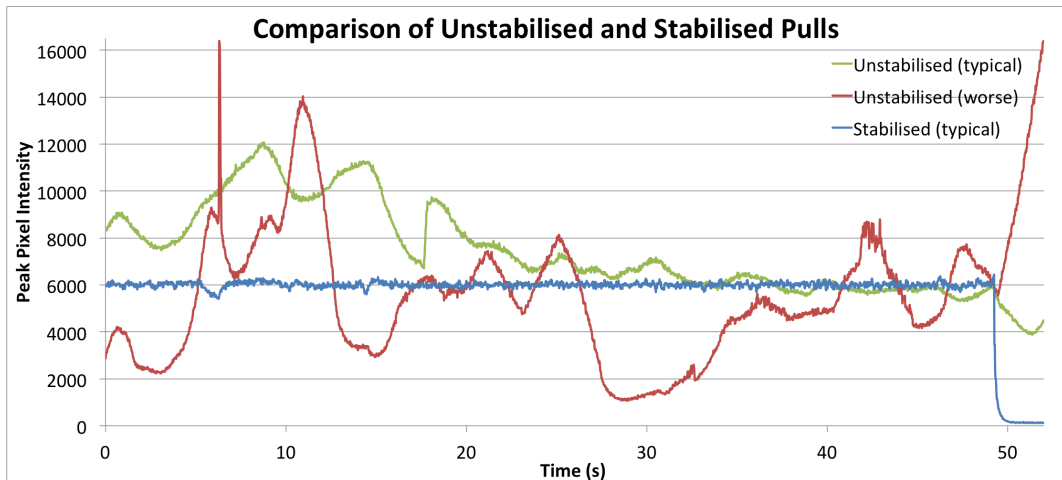
Figure 4.33: One example of a pull with a random fluctuation while pulling the thin section. Despite the fluctuation, the average, standard deviation, minimum and maximum values of the peak pixel intensity were all improved compared to unstabilised pulls.

Figure 4.34a shows 4 different fibre pulls (Pull 1 to 4) without the stabilisation system, performed after 900 seconds of polishing, which eliminated extreme startup fluctuations. Although the laser power was set to be 49% consistently for all 4 pulls, the peak pixel intensity was varying throughout each pull, and the average pixel intensity of each was also inconsistent in between pulls, from 1000 to 13000.

Figure 4.34b shows the comparison between unstabilised and stabilised pulls. The green line shows a typical peak pixel intensity variation during an unstabilised pull, and the



(a) 4 pulls under the same aLIGO conditions without stabilisation.



(b) Comparison between a typical unstabilised pull, one of the worst unstabilised pulls, and a typical stabilised pull.

Figure 4.34: Comparison between unstabilised and stabilised pulls.

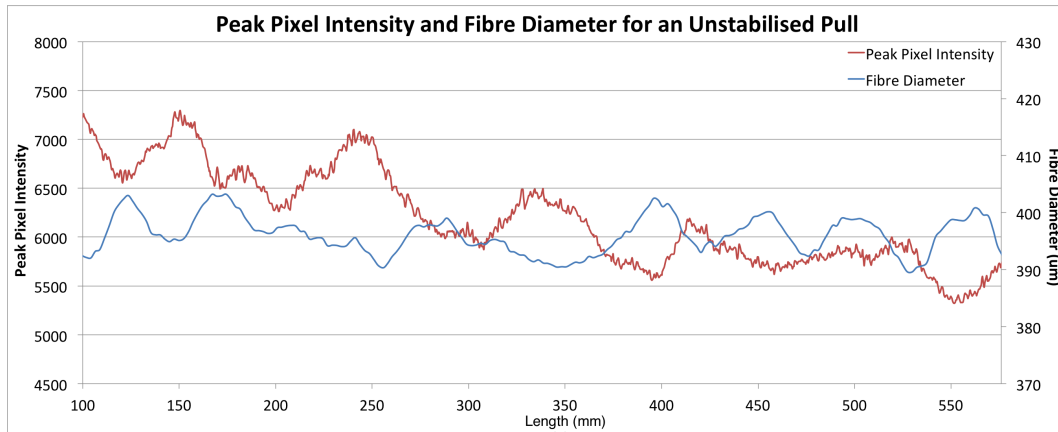
red line shows one of the worse unstabilised pulls with more significant pixel intensity variation. The blue line shows the peak pixel intensity data of a typical stabilised pull. For the stabilised pull, the heating temperature fluctuation at the beginning and at the end of the pull improved to show the average peak pixel intensity of 5997. By contrast, for unstabilised pulls, the pixel brightness varied from 3883 to 12057 for a typical pull

and from 1000 to 16383 for the worst pull, and fluctuated continuously during the entire pull. The average percentage error of peak pixel intensity, from a setpoint of 6000, for the unstabilised pulls was 23.8% for a typical pull and 64% for the worst pull, and that of a typical stabilised pull was 0.04%. Unstabilised pulls had a standard deviation of 1914 for a typical pull and 2294 for the worst pull, while the standard deviation of typical stabilised pulls was 84. These results confirm that the intensity stabilisation can keep the heating intensity much more consistent.

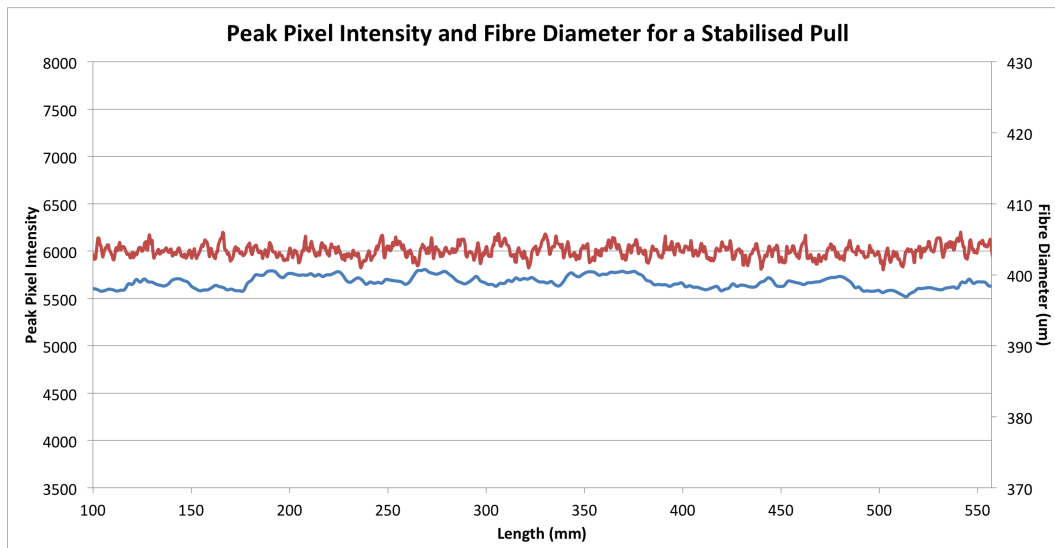
One of the main purposes of the stabilisation system is to have a better control over the fibre diameter consistency. Therefore, typical pulls with the unstabilised and the stabilised conditions were chosen for further fibre diameter profile comparison. Figure 4.35 shows comparisons between peak pixel intensity and fibre diameter profile for a typical unstabilised pull and a typical stabilised pull. As expected, the fibre fabricated from the stabilised pull, without discernible fluctuations during the pulling process, showed a much flatter diameter tendency without dips, while the unstabilised fibre showed multiple dips and bumps throughout the thin section.

When 25 fibres from each fabrication condition were compared, stabilised fibres not only showed 10.7% decrease in the standard deviation of the diameter, but also showed 20% decrease in the spread of average diameter, compared to unstabilised fibres. In addition, the inverse correlation between the peak pixel intensity and the diameter of the fibre was shown in these fibres, too, confirming the results presented in Figure 4.28, 4.29, 4.30, and 4.31. The fibres presented in Figure 4.35 are not special cases, and this correlation was confirmed for over 90% of fibres.

This result proves that the stabilisation system improves the reproducibility of fibres and allows better control over the fibre's geometry. Since the strength of fused silica fibres is directly related to a more consistent diameter of the fibre, this result shows that a more stable laser output can produce fibres without significant dips on the surface, which might also be able to improve the maximum tensile strength of fused silica fibres. The result of



(a) Comparison between peak pixel intensity and fibre diameter profile for a typical unstabilised pull.



(b) Comparison between peak pixel intensity and fibre diameter profile for a typical stabilised pull.

Figure 4.35: Comparison between the peak pixel intensity and the fibre diameter profile for a typical unstabilised pull and a typical stabilised pull. These figures show only the thin middle section which can demonstrate the correlation more clearly. The whole fibre comparison is shown in Appendix E.

strength tests will be presented in the next chapter, along with breaking point analysis, to further investigate the impact of the enhanced fibre fabrication technologies.

4.6 Conclusions

In this chapter, enhanced fibre fabrication via intensity monitoring and control were investigated. By comparing the peak pixel intensity data to the profiled fibre geometry data, it was shown that the laser output power can influence the fibre geometry. Since the laser by itself has an output fluctuation due to mode hopping on startup and long term drift after extended continuous running, it was felt important to establish a more robust control system for the laser. A camera system was used to monitor the heating intensity variation during fibre manufacturing process, and a PID feedback system was used to control the laser power. Various conditions were investigated to stabilise the heating intensity. Higher water flow rate to provide more consistent flow gave a more stable laser output. Optimised PID values were needed for fibre pull as the motor started to move, and 5 minutes of wait time was applied to reduce influence of startup mode hop associated fluctuations. In addition, a specific observation point was set to monitor the temperature, instead of auto-peak function, when the stock diameter decreased due to pulling speed increase. Under these conditions, not only the heating intensity was consistent around the setpoint, but standard deviation, minimum, and maximum values were also very consistent, which indicates that fibres can be produced more consistently with reduced influence from laser power. To ultimately check the influence of this system on fibre strength, strength tests were performed, and the results and analysis of this will be presented in the next chapter.

Chapter 5

Strength Tests

5.1 Introduction

In Chapter 4, various techniques to improve the stability of the light intensity at the heating point, while polishing and pulling fibres, have been discussed. Using the profiling machine, a correlation between the diameter profile of fibre and the stability of the heating intensity was confirmed. As the ultimate goal of these techniques is to improve the consistency and reproducibility of fibres, which can improve statistical strength⁶ of fibres, strength tests were performed to investigate the impact of this technology on fibre's statistical strength. In this chapter, the strength test technique will be discussed (Section 5.2). Breaking stress results are then presented (Section 5.4.1), followed by a more detailed breaking point analysis, examining correlation to the fibre profile and the heating intensity during the pull (Section 5.4.2).

⁶“Improved statistical strength” means both higher average breaking stress and reduced spread of breaking stress.

5.2 Experimental Design

A tensile strength testing machine, specifically designed for fibres [181], was used to perform destructive strength tests (Figure 5.1). Each fibre was clamped into the strength testing machine, and the upper clamp was connected to a load cell and the lower clamp gradually driven down by a geared motor to increase the load on the fibre. When the fibre broke, the maximum load was recorded by the load cell.

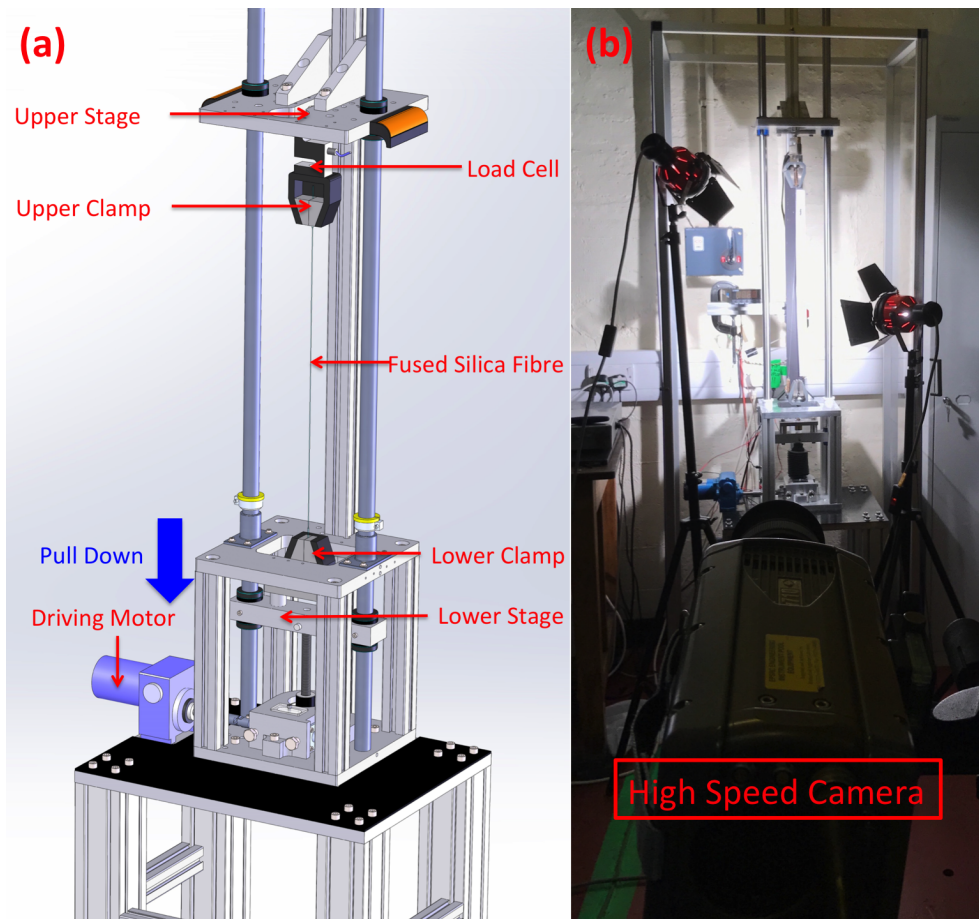


Figure 5.1: (a) CAD image of the strength testing machine used to investigate the maximum tensile stress of fused silica fibres (b) A high speed camera monitoring system setup in front of the strength testing machine

Figure 5.1 (a) shows a CAD image of the strength testing machine used for these tests. The clamps were specifically chosen, as they are self tightening (Figure 5.3), giving a stronger grip as the tensile force applied to the fibre increases. Since the strength of fused silica is highly dependent on surface cracks, the ends of the stock could not be directly clamped by the toothed faces of the clamps. Instead, a resilient interface layer was introduced with both fibre ends attached to cardboard pieces by “Araldite Rapid” 2-component epoxy adhesive [182]. To minimise the possibility of the cardboard pieces slipping from the clamps, thin copper plates were attached to each outer side of cardboard pieces (Figure 5.2). These copper plates provided soft surfaces so that the clamp teeth could grab the sample tighter. For secure attachment, the fibres were left overnight after application of the epoxy adhesive, and then fully tightened using the clamps. Figure 5.3 shows one end of a fibre clamped for the strength test.

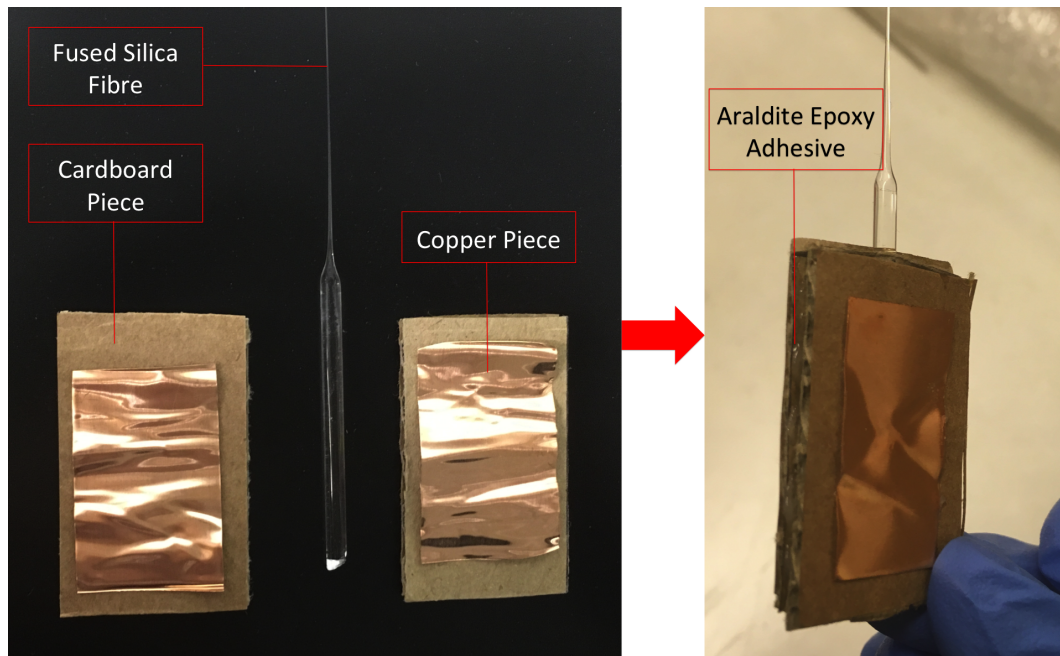


Figure 5.2: Fused silica fibre bonded to two cardboard pieces and clamped for the strength test.

To confirm how diameter fluctuations due to laser instability can influence the breaking

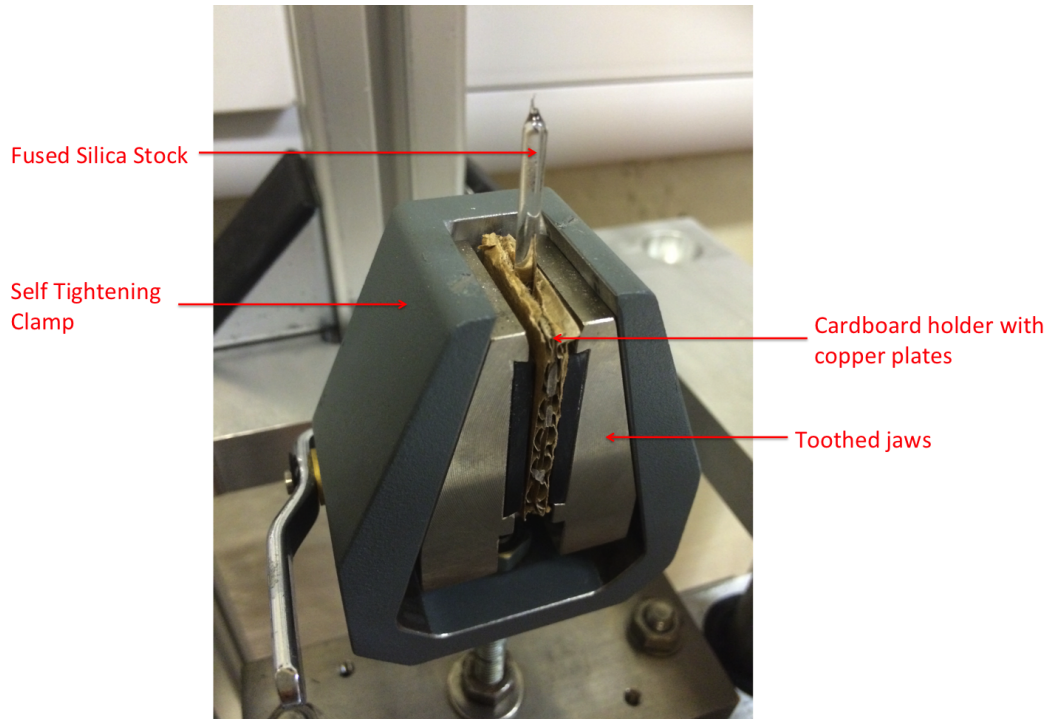


Figure 5.3: *Fused silica fibre bonded to two cardboard pieces and clamped for the strength test.*

point of the fibre, it is important to observe the physical location of the breaking point of each fibre along its length. Therefore, a Phantom V710 (high speed camera) was set up to monitor the breaking moment of each fibre. With a resolution of 640×480 , the frame rate was 22000 fps. When the trigger was manually pulled immediately after the breaking moment, 1.67 seconds before the trigger was recorded as a video file. Then, each frame was carefully investigated to find out the initial breaking point of the fibre. Figure 5.1 (b) shows the overall strength test setup with the high speed camera monitoring system. Due to high frame rate and short exposure time, two halogen lights were used to improve the light exposure for the thin fibres.

5.3 Detailed Analysis Methods

Two main analysis types were used to investigate the strength test results: breaking stress analysis and breaking point analysis. For the breaking stress analysis, the necessary variables are the minimum diameter of the fibre, which is likely to be the breaking point, and the breaking load of the fibre. The diameter data ⁷ was acquired from the profiling process (Section 4.4), and the breaking load (kg) was acquired by the strength tester (Section 5.2). Then, the breaking stress at the minimum diameter point was calculated using the diameter data and the breaking load.

For the breaking point analysis, the required variables are the diameter profile data of fibres and the breaking point observed from the video file. Figure 5.4 shows a screenshot of a video file. A ruler was attached as close to the fibre being tested as possible. Two main measurements were taken from this ruler: 1) the breaking point position, and 2) the initial and the final positions of each clamp which were used to calculate, and adjust for the stretch of the fibre.

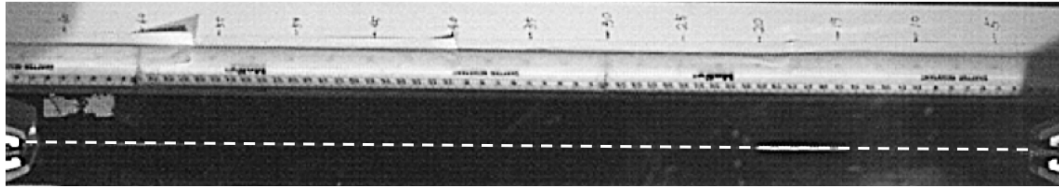


Figure 5.4: Screenshot of a fibre break taken from a video file (rotated 90 degrees). A ruler was attached next to the strength tester to measure the position of the breaking point. Due to a technical difficulty to show the thin fibre clearly from a screenshot, dotted lines were added to indicate the fibre.

When the video file of the break was obtained, each frame was observed carefully to

⁷The minimum diameter used for the breaking stress calculations was unstressed diameter, since it was not possible to measure the stressed minimum diameter. This is a conventional method to calculate aLIGO fibres' breaking stress.

determine the breaking point as accurately as possible. Figure 5.5 shows an example of the instant at which a fibre broke. Using the VirtualDub video editing software [183], the video file was closely investigated frame by frame to find the exact breaking frame. Frame 1 is the frame right before the breaking moment, and Frame 2 is the next frame. The zoomed-in section (red rectangle) shows the breaking point (red circle) caught in Frame 1 and Frame 2. The following frames (Frame 3, 4, 5) give confirmation that it is the correct breaking point, as we can see the broken fibre ends traveling away from each other (blue arrow). The red box area shows the range of potential breaking point, and from observing the direction of shattered silica powder travelling, the estimated breaking point was determined to be at the middle of the red box. When the breaking point was determined with respect to the fibre, the position of that breaking point was quantified using the ruler attached to the strength tester. (Figure 5.4)

Figure 5.5 shows multiple frames before and after the breaking moment. In this example, the camera could catch the breaking point relatively well. Compared to the previous frame, the broken point was clearly shown. For instance, in the case of Figure 5.5, the breaking point can be determined with an error of ± 1 mm.

However, even with the high speed camera, it was very difficult to catch the exact breaking point every time. In this situation, more frames before and after the breaking moment were investigated to determine the travel direction of broken parts from the fibre (Figure 5.6). Even when the broken fibre ends were not clear, by checking further frames, the possible position could be estimated. For instance, in Figure 5.6, the yellow rectangle shows the possible range of breaking point with the most likely breaking point (red dotted line) with an error of ± 4 mm.

To compare the breaking position to the diameter profile data, a more complicated process than simply overlaying on the fibre profile was required. Since fused silica fibres are relatively soft, they stretch significantly during tensile load application, typically about 3 cm for the breaking stresses above 4 GPa. Therefore, it was necessary to take this

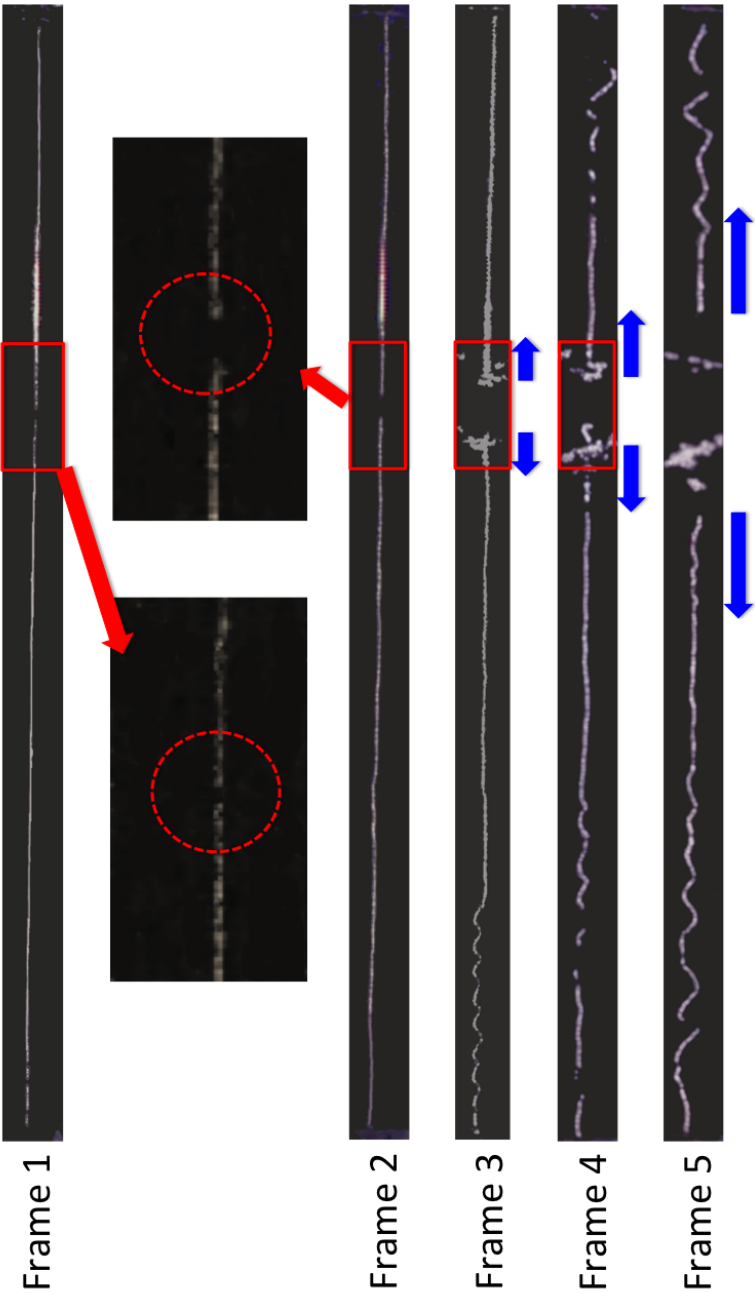


Figure 5.5: An example of the instant at which a fibre broke. The video file was investigated frame by frame to find the exact breaking frame.

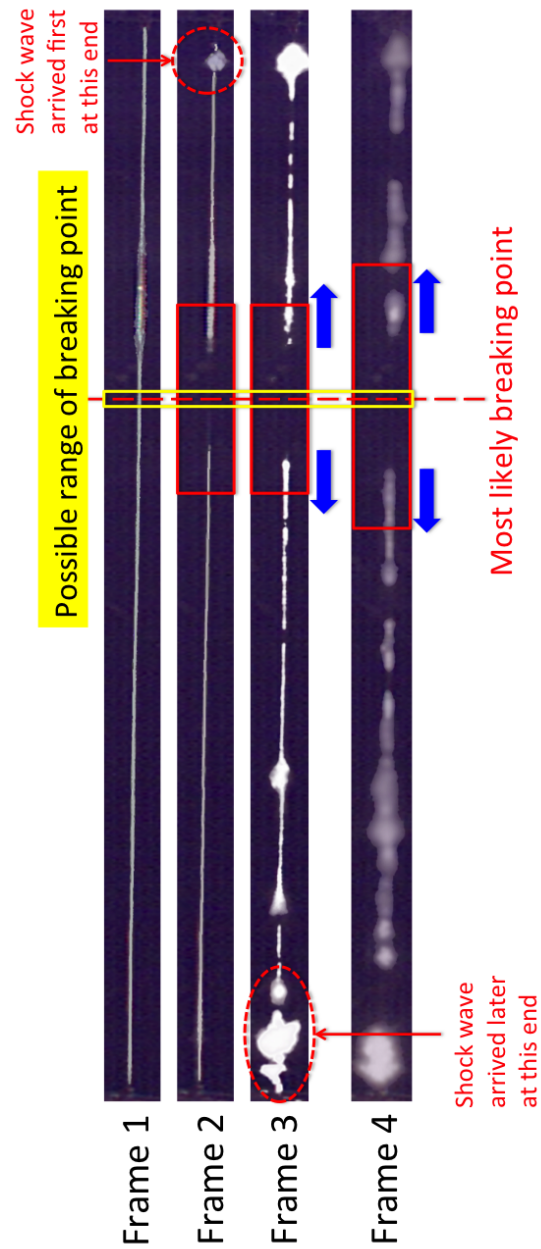


Figure 5.6: An example of the instant at which a fibre broke. When the breaking frame was not as clear, the expected breaking point was deduced from the shattering direction of the fibre pieces.

stretch into account when comparing the video data to the diameter profile data.

For accuracy, two sets of measurements were taken to determine the stretch and cross-check the results: (1) the before and after position of the clamps (2) the before and after position of the neck of the fibres. Since the top surface of the clamp is flat, which made it easier to get more accurate measurements, the position of the clamps were used to confirm the fibre neck position measurements. Since it is only the bottom clamp that is connected to the motor to pull the fibre down, the top clamp position should not be changed. Thus, the photos of the top clamp were also used as a confirmation that there wasn't any technical problem, such as loose top clamp, that could cause an error in the stretch calculation.

The result assured that this measurement method was accurate, as only 2 out of 102 fibres showed any difference between the clamp-based stretch measurement and the neck-based stretch measurement, and even for those two fibres, the difference was no more than 1 mm.

Figure 5.7 shows an example of a clamp-based stretch measurement process. When the fibre was placed in the strength tester, photos of each clamp with respect to the ruler were taken to mark the initial position (Figure 5.7 (a), (c)). After the break of the fibre, photos were taken again to mark the final position (Figure 5.7 (b), (d)). Photos were taken at the position where the top surface of the clamp looked flat, to minimise the possible parallax error. Then, the "before" and "after" photos were compared to find the overall stretch of the fibre due to the tensile stress. The red dotted lines show the points where the position measurements were taken. For example, in this case, the initial bottom clamp position was 39 ± 0.5 mm and that of the top clamp was 646 ± 0.5 mm, which were typical values for most fibres. The final position of the top clamp was kept constant, but the bottom clamp position varied depending on the breaking load. In Figure 5.7, the final position of the bottom clamp was 6 ± 0.5 mm and that of the top clamp was 646 ± 0.5 mm, which results in a stretch of 33 ± 0.5 mm.

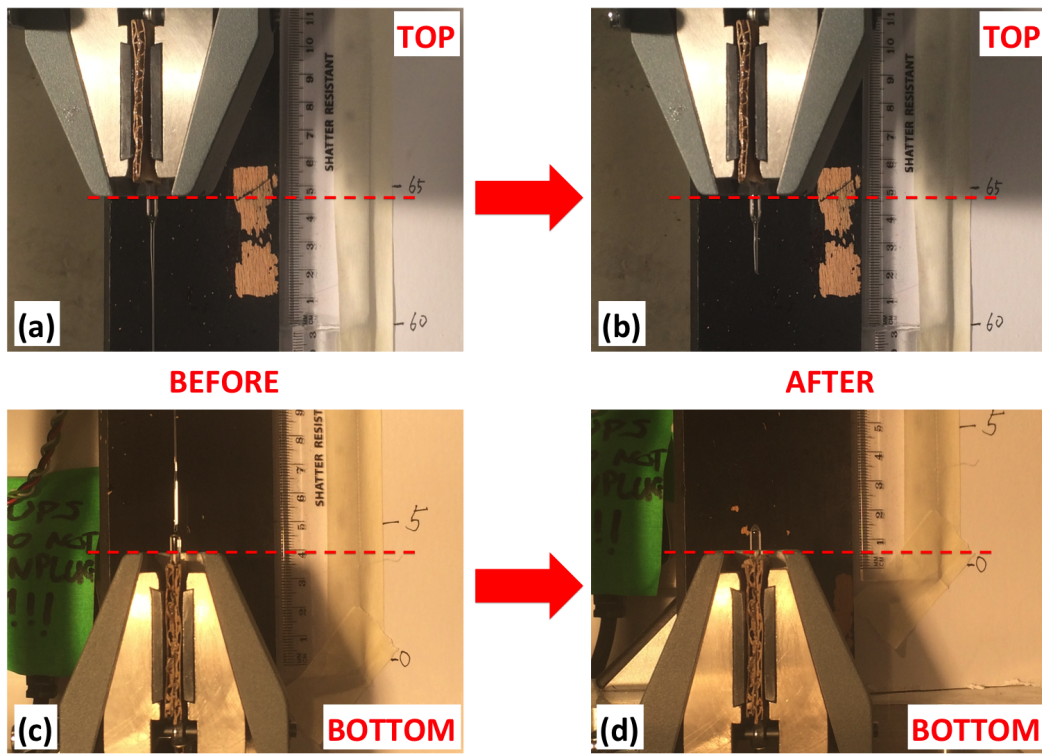


Figure 5.7: The position of the top clamp and the bottom clamp before and after the strength test: (a) Initial position of the top clamp (b) Final position of the top clamp (c) Initial position of the bottom clamp (d) Final position of the bottom clamp.

To measure the neck-based stretch, the same pictures and process were used, but the measurement points were different. Figure 5.8 shows one example of the neck starting point (red dotted line) for the initial length of the fibre on the video file.

Using this information, the breaking point position from the video file was adjusted. The stretch of the fused silica fibre was also calculated and confirmed by Equation 5.1:

$$Y = \frac{mg}{\pi r^2} \frac{L_0}{\Delta L} \quad (5.1)$$

where ΔL is the stretched length of the fibre, m is the breaking load, L_0 is the initial

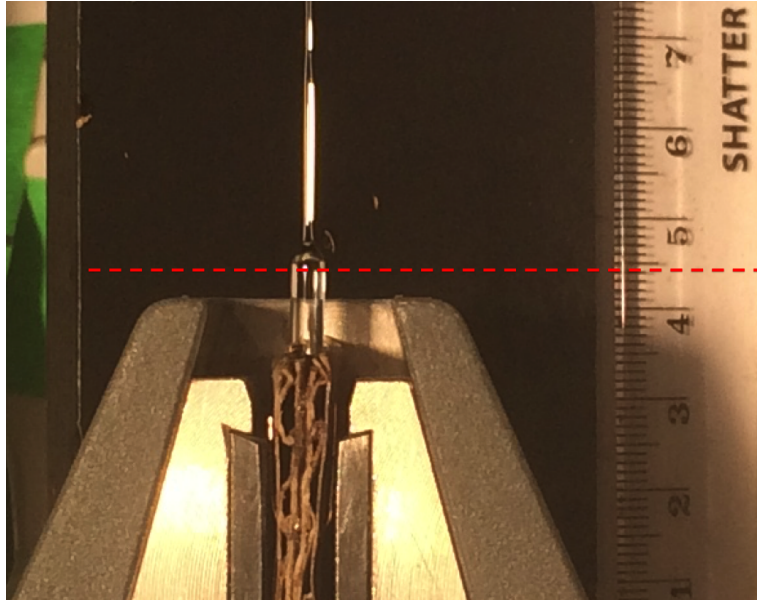


Figure 5.8: The neck starting point for the initial length measurement of the fibre on the video file.

length of the fibre, r is the average radius of the thin section, and Y is the Young's modulus. Since the stretch in length for both the neck and the stock section was negligible, compared to that of the thin section, only the thin section of the fibre was considered for this calculation. A typical stretch of a fibre with a breaking stress of 3 GPa was 20 mm and 33 mm for 4.6 GPa.

Finally, the minimum diameter point was adjusted in terms of the length of the fibre to be compared to that from the video file. Figure 5.9 shows the schematic diagram of the initial and the final fibre length change. Equation 5.2 shows the relation between the breaking position at the profile data (x_0) and that of the strength test video file (x).

$$x = x_0 \times \frac{(L_0 + \Delta L)}{L_0} \quad (5.2)$$

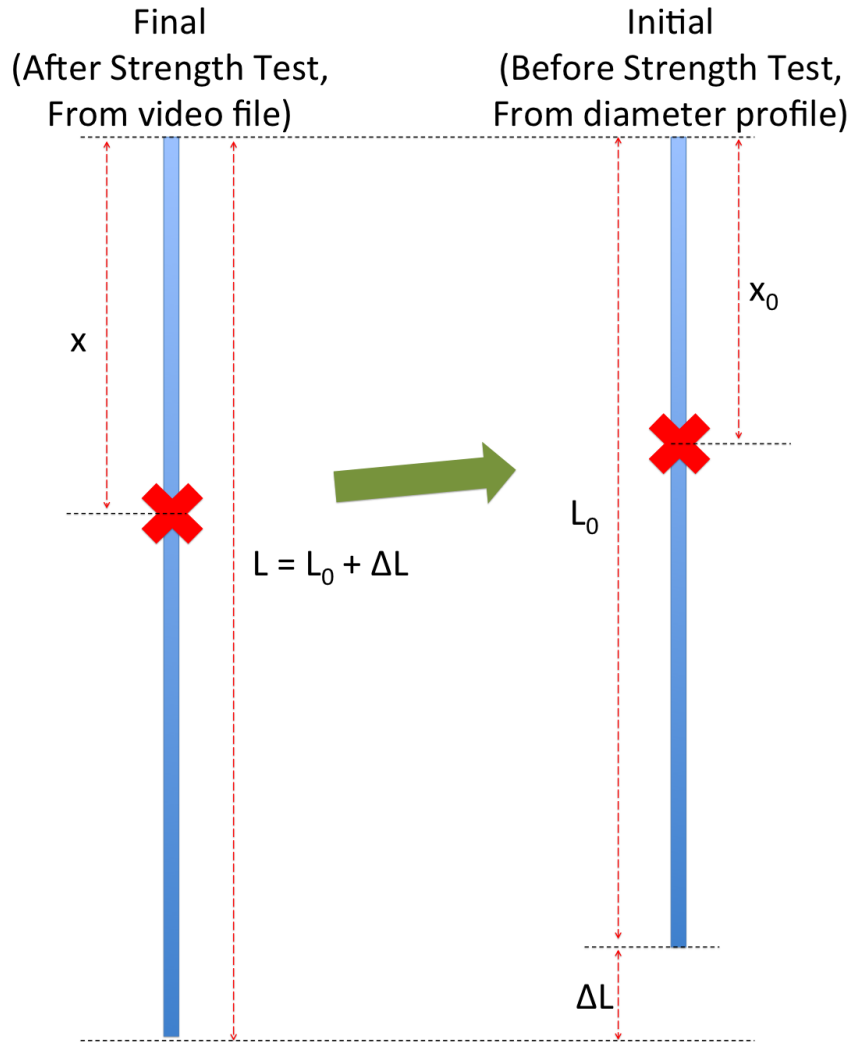


Figure 5.9: Schematic diagram of stretched fibre and how the breaking point position was adjusted with respect to the initial and final length of the fibre.

5.4 Results and Analysis

5.4.1 Breaking Stress Comparison

Figure 5.10 shows a comparison of strength test results between different polishing conditions: (1) current aLIGO conditions, without stabilisation, 900 s polish, (2) stabilised,

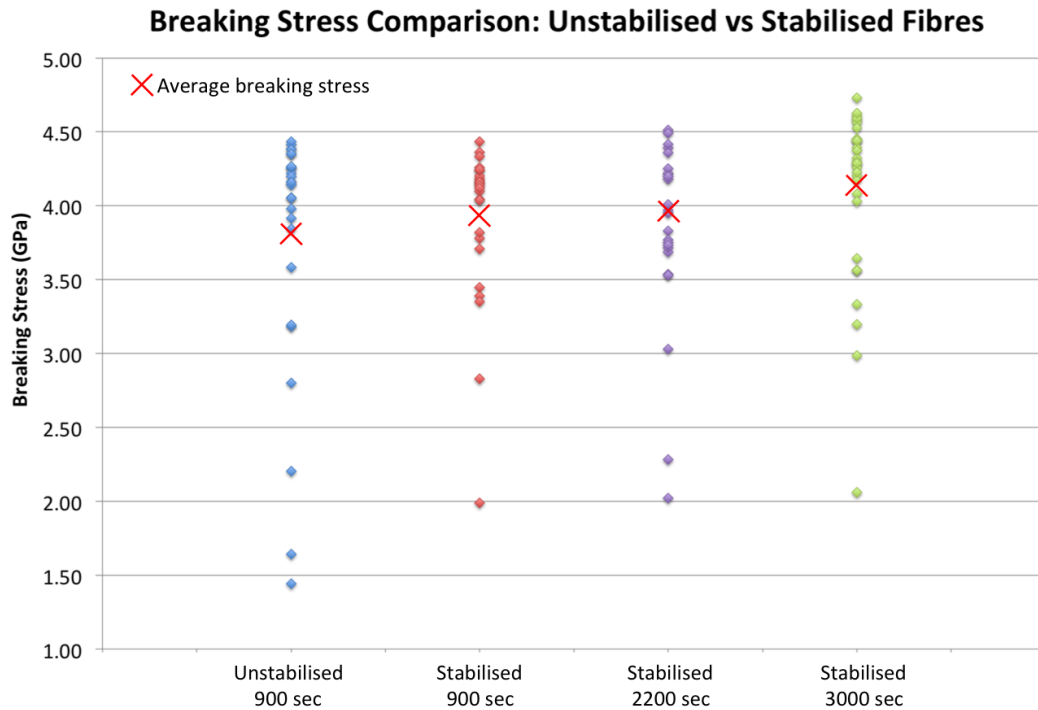


Figure 5.10: Strength test results comparison between different conditions: (1) current aLIGO condition, without stabilisation, 900 s polish, 25 fibres (2) stabilised, 900 s polish, 27 fibres (3) stabilised, 2200 s polish, 26 fibres (4) stabilised, 3000 s polish, 30 fibres. Stabilised fibres showed a 30% decrease in standard deviation of breaking stress compared to unstabilised fibres. Longer polish conditions were chosen according to Dr. Alastair Heptonstall's data [144].

900 s polish, (3) stabilised, 2200 s polish, (4) stabilised, 3000 s polish. (1) and (2) show the direct comparison between the unstabilised and stabilised conditions. (3) and (4) were compared to further investigate the effect of different polishing conditions, which were indicated to be better from Dr. Alastair Heptonstall's data [144].

The data shows that the stabilised pulls have a smaller spread in the breaking stress. This is also confirmed by the standard deviation comparisons: stabilised fibres show a 30% decrease in the standard deviation compared to that of unstabilised fibres. In

addition, the stabilisation system increased the minimum breaking stress of fibres. All stabilised fibres had breaking stresses greater than 2 GPa, which is comfortably above a potential suspension upgrade condition of 1.2 GPa. With a longer polish duration of 3000s, the average breaking stress of stabilised fibres showed a 9% increase, compared to that of unstabilised fibres. Using enhanced fibre fabrication techniques, not only is the maximum breaking stress increased, but also the percentage of ‘strong’ fibres, which have a breaking stress greater than 4 GPa, increased from 60% to 80%. This result indicates that the enhanced fibre fabrication technique via intensity stabilisation, can improve the reproducibility of fibre fabrication. Figure 5.11 shows a histogram version of Figure 5.10 to clearly show the distribution of the breaking stress.

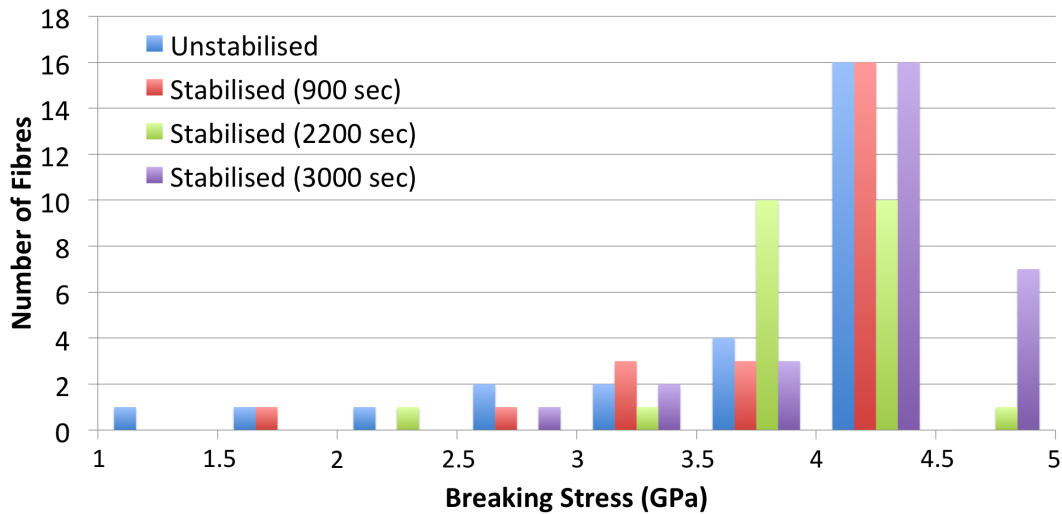


Figure 5.11: Strength test results comparison in histogram to show the breaking stress distribution.

This analysis provided information on the average breaking stress, the minimum and the maximum breaking stress, and the percentage of weak or strong fibres, depending on different fabrication technique / conditions. To further investigate each fibre’s result, the breaking point analysis was performed.

5.4.2 Breaking Point Analysis

The main purpose of the breaking point analysis is to check where each fibre broke and see if there is any tendency or significant reason for the breakage, such as an abrupt diameter decrease (a dip) on the fibre to trace back to a pixel intensity fluctuation.

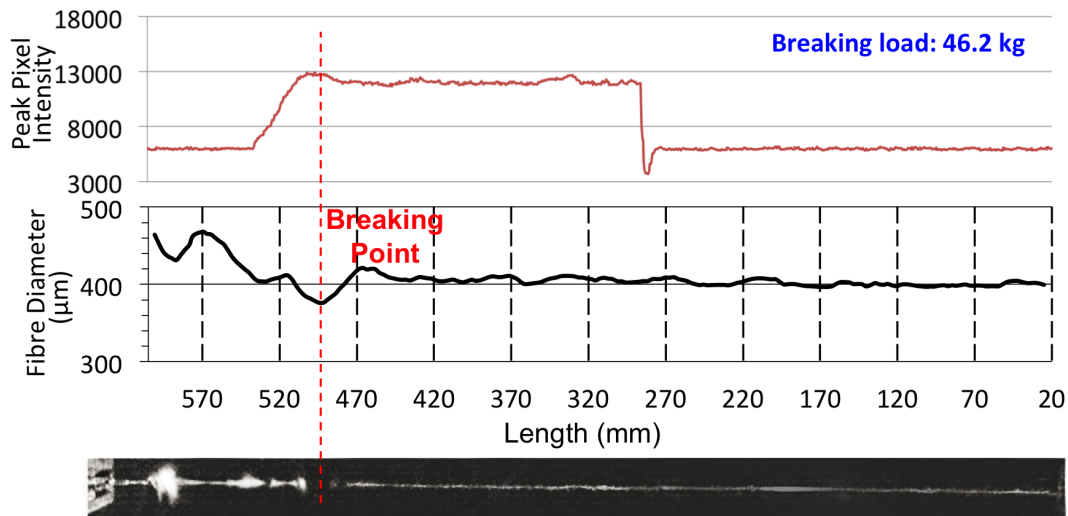


Figure 5.12: Breaking point analysis for a high step fluctuation fibre, as in Figure 4.28. The fibre's peak pixel intensity data and diameter profile data are overlaid on a screenshot of the breaking moment taken by the high speed camera. Due to a technical difficulty to show the thin fibre clearly from a screenshot, dotted lines were added to indicate the fibre. Red lines indicate the breaking point of the fibre.

Figures 5.12 to 5.14 show three breaking point analysis results of fibres with various pulling conditions: Figure 5.12 shows a deliberate high-step fluctuation of heating intensity applied during pulling process as in Figure 4.28, Figure 5.13 shows a deliberate low-step fluctuation applied during pulling process as in Figure 4.29, and Figure 5.14 shows a series of deliberate continuous-step fluctuations applied during pulling process as in Figure 4.30. Figures 5.15a and 5.15b show two breaking point analysis results of two typical fibres: Figure 5.15a shows a stabilised fibre with no fluctuation during the

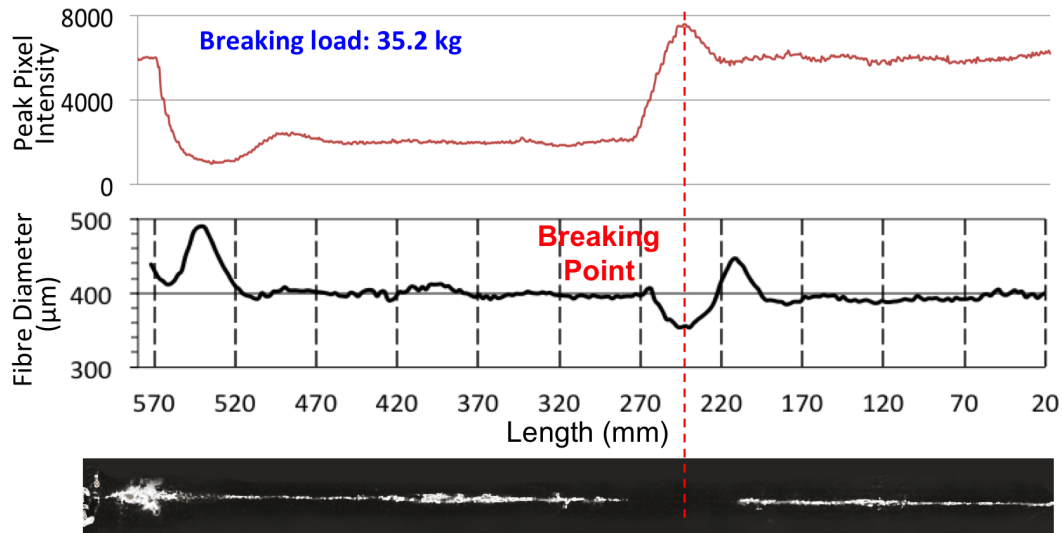


Figure 5.13: Breaking point analysis for a low step fluctuation fibre, as in Figure 4.29.

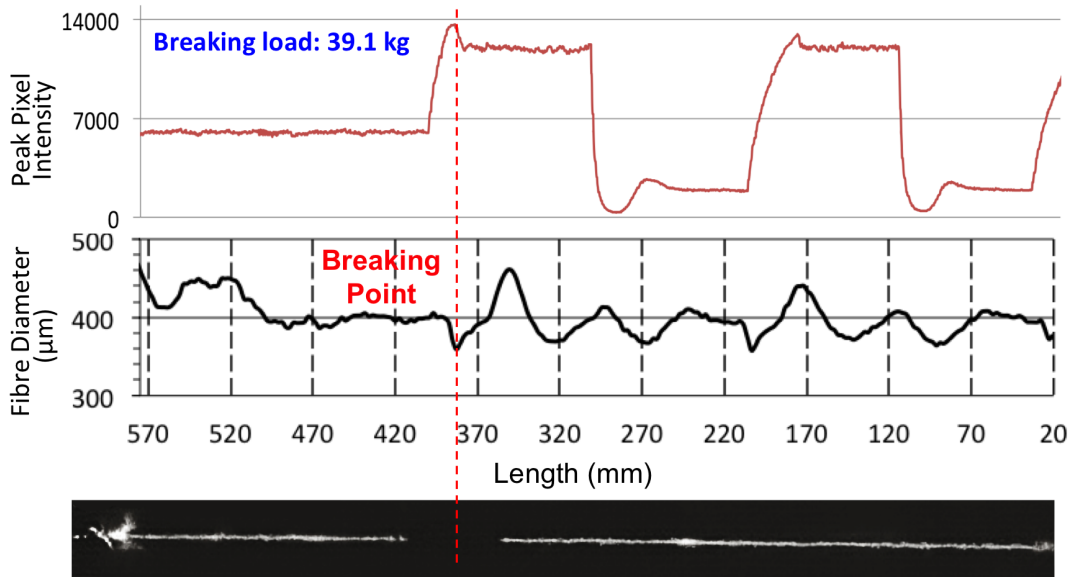


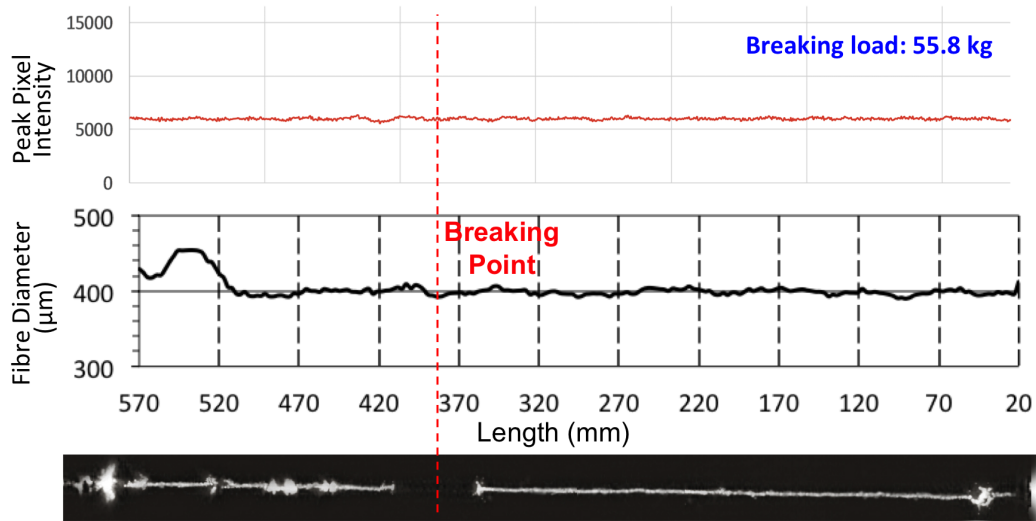
Figure 5.14: Breaking point analysis for a continuous fluctuation fibre, as in Figure 4.30.

pull process, while Figure 5.15b shows a stabilised fibre with no fluctuation during the pull process, but which was touched (by gloves, by other fibres, etc) while handling the fibre. Each figure has a diameter profile graph and a screenshot image of the high speed camera video file of the breaking moment. The red line indicates the initial breaking point.

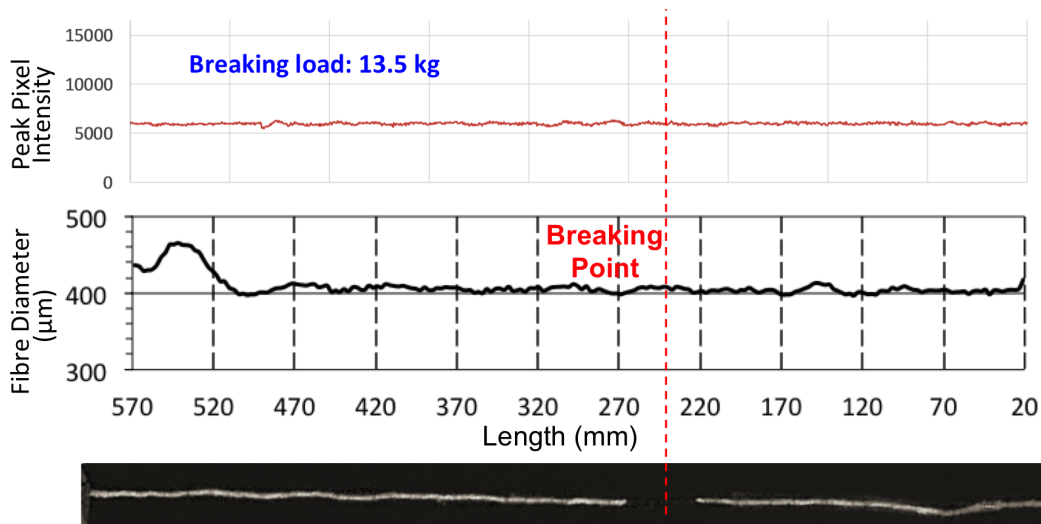
Taking account of the stretch of the fibre at the breaking moment, which is about 30 mm for fibres with breaking load above 40 kg, the breaking point and the fibre diameter data were aligned to see how well they match.

After adjusting the breaking point relative to the fibre diameter profile data, the correlation to the minimum diameter point was checked first, and if that did not match, the fibre profile was investigated further to see if there were any equivalent thin points around that breaking range. As shown in Figures 5.12 to 5.15a, most of the fibres' initial breaking point matched with the minimum diameter point of the profile data. This tendency was consistently observed in most other strong fibres. However, fibres with low breaking stress tend to break at their non-minimum diameter points (Figure 5.15b). For further analysis, these fibres will be referred to as "mismatched fibres." Table 5.1 shows the number of mismatched fibres compared to the total number of fibres, organised in terms of their breaking stress range.

One critical factor that can lower the fibre strength is whether the fibre was inadvertently touched or not in the process of fabrication and handling. As mentioned in Section 4.2, the strength of fused silica fibres highly depends on the surface quality, and any contact with the fibre can potentially weaken the fibre via surface damage. This makes handling fibres difficult, such that there are always some percentage of fibres that get touched by gloves or by another fibre during the transportation, bonding, and storing process. There were four transportation processes after the fabrication: from the pulling machine to the profile machine, from the profile machine to the bonding area, from the bonding area to the storage, from the storage to the strength tester.



(a) Breaking point analysis for one of the stable pulls



(b) Breaking point analysis for one of the touched fibres

Figure 5.15: Fibre peak pixel intensity data and diameter profile data overlaid on a screenshot of the breaking moment taken by the high speed camera. Due to the technical difficulty to show thin fibre clearly from a screenshot, dotted lines were added to indicate the fibre. Red lines indicate the breaking point of the fibre.

Breaking Stress Range (GPa)	Total Number of Fibres	Number of Mismatched Fibres	% of Mismatched Fibres (%)
0 ~ 0.49	4	4	100
0.5 ~ 0.99	6	6	100
1 ~ 1.49	2	2	100
1.5 ~ 1.99	2	2	100
2 ~ 2.49	5	5	100
2.5 ~ 2.99	6	3	50
3 ~ 3.49	5	1	20
3.5 ~ 3.99	12	1	8.3
4 ~ 4.49	44	3	6.8
4.5 ~ 4.99	16	1	6.2
TOTAL	102	28	N/A

Table 5.1: The number of mismatched fibres compared to the total number of fibres, as a function of the breaking stress range.

Fibres with the breaking stress in range of 0 to 2.49 GPa never broke at their minimum diameter points. Specifically, for the fibres with a breaking stress of less than 1 GPa, all fibres were known to have been touched by gloves in the process of handling. For fibres with a breaking stress range of 1 to 2.49 GPa, 6 out of 9 fibres were touched by another nearby fibre in the process of handling. As surface cracks and contamination play a critical role in weakening the strength of fused silica fibres, this result suggests that one of the mechanisms for weaker fibres, not just the ones below 1 GPa but even ones with a breaking stress less than 2.49 GPa, can be unintentional touching of fibres.

The percentage of mismatched fibres decreased as the breaking stress increased. In the range of 2.5 to 2.99 GPa, the mismatched fibre percentage decreased to 50%. These mismatched fibres could not be explained with the unintentional touching of fibres. One potential reason for these fibres is the angle misalignment of stock and / or neck section. Figure 5.16 shows an example of a misaligned fibre. This fibre has a misalignment problem in both stock region and fibre region. The stock region misalignment is due to the misaligned fibre clamps of the pulling machine. This misalignment happens during the polishing process. The misalignment in the fibre region is due to the laser beam

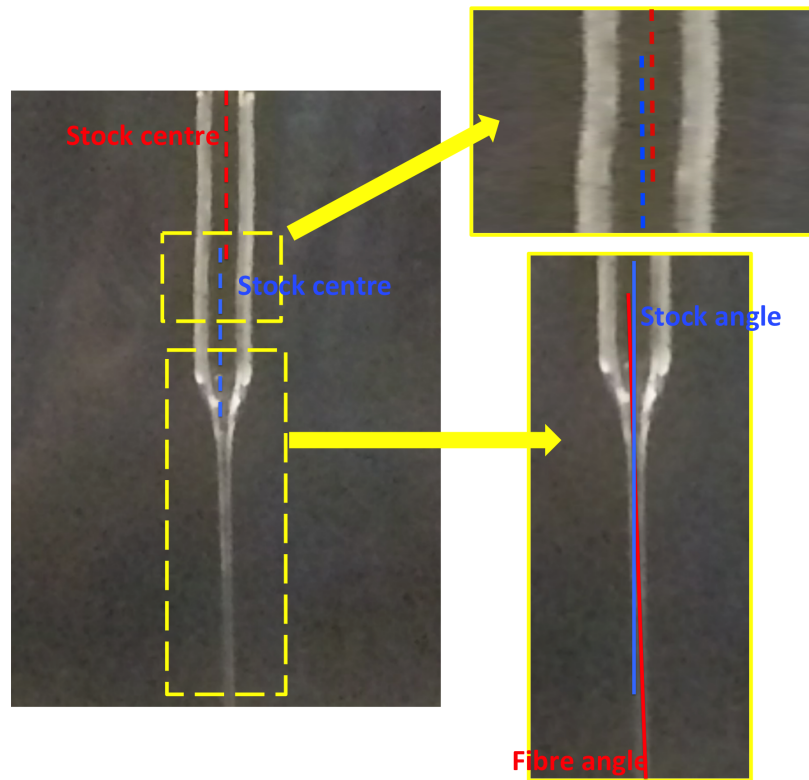


Figure 5.16: Example of a misaligned fibre: both the stock region and the fibre region have a misalignment. The stock region misalignment is due to the misaligned fibre clamps of the pulling machine. This misalignment happens during the polishing process. The misalignment in the fibre region is due to the laser beam misalignment.

misalignment. This can increase the stress in the neck region which could reduce the strength of the fibre. Since there has been circumstantial evidence that misaligned fibres demonstrated lower breaking stress [184], this could be a reason for the mismatched fibres in this range. A possible solution to filter these fibres is to take a photo of the stock region and the fibre region before the strength test.

For the ‘strong’ fibres (breaking stress range above 4 GPa), the percentage of mismatched fibres decreased even more. For the most common breaking stress range, 4 to 4.49 GPa,

6.8% of the fibres were mismatched fibres. For the highest breaking stress range, 4.5 to 4.99 GPa, only 6.2% of fibres did not break at their minimum diameter point. As 93.3% of strong fibres broke at their minimum diameter points, it is important to minimise the possibility of forming dips in the fibre profile, which can be formed by unexpected fluctuations in the heating intensity. This result suggests that we can distinguish fibres with potential lower breaking stress just by investigating the intensity stability during the pull, before we even test the strength or profile the diameter of the fibres. This suggests the more stable the pull the less likely there will be variations in the fibre strength.

In addition to the current aLIGO fibre production and testing procedures [185], a close investigation on the peak pixel intensity data could be performed before profiling the fibre. The stability of the heating intensity during the pull can become a criterion to decide a future fibre test procedure. If there is any significant fluctuation during the pulling process, that fibre can be marked for extra attention; to either not use at all, or go through more strict tests. If it is required to use such a fibre, suggested tests would be strength tests with a higher tensile stress for longer duration, and a more detailed examination of the fibre profile.

5.5 Conclusion

As one of the ultimate goals of enhanced fibre fabrication technology is to improve the statistical strength of fused silica fibres, strength tests were performed on a range of fibres, some with known imperfections. Using a Phantom V710 high speed camera, each breaking moment was recorded as a video file to determine the location of the initial break in the fibre. Two main analyses were performed: a breaking stress analysis and a breaking point analysis. The thinnest point of each fibre was determined by the fibre diameter profile data, and the breaking point from the video file was adjusted to take into account the stretch of the fibre.

From the breaking stress analysis, it was shown that the stabilisation system could decrease the spread of the breaking stress: the standard deviation was decreased by 30% compared to the unstabilised fibres and the percentage of strong fibres (breaking stress above 4 GPa) increased from 60% to 80%. The maximum breaking stress increased from 4.45 GPa to 4.7 GPa and the average breaking stress also increased by 9% for stabilised fibres. In addition, the minimum breaking stress of stabilised fibres showed an improvement: for all different polishing conditions, the minimum breaking stress was above 2 GPa, while that of unstabilised fibres was below 1.5 GPa.

For the breaking point analysis, the breaking point from the video file was compared to the diameter profile data and the peak pixel intensity data. It was shown that the fluctuations of the heating intensity during the pull was translated to the fibre diameter, resulting in the thinnest point of the fibre which ended up becoming the breaking point observed in the video file. However, there were some “mismatched” fibres, which did not break at their thinnest points. Since 100% of mismatched fibres with breaking stress less than 2.49 GPa were touched by gloves or other fibres, the most probable breaking mechanism is the surface contamination or damage, most likely caused by touching. One potential reason for the mismatched fibres that were not touched is the angle misalignment of fibres in the stock region and / or the fibre region. The percentage of mismatched fibres decreases quickly as the breaking stress increases. For strong fibres with a breaking stress above 3.5 GPa, 94% of the fibres broke at their thinnest points.

This result indicates that unless the fibre had external contact during the handling process, we can predict potential weak fibres by observing the peak pixel intensity data during the pull, even before profiling the fibres. This could be used as a new qualifying test for future LIGO fibre production. After fabricating the fibre, the peak pixel intensity can be investigated to check if there is any significant fluctuation during the pull. Through this checking process, potential weak fibres can be identified easily.

For fibres fabricated without any significant fluctuations during the pulling process, there are several potential factors that could have caused the imperfection (thus, reduced strength) on the fibre. For instance, a small variation in the motor speed could affect the fibre. This error was not observed so far, but implementing an external monitoring system could provide a double-check point for the motor speed variation. Furthermore, some heating intensity variation could have happened on the other side of the stock, invisible to the viewing camera, since the peak pixel intensity was observed only from one side. As an upgrade of the current stabilisation system, another camera could be used to monitor the opposite side of the heated stock to minimise possible heating intensity variations from both directions.

Now that we have confirmed the positive impact of the stabilisation system for the fibre fabrication process, stress corrosion experiments were performed to investigate the breaking time of these enhanced fibres. This experiment will be discussed in the next chapter.

Chapter 6

Stress Corrosion Experiment

6.1 Introduction

From the Matlab modeling results described in Chapter 3, the detector's sensitivity could be improved with heavier test masses, higher stress in the fibres, and a longer final stage. To achieve these conditions, it is important to test the durability of fibres with higher stress. In Chapter 5, it was shown that enhanced fibre fabrication techniques could improve the statistical strength and geometric reproducibility of fused silica fibres. As a confirmation for the reliability of these novel techniques, it is necessary to fabricate fibres for higher tensile stress and perform an experiment known as "stress corrosion" which comprise hanging a mass under a fibre and monitoring the time it takes for the fibre to break.

In this chapter, the design of the stress corrosion tests will be discussed. Depending on the tensile stress condition, some fibres were tested in-air and some were put under vacuum, as the aLIGO operating condition is under vacuum and the initial installation is carried out in air. The results were then compared to that of similar experiments performed in LIGO Hanford Laboratory, USA, by Karl Toland [186]. Since Proctor *et*

al. also performed a similar experiment in 1967 [175], the results from the Glasgow and Hanford stress corrosion experiments were compared to that of Proctor's.

6.2 Motivations for the Experimental Conditions

6.2.1 In-air and Vacuum

One of the main failure mechanisms of the fused silica fibres is the water molecules. Michalske and Freiman suggested that the water molecules (H_2O) can attack the strains bonds to form two saline groups [187]:



which can explain the crack growth mechanism in fused silica. Duncan *et al.* also showed that the breaking time became shorter as the humidity increased [188]. Therefore, it is obvious that the fibre strength would be better under vacuum, compared to in-air condition. However, there are two main reasons to choose both in-air and vacuum for the stress corrosion experiment.

Firstly, for the aLIGO suspension installation, it takes about two months for fibres hung under the stress to go into vacuum. Since the time that a fibre is under the in-air condition is not negligible, it is important to test the hang time for this configuration. Furthermore, since the operating condition for the detectors is under vacuum, it is necessary to check the strength of the fibres under vacuum too. Therefore, it is appropriate to perform the corrosion experiment under both conditions to confirm the safety factor for the upgrade.

Secondly, Proctor *et al.* performed a similar experiment for both in-air and vacuum in 1967 [175], which can provide a good comparison. As Proctor's experiment was performed 50 years ago, it is desirable to run the experiment under the same condition with modern techniques and modern fused silica material to compare the results. Figure 6.1 shows the extracted data from his graph, using the GraphClick software [189], which shows the

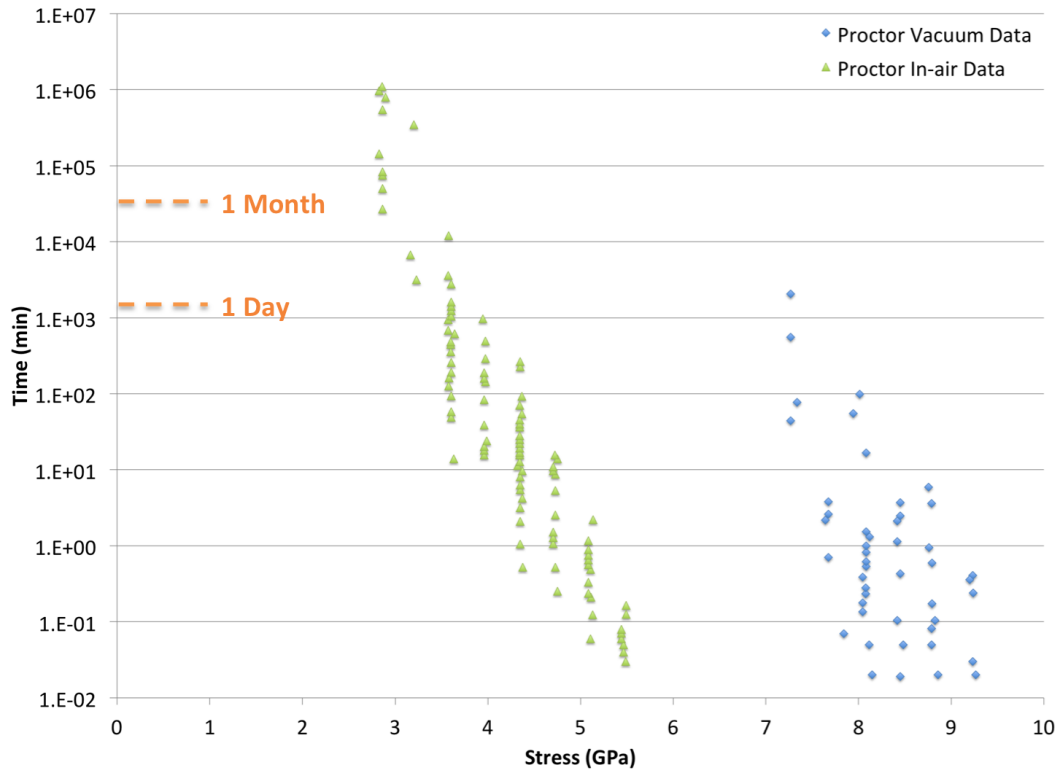


Figure 6.1: Hang time of fused silica fibres in air and in vacuum depending on the applied tensile stress [175].

hang time of fused silica fibres in air and in vacuum, depending on the applied tensile stress. After gathering the data from the experiment, the results were compared to Proctor's data in Figure 6.1.

6.2.2 Range of Stress Tested

The biggest challenge in the stress corrosion experiment for fused silica fibres is the time it takes for the fibres to break. Fibres at high stress break too fast to test the vacuum condition; while low stress fibres take too long to break, and experiments take several years. As mentioned in Chapter 3, one potential stress condition considered for the A+ upgrade scenario is 1.2 GPa. However, it is impossible to run the experiment until fibres

break under this stress, as it can take up to 752 years (in-air condition, calculated using Proctor's in-air data) to thousands of years (vacuum condition, approximated using Proctor's vacuum data). Therefore, the experiment was performed for a subset of fibres that can be managed within the available time scale, and some overlapping subsets with similar conditions such as Proctor's to confirm the repeatability.

Other than Proctor's experiment, another similar experiment considered was in-air stress corrosion tests performed in LIGO Hanford by Karl Toland. Figure 6.2 shows the results of this experiment. As the main target of this experiment was high stress fibres, all tests were performed in-air. The fit line was drawn to show the expected hang time for the lower stress range.

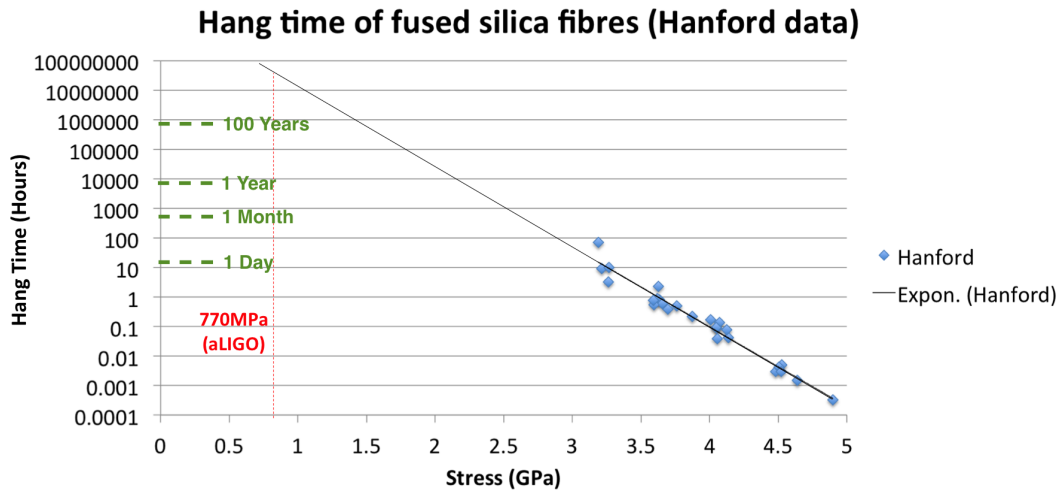


Figure 6.2: Stress corrosion experiment for different tensile stress performed in LIGO Hanford by Karl Toland [190].

For the experiment performed in Glasgow, fibres with relatively lower stress were also considered. To confirm the repeatability of the experiment, an overlapping range of fibres with Hanford experiment was desirable, which decided the maximum stress condition to be tested (4 GPa). The minimum stress condition was decided solely by considering the expected hang time: 2.5 GPa with an expected hang time in-air of 22 days.

The in-air experiment could have an overlapping range with both Proctor's and the Hanford experiment (3 to 4 GPa). However, for the vacuum condition, it was impossible to reproduce Proctor's range (7 GPa - 9 GPa) since it was too high to be tested in Glasgow's vacuum tank which takes a full day to pump down, and the Hanford experiment only covered the in-air condition. Therefore, the maximum stress condition under vacuum was decided by considering the estimated hang time in-air: 2.78 GPa, with the expected hang time in-air of 3 days. Although the expected hang time in-air is short, that of vacuum condition can be 10 to 100 times longer according to Proctor.⁸ Therefore, the lower range of the vacuum condition was chosen to get some overlap with the in-air condition to confirm the impact of vacuum. The minimum stress condition decided was 2.3 GPa which has an expected hang time of a hundred to a thousand years according to Proctor [175]. The main purpose of testing this range is to get a possible upper limit for the vacuum data fit line.

6.3 High Stress Fibre Fabrication

Table 6.1 shows the calculation of fibre diameters for different stress conditions. A 10 kg mass was chosen because it is heavy enough to comfortably pull the thin section of the highest tensile stress condition, and, at the same time, it is light enough to transport without a crane. The two diameters presented are the thermoelastic nulling diameter (explained in Section 2.4.1) and the thin section diameter, which decides the tensile stress applied on the fibre. Among these conditions, 5 conditions (2, 2.5, 3, 3.5, 4 GPa) were chosen for the high stress fibre development, as that range covers some lower breaking stress fibres up to higher ones that overlap with the Hanford experiment (Section 6.2.2). A new set of voltage profiles for the laser pulling process were developed to produce those fibres. The upper and lower motor speeds were adjusted to produce fibres with a

⁸As mentioned in Section 6.2.1, the most well-known theory for this strength difference is the humidity in the atmosphere that can cause failure in fused silica fibres.

diameter that gave an appropriate stress in the thin section of the fibre.

Mass (kg)	Stress (GPa)	Null diameter (μm)	Thin diameter (μm)
10	1	822.3	353.4
	1.54		284.8
	2		249.9
	2.5		223.5
	3		204.0
	3.5		188.9
	4		176.7

Table 6.1: Fibre diameter calculations for different stress conditions.

In this experiment, due to breakdown of the 120 W laser used previously, a new 400 W laser was used to produce the fibres. The same stabilisation system was implemented for the fabrication processes. The only change required was to modify the PID gain parameters for the new alignment and laser response. Figure 6.3 shows one of the stabilised pulls using the new laser, which confirms that the stabilisation system is totally transferable for different lasers. The average peak pixel intensity was 5997 (percent error of 0.05%) and the standard deviation was 93, which is very similar to the stabilised pull results presented in Chapter 4.

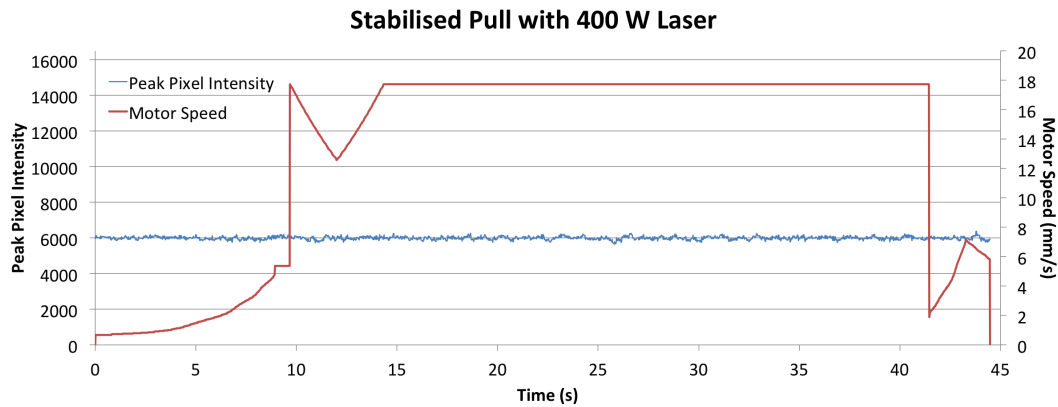


Figure 6.3: A typical stabilised pull using the new 400 W laser.

To fabricate fibres for this experiment, each end of a stock piece was attached to a “fuse end” aluminum handling piece [161] by “Araldite 2012” dual cartridge epoxy adhesive

[191]. When the adhesive was applied, bonded stock sections were set on a L-shaped cartridge to make sure that both fuse ends were aligned axially in respect to each other. Figure 6.4 shows one of the stock pieces bonded to fuse ends using epoxy adhesive and put on the L-shaped cartridge. After waiting the required 24 hours, the stock surface was cleaned with methanol to remove any light surface dust particles before polishing and pulling a fibre, as this is the established aLIGO production cleaning method [185].

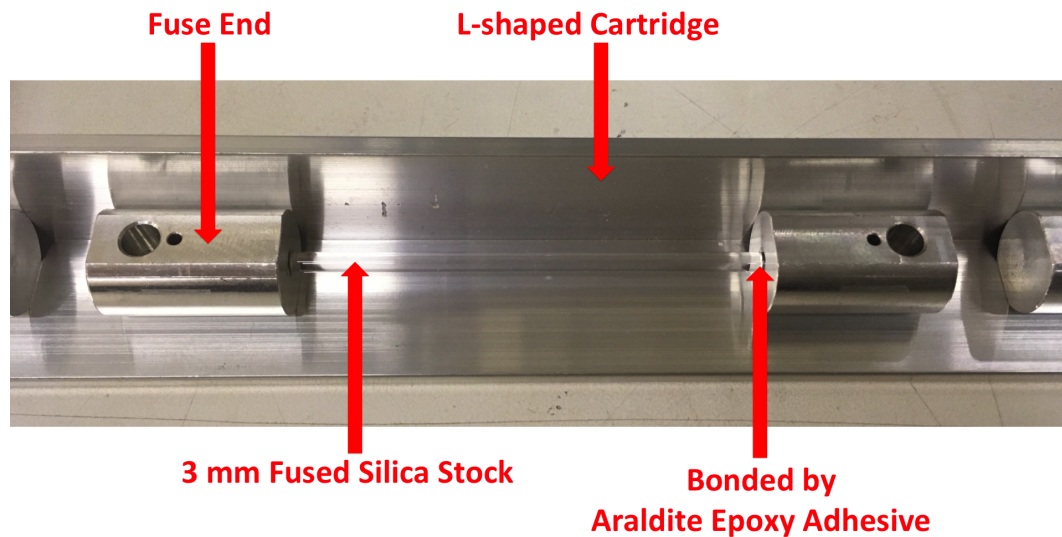


Figure 6.4: One of the stocks bonded to fuse ends using epoxy adhesive and placed on the L-shaped cartridge.

Since there has been circumstantial evidence that misaligned fibres demonstrated lower breaking stress [184], both the top and the bottom stages were carefully aligned to avoid any additional stress caused by misaligned stock when it was set up for pulling. Figure 6.5 shows an example of a fibre pulled from a misaligned stock piece. The centre of the stock and the neck section are not concentric, with a difference of 0.43 mm, which may weaken the fibre's strength [184]. Therefore, for each pull, two cameras with ND filters monitored the shape of the heating area to make sure the beam alignment was consistent. When the heated stock showed any evidence of misalignment, the laser was turned off and both clamps were aligned again until the stock looked perfectly straight

from both camera angles.

In addition, the laser feed voltage was checked to confirm the alignment. When the laser beam is misaligned, the stock is heated nonuniformly with one side of the stock intensely heated (thus brighter) and the other side relatively cool (thus dimmer). If the monitoring camera sees the intensely heated side of the stock, the brighter region, the feedback system will think that the stock is heated too much and will decrease the laser feed voltage. Likewise, if the camera sees the relatively cool side of the stock, the dimmer region, the feedback system will increase the laser feed voltage to meet the setpoint. Therefore, significantly higher or lower laser feed voltage compared to typical ones means that the laser beam is skewed towards one side so that the laser power requires significant change in the laser feed voltage to achieve the same peak pixel intensity setpoint.

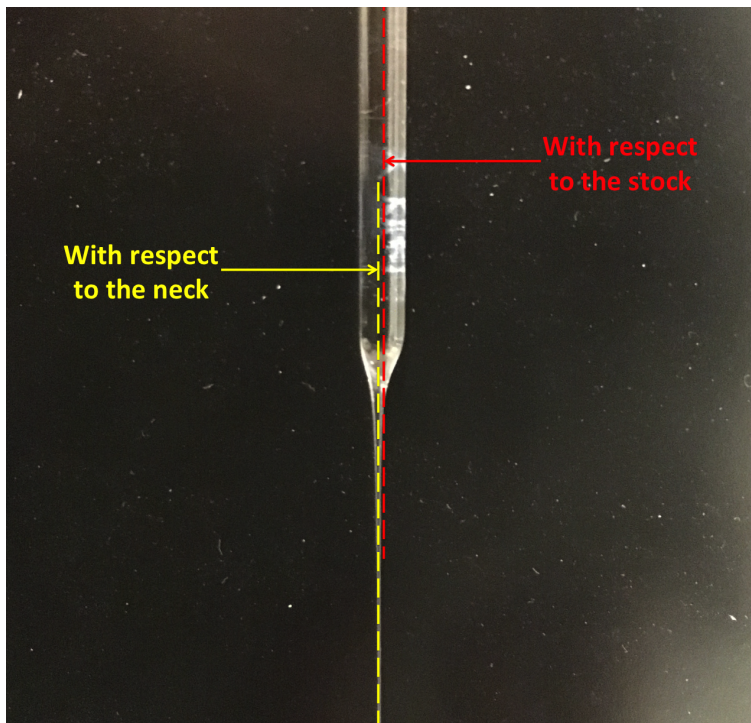


Figure 6.5: One example of a misaligned fibre.

After the fibre fabrication, all fibres were profiled to investigate the minimum diameter

for the breaking stress calculation. Since more than 94% of strong fibres (breaking stress above 3.5 GPa) broke at their thinnest points, it was assumed that the minimum diameter point is the breaking point for fibres in this experiment (Section 5.4.2). To transport the fibre safely from the pulling machine to the profiler, the aLIGO “cartridge” which consists of two L-section posts attached to both the top and the bottom clamps after fabrication, was used so that the fibre could be transported within both stages without getting touched. Figure 6.6 shows this system: fuse ends hold the end of the stock as a connector between the fused silica stock and the top clamp of the pulling machine, and two L-section posts hold the top and the bottom clamp to keep the fibre straight and untouched. After profiling, the posts were removed to store the fibre [161, 185].



Figure 6.6: Two long L-section posts were attached to both the top and the bottom clamps after fabrication to minimise the risk of fibres getting touched during handling process.

6.4 Experimental Design

For this experiment, a 10 kg steel mass was suspended with fused silica fibres with different diameters to give tensile stresses in the range of 2 GPa to 4 GPa. The “hang time”, the time taken for each fibre to break, was observed. Since the expected hang time of high stress fibres (above 2.8 GPa) was too short to put in a vacuum tank, those fibres were tested in-air. For example, the expected hang time for a fibre with 2.9 GPa tensile stress is 1.6 days in air, and the time required to pump down the vacuum tank is about one day. Therefore, for these fibres, applying a vacuum condition is not practical. Other fibres with relatively lower stress (below 2.8 GPa) were tested in a vacuum tank with pressure of 10^{-5} mbar.

In previous stress corrosion experiments, the common method to hang the mass was to slowly lower the mass rest plate until the mass was suspended. However, it was challenging to do so in a vacuum tank containing many fibres in close proximity. Therefore, the fibre was lifted up to hang the mass using a shaved screw and a height control nut.

Figure 6.7 shows the detailed parts of setup. The 10 kg steel mass was hung under each fused silica fibre. Each mass was connected to the fibre using fuse ends (Section 6.3), and a shaved screw with two bolts was used to lift up the mass. Two aluminum channels were set up around the fibre and the mass to isolate the setups, as uncontained shattered fused silica pieces and powder would pose a risk of causing failures to other nearby fibres. Two microswitches were setup in series, operating normally closed. When the fibre broke, the mass fell to the rest plate where two microswitches were attached, to press the switches. If either of the microswitches was pressed, a signal was sent to record the breaking time.

A Raspberry Pi 3 running a Python script was used to monitor the breaking time of each setup. Figure 6.8 shows the circuit of this Raspberry Pi 3 system. The starting time and the breaking time were recorded to calculate the total hang time. The link to

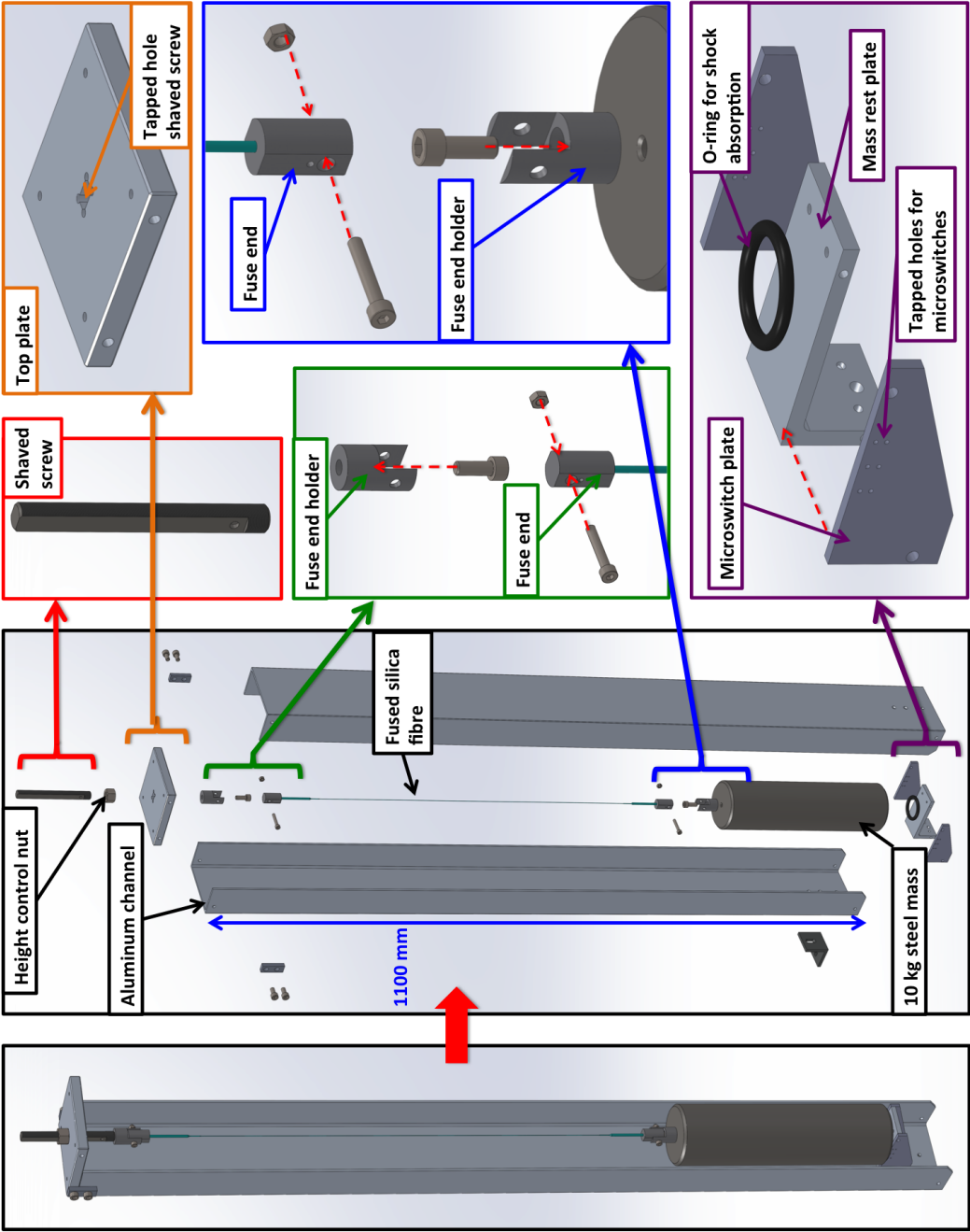


Figure 6.7: Experimental set up to measure breaking time of fused silica fibres as a function of tensile stress.

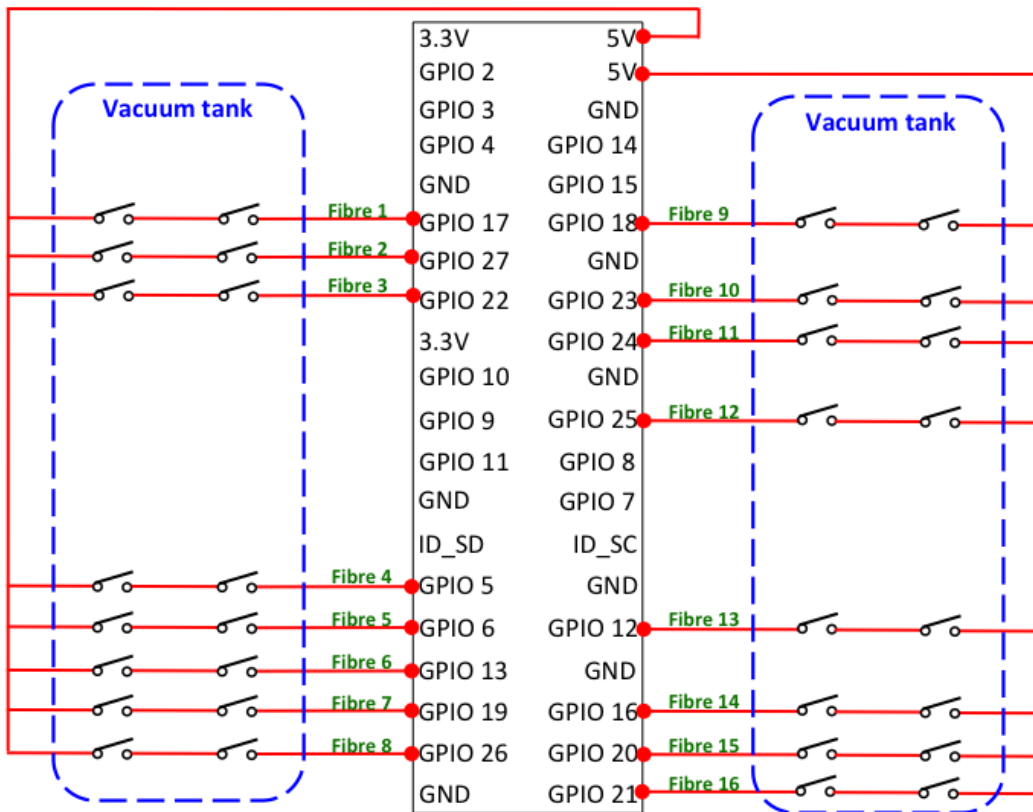


Figure 6.8: Raspberry Pi 3 circuit for the stress corrosion experiment. Microswitches are operating normally closed, so that it would open when a fibre breaks.

the Python code used for this setup is presented in Appendix D.

Since building each setup takes about 30 minutes, it would have been ideal if fibres could be hung after building all 16 setups. However, if any fibre located towards the centre of the vacuum chamber breaks, it would be very challenging to replace that fibre without damaging or knocking fibres nearby. Therefore, each fibre was hung right after the setup was built, and the start time was recorded separately for each setup. Each microswitch system connected to the Raspberry Pi program was tested before hanging the fibre to make sure that there won't be any technical failure in triggering the switches. After hanging each fibre, the program was run to check both microswitches were released.

When the last fibre was hung, the final run of the program was started, and the start time of each fibre, which was separately recorded earlier, was added on to this final start time later.

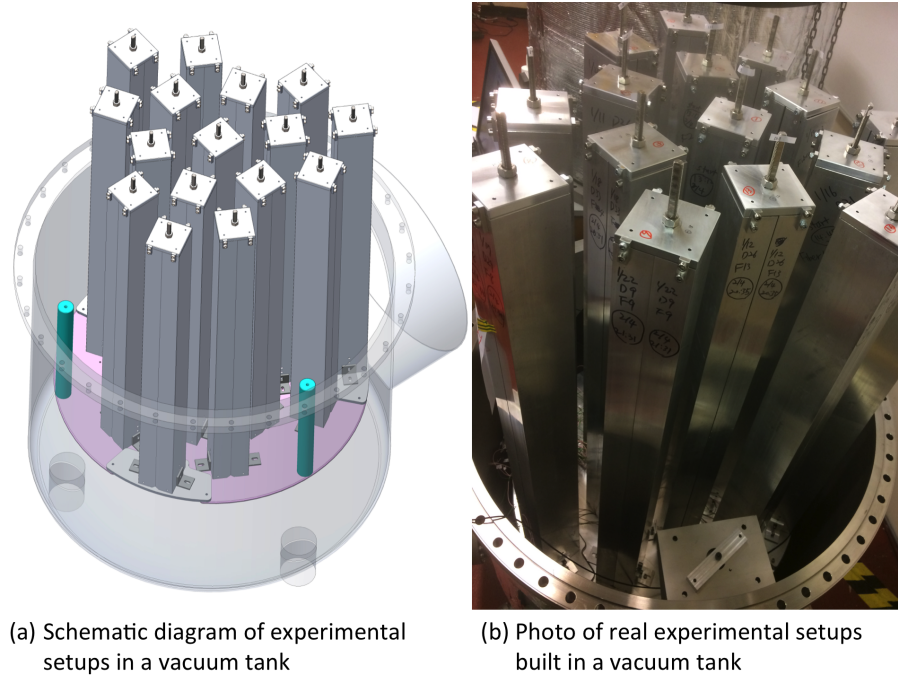


Figure 6.9: Schematic diagram of experimental setup in the vacuum tank to measure breaking time of fused silica fibres.

Figure 6.9 (a) shows the schematic diagram of the general arrangement of the experimental setup in the vacuum tank to measure breaking time of fused silica fibres, and (b) shows the real experimental setup built in the tank.

Figure 6.10 shows the schematic diagram of the arrangement of 16 stress corrosion test setups in the vacuum tank. Each setup was built from inside (low tensile stress fibres) to outwards (high tensile stress fibres) to minimise risk of failure due to external impact. Red arrows indicate the order of installation.

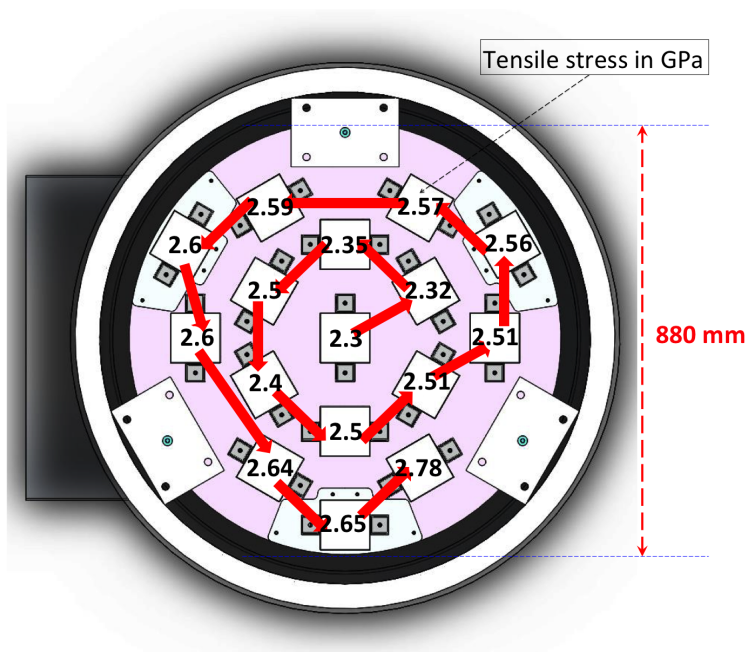


Figure 6.10: Schematic diagram of the arrangement of 16 stress corrosion test setups in a vacuum tank. Red arrows indicate the order of installation.

6.5 Results

6.5.1 In-air Condition

As the expected hang time for high stress fibres is too short to be put under vacuum, stress corrosion tests for high stress fibres were performed in-air. Among fabricated fibres, those with tensile stress in the range of 2.77 to 4.2 GPa were tested in-air so that part of the range overlaps with the fibres tested in LIGO Hanford by Karl Toland, to see if the result shows any difference. The in-air condition is also consistent with the Hanford experiment.

In addition to the range mentioned above, two extra fibres with tensile stress of 2.53 GPa and 2.6 GPa were tested in air. Although they had a hang time which was expected to be long, they were hung as a first shakedown test run for a long-term monitoring experiment to be performed in a vacuum tank. Furthermore, these two fibres provide some overlapping range with the vacuum condition fibres to confirm the impact of applying a vacuum condition.

Figure 6.11 shows results of stress corrosion experiment performed in LIGO Hanford and Glasgow. The two experiments were performed independently under the same conditions. However, the two datasets showed a very similar trend with an offset. To investigate the reason for this offset, the profile machines of each laboratory were checked. The same fibre was carefully shipped between sites and was profiled multiple times using both profile machines.

The general difference between the profile machine in Glasgow and that of Hanford was that the Hanford results showed a thinner diameter than the Glasgow results. This tendency can explain the offset introduced in Figure 6.11. Figure 6.12 shows the thin section comparison between the profile data from two laboratory. (a) shows the original data comparison and (b) shows the data averaged over 15 points to eliminate the noise

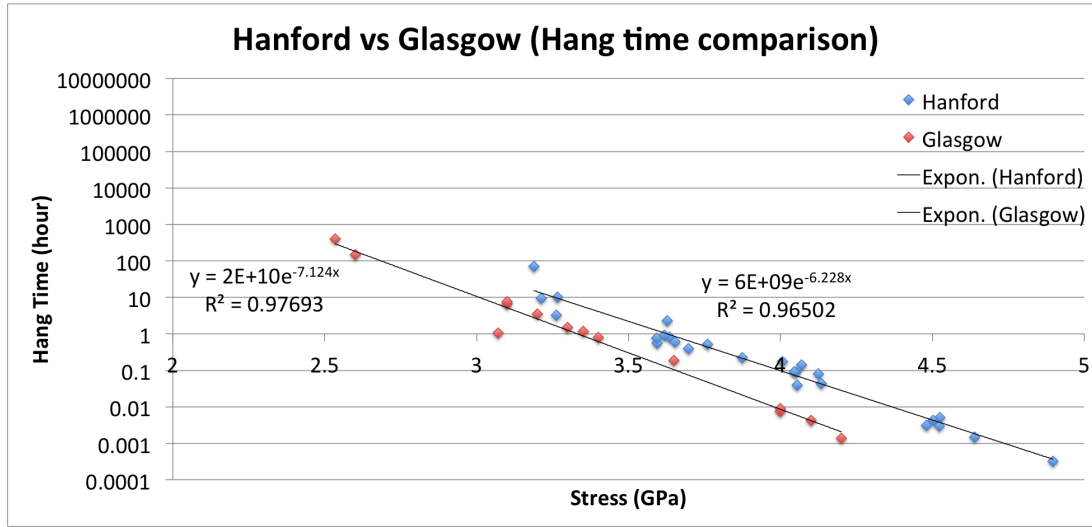
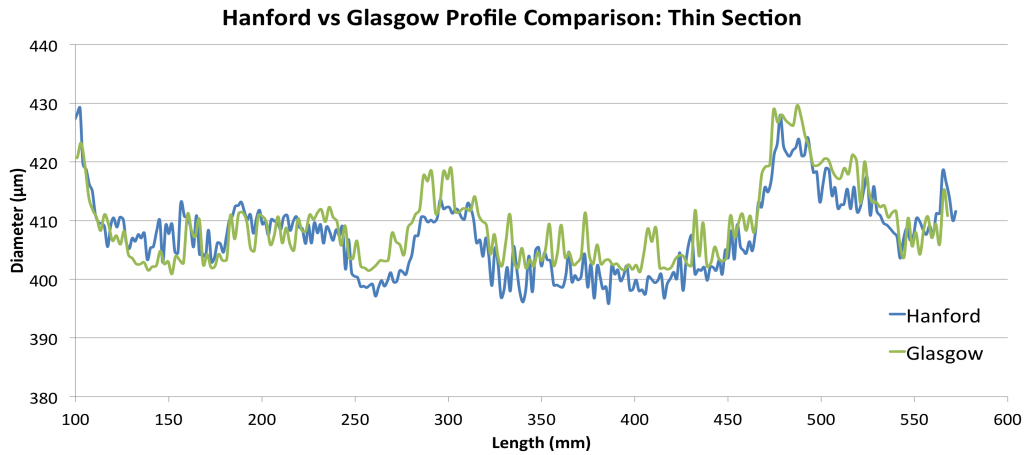


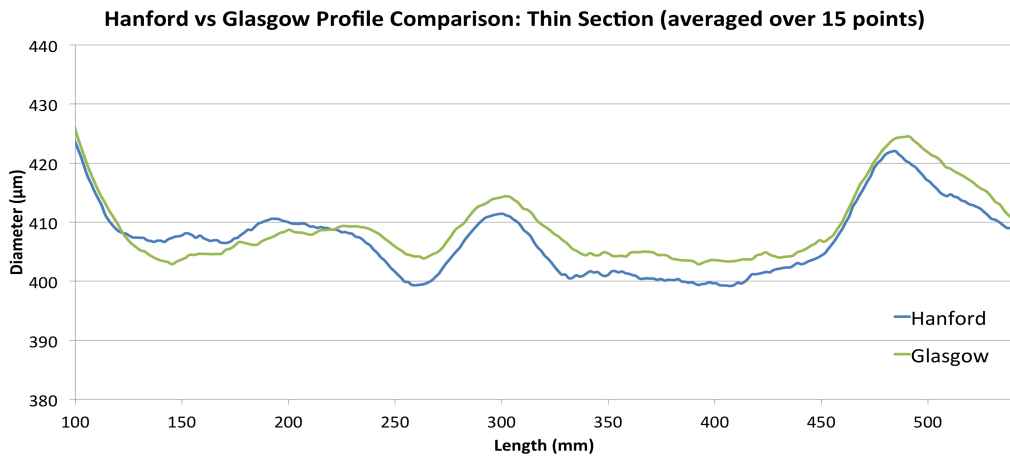
Figure 6.11: Results of stress corrosion experiments performed in LIGO Hanford and Glasgow.

from the profile. The minimum diameter measured in Glasgow was $400.9 \mu\text{m}$ while that of Hanford was $395.9 \mu\text{m}$, showing a difference of $5 \mu\text{m}$ and percentage difference of 1.25%. In the length range between 110 to 210 mm, the Hanford profile data shows a larger diameter result unlike the rest of the profile data. The potential reason for this difference is the varying focus condition of each profiler when measuring that region, as the focus of profile machines is manually controlled by eye.

To confirm which profile result is closer to the real diameter, the profile data in the stock region was compared, as the stock diameter has a manufacturer's dimension specification to check. Figure 6.13 shows the comparison of the stock region. The average stock diameter measured in Glasgow was $2993.1 \mu\text{m}$ while that of Hanford was $2947.6 \mu\text{m}$, showing 1.51% of percentage difference. Since "Suprasil 2 Grade A" stock is manufactured to have a diameter of $3 \pm 0.03 \text{ mm}$ [173], the profile result from Glasgow corresponds to the manufacturer's tolerance while the Hanford data exceeds that. The difference between the manufacturer specification and the Glasgow's measured average stock diameter was $6.9 \mu\text{m}$ which is within the specification error of $30 \mu\text{m}$, while that of



(a) Diameter profile comparison between Hanford and Glasgow data (original data)



(b) Diameter profile comparison between Hanford and Glasgow data (averaged over 15 points)

Figure 6.12: Thin section comparison between the profile data from Hanford and Glasgow.

Hanford measurement was $52.4\ \mu\text{m}$ which is outwith the specification, implying need for the recalibration of the Hanford profile machine.

Since the magnitude of the error varied for the stock region and the thin middle section, the percentage difference in the thin middle section was also investigated to adjust the minimum diameter of fibres. For this section, the difference was 1.03%. Using this profile

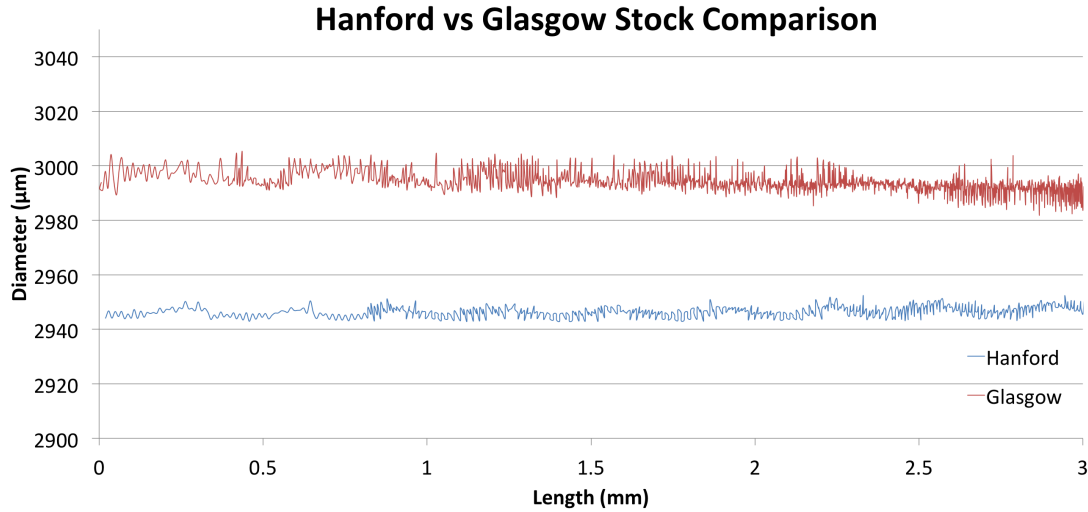


Figure 6.13: Profile data comparison of the stock region.

data difference, the stress corrosion experiment data from LIGO Hanford laboratory was adjusted. Figure 6.14 shows the recalibrated result. After the adjustment, the two datasets matched well with each other, as both datasets lie within the error. This result confirms the repeatability of independently performed stress corrosion experiments.

6.5.2 Vacuum Condition

For lower tensile stress fibres with a longer expected hang time, the vacuum condition was applied for the stress corrosion tests. Table 6.2 shows the summary of the vacuum tank results. The range of fibres set up in the tank was 2.3 to 2.78 GPa. All fibres were set up on 4th of Feb 2018, from 1:10PM until 9:44PM. The total fibre installation time, from the first fibre setup time to the last fibre setup time, was 8.5 hours. The expected hang time under the in-air condition was calculated using the combined and adjusted datasets from the in-air stress corrosion experiments. This calculation confirms that these fibres have long enough expected hang time in-air to measure the vacuum strength even when the vacuum tank takes a day to pump down.

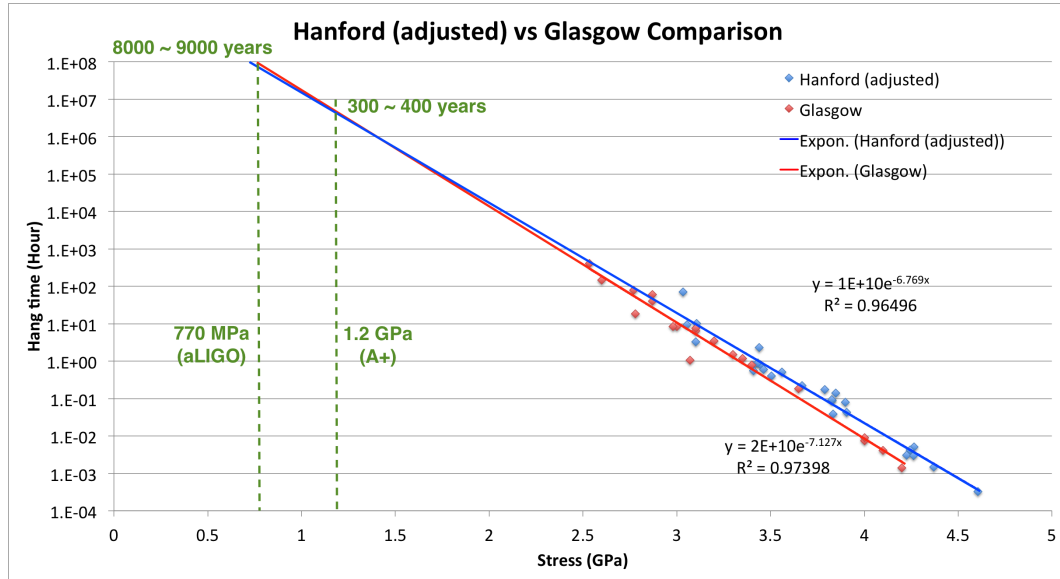


Figure 6.14: Comparison of in-air stress corrosion experiments performed in LIGO Hanford and Glasgow.

After 33 days from starting the experiment, the vacuum tank was opened once to double-check that the monitoring system was still running without any defect. The setup with the lowest tensile stress fibre (2.3 GPa) was slightly opened and the mass was pushed gently to make sure that the mass was still hanging. Then, the mass was lowered to trigger the microswitches to check the monitoring system, and hung again.

To date, 15 fibres are still hanging. One has broken, which was the lowest tensile stress fibre. Considering that the only difference between this fibre and others is the system check mentioned above, it is very likely that the main factor for the fibre failure is an external influence. However, there have been tests where violent shaking the mass (40 kg) hanging under four fibres (770 MPa of stress each) did not break the suspension [192]. Since 770 MPa is much lower stress than 2.3 GPa, it is possible that the impact of that external disturbance was not observed during those tests. These are factors that could be considered for the interpretation of this fibre, but since this is the only one broken so far, it is difficult to make a clear conclusion on the cause of this failure. Therefore, as

Fibre Number	Stress (GPa)	Expected Hang Time In-Air (hour)	Setup Time
1	2.3	2234.3	1:10PM
2	2.325	1869.2	1:13PM
3	2.35	1563.8	1:29PM
4	2.35	1563.8	1:34PM
5	2.4	1094.5	1:36PM
6	2.5	536.2	1:53PM
7	2.51	499.2	2:26PM
8	2.51	499.2	2:47PM
9	2.56	349.4	3:50PM
10	2.57	325.4	7:27PM
11	2.59	282.1	8:15PM
12	2.6	262.7	8:35PM
13	2.6	262.7	8:51PM
14	2.64	197.4	9:12PM
15	2.65	183.8	9:31PM
16	2.78	83.9	9:44PM

Table 6.2: Details of the experimental setup in the vacuum tank to measure the breaking time of fused silica fibres as a function of tensile stress.

future work, it will be useful to test the relation between any external influence and the fibre's hang time, depending on tensile stress conditions.

6.5.3 Comparison to Proctor data

In comparison to Proctor's data, there were two main differences: the spread of data points and the hang time especially for the higher stress range. The spread of the data decreased significantly for the Glasgow experiment. Since the vacuum condition part of the experiment is still ongoing, only the in-air condition results were compared. In Figure 6.15, two in-air datasets are compared: The green triangles show the Proctor data, and the blue diamonds show the combined data (Glasgow and Hanford). For each dataset, the trend line is also shown. The R-square of the Proctor dataset was 0.87,

while that of combined dataset was 0.97. This improved spread of data points can also contribute to finding a more accurate trend line.

The other interesting point for the in-air data comparison is that the Proctor data generally showed a longer hang time than both the Glasgow and the Hanford data. The trend line comparison indicates that the difference becomes larger for higher tensile stress, and, when the stress is lower than 2.55 GPa, the Proctor data's hang time becomes shorter. There are two possible reasons. Firstly, the diameter of fibres were different. While Glasgow fibres had the diameter range of 170 to 240 μm , Proctor's fibres had the diameter range of 20 to 40 μm . There have been cases where thinner fibres showed higher strength when the stress condition was kept the same [193]. To fully confirm this, Karl Toland has pulled some thin fibres with a diameter around 10 μm and more fibres will be tested to get better statistical confidence. Another factor could be the stock material difference. Proctor states that 1 mm diameter transparent Vitreosil rods were used, but it was impossible to find the exact datasheet for that material. Therefore, it cannot be concluded that there is a significant difference in the stock material, but it still is a potential factor.

Due to the limitation in extracting detailed data from the paper, it was not possible to find the exact trend line for the vacuum fibre datapoints. The closest conclusion at this point would be finding the range where the potential trend line would be located. In Figure 6.16, that range is marked with a red dotted rectangle. To define the exact location of the vacuum data trend line, more data should be collected. That will be one of the most significant outcomes of this vacuum stress corrosion experiment. This experimental setup will remain operational in order to get as much data as possible.

Although it is desirable to get a more accurate fit equation for the vacuum condition, this range (red rectangle in Figure 6.16) already can give the safety required for the A+ upgrade with high stress fibres. According to the graph, the expected hang time of 1.2 GPa fibres (potential A+ upgrade stress) is about 363 years, which is definitely

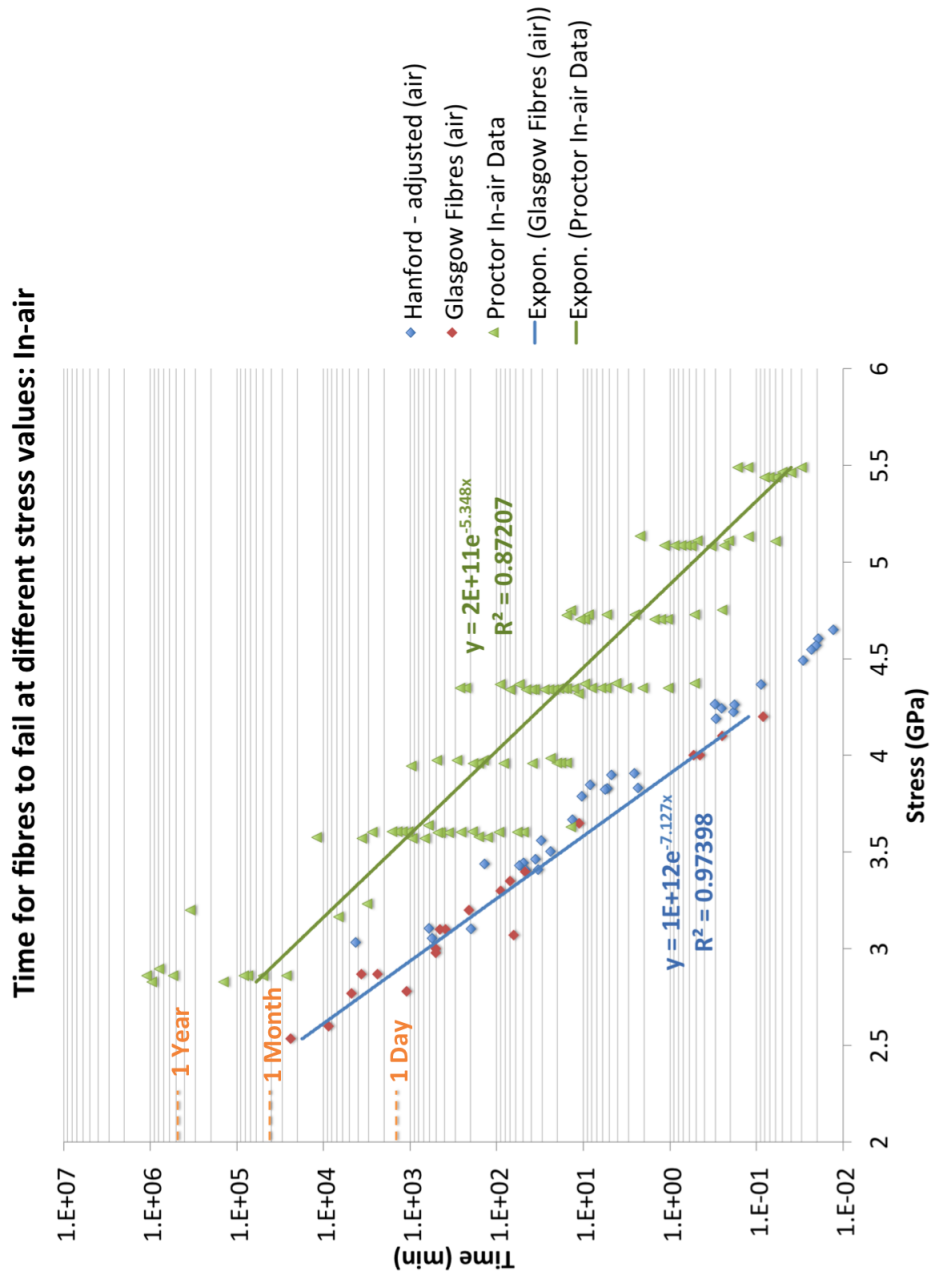


Figure 6.15: Comparison between different trend lines calculated using different methods.

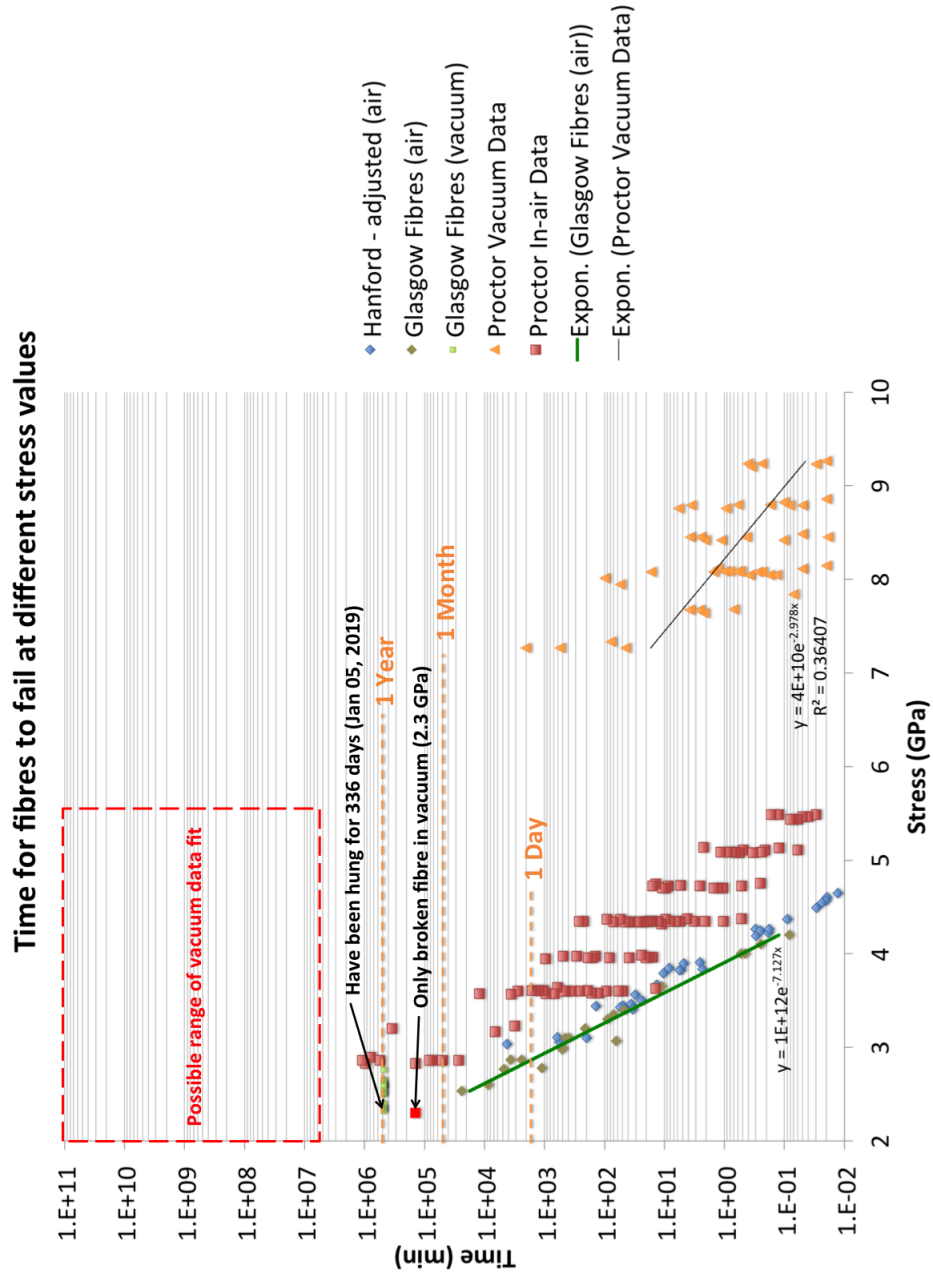


Figure 6.16: Summary of all stress corrosion experiments (Glasgow, Hanford, and Proctor) conducted in air and under vacuum.

longer than the operational duration of the A+ detectors.

6.6 Conclusions

As a final safety test for the high stress fibres produced by the enhanced fabrication technology, to be used for the next upgrade scenario of aLIGO, a stress corrosion experiment was set up. Fibres were tested under two conditions: high stress fibres with tensile stress above 2.8 GPa were tested in-air, and other fibres with relatively lower tensile stress were tested in vacuum. The tensile stress range investigated was from 2.3 to 4.2 GPa. High stress fibres tested in-air had an overlap with experiments run at Hanford. After adjusting the Hanford profile data, the hang time results from Hanford and Glasgow matched well, with both datasets agreeing within errors. This result confirms the repeatability of this experiment.

Furthermore, lower stress fibres were hung in a vacuum chamber, as the aLIGO operation condition is under vacuum. So far, one fibre with the tensile stress of 2.3 GPa failed after 98 days. However, that fibre was the one tested to confirm the status of the monitoring system, and the main cause of this failure could be an external factor.

Since Proctor *et al.* performed stress corrosion experiments in 1967, the Proctor data were compared to Glasgow and Hanford stress corrosion experiment result. Using extracted data points from Proctor's graph, the possible range of the vacuum trend line was found, and using the result from Glasgow's vacuum stress corrosion experiment, the fit equation will be specified. In addition, with improved scientific technologies, the dataset of Glasgow and Hanford showed a smaller spread than that of Proctor's, which can also contribute to improved accuracy. For future improvements, developing a remote mass loader would be useful. The main limiting factor to test the high stress fibres under vacuum was the time required for pumping down. If the mass can be loaded remotely from outside of the tank, much higher stress conditions can also be tested.

Most importantly, this experiment provides confirmation of a sufficient safety factor for the potential A+ upgrade fibres with a higher stress of 1.2 GPa. Though the accurate fit equation was not determined for the vacuum condition, the possible range of the fit equation was found. Even if the fit equation falls into the minimum of that range, 1.2 GPa fibres have the expected hang time of 363 years, which is definitely longer than the operation duration of the A+ detectors. In the next chapter, using this stress condition of 1.2 GPa which is proven to be safe, the suspension thermal noise simulation results for further aLIGO upgrade scenario will be presented.

Chapter 7

Advanced LIGO Room-Temperature Upgrades

7.1 Introduction

From the simulation result presented in Chapter 3, it was shown that a higher working stress on the fibres can contribute to expanding the sensitive detection band without any disadvantages on other noise sources. Furthermore, from the experimental work presented in Chapters 4, 5, and 6, the average breaking stress of fused silica fibres was determined, to provide some stress upgrade options with reasonable safety factors. Further upgrade scenarios for the Advanced LIGO were investigated using these data, and described in this chapter.

Following Chapter 3, analytical models were generated for different suspension configurations to investigate the seismic noise, suspension thermal noise, and coating Brownian noise. The analytical expressions presented in Chapter 3 were used again here.

Along with higher stress in the fibres, two other upgrade options were investigated: a heavier payload and a longer suspension, which are design conditions considered for

the next generation detectors such as Cosmic Explorer and Einstein Telescope. Firstly, applying higher stress in the fibres will decrease the vertical bounce mode frequency of the suspension thermal noise and push up the violin mode frequency [143]. Considering the average breaking stress of fused silica fibres was 4.2 GPa for 3000 s polished fibres, a higher working stress of 1.2 GPa was compared to the current aLIGO condition of 770 MPa. Secondly, increasing the mass of the test masses and total payload can improve seismic noise, and suspension thermal noise [194]. For this simulation, the current aLIGO 40 kg test mass, and increased masses of 80 kg and 160 kg were compared. Lastly, having longer fibres for the final stage of the suspension can increase the dilution factor and thus improve the suspension thermal noise. Two conditions were compared: the current aLIGO length of 0.6 m; and 1.1 m, which is the maximum length allowed in the current vacuum chamber [195].

7.2 Investigated Conditions

7.2.1 Mass

There are multiple masses in the pendulum chain that can be changed (Figure 3.1): the mass of the mirror (m_4), the mass arrangement of the suspension (m_1, m_2, m_3), and the total payload of the suspension (P). Since the test mass (m_4) condition affects all three low frequency range noise sources (seismic noise, suspension thermal noise, coating Brownian noise), while m_1, m_2, m_3, P values do not affect suspension thermal noise or coating Brownian noise, m_4 was the main independent variable to decide other mass conditions.

Initially, seven sets of m_4 mass and total payload were considered (Table 7.1); mass of m_4 was varied from 40 kg to 160 kg in steps of 20 kg. The total payload was calculated by increasing m_1, m_2, m_3 by the same ratio. The maximum m_4 condition of 160 kg and the maximum total payload of 390 kg were chosen because those were the conditions

Test Mass (kg)	Provisional m_1 (kg)	Provisional m_2 (kg)	Provisional m_3 (kg)	Total Payload (kg)
40 (aLIGO)	22	22	40	124
60	33	33	60	186
80	44	44	80	248
100	55	55	100	310
120	66	66	120	372
140	If calculated in the same method, the total payload exceeds 390 kg.			390
160				390

Table 7.1: List of different “test mass - total payload” sets. m_1 , m_2 , m_3 values were only used to calculate the total payload. After getting total payload, new m_1, m_2, m_3 values were assigned for each condition according to seismic optimisation.

investigated in the LIGO Strawman Red Design [195]; the load that the suspension structure can safely support [162]. Therefore, for m_4 conditions of 140 kg and 160 kg, the total payload was not calculated but set to be 390 kg, as the calculated values would exceed 390 kg if calculated with the same method (434 kg and 496 kg respectively). Among the seven sets, 80 kg and 160 kg were chosen as the final test mass conditions to investigate. As mentioned, 160 kg was chosen because it is the highest m_4 condition that the suspension structure can support, and the doubled condition of 80 kg was chosen because it is in between the current condition (40 kg) and the maximum condition.

After setting m_4 and P , the optimum mass arrangement was calculated for each condition. In T1300786-v7 (LIGO Technical Note) [74], Dr. Brett Shapiro has established some analytical equations to calculate the optimum mass arrangement that can optimise the seismic isolation properties of suspension system. The symbols used are consistent with those used in Chapter 3 (Figure 3.1).

Mass Arrangement Equations:

$$m_2^* = -(m_3 + m_4) + \sqrt{P(m_3 + m_4)}, P = m_1 + m_2 + m_3 + m_4 \quad (7.1)$$

$$m_3^* = -A + A\sqrt{A + P - m_2 - m_4}, A = \frac{m_4(m_2 + m_4)}{P + m_4} \quad (7.2)$$

Equations 7.1 and 7.2 calculate the optimal values of m_2 and m_3 when the total payload (P) and test mass (m_4) are provided. These equations are derived from minimising the longitudinal seismic transmission. The symbol “*” was used to emphasise that m_2 and m_3 from Eq. 7.1 and 7.2 are calculated mass values for a given condition, and they can be different from that of Eq. 3.1.

Specific values of m_1 , m_2 , m_3 presented in Table 7.1 were only used to calculate the total payload (P), and were replaced after running the Matlab code which calculated the new optimal values (Table 7.2) using Equation 7.1 and 7.2, 3.2. Minimising the longitudinal seismic isolation (C_1) via ten iterations, the optimum mass configuration was calculated for different m_4 mass conditions. (Note that this calculation only considers the longitudinal seismic isolation factor.) Figure 7.1 and 7.2 show the process of the mass arrangement optimisation.

Figure 7.1 shows that the longitudinal optimum mass configuration for $m_4 = 80$ kg, $P = 248$ kg is: $m_1 = 77.9$ kg, $m_2 = 53.4$ kg, $m_3 = 36.7$ kg. Figure 7.2 shows that the longitudinal optimum mass configuration for $m_4 = 160$ kg is: $m_1 = 100.2$ kg, $m_2 = 74.5$ kg, $m_3 = 55.3$ kg.

With these mass arrangement results, the final mass conditions for both 80 kg and 160 kg test masses were found (Table 7.2). For convenience, the $m_4 = 80$ kg condition is referred to as “set 1” and the $m_4 = 160$ kg condition is referred to as “set 2”.

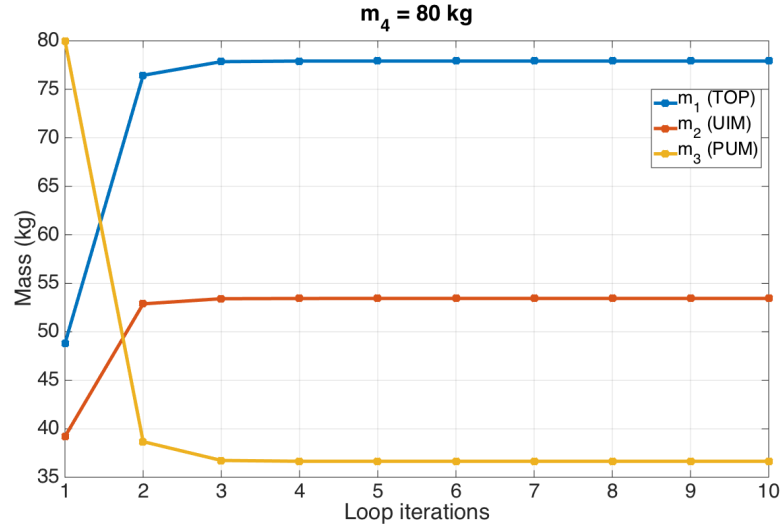


Figure 7.1: Optimum mass configuration for: $m_4 = 80$ kg, $P = 248$ kg

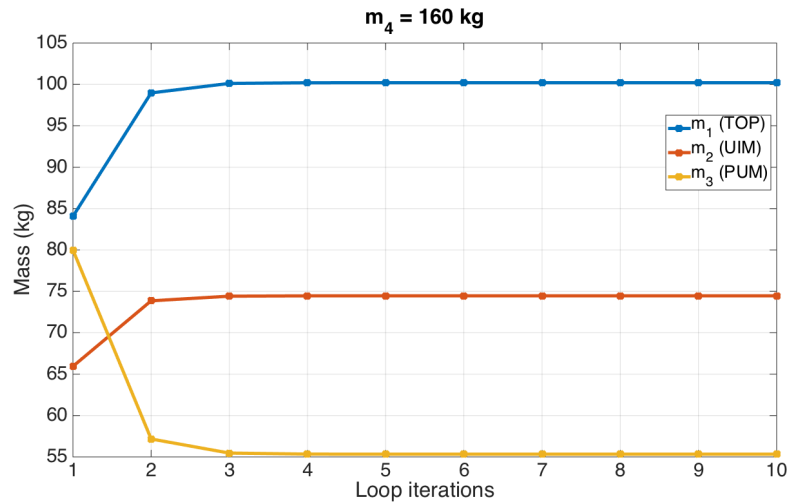


Figure 7.2: Optimum mass configuration for: $m_4 = 160$ kg, $P = 390$ kg

7.2.2 Length

The suspension length can affect both the seismic noise and the suspension thermal noise. As mentioned in Section 3.2.1, the longitudinal seismic isolation (C_1) worsens as L_4 increases, since longitudinal seismic isolation can be minimised when $L_1 = L_2 = L_3 = L_4$

Mass	Test Mass (kg)	Final m_1 (kg)	Final m_2 (kg)	Final m_3 (kg)	Total Payload (kg)
aLIGO	40	22	22	40	124
Set 1	80	77.9	53.4	36.7	248
Set 2	160	100.2	74.5	55.3	390

Table 7.2: Final mass conditions for two different test masses: 80 kg and 160 kg. The aLIGO condition is presented as a reference.

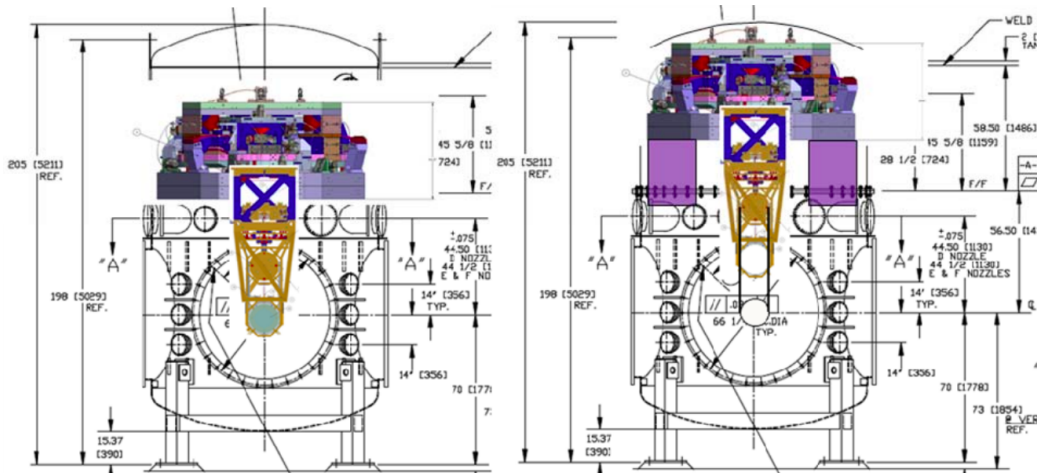


Figure 7.3: Comparison between the aLIGO QUAD and a potential upgrade of the QUAD showing the limitation of the BSC vacuum chamber in which the suspension is located [195].

(Eq. 3.2). Although a longer final stage gives a disadvantage in terms of the seismic noise, it is advantageous in respect of the suspension thermal noise (Equation 2.69, 2.72). To compensate this disadvantage in the seismic noise, the total length of the suspension (L_T) can be lengthened from 1.6 m (as aLIGO is currently) to 2.14 m, considering the physical limitation from the current vacuum chamber height (Figure 7.3). For L_4 , the current aLIGO condition of 0.6 m and the increased condition of 1.1 m were compared. Table 7.3 shows two different sets of length conditions for two different L_4 where $L_T = 2.14$ m.

For convenience, the $L_4 = 0.6$ m condition is referred to as “Set A” and the $L_4 = 1.1$ m condition is referred to as “Set B”.

Length	L_4 (m)	Total Length L_T (m)	Final L_1 (m)	Final L_2 (m)	Final L_3 (m)
aLIGO	0.6	1.6	0.33	0.33	0.33
Set A	0.6	2.14	0.5	0.5	0.5
Set B	1.1	2.14	0.35	0.35	0.35

Table 7.3: Final length conditions for two different L_4 (0.6 m and 1.1 m) where $L_T = 2.14$ m. The aLIGO parameters are presented as a reference.

7.2.3 Stress

Unlike the masses and length, which have influence over multiple noise sources, the final stage fibre stress only affects the suspension thermal noise. As the vertical bounce mode frequency and the violin mode frequency depend on the stress applied to the fibres (Equation 2.72, 2.71), the best direction to proceed is to increase the stress condition so that the vertical bounce mode frequency can be lowered and the violin mode frequency can be increased. Therefore, 1.2 GPa which is one of potential upgrade options for the A+ detector was compared to 770 MPa which is the current aLIGO condition. Considering the average breaking stress of fused silica fibres was 4.2 GPa, the increased stress of 1.2 GPa still gives a safety factor of 3.5. For convenience, the $\sigma = 1.2$ GPa condition is referred to as “Set H” and the $\sigma = 770$ MPa condition is referred to as “Set L”.

Table 7.4 shows the naming strategy for all possible scenarios with different mass, length, and stress conditions. Set numbers are assigned by accumulating set numbers of each condition. For example, set 1AH means set 1 ($m_4 = 80$ kg), Set A ($L_4 = 0.6$ m), Set H ($\sigma = 1.2$ GPa). $m_4 = 40$ kg has two additional sets: set aAL-2.14 and set aAH-2.14. These sets have identical condition as aLIGO and set aAH respectively, with increased total length of the suspension (L_T).

Set Number	Test Mass m_4 (kg)	Final Stage Length L_4 (m)	Stress σ (GPa)
aLIGO	40	0.6 ($L_T = 1.6$ m)	0.77
Set aAH			1.2
Set aAL-2.14		0.6 ($L_T = 2.14$ m)	0.77
Set aAH-2.14			1.2
Set aBL		1.1 ($L_T = 2.14$ m)	0.77
Set aBH			1.2
Set 1AL	80	0.6 ($L_T = 2.14$ m)	0.77
Set 1AH			1.2
Set 1BL		1.1 ($L_T = 2.14$ m)	0.77
Set 1BH			1.2
Set 2AL	160	0.6 ($L_T = 2.14$ m)	0.77
Set 2AH			1.2
Set 2BL		1.1 ($L_T = 2.14$ m)	0.77
Set 2BH			1.2

Table 7.4: Naming strategy for all possible scenarios with different mass, length, and stress conditions.

7.2.4 Suspension Thermal Noise Calculation: Thermoelastic Nulling and Dilution Factor

To calculate the suspension thermal noise, there are two factors that need to be modified for each condition: the thermoelastic nulling diameter and the dilution factor.

Firstly, to assume that the thermoelastic loss is cancelled for the calculations, the thermoelastic nulling radius needs to be modified when the test mass condition changes. From Equation 2.47 in Section 2.4.1, the appropriate radius of fibres to cancel out the thermoelastic loss were calculated. Table 7.5 shows the thermoelastic nulling radius of fibres for different test mass conditions.

Secondly, the length of the final stage (L_4) can increase the dilution factor (Equation 2.69)

Test Mass (m_4)	Thermoelastic nulling radius (μm)
40 kg	410
80 kg	581
160 kg	822

Table 7.5: Thermoelastic nulling radius of fibres for different test mass conditions.

to reduce the thermal noise and also lower the vertical bounce mode frequency (Equation 2.72). In addition to L_4 , the test mass (m_4) and the stress applied to the fused silica fibres (σ) can contribute to pushing the vertical bounce mode frequency down and pushing the violin mode frequency up (Equation 2.72, 2.71).

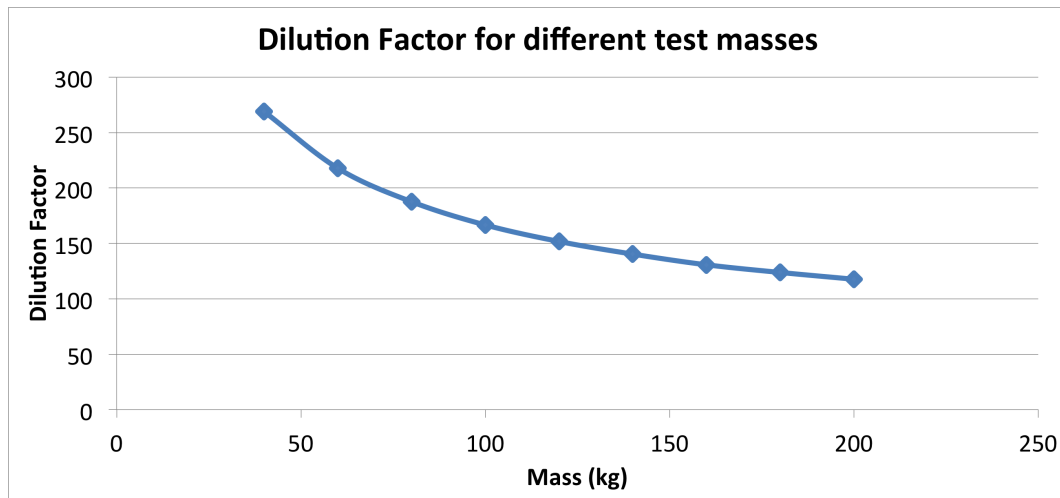


Figure 7.4: Dilution factor for different test masses calculated by Dr. Alan Cumming. (m_4 was varied from 40 kg to 200 kg in steps of 20 kg, with $L_4 = 1.1$ m)

The dilution factors for the new length and mass conditions were calculated by Dr. Alan Cumming using ANSYS [161]. Figure 7.4 shows the results of dilution factors for each mass condition where $L_4 = 1.1$ m, and Figure 7.5 shows the FEA ANSYS model of the

fused silica fibre used for the calculation. This result was used for calculating suspension thermal noise.



Figure 7.5: FEA ANSYS model of the fused silica fibre used to calculate the dilution factors for different test masses. Provided by Dr. Alan Cumming [161].

7.3 Results

Using Matlab, each condition in Table 7.4 was thoroughly investigated. For most comparison figures, the current aLIGO condition was included as a reference. (The height of peaks are not the same due to the plotting resolution.)

7.3.1 Stress Condition Comparison

First of all, the most straight forward analysis is the stress condition comparison, as it only affects the suspension thermal noise. Since current aLIGO has 770 MPa of stress in

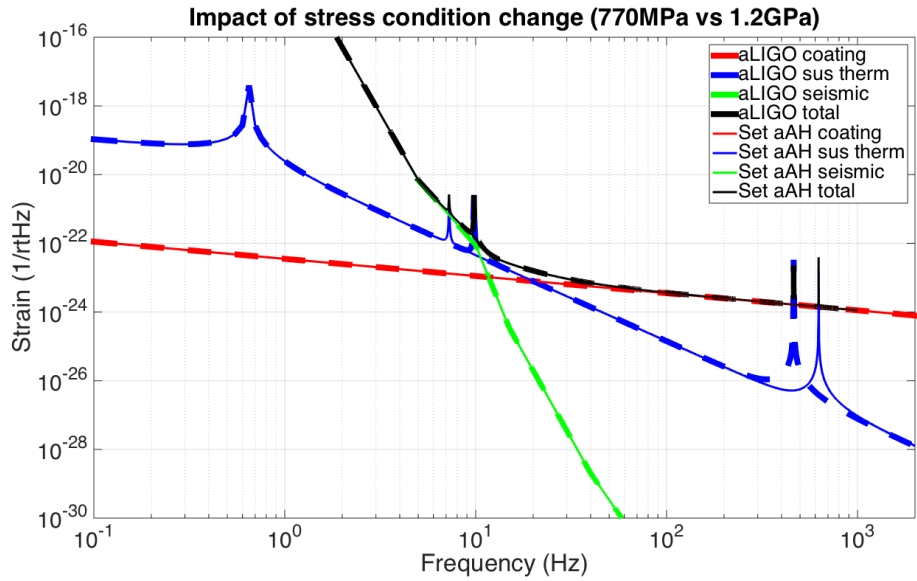


Figure 7.6: Impact of the stress condition change while keeping all other conditions the same. The current aLIGO condition was compared to the higher stress condition (770 MPa vs 1.2 GPa).

the thin section of the fibre, the models with increased stress (1.2 GPa) were investigated. As shown in Chapter 3, even higher stress would further widen the detection band, but to ensure an appropriate safety factor of 3 - 4, the maximum stress condition was set as 1.2 GPa in this simulation.

Figure 7.6 shows the comparison between two models (aLIGO and set aAH), which have identical conditions for the mass and length arrangement, but different stress. Both seismic and coating Brownian noise were unaffected; but the vertical bounce mode resonant peak was pushed down from 9.8 Hz to 7.2 Hz as the stress was increased. By reducing the vertical bounce mode frequency, the thermal noise at 10 Hz also decreased by factor of 2.2 for the higher stress condition. In addition, the first violin mode frequency was pushed up to 625.2 Hz from 462.9 Hz. Since this option pushes the resonant mode frequencies of the suspension thermal noise away from the detection band only by replacing the fused silica fibres of the final stage, this scenario is considered for the A+

upgrade.

7.3.2 Mass Condition Comparison

Secondly, the impact of test mass condition change was investigated. Figure 7.7 shows the comparison between three mass conditions (40 kg, 80 kg, 160 kg) while keeping all other conditions identical ($L_4 = 0.6$ m, $L_T = 2.14$ m, $\sigma = 770$ MPa). From this point, all conditions have newly assigned m_1, m_2, m_3 according to the seismic noise optimisation (Section 3.2.1). Note that m_1, m_2, m_3 values can affect the seismic noise only.

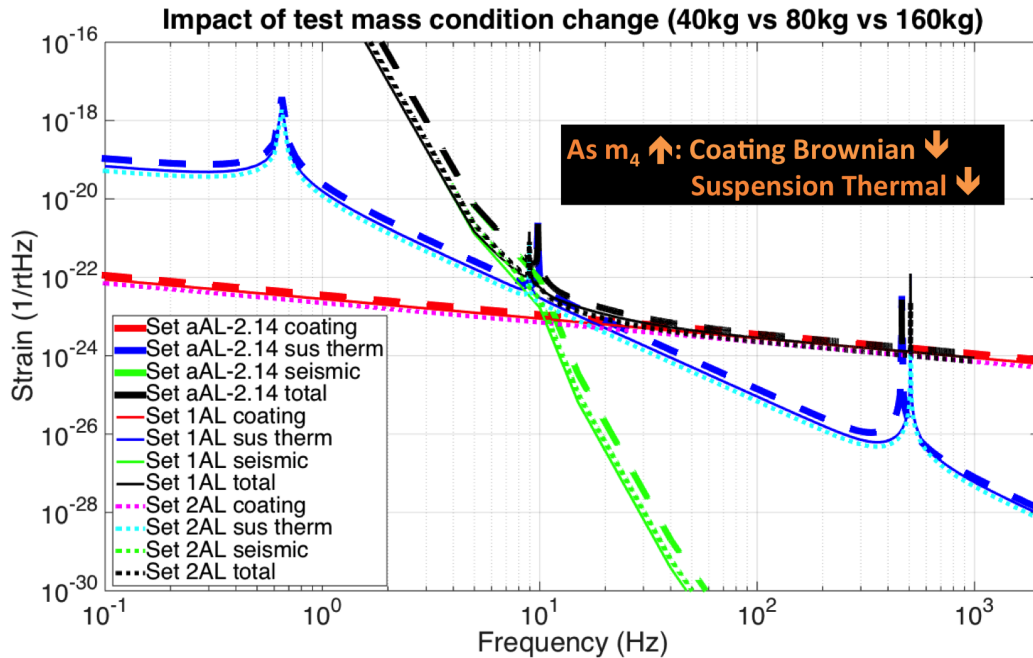


Figure 7.7: Impact of the test mass condition change while keeping all other conditions the same (40 kg vs 80 kg vs 160 kg).

Figure 7.7 shows a comparison between different mass conditions, while keeping all other conditions the same (set aAL-2.14, set 1AL, set 2AL). Seismic noise improves when the test mass condition changes from 40 kg to 80 kg. The seismic noise strain at 10 Hz for 40 kg was $2.45 \times 10^{-23} / \sqrt{Hz}$, and for 80 kg was $1.68 \times 10^{-23} / \sqrt{Hz}$. However,

when the test mass becomes 160 kg, the seismic noise increases as the total payload restriction of 390 kg limits the seismic optimisation. The seismic noise strain at 10 Hz for 160 kg was $2.77 \times 10^{-23} / \sqrt{Hz}$. This is because the test mass of 160 kg starts to deviate significantly from the ideal as the differential from m_1, m_2 , and m_3 gets too large in respect of the total payload of 390 kg. Thus, the mass arrangement optimisation could not be as efficient as 80 kg.

Conversely, for both suspension thermal noise and coating Brownian noise, the heavier test mass yields more improvement. Both Chapter 2 and Section 3.2.2 show that thermal noise decreases by a factor of \sqrt{m} , meaning heavier test masses improve the suspension thermal noise. As explained in Section 3.2.3, the coating Brownian noise does not have a direct correlation to the test mass (m_4) but it decreases when the mirror thickness increases [171]. Therefore, since the aspect ratio (radius/thickness) of the mirror was kept constant and the mass of the mirror increased, the thickness and radius also increased to reduce the coating Brownian noise.

The suspension thermal noise strain at 10 Hz for 40 kg was $4.63 \times 10^{-23} / \sqrt{Hz}$, while that of 80 kg was $2.77 \times 10^{-23} / \sqrt{Hz}$ and 160 kg was $2.15 \times 10^{-23} / \sqrt{Hz}$. The coating Brownian noise strain at 10 Hz was $1.12 \times 10^{-23} / \sqrt{Hz}$ for 40 kg, while that of 80 kg was $8.85 \times 10^{-24} / \sqrt{Hz}$ and 160 kg was $7.02 \times 10^{-24} / \sqrt{Hz}$. To summarise, increasing the test mass to 160 kg increases the seismic noise but decreases both suspension thermal noise and coating Brownian noise in the most sensitive detection frequency range.

7.3.3 Length Condition Comparison

Thirdly, the length of the final stage (L_4) was investigated. Again, all conditions were kept the same ($m_4 = 40$ kg, $L_T = 2.14$ m, $\sigma = 770$ MPa) and only the L_4 was increased from 0.6 m to 1.1 m.

Figure 7.8 shows a comparison between different final stage length conditions (set aAL-2.14 and set aBL). As expected from the seismic optimisation equations, which give the

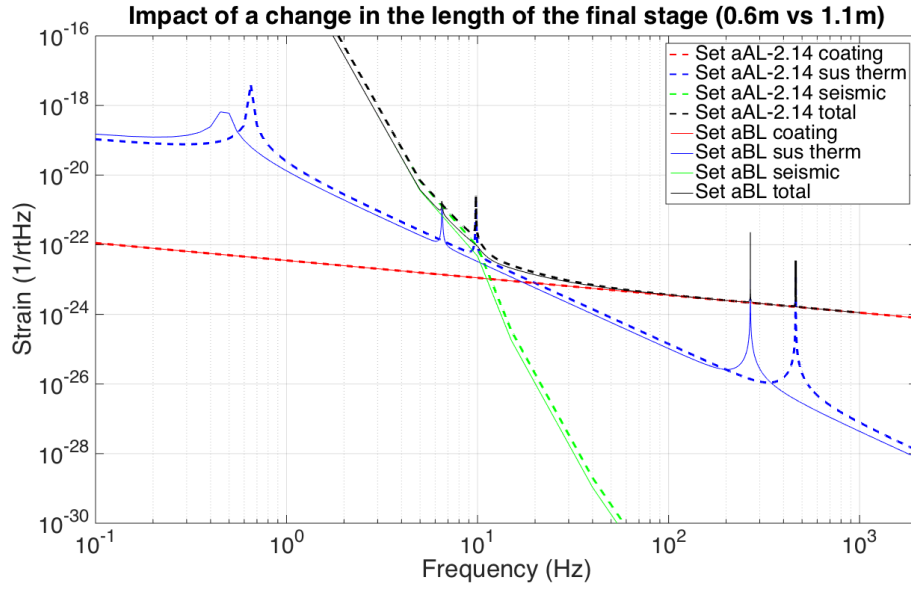


Figure 7.8: Impact of a change in the length of the final stage (0.6 m vs 1.1 m).

best longitudinal seismic isolation when $L_1 = L_2 = L_3 = L_4$, the seismic noise increased as the L_4 increased. The seismic noise strain at 10 Hz for 0.6 m was $2.45 \times 10^{-23} / \sqrt{Hz}$, and for 1.1 m was $3.26 \times 10^{-23} / \sqrt{Hz}$.

Since the test mass condition did not change, the coating Brownian noise did not change.

However, in the case of the suspension thermal noise, the longer final stage not only increases the dilution factor to improve the strain noise at 10 Hz, but also pushes down the vertical bounce mode frequency as it decreases by a factor of $1/\sqrt{L}$. The suspension thermal noise strain at 10 Hz was $4.63 \times 10^{-23} / \sqrt{Hz}$ for 0.6 m, while that of 1.1 m was $3.28 \times 10^{-23} / \sqrt{Hz}$. The vertical bounce mode frequency for 0.6 m was 8.8 Hz, while that of 1.1 m was 7.14 Hz. One downside is that the violin mode frequency decreased for the longer final stage, as it also decreases by a factor of $1/\sqrt{L}$. The first violin mode frequency for 0.6 m was 462.9 Hz, while that of 1.1 m was 267.9 Hz. This is a critical disadvantage in widening the sensitive detection band, as this resonant peak sits right

in the middle of the most sensitive region of the detection band. To compensate the impact of longer final stage on the violin mode frequency, applying higher stress in the fibre can be a potential solution, giving even stronger motivation to increase the stress condition of the fibres.

7.3.4 Investigation of the Optimum Condition

Now that the impact of each condition on the different noise sources has been investigated, the next stage was to find the optimum combination of all conditions.

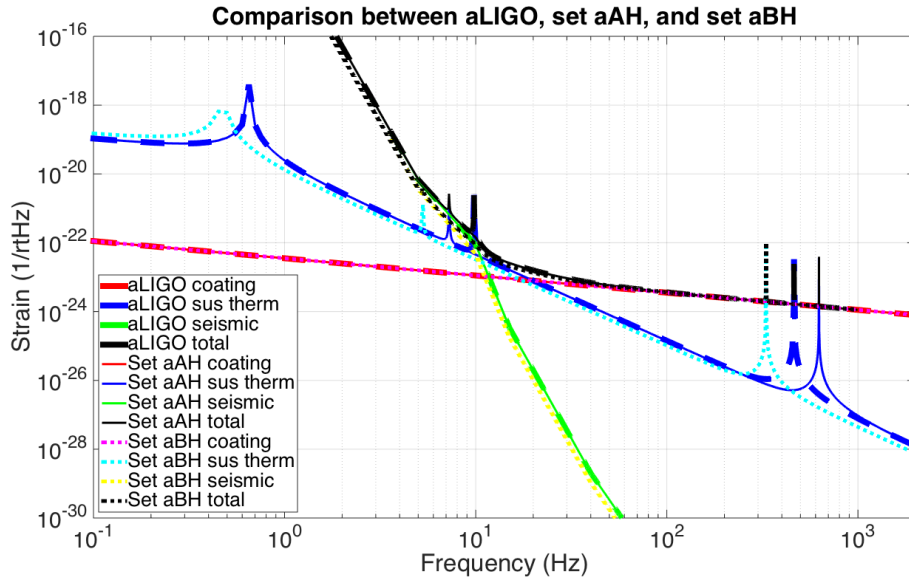


Figure 7.9: Comparison between the current aLIGO condition, set aAH ($m_4 = 40$ kg, $L_4 = 0.6$ m, $L_T = 2.14$ m, $\sigma = 1.2$ GPa), aBH ($m_4 = 40$ kg, $L_4 = 1.1$ m, $L_T = 2.14$ m, $\sigma = 1.2$ GPa).

Figure 7.9 shows the comparison between three conditions with $m_4 = 40$ kg: the first set is the current aLIGO condition, the second is set aAH ($m_4 = 40$ kg, $L_4 = 0.6$ m, $L_T = 2.14$ m, $\sigma = 1.2$ GPa), and the third is set aBH ($m_4 = 40$ kg, $L_4 = 1.1$ m, $L_T = 2.14$ m, $\sigma = 1.2$ GPa). Set aAH was chosen because this option is considered for the A+ upgrade,

and set aBH was chosen because it can show that the seismic noise disadvantage from longer L_4 can be compensated by lengthening the total suspension length (L_T). However, in the higher frequency range, the violin mode frequency decreased for a longer final stage. For all three cases, the coating Brownian noise did not change, as m_4 was kept constant. The aLIGO set and set aAH have identical conditions except for the stress (σ), the seismic noise is also the same, while the vertical bounce mode frequency for aLIGO set was 9.81 Hz, for set aAH it was 7.19 Hz, and for set aBH it was 5.23 Hz. However, for set aBH which has longer L_T , both seismic and suspension thermal noise showed improvement. The seismic noise strain at 10 Hz for both aLIGO set and set aAH was $8.82 \times 10^{-23} / \sqrt{\text{Hz}}$, and for set aBH it was $3.26 \times 10^{-23} / \sqrt{\text{Hz}}$. The suspension thermal noise strain at 10 Hz for the aLIGO set it was $1.02 \times 10^{-22} / \sqrt{\text{Hz}}$, for set aAH it was $4.51 \times 10^{-23} / \sqrt{\text{Hz}}$, and for set aBH it was $3.26 \times 10^{-23} / \sqrt{\text{Hz}}$.

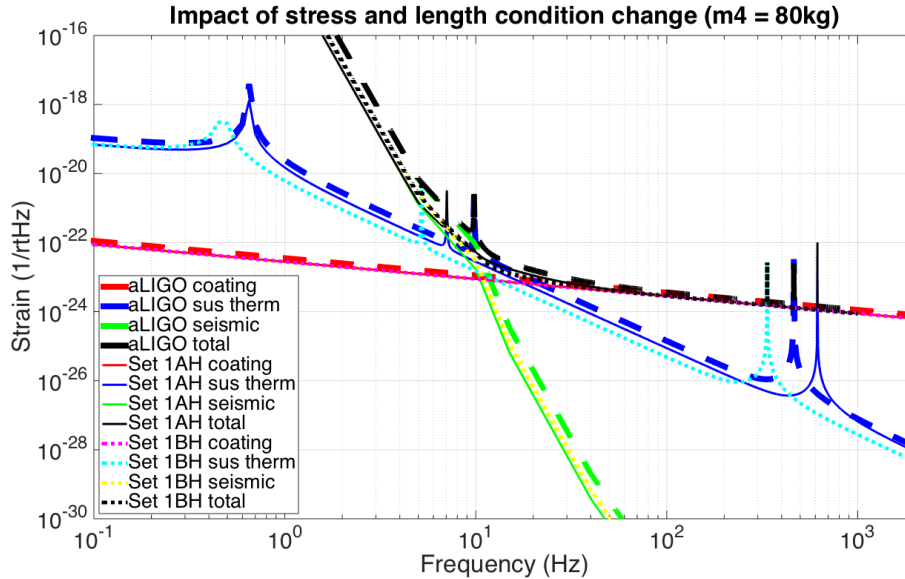


Figure 7.10: Comparison between the current aLIGO condition, set 1AH ($m_4 = 80$ kg, $L_4 = 0.6$ m, $L_T = 2.14$ m, $\sigma = 1.2$ GPa), 1BH ($m_4 = 80$ kg, $L_4 = 1.1$ m, $L_T = 2.14$ m, $\sigma = 1.2$ GPa).

Figure 7.10 shows the comparison between three conditions with $m_4 = 80$ kg: the first

set is the current aLIGO condition, the second is set 1AH, and the third is set 1BH. Since m_4 increased from 40 kg to 80 kg, the coating Brownian noise showed improvement: the coating Brownian noise strain at 10 Hz for the aLIGO set was $1.12 \times 10^{-23} / \sqrt{\text{Hz}}$, and for set 1AH and 1BH it was $8.85 \times 10^{-24} / \sqrt{\text{Hz}}$. In case of the seismic noise, set 1AH showed the most improvement, as it had shorter L_4 and longer L_T . Even for set 1BH, which showed higher seismic noise strain than that of set 1AH, the seismic noise showed improvement compared to the aLIGO set. The seismic noise strain at 10 Hz for the aLIGO set was $8.82 \times 10^{-23} / \sqrt{\text{Hz}}$, for set 1AH it was $1.68 \times 10^{-23} / \sqrt{\text{Hz}}$, and for set 1BH it was $2.98 \times 10^{-23} / \sqrt{\text{Hz}}$. However, set 1BH provided more improvement in terms of the suspension thermal noise. The suspension thermal noise strain at 10 Hz for aLIGO set was $1.02 \times 10^{-22} / \sqrt{\text{Hz}}$, for set 1AH it was $2.79 \times 10^{-23} / \sqrt{\text{Hz}}$, and for set 1BH it was $1.52 \times 10^{-23} / \sqrt{\text{Hz}}$. In addition, the vertical bounce mode frequency for aLIGO set was 9.81 Hz, for set 1AH it was 7.05 Hz, and for set 1BH it was 5.2 Hz.

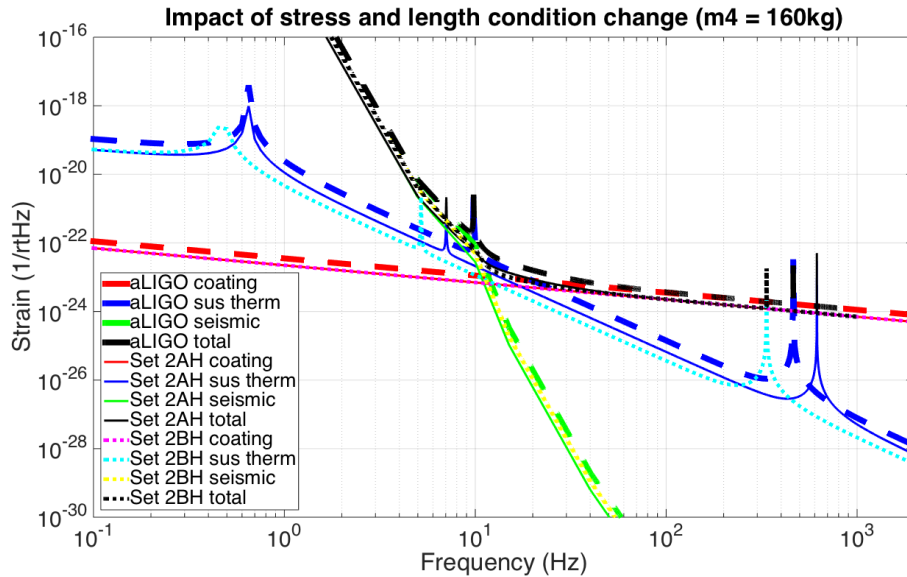


Figure 7.11: Comparison between the current aLIGO condition, set 2AH ($m_4 = 160$ kg, $L_4 = 0.6$ m, $L_T = 2.14$ m, $\sigma = 1.2$ GPa), 2BH ($m_4 = 160$ kg, $L_4 = 1.1$ m, $L_T = 2.14$ m, $\sigma = 1.2$ GPa).

Figure 7.11 shows the comparison between three conditions with $m_4 = 160$ kg: the first set is the current aLIGO condition, the second is set 2AH, and the third is set 2BH. The general trend of noise strain changes were identical to that of Figure 7.10. Since m_4 increased from 40 kg to 160 kg, the coating Brownian noise showed improvement: the coating Brownian noise strain at 10 Hz for the aLIGO set was $1.12 \times 10^{-23} / \sqrt{Hz}$, and for set 2AH and 2BH it was $7.02 \times 10^{-24} / \sqrt{Hz}$. For the seismic noise, set 2AH with shorter L_4 and longer L_T showed the most improvement. The seismic noise strain at 10 Hz for the aLIGO set was $8.82 \times 10^{-23} / \sqrt{Hz}$, for set 2AH it was $2.77 \times 10^{-23} / \sqrt{Hz}$, and for set 2BH it was $4.90 \times 10^{-23} / \sqrt{Hz}$. However, set 2BH provided more improvement in terms of the suspension thermal noise. The suspension thermal noise strain at 10 Hz for the aLIGO set was $1.02 \times 10^{-22} / \sqrt{Hz}$, for set 2AH it was $2.10 \times 10^{-23} / \sqrt{Hz}$, and for set 2BH it was $1.14 \times 10^{-23} / \sqrt{Hz}$. In addition, the vertical bounce mode frequency for the aLIGO set was 9.81 Hz, for set 2AH it was 7.05 Hz, and for set 2BH it was 5.2 Hz.

Three summary tables show the comparison between all investigated conditions in respect of the seismic, suspension thermal, and coating Brownian noise: Table 7.6, 7.7, 7.8. Each cell of the table was colour coordinated to clearly show the trend of the improvement in the noise sources. Darker blue means lower strain, and darker orange means higher strain. For each comparison item (such as suspension thermal noise strain at 10 Hz, etc), all sets (including 40 kg, 80 kg, 160 kg) were compared to assign the colour. The best value was assigned to be the darkest blue, and the worst value was assigned to be the darkest orange. Other values in the middle were assigned in respect of the best and the worst values.

m₄ = 40 kg (m ₁ = 38.56 kg, m ₂ = 26.45 kg, m ₃ = 18.14 kg, P = 122 kg) *For L ₄ = 0.6 m, the mass arrangement was kept the same as aLIGO condition.					
L ₄	0.6 m			1.1 m	
Total Length (L _T)	1.6 m		2.14 m	2.14 m	
Stress (σ)	770 MPa	1.2 GPa	770 MPa	770 MPa	1.2 GPa
Set Number	aLIGO	aAH	aAL-2.14	aBL	aBH
Seismic: min C1 (longitudinal, m/m)	5.54 × 10 ⁻⁸		1.52 × 10 ⁻⁸	2.68 × 10 ⁻⁸	
Seismic: vertical bounce mode (Hz)	8.8	7.05	8.8	6.5	5.21
Seismic: strain at 10Hz (1/√Hz)	8.82 × 10 ⁻²³		2.45 × 10 ⁻²³	3.26 × 10 ⁻²³	
Sus Therm: strain at 10Hz (1/√Hz)	1.02 × 10 ⁻²²	4.51 × 10 ⁻²³	1.02 × 10 ⁻²²	3.28 × 10 ⁻²³	3.26 × 10 ⁻²³
Sus Therm: vertical bounce mode (Hz)	9.8	7.2	9.8	7.1	5.2
Sus Therm: first violin mode (Hz)	462.9	625.2	462.9	268.8	330.8
Coating Brownian: strain at 10 Hz (1/√Hz)	1.12 × 10 ⁻²³				

High noise (bad)  Low noise (good)

Table 7.6: Summary of seismic, suspension thermal, coating Brownian noise for: test mass = 40 kg. Darker blue means lower strain, and darker orange means higher strain. For each comparison item, all sets (including 40 kg, 80 kg, 160 kg) were compared to assign the colour. The best value was assigned to be the darkest blue, and the worst value was assigned to be the darkest orange. Other values in the middle were assigned in respect of the best and the worst values.

m₄ = 80 kg (m ₁ = 77.92 kg, m ₂ = 53.44 kg, m ₃ = 36.65 kg, P = 248 kg)				
L ₄	0.6 m		1.1 m	
Total Length (L _T)	2.14 m		2.14 m	
Stress (σ)	770 MPa	1.2 GPa	770 MPa	1.2 GPa
Set Number	1AL	1AH	1BL	1BH
Seismic: min C1 (longitudinal, m/m)	1.52 × 10 ⁻⁸		2.68 × 10 ⁻⁸	
Seismic: vertical bounce mode (Hz)	11.1	8.89	8.2	6.57
Seismic: strain at 10Hz (1/√Hz)	1.68 × 10 ⁻²³		2.98 × 10 ⁻²³	
Sus Therm: strain at 10Hz (1/√Hz)	2.77 × 10 ⁻²³	2.79 × 10 ⁻²³	1.53 × 10 ⁻²³	1.52 × 10 ⁻²³
Sus Therm: vertical bounce mode (Hz)	8.8	7.05	6.5	5.2
Sus Therm: first violin mode (Hz)	492.5	615.5	268.6	335.8
Coating Brownian: strain at 10 Hz (1/√Hz)	8.85 × 10 ⁻²⁴			

High noise (bad)  Low noise (good)

Table 7.7: Summary of seismic, suspension thermal, coating Brownian noise for: test mass = 80 kg. Darker blue means lower strain, and darker orange means higher strain. For each comparison item, all sets (including 40 kg, 80 kg, 160 kg) were compared to assign the colour. The best value was assigned to be the darkest blue, and the worst value was assigned to be the darkest orange. Other values in the middle were assigned in respect of the best and the worst values.

$m_4 = 160$ kg ($m_1 = 100.21$ kg, $m_2 = 74.46$ kg, $m_3 = 55.33$ kg, $P = 390$ kg)				
L_4	0.6 m		1.1 m	
Total Length (L_T)	2.14 m		2.14 m	
Stress (σ)	770 MPa	1.2 GPa	770 MPa	1.2 GPa
Set Number	2AL	2AH	2BL	2BH
Seismic: min C1 (longitudinal, m/m)	2.77×10^{-8}		4.90×10^{-8}	
Seismic: vertical bounce mode (Hz)	12.28	9.83	9.07	7.26
Seismic: strain at 10Hz ($1/\sqrt{\text{Hz}}$)	2.77×10^{-23}		4.90×10^{-23}	
Sus Therm: strain at 10Hz ($1/\sqrt{\text{Hz}}$)	2.15×10^{-23}	2.10×10^{-23}	1.15×10^{-23}	1.14×10^{-23}
Sus Therm: vertical bounce mode (Hz)	8.8	7.05	6.5	5.2
Sus Therm: first violin mode (Hz)	492.5	615.5	268.6	335.8
Coating Brownian: strain at 10 Hz ($1/\sqrt{\text{Hz}}$)	7.02×10^{-24}			

High noise (bad)  Low noise (good)

Table 7.8: Summary of seismic, suspension thermal, coating Brownian noise for: test mass = 160 kg. Darker blue means lower strain, and darker orange means higher strain. For each comparison item, all sets (including 40 kg, 80 kg, 160 kg) were compared to assign the colour. The best value was assigned to be the darkest blue, and the worst value was assigned to be the darkest orange. Other values in the middle were assigned in respect of the best and the worst values.

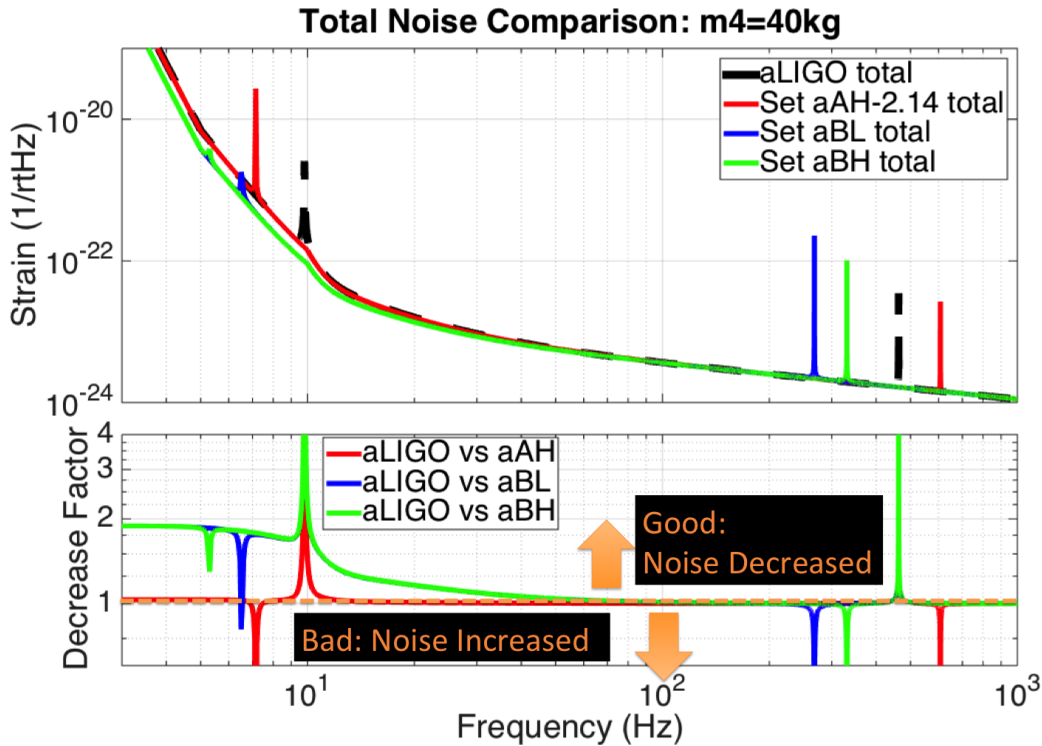


Figure 7.12: Total noise comparison between the current aLIGO condition, set aLIGO214 ($m_4 = 40$ kg, $L_4 = 0.6$ m, $L_T = 2.14$ m, $\sigma = 770$ MPa), set aAH ($m_4 = 40$ kg, $L_4 = 0.6$ m, $L_T = 2.14$ m, $\sigma = 1.2$ GPa), set aBL ($m_4 = 40$ kg, $L_4 = 1.1$ m, $L_T = 2.14$ m, $\sigma = 770$ MPa), and set aBH ($m_4 = 40$ kg, $L_4 = 1.1$ m, $L_T = 2.14$ m, $\sigma = 1.2$ GPa).

For easier comparison between different conditions, Figure 7.12, 7.13, 7.14 show the total noise (seismic, suspension thermal, coating Brownian noise) of each set. Again, the current aLIGO condition was included in all figures to provide the reference. Figure 7.12 shows the total noise comparison between the current aLIGO condition, set aAL-2.14, set aAH, set aBL, and set aBH. As shown in the graph, all four sets showed improved total noise compared to the aLIGO set. Two interesting sets are set aAH and set aBH. Set aAH shows a better result below 10 Hz, but set aBLH shows lower vertical bounce mode frequency and lower noise above 10 Hz. This trend is repeated in all other mass conditions.

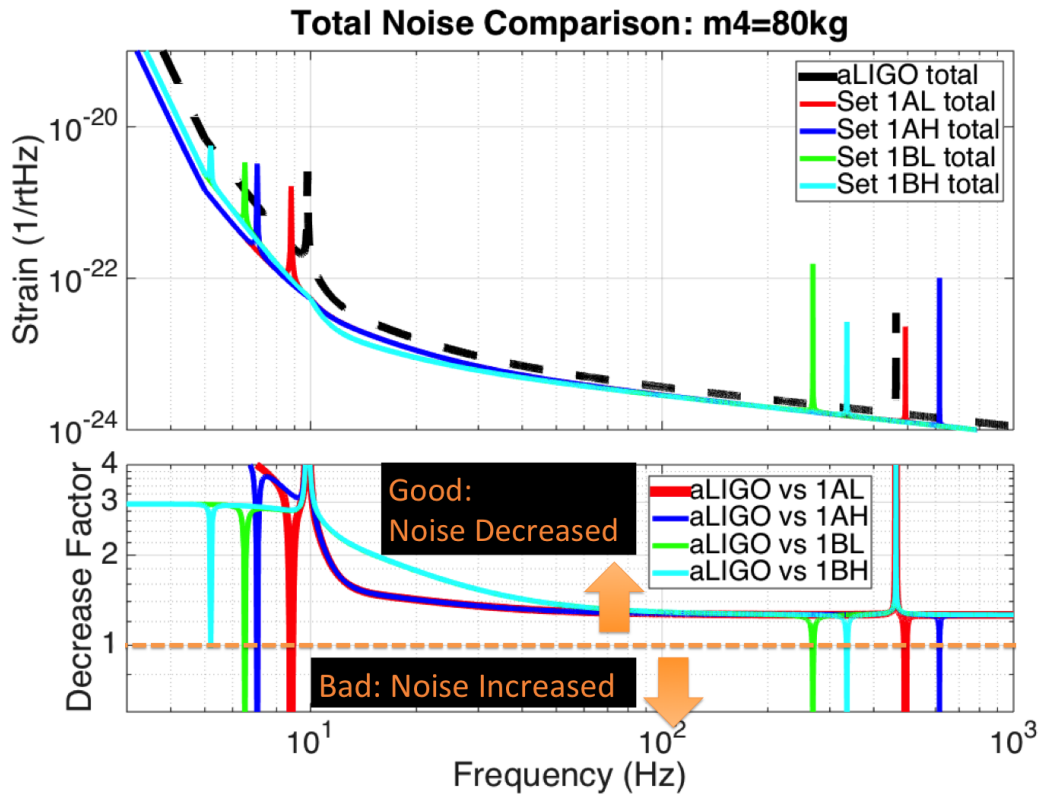


Figure 7.13: Total noise comparison between the current aLIGO condition, set 1AL ($m_4 = 80$ kg, $L_4 = 0.6$ m, $L_T = 2.14$ m, $\sigma = 770$ MPa), set 1AH ($m_4 = 80$ kg, $L_4 = 0.6$ m, $L_T = 2.14$ m, $\sigma = 1.2$ GPa), set 1BL ($m_4 = 80$ kg, $L_4 = 1.1$ m, $L_T = 2.14$ m, $\sigma = 770$ MPa), and set 1BH ($m_4 = 80$ kg, $L_4 = 1.1$ m, $L_T = 2.14$ m, $\sigma = 1.2$ GPa).

Figure 7.13 shows the total noise comparison between the current aLIGO condition, set 1AL, set 1AH, set 1BL, and set 1BH. Again, two interesting sets are set 1AH and set 1BH.

Figure 7.14 shows the total noise comparison between the current aLIGO condition, set 2AL, set 2AH, set 2BL, and set 2BH. Again, two interesting sets are set 2AH and set 2BH. Among these two sets, set 2BH was chosen for the final total noise comparison, since it showed a significant improvement in the vertical bounce mode frequency. In the

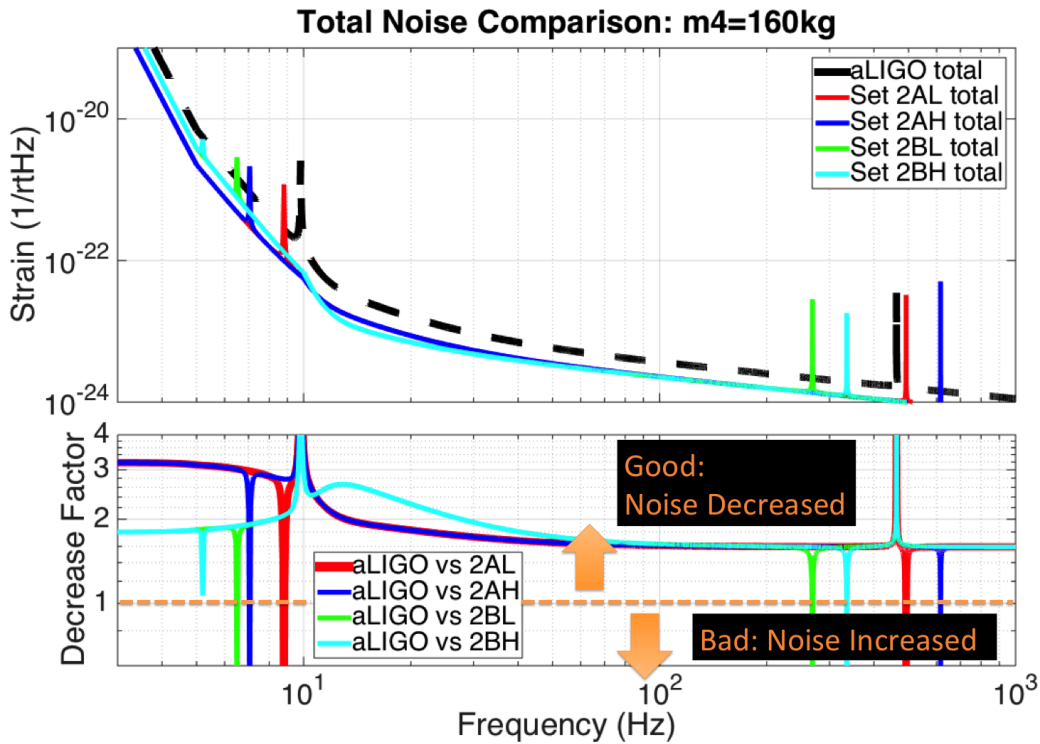


Figure 7.14: Total noise comparison between the current aLIGO condition, set 2AL ($m_4 = 160$ kg, $L_4 = 0.6$ m, $L_T = 2.14$ m, $\sigma = 770$ MPa), set 2AH ($m_4 = 160$ kg, $L_4 = 0.6$ m, $L_T = 2.14$ m, $\sigma = 1.2$ GPa), set 2BL ($m_4 = 160$ kg, $L_4 = 1.1$ m, $L_T = 2.14$ m, $\sigma = 770$ MPa), and set 2BH ($m_4 = 160$ kg, $L_4 = 1.1$ m, $L_T = 2.14$ m, $\sigma = 1.2$ GPa).

same way, set aBH and set 1BH were chosen for $m_4 = 40$ kg and 80 kg respectively. One more condition, set aAH, was also added because that option is considered for the A+ upgrade.

Figure 7.15 shows the total noise comparison between the current aLIGO condition, set aAH which is considered for the A+ upgrade, set aBH, set 1BH, and set 2BH. Among all sets, set 1BH showed the best performance below 10 Hz and set 2BH showed the best performance above 10 Hz. An important point to note is that all chosen sets have a higher stress condition of 1.2 GPa. This result implies that the sensitivity curve can further improve if we can develop fused silica fibre fabrication techniques to apply higher

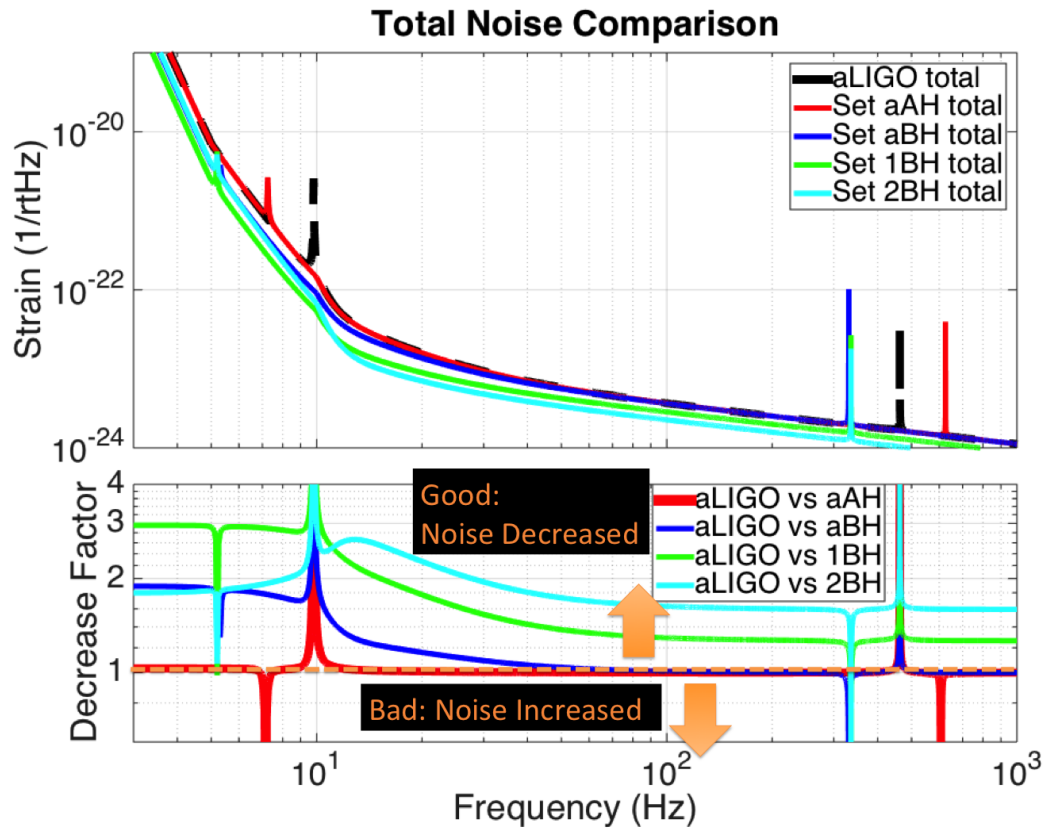


Figure 7.15: Total noise comparison between the current aLIGO condition, set aAH ($m_4 = 40$ kg, $L_4 = 0.6$ m, $L_T = 1.6$ m, $\sigma = 1.2$ GPa), set aBH ($m_4 = 40$ kg, $L_4 = 1.1$ m, $L_T = 2.14$ m, $\sigma = 1.2$ GPa), set 1BH ($m_4 = 80$ kg, $L_4 = 1.1$ m, $L_T = 2.14$ m, $\sigma = 1.2$ GPa), and set 2BH ($m_4 = 160$ kg, $L_4 = 1.1$ m, $L_T = 2.14$ m, $\sigma = 1.2$ GPa).

stress on fibres.

Since each condition shows different advantages in different ranges of frequencies, it is difficult to conclude which one has the optimum arrangement. However, there are still other noise sources not considered yet in this modelling. For future modelling work, considering other noise sources like gravity gradient noise and radiation pressure noise will give a better idea for the optimum suspension upgrade arrangement.

7.4 Conclusion

From the various Matlab simulation results, it is shown that heavier test masses, longer final stage suspension, and higher stress in the fibre can improve noise sources in the low frequency range (seismic noise, suspension thermal noise, and coating Brownian noise). For different test mass conditions, longitudinal seismic isolation factor can be minimised by calculating the optimum mass configurations. A longer final stage and higher stress in the fibre improve suspension thermal noise, but the seismic noise increases as the final stage gets longer and the upper stages become shorter. By increasing the stress in the fibre and the total length of the suspension to the maximum length that the current aLIGO BSC-ISI can allow, we can not only compensate this disadvantage but also improve the overall sensitivity of the detector. Utilising the fibre fabrication technique with the stabilisation system presented in previous chapters, it is possible to produce fused silica fibres with higher tensile stress of 1.2 GPa with a safety factor of 3.5.

Chapter 8

Conclusion

After the significant first direct detection of the gravitational waves from a binary black hole merger and the first multi-messenger observation of a binary neutron star merger, the next step is further upgrades of the detectors so that more numerous and various sources can be detected even with better SNR. The first near-term upgrade of the Advanced LIGO detectors is the A+ upgrade. One potential upgrade option is to increase the stress in the fused silica fibres used in the monolithic final stage of the suspension. The research presented in this thesis focuses on the upgrade options in respect to the suspensions, especially fused silica fibres.

The main reason that a higher stress condition is considered for the A+ upgrade is that it is a simple replacement which can bring improvements in sensitivity without any disadvantages in respect to other noise sources. It was shown from Matlab simulations that the higher stress condition does not affect the seismic noise and the coating Brownian noise, but lowers the vertical bounce mode frequency of the suspension, which limits the low frequency sensitivity band, and pushes up the violin mode frequency to widen the sensitive detection band. For instance, with the current Advanced LIGO stress condition (770 MPa), the vertical bounce mode frequency is around 9.7 Hz and the first violin mode frequency is around 516 Hz, but when the stress condition is increased to

1.2 GPa, the vertical bounce mode frequency is reduced to 7.2 Hz and the violin mode frequency is increased to 625 Hz.

The challenge of increasing the stress condition is to fabricate thin but robust fused silica fibres that can support a heavier test mass with a sufficient safety factor. Further experiments were conducted to investigate techniques to enhance the statistical strength of the fibres and to confirm the intended stress condition for the A+ upgrade has a sufficient safety factor.

First of all, stabilisation techniques for the fibre fabrication process were investigated. From various cases, it was shown that instabilities in the laser intensity during the fibre fabrication process can cause unexpected dips and bumps on the surface of the fibre. The concept of a camera monitoring system was developed to closely observe any laser instability through monitoring the peak pixel intensity of the heated stock. In addition, a PID feedback control system was implemented to minimise the impact from the laser instability. Various causes of laser fluctuations, such as mode hopping and water flow rate, were confirmed and minimised. Compared to the unstabilised fibres which showed the average peak pixel intensity percentage error range of 7.6 to 97.4%, stabilised fibres with the enhanced techniques applied showed the percentage error range of 0.02 to 0.06% in peak pixel intensity. The standard deviation of peak pixel intensity of stabilised fibres was also 10 to 20 times smaller than that of unstabilised fibres.

To investigate the impact of these enhanced techniques in terms of the fibres' statistical strength, tensile breaking tests were performed. A high speed camera was setup to record the breaking moment of each fibre to identify the location of the breaking point. Through the breaking stress analysis, the positive impact of stabilisation technique was confirmed: improved statistical strength of fused silica fibres. The standard deviation of the stabilised fibre group was decreased by 30% compared to that of the unstabilised fibre group. In addition, the percentage of strong fibres which have breaking stress above 4 GPa increased to 80%; while that of unstabilised fibres was 60%. The maximum

breaking stress also increased from 4.45 GPa to 4.7 GPa, and the minimum breaking stress increased from 1.5 GPa to 2 GPa. The average breaking stress increased by 9% for the stabilised fibres. As it was possible to achieve the average breaking stress of 4.2 GPa utilising the enhanced fibre fabrication technologies, it is confirmed that the potential A+ upgrade stress of 1.2 GPa has a reasonable safety factor. From the breaking point analysis, it was shown that 94% of strong fibres (breaking stress of 3.5 GPa or above) broke at their thinnest point. This result suggests that potential weak fibres can be predicted by observing the peak pixel intensity data taken during the fabrication process, even before profiling the fibres, unless the fibre had any external contact.

Other than the breaking stress, another important factor is the breaking time. A stress corrosion experiment was designed and setup to investigate the breaking time of fused silica fibres in-air and in vacuum. Tests in vacuum are necessary since the detectors operate in vacuum, and in-air tests are also meaningful because the fibres' fabrication and storage condition is in-air. Higher stress fibres were tested in air and lower stress fibres were tested in vacuum. Compared to Proctor's experiment in 1967, the in-air dataset from this experiment showed a smaller spread than that of Proctor's in-air results, which can contribute to find a more accurate fit equation. Since fibres in vacuum have significantly longer breaking time, the vacuum experiment is still running as of time of writing (30th of Sep, 2018). 16 fibres were setup in a vacuum chamber on 4th of February 2018, and 15 fibres are still hanging. One fibre that failed after 98 days was the one tested to confirm the status of the monitoring system, which could be the main cause of the failure. The experimental setup will remain operational in order to get as much data as possible. Since Proctor's vacuum experiment data had a large spread, one of the meaningful outcomes from this experiment will be defining more accurate vacuum data trend line. However, even with the most pessimistic prediction, the expected breaking time for the tensile stress of 1.2 GPa is about 363 years, which provides another confirmation of sufficient safety factor for the potential A+ upgrade stress.

Based on confirmations for the higher stress condition, further upgrade scenarios were investigated. Among various options, the stress, mass and the length conditions were varied. For the stress condition, the current aLIGO condition of 770 MPa was compared to higher stress of 1.2 GPa. For the mass condition, the current aLIGO mass of 40 kg was compared to heavier test mass of 80 kg and 160 kg. For the final stage length condition, the current aLIGO length of 0.6 m was compared to the longer length of 1.1 m. Lastly, for the total suspension length condition, the current aLIGO length of 1.6 m was compared to the longer length of 2.14 m. Many conditions bring advantages and disadvantages at the same time, which makes the decision more difficult. For instance, the longer final stage improved the suspension thermal noise, but at the same time, it increases the seismic noise. It can be partially compensated by increasing the stress in the fibre and the total length of the suspension to the maximum length that the current aLIGO vacuum chamber can allow. That is the reason why the fibre stress is important: unlike many other conditions, it brings improvement in the detection band without any disadvantages. With the enhanced techniques introduced in this thesis and further research to improve the statistical strength of fused silica fibres, the sensitivity of detectors can be improved for future upgrades. Better sensitivity in low frequency range and wider detection band will enable observations of more astronomical sources for longer observation time.

Appendix A

Derivation of Seismic Noise Optimisation Equations

Dr. Brett Shapiro derived seismic noise optimisation equations in LIGO Document T1300786 [74]. Following is the derivation he presented in the document.

Notation conventions:

- Bold upper case letters, e.g. \mathbf{M} , denote matrices.
- Bold lower case letters, e.g. \mathbf{x} , denote vectors. All vectors are column vectors.
- Non-bold lower or upper case letters, e.g. ω , denote scalar values.
- Subscripts on scalars, e.g. m_1 , refer to the pendulum stage, 1 through 4 top down.
- Subscripts on matrices, e.g. \mathbf{C}_{14} refer to the row and column of a matrix element.

A.1 Generalised System

By simplifying a four stage quadruple pendulum to movement along a single axis (longitudinal, vertical, etc), the equations of motion become much more tractable, yet have sufficient detail to accurately reproduce seismic isolation properties [74].

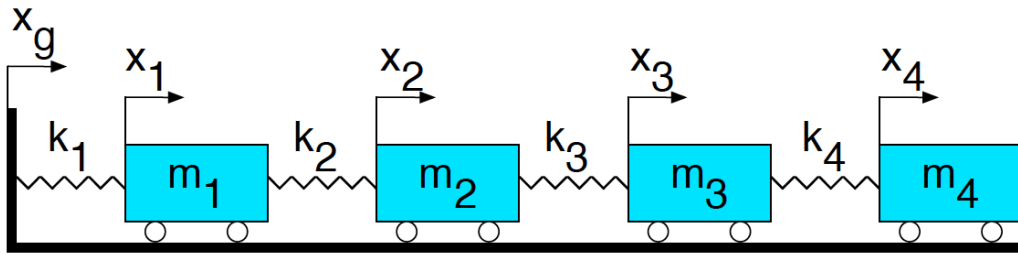


Figure A.1: Single-axis mass spring system used to simplify and generalise the dynamics of the quadruple pendulum [74].

The equations of motion of this system are:

$$\mathbf{M}\ddot{\mathbf{x}} + \mathbf{K}\mathbf{x} = \begin{bmatrix} k_1 \\ 0_{3 \times 1} \end{bmatrix} x_g \quad (\text{A.1})$$

where,

$$\mathbf{M} = \begin{bmatrix} m_1 & 0 & 0 & 0 \\ 0 & m_2 & 0 & 0 \\ 0 & 0 & m_3 & 0 \\ 0 & 0 & 0 & m_4 \end{bmatrix} \quad (\text{A.2})$$

$$\mathbf{K} = \begin{bmatrix} k_1 + k_2 & -k_2 & 0 & 0 \\ -k_2 & k_2 + k_3 & -k_3 & 0 \\ 0 & -k_3 & k_3 + k_4 & -k_4 \\ 0 & 0 & -k_4 & k_4 \end{bmatrix} \quad (\text{A.3})$$

$$\mathbf{x} = \begin{bmatrix} x_1 \\ x_2 \\ x_3 \\ x_4 \end{bmatrix} \quad (\text{A.4})$$

where \mathbf{M} is the diagonal mass matrix, \mathbf{K} is the symmetric positive definite stiffness matrix, and \mathbf{x} is the vector of displacement coordinates for the four masses.

A.2 Vertical Seismic Isolation

From Equation A.1, multiply both sides by the inverse of \mathbf{M} :

$$\ddot{\mathbf{x}} + \mathbf{M}^{-1}\mathbf{K}\mathbf{x} = \begin{bmatrix} k_1/m_1 \\ 0_{3 \times 1} \end{bmatrix} x_g \quad (\text{A.5})$$

Then, take the Laplace transform of both sides where s is the Laplacian variable.

$$\mathbf{x}s^2 + \mathbf{M}^{-1}\mathbf{K}\mathbf{x} = \begin{bmatrix} k_1/m_1 \\ 0_{3 \times 1} \end{bmatrix} x_g \quad (\text{A.6})$$

Solving for \mathbf{x} ,

$$\mathbf{x} = [\mathbf{M}^{-1}\mathbf{K} + s^2\mathbf{I}_{4 \times 4}]^{-1} \begin{bmatrix} k_1/m_1 \\ 0_{3 \times 1} \end{bmatrix} x_g \quad (\text{A.7})$$

To find the magnitude and phase relation between x_g and x_4 , we set $s = i\omega$, where ω is the frequency in radians/second.

$$\mathbf{x} = [\mathbf{M}^{-1}\mathbf{K} - \omega^2\mathbf{I}_{4 \times 4}]^{-1} \begin{bmatrix} k_1/m_1 \\ 0_{3 \times 1} \end{bmatrix} x_g \quad (\text{A.8})$$

Set an intermediate variable \mathbf{V} as the matrix that gets inverted:

$$\mathbf{V} = [\mathbf{M}^{-1}\mathbf{K} - \omega^2\mathbf{I}_{4 \times 4}] \quad (\text{A.9})$$

$$\mathbf{V} = \begin{bmatrix} \frac{k_1+k_2}{m_1} - \omega^2 & \frac{-k_2}{m_1} & 0 & 0 \\ \frac{-k_2}{m_2} & \frac{k_2+k_3}{m_2} - \omega^2 & \frac{-k_3}{m_2} & 0 \\ 0 & \frac{-k_3}{m_3} & \frac{k_3+k_4}{m_3} - \omega^2 & \frac{-k_4}{m_3} \\ 0 & 0 & \frac{-k_4}{m_4} & \frac{k_4}{m_4} - \omega^2 \end{bmatrix} \quad (\text{A.10})$$

$$\mathbf{x} = \mathbf{V}^{-1} \begin{bmatrix} k_1/m_1 \\ 0_{3 \times 1} \end{bmatrix} x_g \quad (\text{A.11})$$

Although it is difficult to invert this matrix analytically, for the ground to test mass isolation, all we need is the lower left element (index 4,1) of \mathbf{V}^{-1} . This element is equal to:

$$(\mathbf{V}^{-1})_{41} = \frac{1}{\det V} \mathbf{C}_{14} \quad (\text{A.12})$$

where \mathbf{C} is the matrix of cofactors. The \mathbf{C}_{14} element is equal to the negative determinant of the 3×3 lower left corner of \mathbf{V} [196].

$$\mathbf{C}_{14} = - \begin{vmatrix} \frac{-k_2}{m_2} & \frac{k_2+k_3}{m_2} - \omega^2 & \frac{-k_3}{m_2} \\ 0 & \frac{-k_3}{m_3} & \frac{k_3+k_4}{m_3} - \omega^2 \\ 0 & 0 & \frac{-k_4}{m_4} \end{vmatrix} = \frac{k_2 k_3 k_4}{m_2 m_3 m_4} \quad (\text{A.13})$$

Up to this point, there was no approximations. To find the determinant of \mathbf{V} , we assume high frequencies, where $\omega \gg$ resonance frequencies. In this regime, \mathbf{V} approaches the diagonal matrix:

$$\mathbf{V} \approx \begin{bmatrix} -\omega^2 & 0 & 0 & 0 \\ 0 & -\omega^2 & 0 & 0 \\ 0 & 0 & -\omega^2 & 0 \\ 0 & 0 & 0 & -\omega^2 \end{bmatrix} \quad (\text{A.14})$$

Therefore, the determinant of \mathbf{V} at these high frequencies is:

$$\det V \approx \omega^8 \quad (\text{A.15})$$

Applying this to Equation A.11,

$$\frac{x_4}{x_g} = \frac{1}{\omega^8} \frac{k_1 k_2 k_3 k_4}{m_1 m_2 m_3 m_4} \quad (\text{A.16})$$

Plugging in $\omega = 2\pi f$, we can find the transmission of seismic noise through the system:

$$\frac{x_4}{x_g} \approx \frac{1}{2\pi f^8} \frac{k_1 k_2 k_3 k_4}{m_1 m_2 m_3 m_4} \quad (\text{A.17})$$

This equation can be used directly for the quadruple pendulum vertical isolation, where k values are the net blade spring stiffness at each stage.

A.3 Longitudinal Stiffness Derivation

To use Equation A.17 for longitudinal isolation, we need to derive longitudinal k values.

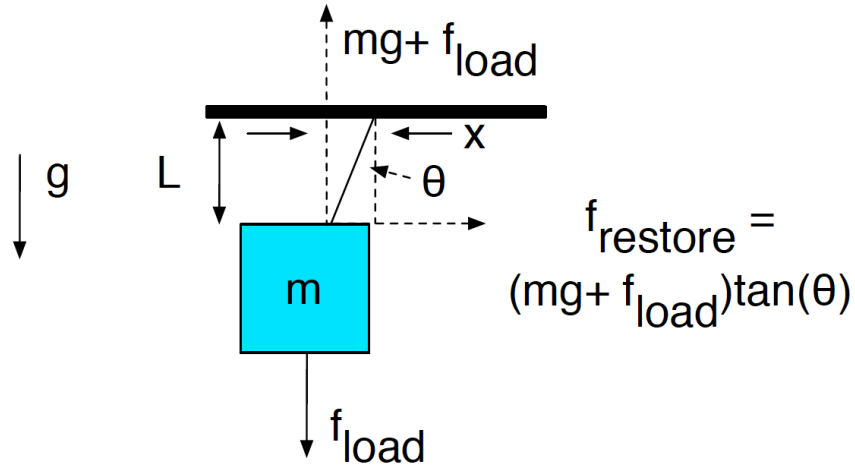


Figure A.2: Forces on a suspended stage of mass m hanging from a wire of length L at an angle θ [74].

Figure A.2 shows a mass m hanging from a wire of length L , and supporting a vertical load f_{load} . When the mass is displaced in the longitudinal direction by a distance x , this displacement causes the wire to pivot at an angle θ . The restoring force is:

$$f_{restore} = (mg + f_{load}) \tan \theta \quad (\text{A.18})$$

But for small angles,

$$f_{restore} \approx (mg + f_{load}) \frac{x}{L} \quad (\text{A.19})$$

Therefore,

$$k \approx \frac{f_{restore}}{x} = \frac{(mg + f_{load})}{L} \quad (\text{A.20})$$

Thus, the stiffness for a suspended mass can be stated as a tension in the wire divided by the wire length. In general, for an N stage pendulum,

$$k_i = g \frac{\sum i N m_i}{L_i} \quad (\text{A.21})$$

where i is the index of the stage in order of top down. Plugging this into Equation A.11,

$$\frac{x_4}{x_g} \approx \frac{g^4}{2\pi f^8} \frac{1}{L_1 L_2 L_3 L_4} \frac{(m_1 + m_2 + m_3 + m_4)(m_2 + m_3 + m_4)(m_3 + m_4)m_4}{m_1 m_2 m_3 m_4} \quad (\text{A.22})$$

A.4 Optimal Masses

The goal is to minimise Equation A.22 with respect to the four mass parameters. By setting two mass constraints, we can reduce the four parameter minimisation to two parameters. For instance, let's set

$$m_4 = 80P = m_1 + m_2 + m_3 + m_4 = 390 \quad (\text{A.23})$$

Thus, $m_1 = P - m_2 - m_3 - m_4$, etc. Then,

$$\frac{x_4}{x_g} = \frac{g^4}{2\pi f^8} \frac{P}{L_1 L_2 L_3 L_4} \left[\frac{(m_2 + m_3 + m_4)(m_3 + m_4)}{(P - m_2 - m_3 - m_4)m_2 m_3} \right] \quad (\text{A.24})$$

where the terms in the square brackets is to be minimised with respect to m_2 and m_3 . For simplification, let's denote the numerator as N and the denominator as D where

$$N = (m_2 + m_3 + m_4)(m_3 + m_4) = m_2 m_3 + m_2 m_4 + 2m_3 m_4 + m_3^2 + m_4^2 \quad (\text{A.25})$$

$$D = (P - m_2 - m_3 - m_4)m_2 m_3 = P m_2 m_3 - m_2^2 m_3 - m_2 m_3^2 - m_2 m_3 m_4 \quad (\text{A.26})$$

Then, minimising by setting the derivative with respect to m_i to 0,

$$\frac{\partial}{\partial m_i} \left[\frac{N}{D} \right] = \left(\frac{\partial}{\partial m_i} N \right) D^{-1} + N \left(\frac{\partial}{\partial m_i} D^{-1} \right) = 0 \quad (\text{A.27})$$

$$\left(\frac{\partial}{\partial m_i} N \right) D^{-1} - N D^{-2} \left(\frac{\partial}{\partial m_i} D \right) = 0 \quad (\text{A.28})$$

Multiplying both sides by D :

$$\left(\frac{\partial}{\partial m_i} N \right) - N D^{-1} \left(\frac{\partial}{\partial m_i} D \right) = 0 \quad (\text{A.29})$$

Putting derivatives on the left and everything else on the right,

$$\frac{\partial N / \partial m_i}{\partial D / \partial m_i} = \frac{N}{D} \quad (\text{A.30})$$

Then, to solve for the optimal m_2 and m_3 values, solve $\partial N / \partial m_i$ and $\partial D / \partial m_i$ for $i = 2$ and $i = 3$ respectively:

$$\frac{\partial N}{\partial m_2} = m_3 + m_4, \quad \frac{\partial D}{\partial m_2} = P m_3 - 2 m_2 m_3 - m_3^2 - m_3 m_4 \quad (\text{A.31})$$

$$\frac{\partial N}{\partial m_3} = m_2 + 2 m_3 + 2 m_4, \quad \frac{\partial D}{\partial m_3} = P m_2 - 2 m_2 m_3 - m_2^2 - m_2 m_4 \quad (\text{A.32})$$

Let's solve for optimal m_2 first. For m_2 , Equation A.30 is:

$$\frac{m_3 + m_4}{P m_3 - 2 m_2 m_3 - m_3^2 - m_3 m_4} = \frac{(m_2 + m_3 + m_4)(m_3 + m_4)}{(P - m_2 - m_3 - m_4) m_2 m_3} \quad (\text{A.33})$$

Since both sides have $\frac{m_3 + m_4}{m_3}$, that term can be cancelled out:

$$\frac{1}{P - 2 m_2 - m_3 - m_4} = \frac{(m_2 + m_3 + m_4)}{(P - m_2 - m_3 - m_4) m_2} \quad (\text{A.34})$$

Then,

$$(P - m_2 - m_3 - m_4)m_2 = (P - 2m_2 - m_3 - m_4)(m_2 + m_3 + m_4) \quad (\text{A.35})$$

Restate the equation in a quadratic form with respect to m_2 :

$$m_2^2 + 2(m_3 + m_4)m_2 - (m_3 + m_4)(P - m_3 - m_4) = 0 \quad (\text{A.36})$$

Then, the solutions for m_2 are:

$$m_2 = -(m_3 + m_4) \pm 0.5\sqrt{4(m_3 + m_4)^2 + 4(m_3 + m_4)(P - m_3 - m_4)} \quad (\text{A.37})$$

Noting that the negative solution is invalid because it yields negative mass, simplify the final result for the optimal m_2 (m_2^*) is:

$$m_2^* = -(m_3 + m_4) + \sqrt{P(m_3 + m_4)} \quad (\text{A.38})$$

Now, to solve for the optimal m_3 , Equation A.30 is:

$$\frac{m_2 + 2m_3 + 2m_4}{Pm_2 - 2m_2m_3 - m_2^2 - m_2m_4} = \frac{(m_2 + m_3 + m_4)(m_3 + m_4)}{(P - m_2 - m_3 - m_4)m_2m_3} \quad (\text{A.39})$$

Since both sides have $\frac{1}{m_2}$, that term can be cancelled out:

$$\frac{m_2 + 2m_3 + 2m_4}{P - 2m_3 - m_2 - m_4} = \frac{(m_2 + m_3 + m_4)(m_3 + m_4)}{(P - m_2 - m_3 - m_4)m_3} \quad (\text{A.40})$$

Then,

$$(m_2 + 2m_3 + 2m_4)(P - m_2 - m_3 - m_4)m_3 = (P - 2m_3 - m_2 - m_4)(m_2 + m_3 + m_4)(m_3 + m_4) \quad (\text{A.41})$$

Restate the equation in a quadratic form with respect to m_3 :

$$m_3^2 + \frac{2m_4(m_2 + m_4)}{P + m_4}m_3 - \frac{m_4(m_2 + m_4)(P - m_2 - m_3)}{P + m_4} = 0 \quad (\text{A.42})$$

Then, the only valid solution for the optimal m_3 (m_3^*) is:

$$m_3^* = -A + \sqrt{A^2 + A(P - m_2 - m_4)} \quad (\text{A.43})$$

where,

$$A = \frac{m_4(m_2 + m_4)}{P + m_4} \quad (\text{A.44})$$

Appendix B

Calculation of Coating Brownian Noise Estimate

The coating Brownian noise equations used in the Matlab codes for Chapter 3 and 7 were developed by Somiya and Yamamoto [171]. The thermal noise can be defined as:

$$S_x(\omega) = \frac{4k_B T}{\omega} U \phi(\omega) \quad (\text{B.1})$$

where k_B is the Boltzmann constant, T is the temperature, U is the stored strain energy, and $\phi(\omega)$ is the loss angle. From the solution of elastic equation, the displacement vector can be written as the sum of a main term u_0 and a correction term Δu . Thus, the corresponding energy U must be written as $U_0 + \Delta U$. However, the correction term ΔU has a significant value only for $h \ll a$ where h is the thickness and a is the radius of the mirror, so its value is negligible in this analysis [171]. Since the coating is thin, we can assume that the strain and the stress tensor are constant in respect to z , and we have:

$$U = \pi d \int_0^a \sum_{i,j} E_{i,j} T_{i,j} r dr \quad (\text{B.2})$$

where $i, j = r, \phi, z$ are the coordinates, d is the coating thickness ¹, $E_{i,j}$ is the strain tensor and $T_{i,j}$ is the stress tensor, given by the equations:

$$E_{rr} = \sum_m \frac{k_m(\gamma_m + \delta_m)}{2} [J_0(k_m r) - J_2(k_m r)] + \frac{(\lambda_s + 2\mu_s)c_0 + \lambda_s p_0}{2\mu_s(3\lambda_s + 2\mu_s)}, \quad (\text{B.3})$$

$$E_{rr} = \sum_m \frac{k_m(\gamma_m + \delta_m)}{2} [J_0(k_m r) - J_2(k_m r)] + \frac{(\lambda_s + 2\mu_s)c_0 + \lambda_s p_0}{2\mu_s(3\lambda_s + 2\mu_s)} \quad (\text{B.4})$$

$$E_{\phi\phi} = \sum_m \frac{k_m(\gamma_m + \delta_m)}{2} [J_0(k_m r) + J_2(k_m r)] + \frac{(\lambda_s + 2\mu_s)c_0 + \lambda_s p_0}{2\mu_s(3\lambda_s + 2\mu_s)} \quad (\text{B.5})$$

$$E_{zz} = \sum_m \left(\frac{-1}{\lambda_c + 2\mu_c} k_m J_0(k_m r) [\mu_s(\alpha_m - \beta_m) + (\lambda_c + 2\mu_s)(\gamma_m + \delta_m)] \right) \quad (\text{B.6})$$

$$- \frac{\lambda_c(\lambda_s + 2\mu_s)c_0 + (\lambda_s\lambda_c + 3\mu_s\lambda_s + 2\mu_s^2)p_0}{\mu_s(3\lambda_s + 2\mu_s)(\lambda_c + 2\mu_c)} \quad (\text{B.7})$$

$$E_{rz} = 0 \quad (\text{B.8})$$

and,

$$T_{rr} = (\lambda_c + 2\mu_c)E_{rr} + \lambda_s(E_{\phi\phi} + E_{zz}), \quad (\text{B.9})$$

$$T_{\phi\phi} = (\lambda_c + 2\mu_c)E_{\phi\phi} + \lambda_s(E_{zz} + E_{rr}), \quad (\text{B.10})$$

$$T_{zz} = (\lambda_c + 2\mu_c)E_{zz} + \lambda_s(E_{rr} + E_{\phi\phi}), \quad (\text{B.11})$$

$$T_{rz} = 0 \quad (\text{B.12})$$

¹The calculation of thermal noise is made with the monolayer approximation: a single-layer coating with the thickness of multilayer coatings is attached on a substrate.

with

$$\alpha_m = \frac{p_m(\lambda_s + 2\mu_s)}{k_m\mu_s(\lambda_s + \mu_s)} \frac{1 - Q_m + 2k_m h Q_m}{(1 - Q_m)^2 - 4k_m^2 h^2 Q_m}, \quad (\text{B.13})$$

$$\beta_m = \frac{p_m(\lambda_s + 2\mu_s)Q_m}{k_m\mu_s(\lambda_s + \mu_s)} \frac{1 - Q_m + 2k_m h}{(1 - Q_m)^2 - 4k_m^2 h^2 Q_m}, \quad (\text{B.14})$$

$$\gamma_m = -\frac{p_m}{2k_m\mu_s(\lambda_s + \mu_s)} \frac{[2k_m^2 h^2(\lambda_s + \mu_s) + 2\mu_s k_m h]Q_m + \mu_s(1 - Q_m)}{(1 - Q_m)^2 - 4k_m^2 h^2 Q_m}, \quad (\text{B.15})$$

$$\delta_m = -\frac{p_m Q_m}{2k_m\mu_s(\lambda_s + \mu_s)} \frac{2k_m^2 h^2(\lambda_s + \mu_s) + 2\mu_s k_m h + \mu_s(1 - Q_m)}{(1 - Q_m)^2 - 4k_m^2 h^2 Q_m} \quad (\text{B.16})$$

$$Q_m = \exp^{-2k_m h}, \quad (\text{B.17})$$

$$k_m = \frac{\zeta_m}{a}, \quad (\text{B.18})$$

$$p_m = \frac{\exp^{-k_m^2 \omega_0^2 / 8}}{\pi a^2 J_0^2(\zeta_m)}, \quad (\text{B.19})$$

$$p_0 = \frac{1}{\pi a^2}, \quad (\text{B.20})$$

$$c_0 = \frac{6a^2}{h^2} \sum_m \frac{J_0(\zeta_m) p_m}{\zeta_m^2} \quad (\text{B.21})$$

where ζ_m are the zeros of the Bessel function $J_1(x)$, ω_0 is the beam radius, λ and μ are the Lamé coefficients of the substrate and the coating, shown by the indices s and c respectively.

Using this equation, we can see the dependence of coating Brownian noise in respect to the mirror thickness in the case of a cylindrical mirror:

- for $h \gg a$, coating Brownian noise agrees with an infinite mirror approximation
- for $h < a$, coating Brownian noise increase as h^{-2} and it is significantly higher than infinite mirror approximation.

This result allows us to have an estimate of the coating Brownian noise when we change the mirror parameters.

Appendix C

Matlab Codes Used for Noise Source Simulations

Matlab codes used for the noise source simulations can be found in this link: https://gilsay.physics.gla.ac.uk/dokuwiki/doku.php?id=igr-public:kyung_ha_thesis_code

- List of constants: list_constants.m
- Mass optimisation: Figs3_4.m
- Seismic noise (longitudinal): long_seis_approx.m
- Seismic noise (vertical): vertical_seis_approx.m
- Suspension thermal noise: total_sus_therm.m
- Coating Brownian noise: total_coating_therm_final.m
- Final noise strain result: func_test.m

Appendix D

Python Code Used for the Stress Corrosion Experiment

The Python code used for the stress corrosion experiment can be found in this link: https://gilsay.physics.gla.ac.uk/dokuwiki/doku.php?id=igr-public:kyung_ha_thesis_code

- File name: DetectorV5.16setup.py

Appendix E

Peak pixel intensity and fibre diameter

In Figure E.1 in Chapter 4 Section 4.5, only the middle region of the fibre was shown to emphasise the correlation between the peak pixel intensity stability and corresponding fibre diameter variation. In this section, the same comparison between peak pixel intensity and fibre diameter is presented for the whole fibre. Figure E.1 shows a peak pixel intensity variation during a pull and corresponding fibre diameter profile.

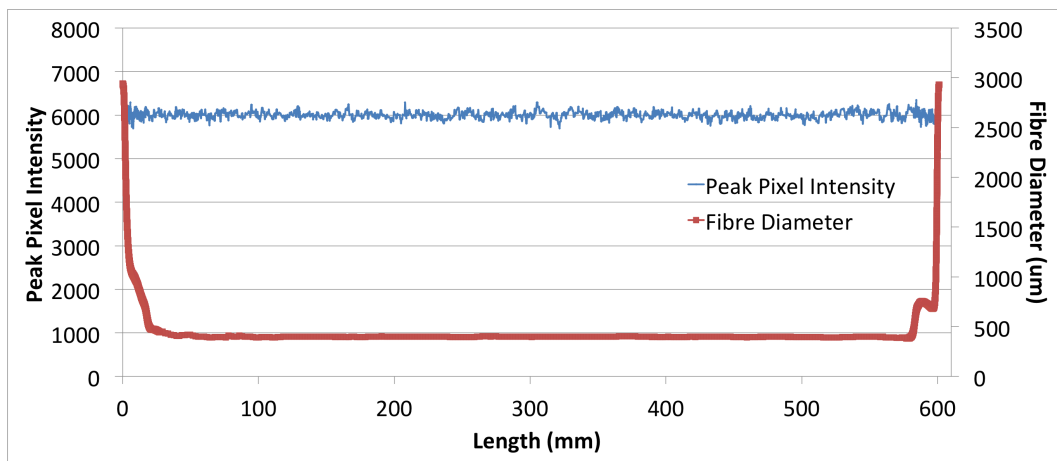


Figure E.1: Peak pixel intensity variation during a pull and corresponding fibre diameter profile.

Bibliography

- [1] A. Einstein. The Foundation of the General Theory of Relativity. *Annalen de Physik* 49, 6769, 1916.
- [2] G. Harry and et al. (LIGO Scientific Collaboration). Advanced LIGO: the next generation of gravitational wave detectors. *Class. Quant. Grav*, 27(8):084006, 2010.
- [3] P. Saulson. *Fundamentals of Interferometric Gravitational Wave Detectors*. World Scientific Publishing Co. Pte. Ltd, 1994.
- [4] <https://www.nasa.gov/goddard>, (2018).
- [5] M. Gilfanov and A. Bogdan. An upper limit on the contribution of accreting white dwarfs to the type 1a supernova rate. *Nature*, Vol. 463, pp. 924-925, 2010.
- [6] A. Alsabti and P. Murdin. *Handbook of Supernovae*. Springer International Publishing, 2017.
- [7] E. Chaisson and S. McMillan. *Astronomy today*. Prentice Hall Upper Saddle River, NJ, 2005.
- [8] S. Chandrasekhar. Stellar cconfiguration with degenerate cores. *The Observatory* 57, 373, 1934.

-
- [9] C. Cutler and K. Thorne. An Overview of Gravitational-Wave Sources. *General Relativity and Quantum Cosmology*, *arXiv:gr-qc/0204090*, 2002.
- [10] B. Sathyaprakash and B. Schutz. Physics, astrophysics and cosmology with gravitational waves. *Living Reviews in Relativity*, *Vol. 12, No. 2, pp. 18-19*, 2009.
- [11] C. Ott. The Gravitational Wave Signature of Core-Collapse Supernovae. *Class. Quant. Grav* *26:063001*, 2009.
- [12] B. Sathyaprakash and B. Schutz. Physics, Astrophysics and Cosmology with Gravitational Waves. *Living Reviews in Relativity*, *12, No. 2*, 2009.
- [13] B. Abbott and et al. First low-frequency Einstein@Home all-sky search for continuous gravitational waves in Advanced LIGO data. *Phys. Rev. D* *96*, 2017.
- [14] B. Abbott and Virgo Collaboration) et al. (LIGO Scientific Collaboration. Observation of Gravitational Waves from a Binary Black Hole Merger. *Phys. Rev. Lett.* *116, 061102*, 2016.
- [15] B. Abbott and Virgo Collaboration) et al. (LIGO Scientific Collaboration. GW151226: Observation of Gravitational Waves from a 22-Solar-Mass Binary Black Hole Coalescences. *Phys. Rev. Lett.* *116, 241103*, 2016.
- [16] B. Abbott and Virgo Collaboration) et al. (LIGO Scientific Collaboration. GW170104: Observation of a 50-Solar-Mass Binary Black Hole Coalescences at Redshift 0.2. *Phys. Rev. Lett.* *118, 221101*, 2017.
- [17] B. Abbott and et al. (LIGO Scientific Collaboration). GW170608: Observation of a 19 Solar-mass Binary Black Hole Coalescence. *Astrophys. J. Lett., Volume 851, Number 2*, 2017.
- [18] B. Abbott and et al. (LIGO Scientific Collaboration). GW170814: A Three-Detector Observation of Gravitational Waves from a Binary Black Hole Coalescence. *Phys. Rev. Lett.* *119, 141101*, 2017.

-
- [19] B. Abbott and Virgo Collaboration) et al. (LIGO Scientific Collaboration. GW170817: Observation of Gravitational Waves from a Binary Neutron Star Inspiral. *Phys. Rev. Lett.* 119, 161101, 2017.
- [20] B. Schutz. *The Detection of Gravitational Waves. in Proceedings of the 1995 Houches School on Astrophysical Sources of Gravitational Radiation.* Springer Berlin, 1996.
- [21] D. Blair, E. Howell, L. Ju, and C. Zhao. *Advanced Gravitational Wave Detectors.* Cambridge University Press, 2012.
- [22] A. Hewish, S. Bell, F. Pilkington, P. Scott, and R. Collins. Observation of a Rapid Pulsating Radio Source. *Nature Physics* 217, pp. 709-713, 1968.
- [23] U. Kraus, H. Nollert, H. Ruder, and H. Riffert. Analyzing X-ray pulsar profiles: Asymmetry as a key to geometry and beam pattern. *The Astrophysical Journal*, 450:763-783, 1995.
- [24] R. Hulse and J. Taylor. Discovery of a pulsar in a binary system. *Astrophys. J. Lett.*, 195 pp 51-53, 1975.
- [25] R. Hulse. The discovery of the binary pulsar. *Reviews of Modern Physics*, 66: p.699, 1994.
- [26] J. Taylor. Binary pulsars and relativistic gravity. *Reviews of Modern Physics*, 66: p.711, 1994.
- [27] B. Abbott and et al. Coherent search for periodic gravitational waves from unknown isolated sources and Scorpius X-1: results from the second LIGO science run. *Phys. Rev. D*76:082001, 2007.
- [28] B. Abbott and et al. Upper limits on gravitational wave emission from 78 radio pulsars. *Phys. Rev. D*, Vol. 76, No. 4, 042001, 2007.

-
- [29] R. Wagoner. Gravitational radiation from accreting neutron stars. *Astrophysical Journal*, Vol. 22, pp. 345-348, 1984.
- [30] X. Siemens, V. Mandic, and J. Creighton. Gravitational wave stochastic background from cosmic strings. *Phys. Rev. Lett.* 98, 111101, 2007.
- [31] J. Hough and et al. Proposal for a joint German-British Interferometric gravitational wave detector. *Max-Planck Institute fur Quantenopik Report*, 147, 1989.
- [32] B. Abbott and et al. LIGO: the Laser Interferometer Gravitational-Wave Observatory. *Reports on Progress in Physics*, 72 (7), 2009.
- [33] J. Weber. Detection and generation of gravitational waves. *Phys. Rev.* 117, 306, 1960.
- [34] J. Weber. Evidence for discovery of gravitational radiation. *Phys. Rev. Lett.* 22, 1320, 1969.
- [35] J. Weber. Gravitational-wave-detector events. *Phys. Rev. Lett.* 20, 1307, 1968.
- [36] J. Weber. Anisotropy and polarization in the gravitational-radiation experiments. *Phys. Rev. Lett.* 25, 180, 1970.
- [37] J. Hough. Search for continuous gravitational radiation. *Nature* 254, 498, 1975.
- [38] J. Levine. Absence of Gravity-Wave signals in a bar at 1695 Hz. *Phys. Rev. Lett.* 31, 173, 1973.
- [39] M. Cerdonio, L. Franceschini, and G. Fontant. Status of the AURIGA gravitational wave antenna and perspectives for the gravitational waves search with ultracryogenic resonant detectors. *Gravitational Wave Experiments*, pp. 176-194, 1995.
- [40] M. Cerdonio and et al. The ultracryogenic gravitational-wave detector AURIGA. *Class. Quant. Grav*, vol. 14, no. 6, p. 1491, 1997.

-
- [41] P. Astone and et al. Long-term operation of the Rome "Explorer" cryogenic gravitational wave detector. *Phys. Rev. D*, vol. 47, no. 2, p. 362, 1993.
- [42] P. Astone, M. Bassan, and P. Bonifazi. The EXPLORER gravitational wave antenna: recent improvements and performances. *Class. Quant. Grav*, vol. 19, pp. 1905-1910, 2002.
- [43] P. Astone and et al. The gravitational wave detector NAUTILUS operating at $t=0.1k$. *Astropart. Phys.*, vol. 7, no. 3, pp. 231-243, 1997.
- [44] M. McHugh, Z. Allen, and W. Hamilton. The ALLEGRO gravitational wave detector. In *The Ninth Marcell Grossmann Meeting*, 2002.
- [45] E. Mauceli, M. McHugh, W. Hamilton, W. Johnson, and A. Morse. Search for periodic gravitational radiation with the ALLEGRO gravitational wave detector. *arXiv preprint gr-qc/0007023*, 2000.
- [46] P. Astone, L. Baggio, and M. Bassan. IGEC2: A 17-month search for gravitational wave bursts in 2005-2007. *Phys. Rev. Lett. D*, vol. 82, no. 2, p. 022003, 2010.
- [47] O. Aguiar. Past, present and future of the Resonant-Mass gravitational wave detectors. *Res. Astron. Astrophys.*, Vol. 11, No. 1, 2010.
- [48] J. Aasi and Virgo Collaboration) et al. (LIGO Scientific Collaboration. Advanced LIGO. *Class. Quant. Grav.* 32, 074001, 2015.
- [49] H. Luck. Status of the Gravitational-Wave Detector GEO600 (LIGO Document P070061), 2007.
- [50] F. Acernese and et al. Advanced Virgo: a 2nd generation interferometric gravitational wave detector. *Class. Quant. Grav.* 32, 024001, 2015.
- [51] K. Kuroda and et al. (LCGT Collaboration). Status of LCGT. *Class. Quant. Grav.* 27, 084004 (8pp), 2010.

-
- [52] B. Iyer and et al. LIGO-M1100296, LIGO-India: Proposal of the Consortium for Indian Initiative in Gravitational-wave Observation (IndIGO). 2012.
- [53] T. Souradeep. LIGO-G1600673, LIGO-India. 2016.
- [54] S. Fairhurst. Triangulation of gravitational wave source with a network of detectors. *New Journal of Physics*, Vol. 13, 2011.
- [55] Outline world map blank, <http://atlantislsc.com/outline-world-map/outline-world-map-blank-world-map-black-and-white-johomaps-my-maps/>, 2018.
- [56] M. Gertsenshtein and V. Pustovoit. On the Detection of Low Frequency Gravitational Waves. *Soviet Physics JETP*, Volume 16, Number 2, 1962.
- [57] R. Forward. WidWaves laser-interferometer gravitational-radiation experiment. *Phys. Rev. D*, 17, 379, 1978.
- [58] A. Michelson. On the Relative Motion of the Earth and the Luminiferous Ether. *The American Journal of Science*, 34, 333, 1887.
- [59] T. Fricke and et al. DC readout experiment in Enhanced LIGO. *Class. Quant. Grav.* 29 065005, 2012.
- [60] A. Buonanno, Y. Chen, and N. Mavalvala. Quantum noise in laser-interferometer gravitational-wave detectors with a heterodyne readout scheme. *Phys. Rev. D* 67, 122005, 2003.
- [61] P. Fritschel and et al. Readout and control of a power-recycled interferometric gravitational-wave antenna. *Applied Optics*, Vol. 40, Issue. 28, pp. 4988-4998, 2001.
- [62] LIGO/Caltech/MIT/LSC. Laser Interferometer Gravitational-Wave Observatory, <http://www.ligo.caltech.edu>, 2017.
- [63] A. Chaudhuri. Gravitational wave for a pedestrian, arxiv:1605.00761. 2016.

-
- [64] B. Meers. Recycling in laser-interferometric gravitational-wave detectors. *Phys. Rev. D*, Vol. 38, No. 8, pp. 2317-2326, 1988.
- [65] J. Smith and et al. (LIGO Scientific Collaboration). The path to the enhanced and advanced ligo gravitational-wave detectors. *Class. Quant. Grav.*, Vol. 26, No. 11, 114013, 2009.
- [66] K. Strain and B. Meers. Experimental demonstration of dual recycling for interferometric gravitational wave detectors. *Phys. Rev. Lett.*, Vol. 66, No. 11, pp. 1391-1394, 1991.
- [67] K. Dooley, T. Akutsu, S. Dwyer, and P. Puppó. Status of advanced ground-based laser interferometers for gravitational-wave detection. *Journal of Physics: Conference Series* 610, 012012, 2015.
- [68] A. Buonanno and Y. Chen. Quantum noise in second generation, signal-recycled laser interferometric gravitational-wave detectors. *Phys. Rev. D* 64, p. 042006, 2001.
- [69] G. Hammond, S. Hild, and P. Pitkin. Advanced technologies for future ground-based, laser-interferometric gravitational wave detectors. *Journal of Modern Optics*, vol. 61, no. S1, pp. S10-S45, 2014.
- [70] Gravitational Wave Interferometer Noise Calculator, <https://awiki.ligo-wa.caltech.edu/wiki/GWINC>, 2016.
- [71] F. Acernese and et al. (The Einstein Telescope Collaboration). Einstein gravitational wave telescope conceptual design study. Technical report, European Gravitational Observatory, Issue 3, ET-0106A-10, 2011.
- [72] S. Aston and et al. Update on quadruple suspension design for Advanced LIGO. *Class. Quant. Grav.* 29, 235004 (25pp), 2012.

-
- [73] A. Effler and et al. Environmental Influences on the LIGO Gravitational Wave Detectors during the 6th Science Run. *Class. Quant. Grav* 32, No. 3, 035017, 2015.
- [74] B. Shapiro, D. Madden-Fong, and B. Lantz. LIGO III Quad Pendulum Conceptual Design Optimization. Technical Report LIGO-T1300786-v7, LIGO Collaboration, 2014.
- [75] P. Saulson. Terrestrial gravitational noise on a gravitational wave antenna. *Phys. Rev. D*, 30, 732, 1984.
- [76] J. Driggers, J. Harms, and R. Adhikari. Subtraction of newtonian noise using optimized sensor arrays. *Phys. Rev. D*, vol. 86, pp. 102001-1, 2012.
- [77] J. Driggers and et al. Active noise cancellation in a suspended interferometer. *Rev. Sci. Instrum.* 83, 024501, 2012.
- [78] J. Harms, R. DeSalve, S. Dorsher, and V. Mandic. Simulation of underground gravity gradients from stochastic seismic fields. *General Relativity and Quantum Cosmology*, *arXiv:0909.3341 [gr-qc]*, 2009.
- [79] KAGRA Collaboration. The status of KAGRA underground cryogenic gravitational wave telescope. *arXiv:1710.04823 [gr-qc]*, 2017.
- [80] B. Puntaro and et al. The Einstein Telescope: a third-generation gravitational wave observatory. *Class. Quant. Grav.* 27 194002, 2010.
- [81] G. Cella. LIGO-G060331, Underground reduction of gravity gradient noise. 2006.
- [82] K. Danzmann and et al. (LISA study team). LISA: laser interferometer space antenna for gravitational wave measurements. *Class. Quant. Grav* 13.11A, A247., 1996.
- [83] P. Amaro-Seoane and et al. Low-frequency gravitational-wave science with eLISA/NGO. *Class. Quant. Grav* 29.12, p. 124016., 2012.

- [84] W. Edelstein, J. Hough, J. Pugh, and W. Martin. Limits to the measurement of displacement in an interferometric gravitational radiation detector. *Journal of Physics E: Scientific Instruments*, vol. 11, no. 7, p. 710, 1978.
- [85] B. Picinbono and C. Bendjaballah. Photoelectron shot noise. *Journal of Mathematical Physics*, vol. 11, no. 7, 1970.
- [86] T. Corbitt and N. Mavalvala. Quantum noise in gravitational-wave interferometers. *J Opt. B: Quantum Semiclass. Opt.*, Vol. 6, No. 8, 2003.
- [87] C. Caves. Quantum-mechanical noise in an interferometer. *Phys. Rev. D* 23, pp. 1693-1708., 1981.
- [88] H. Vahlbruch and et al. The GEO 600 squeeze light source. *Class. Quant. Grav* 27, No. 8, 084027, 2010.
- [89] M. Zucker and et al. A+ Proposal Documents. 2018.
- [90] E. Gustafson, D. Shoemaker, K. Strain, and R. Weiss. LIGO-T990080: White Paper on Detector Research and Development.
- [91] A. Ueda and et al. Ultra-High Quality Cavity with 1.5 ppm Loss at 1064 nm. *Opt. Rev.* 3, 369-372, 1996.
- [92] S. Reid and I. Martin. Development of Mirror Coatings for Gravitational Wave Detectors. *Coatings* 6.4, 2016.
- [93] F. Bondu, P. Hello, and Y. Vinet. Mirror thermal noise in interferometric gravitational wave detectors. *Phys. Lett. A*, 246:227-236, 1998.
- [94] Y. Liu and K. Thorne. Thermoelastic noise and homogeneous thermal noise in finite sized gravitational-wave test masses. *Phys. Rev. D*, 62:122002, 2000.
- [95] LIGO - Laser Interferometer Gravitational-Wave Observatory, <http://www.ligo.caltech.edu>, 2007.

-
- [96] L. Carbone and et al. Sensors and actuators for the Advanced LIGO mirror suspensions. *Class. Quant. Grav*, Vol. 29, No. 11, 115005, 2012.
- [97] E. Chassande-Mottin. Data analysis challenges in transient gravitational-wave astronomy. *arXiv:1210.7173 [gr-qc]*, 2013.
- [98] Somiya lab, <http://www.gravity.ircs.titech.ac.jp>, 2015.
- [99] B. Abbott and et al. (LIGO Scientific Collaboration). Astrophysical implications of the binary black hole merger GW150914. *Astrophys. J. Lett.*, 818:L22 (15pp), 2016.
- [100] B. Abbott and et al. Tests of General Relativity with GW150914. *Phys. Rev. Lett.* 116, 221101, 2016.
- [101] J. Healy, C. Lousto, and Y. Zlochower. Remnant mass, spin, and recoil from spin aligned black-hole binaries. *Phys. Rev. D* 90, 104004, 2014.
- [102] C. Mishra, K. Arun, B. Iyer, and B. Sathyaprakash. Parametrized tests of post-Newtonian theory using Advanced LIGO and Einstein Telescope. *Phys. Rev. D* 82, 064010, 2010.
- [103] C. Will. Bounding the mass of the graviton using gravitational-wave observations of inspiral compact binaries. *Phys. Rev. D* 57, 2061, 1998.
- [104] B. Abbott and et al. The rate of binary black hole merger inferred from Advanced LIGO observations surrounding GW150914. *Astrophys. J. Lett.*, Vol. 833, No. 1, 2016.
- [105] W. Farr, J. Gair, I. Mandel, and C. Cutler. Counting and confusion: Bayesian rate estimation with multiple populations. *Phys. Rev. D* 91, 023005, 2015.
- [106] L. Singer and et al. The first two years of electromagnetic follow-up with Advanced LIGO and Virgo. *The Astrophysical Journal*, Vol. 795, No. 2, 2014.

-
- [107] B. Abbott and et al. Multi-messenger Observations of a Binary Neutron Star Merger. *Astrophys. J. Lett.*, 848:L12, 59pp, 2017.
- [108] V. Savchenko and et al. INTEGRAL Detection of the First Prompt Gamma-Ray Signal Coincident with the Gravitational-wave Event GW170817. *Astrophys. J. Lett.* 848, p. L15., 2017.
- [109] A. Kienlin, C. Meegan, and A. Goldstein. GRINTEGRAL: Fermi GBM detection. *GRB Coordinates Network, Circular Service, No. 21520*, 2017.
- [110] A. Goldstein and et al. An Ordinary Short Gamma-Ray Burst with Extraordinary Implications: Fermi-GBM Detection of GRB 170817A. *Astrophys. J. Lett.*, Vol. 848, No. 2, 2017.
- [111] B. Abbott and et al. A gravitational-wave standard siren measurement of the hubble constant. *Nature*, 551 (7678), 85-88, 2017.
- [112] P. Ade and et al. Planck 2015 results. XIII. Cosmological parameters. *A&A* 594, A13, 2016.
- [113] B. Abbott and et al. Gravitational Waves and Gamma-Rays from a Binary Neutron Star Merger: GW170817 and GRB 170817A. *Astrophys. J. Lett.*, 848:L13, 27pp, 2017.
- [114] I. Arcavi and et al. Optical emission from a kilonova following a gravitational-wave-detected neutron-star merger. *Nature*, 551 (7678), 2017.
- [115] M. Drout and et al. Light Curves of the Neutron Star Merger GW170817/SSS17a: Implications for R-Process Nucleosynthesis. *Science*, 358, 6370, pp. 1570-1574, 2017.
- [116] M. Zucker and et al. (LIGO Scientific Collaboration). LIGO-M1800040, The A+ Upgrade: Expanding the Advanced LIGO Horizon. 2018.

-
- [117] K. Kuroda, M. Ohashi, and S. Miyoki. Large-scale cryogenic gravitational wave telescope. *International Journal of Modern Physics D*, Vol. 8, pp. 557-579, 1999.
- [118] M. Puntaro, M. Abernathy, and F. Acernese. The third generation of gravitational wave observatories and their science reach. *Class. Quant. Grav.*, Vol. 27, No. 8, 084007, 2010.
- [119] D. McClelland and et al. LIGO-T1500290: Instrument Science White Paper 2015. Technical report, LIGO Scientific Collaboration, 2015.
- [120] B. Abbott and Virgo Collaboration) et al. (LIGO Scientific Collaboration. Exploring the Sensitivity of Next Generation Gravitational Wave Detectors. *Class. Quant. Grav.* 34, 044001, 2017.
- [121] C. Moore, R. Cole, and C. Berry. Gravitational Wave Detectors and Sources, <http://gwplotter.com/>, 2018.
- [122] K. Danzmann and et al. LISA: Unveiling a Hidden Universe. Report No. ESA/SRE2011, 2011.
- [123] M. Armano and et al. Sub-femto-g free fall for space-based gravitational wave observations: LISA Pathfinder results. *Phys. Rev. Lett.*, Vol. 116, No. 23, 231101, 2016.
- [124] P. McNamara and et al. (LISA Pathfinder Science Working Team). LISA Pathfinder. *Class. Quant. Grav.*, Vol. 25, 114034, 2008.
- [125] M. Armano and et al. Beyond the Required LISA Free-Fall Performance: New LISA Pathfinder Results down to 20 μ Hz. *Phys. Rev. Lett.*, 120, 061101, 2018.
- [126] G. Ciani and et al. Lisa technologies in new light: exploring alternatives for charge management and optical bench construction. *IAU General Assembly*, Vol. 22, 57787, 2015.

-
- [127] A. Einstein. On the Molecular-Kinetic Theory of Heat Required by the Motion of Particles in Stationary Liquids. *Ann. Phys.* 17, p. 549, 1905.
- [128] R. Brown. A brief account of microscopical observations on the particles contained in the pollen of plants. *Edinburgh New Philos. J.*, p. 358, 1828.
- [129] A. Einstein. *Investigation on the Theory of Brownian Motion*. Dover Publications, Inc., 1956.
- [130] H. Callen and R. Greene. On a Theorem of Irreversible Thermodynamics. *Phys. Rev.* 86, 702, 1952.
- [131] H. Callen and T. Welton. Irreversibility and Generalized Noise. *Phys. Rev.* 83, 34, 1951.
- [132] P. Fritschel and M. Evans. LIGO-T1000175: Thinner Compensation Plates for Reduced Squeeze Film Damping. 2010.
- [133] S. Penn and et al. High quality factor measured in fused silica. *Rev. Sci. Instrum.*, vol. 72, no. 9, p. 7630, 2001.
- [134] A. Ageev, B. Palmer, A. De Felice, S. Penn, and P. Saulson. Very high quality factor measured in annealed fused silica. *Class. Quant. Grav.* 21, 3887-3892, 2004.
- [135] S. Traeger, B. Willke, and K. Danzmann. Monolithically suspended fused silica substrates with very high mechanical Q. *Phys. Lett. A*, Vol. 225, Issue 1-3, pp. 39-44, 1997.
- [136] M. Taniwaki, L. Ju, D. Blair, and M. Tobar. Design and verification of low acoustic loss suspension systems for measuring the Q-factor of a gravitational wave detector test mass. *Phys. Lett. A*, Vol. 246, Issue 1-2, pp. 37-42, 1998.
- [137] A. Gillespie. *Thermal Noise in the Initial LIGO Interferometers*. PhD thesis, California Institute of Technology, 1995.

- [138] Y. Levin. Internal thermal noise in the LIGO test mass: A direct approach. *Phys. Rev. D*, 57, 659, 1998.
- [139] A. Cumming and et al. Design and development of the advanced LIGO monolithic fused silica suspension. *Class. Quant. Grav.* 29 035003, 2012.
- [140] C. Zener. Internal Friction in Solids. *Phys. Rev.*, 52, 230, 1937.
- [141] A. Nowick and B. Berry. *Anelastic relaxation in crystalline solids*. Academic Press, 1972.
- [142] C. Bell and et al. Experimental results for nulling the effective thermal expansion coefficient of fused silica fibres under a static stress. *Class. Quant. Grav*, vol. 31, no. 6, p. 065010, 2014.
- [143] A. Heptonstall. *Characterisation of Mechanical Loss in Fused Silica Ribbons for use in Gravitational Wave Detector Suspensions*. PhD thesis, University of Glasgow, 2004.
- [144] A. Heptonstall and et al. Enhanced characteristics of fused silica fibers using laser polishing. *Class. Quant. Grav.* 31, 105006 (14pp), 2014.
- [145] A. Gretarsson and G. Harry. Dissipation of mechanical energy in fused silica fibers. *Rev. Sci. Instrum.* 70 40817, 1999.
- [146] A. Heptonstall, G. Cagnoli, J. Hough, and S. Rowan. Characterisation of mechanical loss in synthetic fused silica ribbons. *Phys. Lett. A* 354, p. 353-359, 2006.
- [147] A. Gretarsson and et al. Pendulum mode thermal noise in advanced interferometers: a comparison of fused silica fibers and ribbons in the presence of surface loss. *Phys. Lett. A*, 270, p.108-114, 2000.
- [148] S. Rowan and I. Martin. *Optical Coatings and Thermal Noise in Precision Measurement (Substrate thermal noise)*. Optical Coatings and Thermal Noise

- in Precision Measurement (Substrate thermal noise), (New York: Cambridge University Press), 2012.
- [149] O. Anderson and H. Bommel. Ultrasonic absorption in fused silica at low temperatures and high frequencies. *J Am. Ceram. Soc.* 38, 125131, 1955.
- [150] V. Braginsky, V. Mitrofanov, V. Panov, and C. Eller. *Systems with Small Dissipation*. University of Chicago Press, 1985.
- [151] P. Saulson. Thermal noise in mechanical experiments. *Phys. Rev. D* 42, p. 2437., 1990.
- [152] P. Willems, V. Sannibale, J. Weel, and V. Mitrofanov. Investigations of the dynamics and mechanical dissipation of a fused silica suspension. *Phys. Lett. A*, 297, p. 37-48., 2002.
- [153] G. Hammond and et al. Reducing the suspension thermal noise of advanced gravitational wave detectors. *Class. Quant. Grav.* 29, 124009 (12pp), 2012.
- [154] N. Robertson, P. Fritschel, B. Shapiro, C. Torrie, and M. Evans. Design of a tuned mass damper for high quality factor suspension modes in Advanced LIGO. *Rev. Sci. Instrum.* 88, 035117, 2017.
- [155] J. Logan, J. Hough, and N. Robertson. Aspects of the thermal motion of a mass suspended as a pendulum by wires. *Phys. Lett. A*, vol. 183, pp. 145-152, 1990.
- [156] G. Gonzalez and P. Saulson. Brownian Motion of a Mass Suspended by An Anelastic Wire. *J. Acoust. Soc. Am.*, 96(1): p.207-212, 1994.
- [157] A. Bohn. Investigation of Silica Fibers in Advanced LIGO Suspensions.
- [158] J. Blackburn. The laser interferometer gravitational wave observatory project LIGO. *Banach Center Publications*, Vol. 41, Issue 2, pp. 95-135, 1997.

- [159] R. Bork, R. Abbott, D. Barker, and J. Heefner. An Overview of the LIGO Control and Data Acquisition System. In *8th International Conference on Accelerator & Large Experimental Physics Control Systems*, 2001.
- [160] Martynov. E and et al. The Sensitivity of the Advanced LIGO Detectors at the Beginning of Gravitational Wave Astronomy. *Phys. Rev. D*, *93*, 112004, 2016.
- [161] A. Cumming. Aspects of mirrors and suspensions for advanced gravitational wave detectors. *PhD Thesis, University of Glasgow*, 2008.
- [162] G. Hammond. Private Communication. 2015.
- [163] N. Robertson and et al. LIGO-T010103: Advanced LIGO Suspension System Conceptual Design. 2001.
- [164] J. Gair and et al. Exploring intermediate and massive black-hole binaries with the einstein telescope. *Gen Relativ Gravit* *43*: 485., 2011.
- [165] P. Amaro-Seoane and L. Santamaria. Detection of IMBHs with ground-based gravitational wave observatories: A biography of a binary of black holes, from birth to death. *Astrophys.J.**722*:1197-1206, 2010.
- [166] B. Sathyaprakash and et al. Scientific objectives of Einstein Telescope. *Class. Quant. Grav.* *29*, 124013, 2012.
- [167] A. Manzotti and A. Dietz. Prospects for early localization of gravitational-wave signals from compact binary coalescences with advanced detectors. *arXiv:1202.4031 [gr-qc]*, 2012.
- [168] LIGO Seismic SVN, <https://svn.ligo.caltech.edu/svn/seismic/>.
- [169] S. Penn and et al. Frequency and surface dependence of the mechanical loss in fused silica. *Phys. Lett. A*, *352*, 3-6, 2006.
- [170] The GEO Suspension Team. LIGO-T000012, LIGO II Suspension: Reference Designs. 2000.

- [171] K. Somiya and K. Yamamoto. Coating thermal noise of a finite-size cylindrical mirror. *Phys. Rev. D*, *79:102004*, 2009.
- [172] A. Heptonstall and et al. Investigation of mechanical dissipation in CO₂ laser-drawn fused silica fibres and welds. *Class. Quant. Grav.* *27*, *035013.*, 2010.
- [173] Heraeus. Quartz Glass for Optics - Data and Properties.
- [174] A. Heptonstall and et al. CO₂ laser production of fused silica fibers for use in interferometric gravitational wave detector mirror suspensions. *Rev. Sci. Instrum.* *82*, *011301.*, 2011.
- [175] B. Proctor and I. Whitney. The strength of fused silica, Proceedings of the Royal Society of London. Series A. *Mathematical and Physical Sciences* *297*, *534*, 1967.
- [176] R. Paschotta. Mode hopping.
- [177] H. Schick. A Thermodynamic Analysis of the High-temperature Vaporization Properties of Silica. *Chem. Rev.* *60* (*4*), 1960.
- [178] Inc. FLIR Systems. <http://www.flir.com/science/display/?id=46623>, 2017.
- [179] B. Schwarz, G. Ritt, M. Koerber, and B. Eberle. Laser-induced damage threshold of camera sensors and micro-optoelectromechanical systems. *Optical Engineering.* *56*(*3*), *034108*, 2017.
- [180] A. Cumming and et al. Apparatus for dimensional characterization of fused silica fibers for the suspensions of advanced gravitational wave detectors. *Rev. Sci. Instrum.*, *82*, *044502*, 2011.
- [181] R. Jones and et al. LIGO-T1000345-v2, The Design of the IGR MKII Strength Testing Machine (2008). July 2010.
- [182] Araldite Rapid 2-Component Epoxy Adhesive, <http://www.go-araldite.com/products/epoxy-adhesives/araldite-rapid-2-x-15ml-tube>.

-
- [183] VirtualDub v1.10.4, <http://www.virtualdub.org/>.
- [184] A. Cumming. Private Communication. 2016.
- [185] A. Bell and et al. LIGO-E1000366-v9, Pulling/Welding Procedures.
- [186] K. Toland. Ligo hanford stress corrosion experiment.
- [187] T. Michalske and S. Freiman. A molecular mechanism for stress corrosion in vitreous silica. *J. Am. Ceram. Soc.* 66[4] 284-288, 1983.
- [188] W. Duncan, P. France, and S. Craig. "The effect of environment on the strength of optical fiber" in "The Strength of Glass". Plenum, New York, 1985.
- [189] GraphClick 3.0, <https://graphclick.en.softonic.com/mac>.
- [190] K. Toland. Private Communication. 2018.
- [191] Araldite 2012 50 ml Yellow Dual Cartridge Epoxy Adhesive for Various Materials, <https://uk.rs-online.com/web/p/epoxy-resins-adhesives/3888954/>.
- [192] A. Cumming. Private Communication. 2015.
- [193] A. Bell. Private Communication. 2018.
- [194] J. Miller, L. Barsotti, S. Vitale, P. Fritschel, and M. Evans. Prospects for doubling the range of Advanced LIGO. *Phys. Rev. D* 91, 062005, 2015.
- [195] B. Barr and et al. LIGO 3 Strawman design, Team Red. Technical Report LIGO-T1200005-v2, January 2012.
- [196] D. Lay. *Linear Algebra and its Applications, 3rd Edition*. Addison Wesley, 2003.